Die approbierte gedruckte Originalversion dieser Dissertation ist an der TU Wien Bibliothek verfügbar.
The approved original version of this doctoral thesis is available in print at TU Wien Bibliothek.
TU Wien Bibliothek Your knowledge hub

DISSERTATION

Interband cascade lasers and detectors: From active region design to devices

ausgeführt zum Zwecke der Erlangung des akademischen Grades
eines Doktors der technischen Wissenschaften

unter der Leitung von

Assoc.-Prof. Dr. Benedikt Schwarz
Institut für Festkörperelektronik

eingereicht an der

TECHNISCHEN UNIVERSITÄT WIEN
FAKULTÄT FÜR ELEKTROTECHNIK UND INFORMATIONSTECHNIK

von

Dipl.-Ing. Hedwig Maria Knötig

Mat.Nr. 01226234

Wien, im Juli 2022

Die approbierte gedruckte Originalversion dieser Dissertation ist an der TU Wien Bibliothek verfügbar.
The approved original version of this doctoral thesis is available in print at TU Wien Bibliothek.

Die approbierte gedruckte Originalversion dieser Dissertation ist an der TU Wien Bibliothek verfügbar.
The approved original version of this doctoral thesis is available in print at TU Wien Bibliothek.

Betreuer:	Assoc.-Prof. Dr. Benedikt Schwarz
Zweitbetreuer:	Prof. Dr. Gottfried Strasser
1. Gutachter:	Prof. Dr. Mikhail Belkin
2. Gutachter:	Prof. Dr. Karl Unterrainer

Tag der mündlichen Prüfung: 29. August 2022

Die approbierte gedruckte Originalversion dieser Dissertation ist an der TU Wien Bibliothek verfügbar.
The approved original version of this doctoral thesis is available in print at TU Wien Bibliothek.

It's a dangerous business, Frodo, going out your door. You step onto the road, and if you don't keep your feet, there's no knowing where you might be swept off to.

J.R.R. Tolkien

Die approbierte gedruckte Originalversion dieser Dissertation ist an der TU Wien Bibliothek verfügbar.
The approved original version of this doctoral thesis is available in print at TU Wien Bibliothek.
TU Bibliothek
WIEN Your knowledge hub

Abstract

The mid-infrared spectral region presents unrivaled opportunities for the spectroscopy of a vast variety of molecules that exhibit their fundamental roto-vibrational absorption lines in this wavelength range. The rapidly advancing technology of interband cascade devices lasers and detectors is attracting increasing attention from both researchers and industry, as it constitutes an ideal platform for novel integrated photonic sensors.

Interband cascade lasers (ICLs) are especially appreciated for their low threshold current densities and low power consumption, accelerating the development of portable, compact, and battery-driven trace gas sensors. They can be seen as a combination of conventional diode lasers and quantum cascade lasers (QCLs), featuring long upper state lifetimes and a voltage-efficient series connection of multiple active regions. These lasers show a performance sweet spot around 3-4 µm and continuous wave (cw) operation at room temperature has been demonstrated at wavelengths from 2.8-5.6 µm in the GaSb material system. However, extending this range towards longer wavelengths has proven difficult, partly originating from a still insufficient understanding of the internal device physics.

The presented thesis fills in one of the missing puzzle pieces of understanding the underlying physical operation principles of ICLs, shedding light on the causative mechanism degrading device performance outside of the sweet spot region. First, the focus lies on the investigation of intersubband absorption in the active region of ICLs. With the help of simulations and experiments a guideline for mitigating these losses is presented. A causal relationship between the $\mathrm{Ga_{1-x}In_xSb}$ hole quantum well (h-QW) thickness and the valence intersubband absorption is unambiguously proven. In the 4-5 µm region, reducing the layer thickness results in improved performance, which is experimentally confirmed. At a wavelength of 4.35 µm, all performance metrics, in particular the characteristic temperature, threshold current density, slope efficiency, and output power are enhanced. These findings, in a second step, are applied to push the room temperature cw operation limit of GaSb-based ICLs beyond 6 µm.

The second topic explored in this thesis is the realization of vertically emitting single-mode ring ICLs. Although frequency combs are gaining momentum, for the vast majority of sensitive sensing schemes lasing in a single spectral mode is an essential prerequisite. Moreover, this device concept offers the possibility of wafer-level testing due to the vertical light emission, which furthermore allows for the integration of the devices in a 2D array. The realization of these devices, including fabrication and achieved performance is discussed. Single-mode emission is observed

in cw operation up to a temperature of 38 °C. This is imperative for sensor miniaturization, avoiding bulky components for cooling. Hence, these results lay a solid foundation for the implementation of devices in compact, possibly battery-powered sensors.

Photodetectors are essential components for spectroscopy, optical communication, and are also imperative for laser characterization. The third topic of this thesis revolves around interband cascade infrared photodetectors (ICIPs). This newly emergent class of mid-infrared detectors features a broad spectral bandwidth, high sensitivity as well as high-speed performance. Devices employing InAs/GaSb superlattice absorbers are realized and investigated. Their tremendous potential for high-speed operation is indisputably confirmed by implementing fully-packaged ICIPs realized during the course of this thesis for two applications: free-space optical communication and the characterization of the temporal waveform and phase-coherence of semiconductor frequency combs.

Die approbierte gedruckte Originalversion dieser Dissertation ist an der TU Wien Bibliothek verfügbar.
The approved original version of this doctoral thesis is available in print at TU Wien Bibliothek.
TU WIEN Bibliothek Your knowledge hub

Die approbierte gedruckte Originalversion dieser Dissertation ist an der TU Wien Bibliothek verfügbar.
The approved original version of this doctoral thesis is available in print at TU Wien Bibliothek.

Kurzfassung

Der mittlere Infrarotbereich bietet unvergleichliche Möglichkeiten für die Spektroskopie einer Vielzahl von Molekülen, die in diesem Wellenlängenbereich ihre fundamentalen Absorptionsbanden aufweisen. Die sich rasch entwickelnde Technologie der Interbandkaskadenlaser und -detektoren findet sowohl in der Forschung als auch in der Industrie zunehmend Beachtung, da sie eine ideale Plattform für neuartige integrierte photonische Sensoren darstellt.

Interbandkaskadenlaser werden besonders wegen ihrer niedrigen Schwellenstromdichte und dem geringen Stromverbrauch geschätzt und beschleunigen so die Entwicklung von tragbaren, kompakten und batteriebetriebenen Spurengassensoren. Sie können als Kombination aus konventionellen Diodenlasern und Quantenkaskadenlasern gesehen werden. Als solche zeichnen sie sich durch lange obere Zustandslebensdauern und eine spannungseffiziente Reihenschaltung mehrerer aktiver Bereiche aus. Diese Laser weisen einen Leistungs-Sweetspot bei 3-4 µm auf und der Dauerstrichbetrieb bei Raumtemperatur wurde bei Wellenlängen von 2.8-5.6 µm im GaSb-Materialsystem nachgewiesen. Die Ausweitung dieses Wellenlängenbereichs hat sich jedoch als schwierig erwiesen, was teilweise auf ein noch unzureichendes Verständnis der internen Physik des Bauelements zurückzuführen ist.

Die vorliegende Arbeit stellt eines der fehlenden Puzzlestücke zum Verständnis der zugrundeliegenden physikalischen Funktionsprinzipien von Interbandkaskadenlasern dar, indem sie den ursächlichen Mechanismus beleuchtet, der die Leistung der Bauelemente außerhalb des Sweetspot-Bereichs beeinträchtigt. Zunächst liegt der Schwerpunkt auf der Untersuchung der Intersubbandabsorption im aktiven Bereich von Interbandkaskadenlasern. Mit Hilfe von Simulationen und Experimenten wird ein Leitfaden zur Abschwächung dieser Verluste vorgestellt. Ein kausaler Zusammenhang zwischen der $\mathrm{Ga_{1-x}In_xSb}$ Loch-Quantentopf-Dicke und der Valenz-Intersubbandabsorption wird eindeutig nachgewiesen. Im Bereich von 4-5 µm führt eine Verringerung der Schichtdicke zu einer verbesserten Leistung, was experimentell bestätigt wird. Bei einer Wellenlänge von 4.35 µm werden alle Leistungskennzahlen, insbesondere die charakteristische Temperatur, die Schwellenstromdichte, die Steigungseffizienz und die Ausgangsleistung verbessert. Diese Erkenntnisse werden in einem zweiten Schritt angewandt, um die Grenze des Dauerstrichbetriebs bei Raumtemperatur von GaSb-basierten Interbandkaskadenlasern über 6 µm hinaus zu erweitern.

Das zweite Thema, das in dieser Arbeit untersucht wird, ist die Realisierung von vertikal emittierenden Single-Mode-Ring-Interbandkaskadenlasern. Obwohl Frequenzkämme immer mehr an Bedeutung gewinnen, ist für die überwiegende Mehr-

heit empfindlicher spektroskopischer Messverfahren die Emission in einer einzigen spektralen Mode eine wesentliche Voraussetzung. Darüber hinaus bietet dieses Bauelementekonzept aufgrund der vertikalen Lichtemission die Möglichkeit des Testens auf Waferebene. Zudem wird die Integration der Bauelemente in einem 2D-Array ermöglicht. Die Realisierung dieser Bauelemente, einschließlich der Herstellung und der erzielten Leistung, wird diskutiert. Single-Mode-Emission wird im Dauerstrichbetrieb bis zu einer Temperatur von 38 °C erreicht. Dies ist für die Miniaturisierung der Sensoren von entscheidender Bedeutung, um sperrige Komponenten zur Kühlung zu vermeiden. Diese Ergebnisse legen somit eine solide Grundlage für die Implementierung der Geräte in kompakten, möglicherweise batteriebetriebenen Sensoren.

Photodetektoren sind unverzichtbare Komponenten für die Spektroskopie, die optische Kommunikation und sind auch für die Charakterisierung von Lasern unabdingbar. Das dritte Thema dieser Arbeit dreht sich um Interbandkaskaden-Infrarot-Photodetektoren. Diese aufstrebende Klasse von Detektoren für das mittlere Infrarot zeichnet sich durch eine große spektrale Bandbreite, hohe Empfindlichkeit und hohe Geschwindigkeit aus. Es wurden Bauelemente mit InAs/GaSb-Übergitterabsorbern realisiert und untersucht. Ihr enormes Potenzial für den Hochgeschwindigkeitsbetrieb wird durch die Implementierung vollständig gehäuster Detektoren, die im Rahmen dieser Arbeit für zwei Anwendungen realisiert wurden, unbestreitbar bestätigt: optische Freiraumkommunikation und die Charakterisierung der zeitlichen Wellenform und Phasenkohärenz von Halbleiter-Frequenzkämmen.

TU Bibliothek
Your knowledge hub
Die approbierte gedruckte Originalversion dieser Dissertation ist an der TU Wien Bibliothek verfügbar.
The approved original version of this doctoral thesis is available in print at TU Wien Bibliothek.

Die approbierte gedruckte Originalversion dieser Dissertation ist an der TU Wien Bibliothek verfügbar.
The approved original version of this doctoral thesis is available in print at TU Wien Bibliothek.
TU WIEN Bibliothek Your knowledge hub

Acknowledgements

If someone had asked me four years ago if I wanted to do a PhD, I would have said no. Well, in fact someone did and I did say no, at least initially. I am eternally grateful for Gottfried Strasser not only asking me if I wanted to do a PhD once, but three times until I was convinced that this was the path that I wanted to follow. His guidance, mentoring and support are truly appreciated.

The credits for the scientific success of this thesis in large parts go to Benedikt Schwarz. In sparking the ideas, he allowed me to find joy in pursuing projects that I deemed meaningful and exciting. Quick papers and results sometimes are not as quick as they might seem, making this especially important. I am deeply thankful for all the scientific discussions and his expertise in the lab, without which none of these projects would have ended in the positive outcome that they did. Apart from his supervision, I am thankful for the many fun evenings and honest conversations.

I want to thank Borislav Hinkov for the supervision on the ring ICL project as well as my master thesis and supporting me in the many ways he did, scientifically as well as not. He shows a lot of understanding combined with good humor, for which I am grateful. I want to thank Erich Gornik for being a true inspiration in forever being passionate about science. I would like to thank my assessors Mikhail Belkin and Karl Unterrainer for sparing the time and putting in the effort to evaluate this thesis as well as taking part in the examination.

A massive thank you goes out to the people at nanoplus and the University of Würzburg, without whom none of the projects presented in this thesis would have been possible. Over the past four years Robert Weih always took the time to share his knowledge on various topics, which I am truly thankful for. I am more than happy to have had the pleasure to work with and meet the genuinely awesome Josephine Nauschütz. Moreover, I am very grateful to Johannes Koeth and Sven Höfling for enabling and supporting this fruitful collaboration.

I thank Pierre Didier, Olivier Spitz and Frédéric Grillot from the LTCI Télécom Paris for the collaboration on the ICIPs for optical communication. Furthermore, a big thank you to Miriam Giparakis for the collaboration on the short wavelength QCDs. Thank you to Stefan Lindner and Bernhard Lendl for the collaboration on the ATMO-SENSE project.

Many more people at the institute helped me in countless ways during the course of my PhD, giving scientific advice, offering support in the cleanroom, manufacturing components (often under immense time pressure) and doing administrative work. For this I want to thank Werner Schrenk, Aaron Maxwell Andrews, Hermann Detz, Martin Holzbauer, Masiar Sistani, Michael Jaidl, Rolf Szedlak, Markus Schinnerl, Anton Tsenov, Andreas Linzer and Christine Brendt.

The past four years have been an emotional rollercoaster, and I am forever grateful for the support and love my friends showed me. They have seen me at my worst and my best, crying my eyes out and laughing uncontrollably. Without Johannes Hillbrand I would be nowhere near to where I am today, and I am deeply grateful for his never-ceasing enthusiasm and his help. I am truly indebted to Sandro Dal Cin who I have always been able to count on and I am thankful for his honesty and always speaking his mind. In not pursuing a PhD I would have missed out on a lot. For once, I would have never made the amazing new friend that I found in Nikola Opačak, who is one of the biggest sources of motivation for me, always pushing through at work and at the gym. Anna Lardschneider has not only given me the best possible holiday experiences over the past years, but is such a genuinely fun and cheerful person that I am thankful to have in my life. Maximilian Beiser is truly always looking out for his friends and I am grateful to call him one of mine. He shows great intuition when it comes to asking the right questions to get to the bottom of things. Florian Pilat is a truly miraculous person, always offering a helping hand, an open ear or if nothing helps a cold beer. More often than not it was a combination of these. I am really counting myself lucky to have been working with people that I was always happy to spend even more time with after work.

The two newest additions to the team have quickly made their way to my heart, making it easy to forget that they have not always been here: Mikołaj Piotrowski and Andreas Windischhofer. Thank you also to Suzanne Lancaster for many good memories, eating cannoli and ice skating. Thank you to the Italian gang (incl. Georg) for many fun conversations and wholehearted laughs at lunch.

To everyone working in the clean room making the countless hours spent there more enjoyable and the waiting times go by in a flash - thank you.

To everyone I spent time with on conferences and project meetings, discussing, drinking, eating, laughing - thank you.

To everyone that contributed to all of the great memories I will forever cherish from countless nights out, playing disc golf, going for lunch together, joking, laughing and having deep conversations with - thank you.

To everyone who I forgot or did not have the space to mention here - I owe you a beer.

My family has given me so much support through it all. I am eternally grateful to my parents for enabling me to follow the path I chose, and my sister for always being there for me no matter what. I know you still will be even if we won't live in the same city anymore.

Die approbierte gedruckte Originalversion dieser Dissertation ist an der TU Wien Bibliothek verfügbar.
The approved original version of this doctoral thesis is available in print at TU Wien Bibliothek.
TU WIEN Bibliothek Your knowledge hub

CONTENTS

1 Introduction **1**

2 Semiconductor fundamentals **5**

2.1 Loss mechanisms in semiconductor lasers 6
  2.1.1 Recombination 6
  2.1.2 Absorption 11
2.2 Modelling 14
  2.2.1 Bloch's theorem 16
  2.2.2 The $\mathbf{k} \cdot \mathbf{p}$ model 16
  2.2.3 Envelope function approximation 22
  2.2.4 Optical transitions 23

3 Interband cascade lasers and detectors **27**

3.1 Interband cascade lasers 28
  3.1.1 State-of-the-art active region 31
  3.1.2 Waveguide 41
  3.1.3 Performance limitations 45
3.2 Interband cascade infrared photodetectors 48
  3.2.1 Functioning principle 48
  3.2.2 State-of-the-art performance 50

4 Active region design of interband cascade lasers **53**

4.1 Motivation 54
4.2 W-quantum well 58
  4.2.1 Design variations of the hole-QW 61
  4.2.2 Experimental investigation at 4.35 µm 69

Die approbierte gedruckte Originalversion dieser Dissertation ist an der TU Wien Bibliothek verfügbar.
The approved original version of this doctoral thesis is available in print at TU Wien Bibliothek.
TU WIEN Bibliothek Your knowledge hub

4.2.3 Experimental investigation beyond 6 µm 80
4.3 Prospects on absorption in the active region 83
4.3.1 Absorption in the hole injector 83
4.3.2 Absorption in the electron injector 89
4.3.3 Experimental indications 90

5 Ring interband cascade lasers 93
5.1 Cavities 94
5.1.1 Fabry-Pérot cavity 94
5.1.2 Ring-shaped cavities 97
5.2 Single mode devices 101
5.2.1 Short cavities 101
5.2.2 External cavity lasers 101
5.2.3 Distributed Bragg reflectors 102
5.2.4 Distributed feedback gratings 104
5.2.5 Single-mode interband cascade lasers 108
5.3 State-of-the-art vertical light emission 109
5.4 Device fabrication 111
5.4.1 Ring interband cascade laser fabrication 115
5.4.2 Geometric considerations 119
5.5 Performance of ring interband cascade lasers 121

6 Interband casdcade infrared photodetectors 129
6.1 Motivation 130
6.2 Realized devices 131
6.2.1 Design and growth 131
6.2.2 Fabrication 134
6.2.3 Performance 135
6.3 High-speed applications 142
6.3.1 Frequency-comb characterization 142
6.3.2 Free-space optical communication 143

7 Conclusion and outlook 145

Bibliography 149

List of Publications 183

Die approbierte gedruckte Originalversion dieser Dissertation ist an der TU Wien Bibliothek verfügbar.
The approved original version of this doctoral thesis is available in print at TU Wien Bibliothek.

Die approbierte gedruckte Originalversion dieser Dissertation ist an der TU Wien Bibliothek verfügbar.
The approved original version of this doctoral thesis is available in print at TU Wien Bibliothek.

CHAPTER 1

INTRODUCTION

Today's research on mid-infrared semiconductor lasers is highly application driven and aims at fulfilling the requirements for a vast range of different areas of operation. While some applications share numerous needs, others differ immensely. Without doubt, the mid-infrared spectral region presents unrivaled opportunities for spectroscopy. A vast variety of molecules exhibit their fundamental roto-vibrational absorption lines in this wavelength range, depicted in Fig. 1.1.

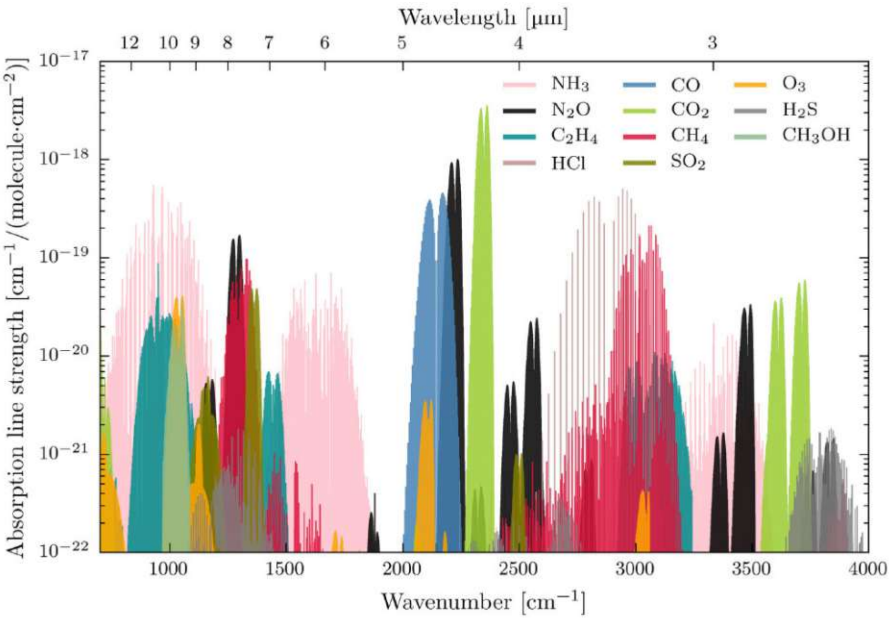

Figure 1.1: Absorption line strength of various gas species in the mid-infrared region. Figure taken from [1].

On the one end portable, battery-driven sensing systems demand for low power consumption, whereas military countermeasures require high output powers. When it comes to light sources, conventional diode lasers, ICLs and QCLs constitute the predominant competing technologies in the mid-infrared. Out of these, ICLs excel when it comes to low threshold currents and low power consumption, making them especially suitable for the realization of compact sensors [2]. However, QCLs outperform them in application scenarios requiring high output powers. In the wavelength range between 3-6 µm ICLs have been employed for the detection of countless molecules, including sulfur dioxide, formaldehyde, methane, ethane, carbon monoxide, carbon dioxide, nitrous oxide and methyl mercaptan [3, 4, 5, 6, 7, 8, 9]. Extending the wavelength range, where ICLs achieve cw operation at room temperature enables to access an increasing amount of absorption lines and continuous effort is made to improve the general performance. High-volume production and testing is of additional interest, when it comes to commercialization. Vertical light-emission offers intriguing advantages over edge-emitting devices in this regard. The quest for ever shrinking dimensions of trace gas sensors make ICL technology increasingly appealing to industry besides proof-of-principle demonstrations. With companies like Nanoplus [10] and VIGO [11], driving the commercialization of mid-infrared light sources and detectors other companies like Aeris [12], NEO Monitors [13] and Airoptic [14] are working on combining these components into gas detection systems, delivering them to the end-user, often for industrial applications.

The topics addressed by the presented thesis all revolve around interband cascade devices, in particular lasers ICLs and detectors ICIPs. The research is not presented in chronological order. Instead, the idea was to tell a coherent story, spanning the three major topics: ICL active region design, ring ICLs and ICIPs for high-speed applications. This is what the title of this thesis is meant to convey 'from active region design to devices' and ultimately their application. While the two first topics mainly fall into the above mentioned area of gas spectroscopy, the purpose for conducting research on ICIPs was initially triggered by the need for high-speed detectors when studying frequency comb characteristics. Although quantum cascade detectors (QCDs) are perfectly suited for this task, they exhibit narrow spectral linewidths. This requires the design, growth and fabrication of a new device, every time the emission wavelength of the studied frequency comb changes. Hence, the broad-band spectrum of ICIPs is more satisfactory for this task, allowing to study frequency combs anywhere between 3-5 µm without the need to exchange the detector.

After the brief introduction in this chapter, chapter 2 is dedicated to equip the reader with the necessary concepts to easily follow chapter 4 on the active region

Die approbierte gedruckte Originalversion dieser Dissertation ist an der TU Wien Bibliothek verfügbar.
The approved original version of this doctoral thesis is available in print at TU Wien Bibliothek.
TU Bibliothek WIEN Your knowledge hub

Die approbierte gedruckte Originalversion dieser Dissertation ist an der TU Wien Bibliothek verfügbar.
The approved original version of this doctoral thesis is available in print at TU Wien Bibliothek.

design of ICLs. The first part is focused on loss mechanisms present in semiconductor lasers, which are divided into recombination and absorption mechanisms. They are introduced in a general way, with an added focus on material systems and heterostructures that are relevant within the context of this thesis. In the second part important concepts employed for the quantitative description of the electronic band structure of semiconductor heterostructures as well as for the transitions between the obtained subbands are presented.

Chapter 3 introduces the device concepts of ICLs and ICIPs in sufficient detail to lay the basis for the subsequent chapters. As the work on ICLs represents the main part of this thesis, this focus reflects in the amount of details provided within this chapter. In addition to a meticulous discussion of design guidelines in literature, performance limitations and open questions are pointed out. Moreover, the current state of the art is highlighted for both devices, setting the stage for the rest of the thesis.

Advances in active region design of ICLs established during the conduction of this thesis are presented in chapter 4. These efforts were targeting the performance improvement of ICLs and provide additional understanding of a performance limiting mechanism previously almost disregarded in literature. Intersubband absorption within the valence band of the light-emitting W-quantum well (QW) is identified as causative mechanism for a performance degradation in the 4-5 µm region. While filling in one of the missing puzzle pieces in understanding the underlying physical operation principles in ICLs, a general design guideline is presented. Experimental evidence underpins and solidifies the theoretical explanations. Subsequently, the design principles are applied and validated for even longer emission wavelengths above 6 µm, unequivocally demonstrating the feasibility of the presented approach. Our results enable high performance cw operation at elevated temperatures as well as increased output powers. Additionally, design modifications of another functional part of ICLs are studied, the hole injector. Once again, both simulations and experimental performance evaluation of realized devices are employed to study adaptations of the heterostructure design.

We leave the active region design of ICLs behind, which is independent of the ultimately chosen device geometry and can in this regard be seen as more fundamental. Our story then moves on to a specific device geometry ring ICLs. The chapter starts by introducing the basic principles necessary for the realization of these devices before proceeding to the achieved results. It covers cavity geometries like Fabry-Pérot and ring cavities, mechanisms to achieve spectral single mode emission, as well as the benefits and state of the art of vertical light emission. A detailed description of the fabrication and achieved performance improvement is given, culminating in the cw emission of these single-mode devices up to a maximum temperature of 38 °C. The chapter concludes with a brief outlook.

The last topic is explored in chapter 6. The investigations conducted on the high-speed characteristics of the realized ICIPs are discussed and two scenarios where these devices are being employed are presented. These broad-band detectors exhibit high photocurrent while still operating sufficiently well around 10 GHz. These properties make them ideally suited for the characterization of mid-infrared frequency combs. Moreover, their applicability for optical free-space communication is demonstrated in an all interband approach for data transmission.

TU WIEN Bibliothek, Your knowledge hub
Die approbierte gedruckte Originalversion dieser Dissertation ist an der TU Wien Bibliothek verfügbar.
The approved original version of this doctoral thesis is available in print at TU Wien Bibliothek.

Die approbierte gedruckte Originalversion dieser Dissertation ist an der TU Wien Bibliothek verfügbar.
The approved original version of this doctoral thesis is available in print at TU Wien Bibliothek.

CHAPTER 2

SEMICONDUCTOR FUNDAMENTALS

In this chapter two fundamental topics are introduced, which are essential for the subsequent chapters, in particular chapter 4. First, loss mechanisms in semiconductor lasers will be discussed, which can be divided into recombination and absorption mechanisms. Particularly the dependence on wavelength and temperature is highlighted and examples of the influence on relevant material systems and heterostructures within the context of this thesis are reviewed. This lays the foundation for the investigation of performance degradating mechanisms in ICLs.

The design of heterostructure optoelectronic devices requires the precise knowledge of the electronic bandstructure. The second part of this chapter introduces important concepts employed for the quantitative description of the electronic band structure of these devices. The essential idea behind the eight-band $\mathbf{k} \cdot \mathbf{p}$ method is described, including spin-orbit coupling and strain effects. After successfully obtaining the electronic bandstructure, the interaction with light is discussed. A general description of how to calculate the absorption between different subbands obtained within the eight-band $\mathbf{k} \cdot \mathbf{p}$ model will be given. The result will be that in order to determine the absorption, the Hamiltonian of the eight-band $\mathbf{k} \cdot \mathbf{p}$ model (or any other derived Hamiltonian) needs to be differentiated with respect to the wavevector along the axis in which the light is polarized. This axis is characterized by the unit vector $\hat{e}$. A generalized expression for the momentum matrix elements for intersubband as well as interband transitions can be used, rendering it obsolete to distinguish between the two different types of transitions. The eight-band $\mathbf{k} \cdot \mathbf{p}$ method and this generalized momentum matrix element model are employed in the simulations presented in chapter 4.

2.1 Loss mechanisms in semiconductor lasers

In order to reach the lasing threshold in any laser, the optical gain needs to overcome the losses. In the following, different loss mechanisms shall be illuminated. In general, they can be divided into two categories: recombination of carriers and absorption of light. While during non-radiative recombination an electron recombines with a hole without generating a photon, absorption reduces the number of already generated photons.

2.1.1 Recombination

At threshold the carrier density required for lasing needs to be maintained by the threshold current, which has to account for all mechanisms, where carriers either recombine or leave the active QW due to leakage. The main recombination processes present in mid-infrared semiconductor lasers are Shockley-Read-Hall (SRH) recombination, radiative recombination, which can be either spontaneous or stimulated, and Auger recombination [15]. Hence, the current density can be written as,

$$J = J_{\mathrm{SRH}} + J_{\mathrm{rad}} + J_{\mathrm{Auger}} + J_{\mathrm{leak}}, \tag{2.1}$$

where the terms on the right side correspond to contributions due to SRH, radiative, and Auger recombination from left to right. The last term relates to injected carriers not recombining within the QW, because they are either insufficiently captured or are lost due to leakage. Leakage can occur if the barrier provided by the conduction band offset of the material is not high enough to block carriers in the high energy tail of the thermal distribution according to the Fermi function. The schematic principles of the different mechanisms are displayed in Fig. 2.1.

Spontaneous emission

Although spontaneous emission is a radiative mechanism, in a laser it constitutes a loss channel. Most photons generated due to spontaneous recombination of carriers do not contribute to lasing, as their phases and direction of emission are uncorrelated. After the spontaneous emission of a photon, the carriers cannot participate in stimulated emission processes anymore, which increases the threshold current.

Shockley-Read-Hall model

The SRH model describes non-radiative carrier recombination that can occur due to trap assisted processes. In a non-ideal semiconductor, traps can arise because

Die approbierte gedruckte Originalversion dieser Dissertation ist an der TU Wien Bibliothek verfügbar.
The approved original version of this doctoral thesis is available in print at TU Wien Bibliothek.

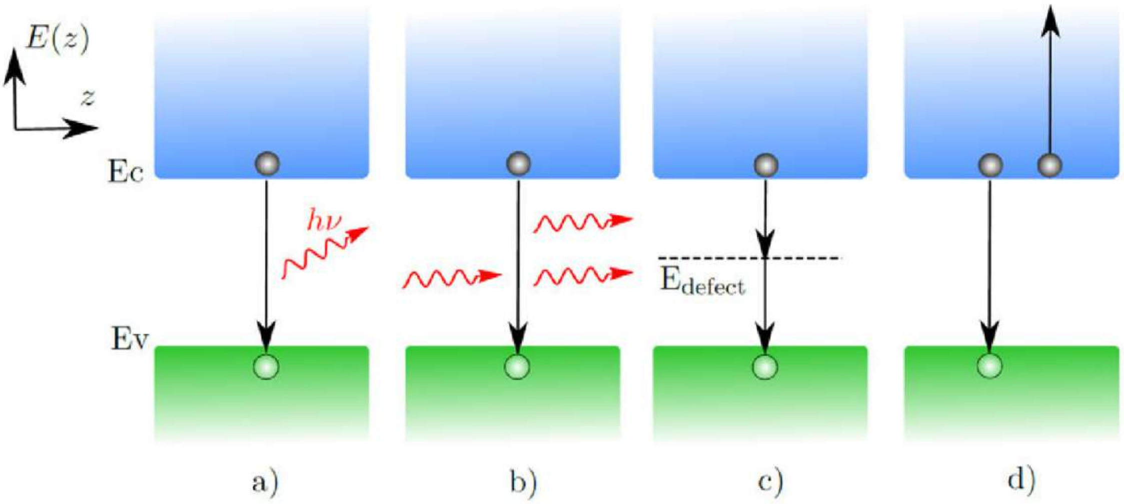

Figure 2.1: Recombination mechanisms in interband lasers: **a)** spontaneous emission, **b)** stimulated emission, **c)** SRH recombination, and **d)** Auger recombination. They are classified as either radiative (a and b) or non-radiative (c and d). Figure reused from [1].

of different crystal defects and impurities in the periodic lattice. These can energetically lie within the bandgap (E$_{\text{defect}}$ in Fig. 2.1c)) and assist in non-radiative recombination of an electron from the conduction band and a hole from the valence band, which was first described by Shockley, Read and Hall in the 50ies [16, 17]. In principle, a trap can induce four different transitions. It can capture an electron from the conduction band, release a previously trapped electron into the conduction band and capture or release a hole from or into the valence band. Trap-assisted recombination can be seen as a sequence of first trapping an electron and then releasing it into the valence band, which corresponds to the capture of a hole. The recombination rate is directly proportional to the density of traps and is, thus, only related to the material quality, meaning that it does not represent a fundamental limit set by the material itself [18]. Thus, high-quality crystal growth is extremely important for the manufacturing of well performing semiconductor lasers. The SRH recombination rate is defined by [17]

$$R_{\text{SRH}} = \frac{np - n_{\text{i}}^2}{t_{\text{p}}(n + n_0) + t_{\text{n}}(p + p_0)}, \tag{2.2}$$

where n, p and n_i denote the injected electron, hole and the intrinsic carrier densities. The time it takes for a trap to capture an electron (hole) from the conduction (valence) band is t_{n} (t_{p}), assuming that all traps are empty (occupied). The parameters n_0 and p_0 represent the carrier concentrations, when the Fermi level coincides

Die approbierte gedruckte Originalversion dieser Dissertation ist an der TU Wien Bibliothek verfügbar.
The approved original version of this doctoral thesis is available in print at TU Wien Bibliothek.

with the trap level E_t, quantified by

$$n_0 = n_\mathrm{i}\left(\frac{E_\mathrm{t} - E_\mathrm{i}}{k_\mathrm{B}T}\right) \quad \& \quad p_0 = n_\mathrm{i}\left(\frac{E_\mathrm{i} - E_\mathrm{t}}{k_\mathrm{B}T}\right). \tag{2.3}$$

Here, E_i denotes the middle of the bandgap. If the injected carrier densities are much larger than the intrinsic one and assumed to be equal ($n = p \gg n_\mathrm{i}$), the recombination rate from Eq. 2.2 simplifies to $R_\mathrm{SRH} \approx n/(t_\mathrm{p} + t_\mathrm{n})$, yielding a linear dependence on the carrier density.

Auger recombination

During an Auger process, instead of a photon being emitted when an electron in the conduction band and a hole in the valence band recombine, the energy is transferred to a third particle, which can either be an electron or a hole. This process needs to abide by the laws of energy and momentum conservation. Subsequently, the third carrier typically relaxes to a lower energy, assisted by phonons, hence, contributing to the heating of the device. Frequently occurring Auger processes are schematically depicted in Fig. 2.2. They are divided and named following the involvement of carriers situated in different bands, in a four-letter notation. The first two letters relate to the recombination of an electron in the conduction band (C) and a hole from the valence band either the heavy hole (H), light hole (L) or split-off band (S). The second set of letters refers to the third carrier and indicates whether it stayed in the same band or moved to a different one due to the acquired energy and momentum. Following this nomenclature, the left-most process in Fig. 2.2 is called CHCC, in-

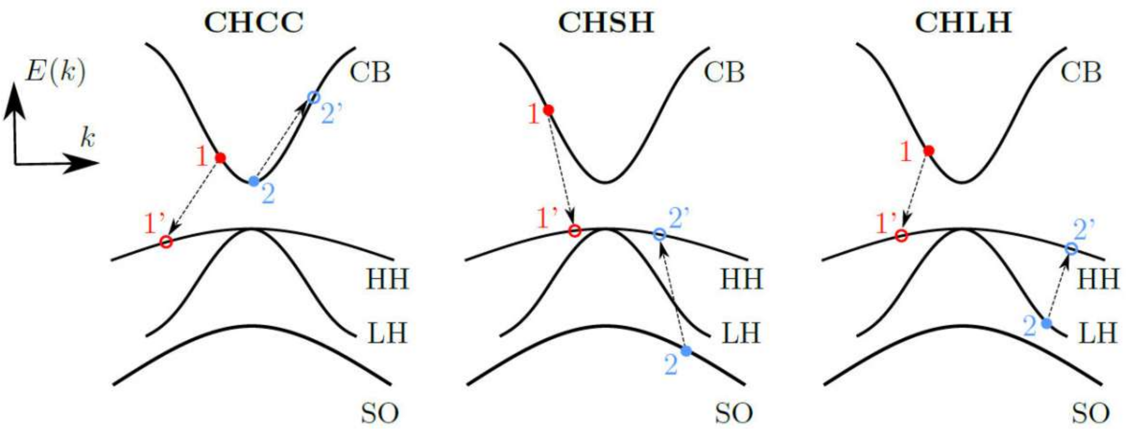

Figure 2.2: Auger recombination processes involving carriers located in different bands, denoted with CB, HH, LH, and SO, for the conduction, heavy hole, light hole and split-off band, respectively. Energy and momentum are conserved, shown with green arrows for the momentum. Figure taken from [1].

Die approbierte gedruckte Originalversion dieser Dissertation ist an der TU Wien Bibliothek verfügbar.
The approved original version of this doctoral thesis is available in print at TU Wien Bibliothek.
TU WIEN Bibliothek Your knowledge hub

Die approbierte gedruckte Originalversion dieser Dissertation ist an der TU Wien Bibliothek verfügbar.
The approved original version of this doctoral thesis is available in print at TU Wien Bibliothek.
TU WIEN Bibliothek Your knowledge hub

dicating that the energy and momentum from the recombination process between carriers in the conduction and heavy hole band (CH) is transferred to an electron that remains in the conduction band (CC). Since these scattering processes involve multiple carriers, the recombination rate is proportional to the densities of the involved carriers. For the multi-electron CHCC process, this relates to $R_{\mathrm{CHCC}} \propto n^2 p$, whereas CHSH and CHLH all involve two holes, yielding $R_{\mathrm{CHSH/CHLH}} \propto np^2$ [19]. If the hole and electron concentrations are assumed to be equal this results in a dependence on the cubed carrier density $R_{\mathrm{Auger}} \propto n^3$.

Looking at the Auger rates in more detail, under the assumptions of parabolic bands and low carrier densities, to which the Boltzmann statistics apply, the CHCC process is quantified by [20]

$$R_{\mathrm{CHCC}} = C_0^{\mathrm{CHCC}}\, e^{-E_{\mathrm{a}}^{\mathrm{CHCC}}/k_{\mathrm{B}}T}\, n^2 p. \tag{2.4}$$

The activation energy is further defined by [21]

$$E_{\mathrm{a}}^{\mathrm{CHCC}} = E_{\mathrm{g}} \frac{m_{\mathrm{CB}}}{m_{\mathrm{CB}} + m_{\mathrm{HH}}}. \tag{2.5}$$

Hence, the recombination rate depends on the band gap energy E_{g} and the in-plane masses of conduction m_{CB} and heavy hole band m_{HH}. For non-degenerate conditions, the highest rate for Auger recombination occurs for the situation, where the three involved carriers have the lowest possible energies that can fulfill the energy and momentum conservation laws. This situation is represented by the activation energy, defined above, which is the sum of the three carrier densities relative to the corresponding band edge [15]. A smaller bandgap or larger heavy hole mass result in a smaller activation energy, making the CHCC process more probable. This can be understood intuitively, because if the bandgap decreases, corresponding to a longer wavelength, the energy and momentum laws can be satisfied by carriers that are located closer to the band edge. Hence, fulfilling the energy and momentum requirements is easier to achieve for smaller transferred energy [22]. Similar reasoning holds for a larger heavy hole mass, as the number of holes occupying states with larger momentum increases, lowering the activation energy [23]. Rising temperature increases the Auger rate as well, according to Eq. 2.4, because more carriers are located at higher energy states according to the Fermi distribution. The CHCC Auger recombination is significant in narrow bandgap materials, i.e., InAs or InSb. The small electron mass associated with antimonide materials further reduces the activation energy, according to Eq. 2.5, leading to even higher Auger scattering probabilities.

Die approbierte gedruckte Originalversion dieser Dissertation ist an der TU Wien Bibliothek verfügbar.
The approved original version of this doctoral thesis is available in print at TU Wien Bibliothek.
TU Bibliothek WIEN Your knowledge hub

For the CHSH process, the recombination rate is given by [21]

$$R_{\mathrm{CHSH}} = C_0^{\mathrm{CHSH}}\, e^{-E_{\mathrm{a}}^{\mathrm{CHSH}}/k_{\mathrm{B}}T}\, np^2, \tag{2.6}$$

with the activation energy

$$E_{\mathrm{a}}^{\mathrm{CHSH}} = (E_{\mathrm{g}} - \Delta_{\mathrm{SO}})\,\frac{m_{\mathrm{SO}}}{2m_{\mathrm{HH}} + m_{\mathrm{CB}} - m_{\mathrm{SO}}} \qquad \text{for } E_{\mathrm{g}} \geq \Delta_{\mathrm{SO}}, \tag{2.7}$$

$$E_{\mathrm{a}}^{\mathrm{CHSH}} = \Delta_{\mathrm{SO}} - E_{\mathrm{g}} \qquad \text{for } E_{\mathrm{g}} < \Delta_{\mathrm{SO}}, \tag{2.8}$$

where m_{SO} is the effective mass in the split-off band. Thus, when the bandgap equals the energy difference at the Γ-point ($k = 0$) between the heavy hole and split-off band ($E_{\mathrm{g}} = \Delta_{\mathrm{SO}}$), strong CHSH Auger rates are expected [24]. The situation, where $E_{\mathrm{g}} < \Delta_{\mathrm{SO}}$, is preferable over $E_{\mathrm{g}} > \Delta_{\mathrm{SO}}$ to suppress this Auger process, because it holds that $m_{\mathrm{SO}}/\left(2m_{\mathrm{HH}} + m_{\mathrm{CB}} - m_{\mathrm{SO}}\right) < 1$. Therefore, the activation energy is larger for $E_{\mathrm{g}} < \Delta_{\mathrm{SO}}$. While in InSb the bandgap (0.17 eV) is significantly smaller than Δ_{SO} (0.81 eV), in InAs CHSH processes become more relevant as the bandgap (0.36 eV) and Δ_{SO} (0.37 eV) are similar [25]. In GaSb, on the other hand, CHSH absorption is suppressed, since the bandgap (0.73 eV) is smaller than Δ_{SO} (0.76 eV) [25].

For the CHLH Auger process, the recombination rate follows the same relation as for the CHSH process, given by Eq. 2.6, with the activation energy [26]

$$E_{\mathrm{a}}^{\mathrm{CHLH}} = E_{\mathrm{g}}\frac{m_{\mathrm{LH}}}{2m_{\mathrm{HH}} + m_{\mathrm{CB}} - m_{\mathrm{LH}}}. \tag{2.9}$$

Like for the CHCC process, the CHLH recombination energy is relatively low in antimonide materials due to the small electron mass and low bandgap energy, making the process probable at room temperature [26].

While the analytic expressions for the Auger recombination rates given above assumed parabolic bands and carrier distributions according to Boltzmann statistics, in semiconductor lasers, Fermi-Dirac statistics, and non-parabolicity allow for a more accurate description [27]. Moreover, in devices employing QWs, the situation is more complex due to the formation of subbands. In general, the Auger recombination in a particular semiconductor device can be influenced by employing different strategies. Compared to bulk material, the Auger coefficients were experimentally found to be reduced in layers forming QWs [28]. Strain engineering has proven to be an efficient tool in heterostructure devices as well, due to the influence on the effective masses [29]. Compressive strain disrupts the degeneracy at the Γ-point for the heavy and light hole band and reduces the in-plane effective mass of the energetically highest heavy hole band [30]. For strained type-II InAs/InGaSb superlattices, suppressed Auger rates were demonstrated experimentally [31]. In type-I mid-infrared InGaAsSb QW lasers, an increase of the Auger rate towards smaller wavelengths (<2 µm) is related to CHSH processes, whereas an increase towards longer wavelengths is traced back to either CHCC or CHLH recombination [32]. In general, avoiding resonances in the band structure with the targeted optical transition and keeping the threshold carrier densities low, is important when designing heterostructure devices.

2.1.2 Absorption

Photons that have been generated via radiative recombination can subsequently be absorbed. The most common processes in semiconductors are free carrier absorption by either electrons or holes, intervalence band absorption and inter-valley conduction band absorption [33]. Depending on parameters, such as the wavelength, material, doping, carrier concentrations and temperature, one or the other can be dominant. In the following, the effects of relevance for interband cascade devices will be introduced in more detail.

Free carrier absorption

Free carrier absorption encompasses all processes, in which a carrier, that is free to move in the band where it is located electron in the conduction band or hole in the valence band absorbs a photon, and is excited to another unoccupied state within the same band [34]. The absorbing carrier was already in an excited state before undergoing the excitation process. Hence, it is fundamentally different from interband absorption. There, an electron transitions from the valence band, where it was in a non-conducting state, to the conduction band, where it can move freely.

If the absorption by electrons is treated classically, for the free carrier absorption coefficient α_{FCA} the Drude-Zener theory yields a quadratic dependence on the wavelength λ and a linear dependence on the free carrier concentration n_{e} according to [33]

$$\alpha_{\mathrm{FCA}} = s\lambda^2 n_{\mathrm{e}} = \frac{e^3}{4\pi^2 c^3 m_0^2 \epsilon_0} \frac{1}{n\mu \left(m^*/m_0\right)^2} n_{\mathrm{e}} \lambda^2. \tag{2.10}$$

The constant prefactor s depends on the refractive index of the material n, mobility μ and effective mass m^*.

In general, free carrier absorption can only occur with the help of an additionally involved scattering partner. Since the photon momentum $\hbar k$ is insignificant and the

Die approbierte gedruckte Originalversion dieser Dissertation ist an der TU Wien Bibliothek verfügbar.
The approved original version of this doctoral thesis is available in print at TU Wien Bibliothek.

free carrier undergoes a change in momentum during the transition, another mechanism needs to be responsible to fulfill the law of momentum conservation. The process can be facilitated by ionized impurities, or by acoustic or optical phonons, transferring the momentum to the crystal lattice. As in principle all of these scattering mechanisms can be present, the total free carrier absorption (now taking quantum mechanical principles into account) is then given by the sum of the different contributions with varying dependence on the wavelength [33]

$$\alpha_{\mathrm{FCA}} = s\left(A\lambda^{1.5} + B\lambda^{2.5} + C\lambda^{3}\right). \tag{2.11}$$

The fitting parameters A, B and C correspond to absorption processes involving acoustic phonons, optical phonons and ionized impurities, respectively, and s is defined according to Eq. 2.10. In practice, it is often easier to reduce the number of fitting parameters to two and omit the distinction between different interaction partners, resulting in [33]

$$\alpha_{\mathrm{FCA}} = K_{\mathrm{FCA}}\lambda^{m}, \tag{2.12}$$

with the fitting parameter m. The constant K_{FCA} depends on the doping concentration, which also includes the influence of doping on carrier mobility, which was not taken into account in Eq. 2.10. The absorption coefficient for holes can be obtained in a similar fashion. In general, for all free carrier absorption mechanisms, the magnitude of the absorption increases with increasing wavelength and increasing doping concentration.

Inter-valley conduction band absorption

Electrons located in the conduction band can transition from the Γ-point to a minimum at a different k value, i.e., to the X or the L valley, when absorbing a photon. For this transition to occur, the photon energy needs to be similar to the energy difference between the two considered valleys ΔE. Due to the change in momentum, inter-valley conduction band absorption is a phonon-assisted process. The absorption coefficient for this mechanism follows [33]

$$\alpha_{\mathrm{CBV}} = K_{\mathrm{CBV}}\left(\hbar\omega - E_0\right)^{1/2}, \tag{2.13}$$

with the photon energy $\hbar\omega$, and the carrier concentration-dependent fitting parameters K_{CBV} and E_0. The threshold energy E_0 depends on ΔE, the phonon energy E_{p}

Die approbierte gedruckte Originalversion dieser Dissertation ist an der TU Wien Bibliothek verfügbar.
The approved original version of this doctoral thesis is available in print at TU Wien Bibliothek.

and the Fermi level position E_F in the following way [35],

$$E_0 = \Delta E + E_\mathrm{p} - E_\mathrm{F}. \tag{2.14}$$

From Eq. 2.13 the wavelength dependence of the absorption coefficient follows to be $\propto \lambda^{-1/2}$, hence, decreasing with increasing λ. For n-GaSb doped with tellurium, electron free carrier absorption and inter-valley conduction band absorption were determined to be the dominant absorption processes [33]. Especially for wavelengths below 5 µm the inter-valley mechanism governs the total absorption coefficient, leading to a decrease in absorption, until the free carrier absorption becomes stronger at higher wavelengths.

Intervalence band absorption

Absorption in semiconductors can arise from processes, where an electron undergoes a transition between different bands in the valence band, while conserving energy and momentum. In particular, intervalence band absorption between the split-off and the heavy hole band plays an important role in bandgap lasers [36, 37]. Since, this mechanism depends on the carrier density, resonances between the lasing wavelength and the split-off energy should be avoided at the Γ-point, where the highest carrier densities are available. In GaSb, this transition is only possible for energies above the bandgap, since $\Delta_\mathrm{SO} > E_\mathrm{g}$ [25]. It was shown, that the intervalence band absorption in GaSb is predominantly caused by transitions between the light hole and heavy hole band [33].

In QW lasers, where one valence band is composed of multiple subbands due to quantization effects, the intervalence band absorption does not differ substantially in magnitude from conventional bandgap lasers [38]. However, using strained layers for QW lasers, was demonstrated to efficiently suppress intervalence band absorption [39].

Moreover, detailed studies on the valence intersubband absorption have been conducted for p-type quantum well infrared photodetectors (QWIPs), where this is the core functioning mechanism for light detection [40]. In contrast, n-type QWIPs rely on intersubband transitions in the conduction band, which are subject to the intersubband selection rule, strongly favoring light polarized in growth direction. Experimentally, GaAs/AlGaAs and $\mathrm{In_{0.1}Ga_{0.9}As}$/AlGaAs QWIPs were confirmed to closely follow this polarization selection rule in the conduction band, only deviating by 0.2 % and 3 %, respectively [41].

When looking at transitions between different subbands in the valence band in

Die approbierte gedruckte Originalversion dieser Dissertation ist an der TU Wien Bibliothek verfügbar.
The approved original version of this doctoral thesis is available in print at TU Wien Bibliothek.
TU Bibliothek WIEN Your knowledge hub

a symmetric QW and assuming small in-plane wave vectors, the light polarization plays an important role as well. The subbands are labelled HH1, HH2, HH3, . . . and LH1, LH2, . . . , starting from the subbands at highest energy for the heavy hole and light hole band, respectively. Under these assumptions, for light polarized parallel to the growth direction (z-direction), HH1 to HH2 is the dominant absorptive transition, and transitions between heavy hole and light hole subbands are negligibly small around the Γ-point [40]. For light polarized perpendicular to the growth direction (x- or y-polarization), transitions are predicted to be dominant between HH1 and LH2, LH4, LH6 and other combinations with odd index difference between heavy and light hole subbands, that show a change in parity [42, 43]. Hence, in a p-QWIP, bringing the LH2 subband in resonance with the top of the barrier, results in a high escape probability and high absorption, which was experimentally confirmed [40].

The polarization dependence of the various valence intersubband transitions is expected to be less pronounced for larger in-plane wave vectors [40]. This is primarily due to interband mixing between the heavy and light hole bands [44, 45]. With increasing temperature, and thus, larger in-plane wave vectors of the holes, the cross sections for transitions between heavy hole subbands increase significantly for light polarized along the x-direction [44]. In InAs/Ga(In)Sb superlattices, the HH1 to HH3 process, which for this polarization is forbidden at $k = 0$, exhibits a strong peak at wave vectors in the range of 0.03 Å^{-1} [46, 47]. Interestingly, the optical matrix element between HH1 and LH1 was found to be much stronger for x-polarized compared to z-polarized light. This transition is a result of intermixing between p-orbital-like light hole states of GaSb and s-orbital-like states of InAs [46], which can be described by a bond-orbital model for superlattices [48, 49]. Therefore, the behavior resembles that of an optical interband transition, favoring light polarized along the x-direction. Since the energy splitting between heavy and light hole band is influenced by strain, the HH1 to LH1 transition can be tuned by modifying the strain [47]. Furthermore, the HH2 subband shows strong light hole and InAs s-like characters caused by band mixing at larger k vectors, which favors x-polarization for the HH1 to HH2 transition as well [46].

2.2 Modelling

A very instructive explanation of all essential considerations needed for the successful description of the electronic and optical properties of semiconductor quantum structures can be found in Ref. [25]. It additionally provides suggested band parameters for all materials that are of relevance to optoelectronic devices and which

Die approbierte gedruckte Originalversion dieser Dissertation ist an der TU Wien Bibliothek verfügbar.
The approved original version of this doctoral thesis is available in print at TU Wien Bibliothek.

have been used for all simulations presented in this thesis. The subsequently presented introduction follows this resource. Another valuable source is Ref. [50] by G. Bastard, who was the first to develop the necessary formalism to apply the $\mathbf{k} \cdot \mathbf{p}$ theory to semiconductor heterostructures.

In order to quantitatively represent the behavior of carriers in a designed heterostructure, the environment that the carriers are situated in needs to be described first. The materials that compose the optoelectronic devices studied within this thesis are III-V semiconductors like InAs, GaSb and AlSb or other alloys. They form crystals with the atoms placed in an organized manner, where each atom is located at a defined position with respect to the others. The unit cell is the basic building block of the crystal, which repeats itself throughout the crystal. Different directions in the crystal often show different electric and optic properties, since the distance or the bonds between the atoms can differ. Most semiconductor materials relevant for optoelectronic devices occur in the so called Zinc blende crystal structure. The unit cell for this type of crystal is displayed in Fig. 2.3. While the structure remains the same, different materials exhibit different distances between the individual atoms, defining the length of the unit cell. This is described by the lattice constant. Materials with the same or similar lattice constant can be stacked on top of each other to form a heterostructure. Choosing materials with varying bandgaps and/or different offset between the band edges (relating to the relative position of the conduction or valence band edge when comparing different materials) allows to shape the electric potential. In this way QWs and barriers can be designed. The lattice constant can be influenced when mixing materials to form alloys. An example would be the ternary alloy $\mathrm{Ga}_{1-x}\mathrm{In}_x\mathrm{Sb}$ with varying composition x between GaSb and InSb. In

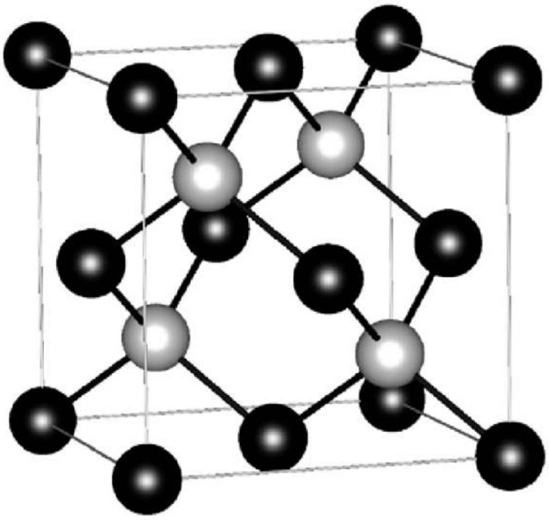

Figure 2.3: The unit cell of a Zinc blende crystal structure. Figure taken from [51].

Die approbierte gedruckte Originalversion dieser Dissertation ist an der TU Wien Bibliothek verfügbar.
The approved original version of this doctoral thesis is available in print at TU Wien Bibliothek.

this way the strain that is introduced when the lattice constant of two stacked materials differs can be modified. If the strain is too large, the crystal can relax, resulting in crystalline defects.

The probabilistic location of the electrons with respect to the nucleus of an atom is described by the orbitals. The two orbitals relevant for the basic understanding of semiconductors are the s- and p-orbitals, since they contain all eight valence electrons. When approaching two or a large number of atoms by reducing the distance between them, the orbitals start to interact with each other and the conduction and valence bands are formed. They exhibit an electronic energy bandgap between them. At these energies, no electrons are found. Essentially, this results in a larger bandgap the denser the atoms are packed. Materials with smaller lattice constants, hence, exhibit larger bandgap energies.

2.2.1 Bloch's theorem

A crystal is a periodic structure, therefore the electrons in the crystal are subject to a periodic electric potential. Bloch's theorem, which is a special case of the more general Floquet theory, describes the essence of how this periodicity is reflected in the probability densities of the electrons, which show the same periodicity as the crystal. This then gives an indication of the location of the electrons in the crystal structure. The electron wavefunction $\psi(\vec{k},\vec{r})$ can be written as

$$\psi(\vec{k},\vec{r}) = \mathrm{e}^{i\vec{k}\vec{r}} u(\vec{k},\vec{r}), \tag{2.15}$$

with the help of the periodic Bloch function $u(\vec{k},\vec{r})$, which shows the same periodicity as the crystal lattice,

$$u(\vec{k},\vec{r}+\vec{R}) = u(\vec{k},\vec{r}). \tag{2.16}$$

The translation vector $\vec{R}$ under which the Bloch functions are invariant is a linear combination of the lattice vectors $\vec{a_1}$, $\vec{a_2}$, $\vec{a_3}$ in real 3D space. In equation 2.15, the wavefunction is described as product of a plane wave $\mathrm{e}^{i\vec{k}\vec{r}}$ and the Bloch function and therefore shows the periodic character of the wavefunction.

2.2.2 The k · p model

Calculating the electronic band structure of a semiconductor is done by solving the time invariant Schrödinger's equation

$$\hat{H}\psi = E\psi, \tag{2.17}$$

TU Bibliothek, WIEN, Your knowledge hub
Die approbierte gedruckte Originalversion dieser Dissertation ist an der TU Wien Bibliothek verfügbar.
The approved original version of this doctoral thesis is available in print at TU Wien Bibliothek.

with the Hamiltonian $\hat{H}$ and wavefunction ψ. The essence of the $\mathbf{k}\cdot\mathbf{p}$ theory is to use perturbation theory to expand an already known solution to the Schrödinger equation at the high-symmetry points of the crystal lattice to other values of the wavevector k. It is used for the calculation of the electronic band structure of bulk as well as heterostructure semiconductors. The solutions are then described as a superposition of the basis functions, that are assumed to be known, although their exact form within the unit cell is not important. The basis functions are chosen to fulfill Bloch's theorem. In general, if an incomplete set of basis functions is used, the solution is only approximate. This means that the more basis functions are used, the more accurate the solution will be. In the simplest case only two basis functions are used, one for the conduction and one for the valence band. Each solution is then defined by evaluating the coefficients for the contributions of each of the two bands, that can intermix when moving away from the Γ-point, where $\vec{k} = 0$. The coupling between the different band contributions is described by the off-diagonal Hamiltonian matrix elements.

The beauty of the $\mathbf{k}\cdot\mathbf{p}$ theory lies in avoiding the need to directly find the 3D wavefunctions that fulfill Schrödinger's equation in order to solve it. Essentially it comes down to solving an Eigenvalue problem, which can efficiently be done numerically. The dimensions of the matrices then correspond to the number of considered basis states. When calculating the electronic band structure in a unipolar device like the QCL, a simplified description of the valence band by one effective band often is enough to determine the influence that the valence band has on the conduction band. However, this approximation is too simple to picture the situation in the valence band itself.

Since the valence band near the edge arises from the three p-orbitals, more precisely the p-bonding states, it is sixfold degenerate if the spin is considered as well. The energetic ordering of the molecular orbitals is schematically shown in Fig. 2.4a. The situation is complicated further because the spin can couple to the orbital angular momentum. The electron orbits around the nucleus in a radially outward directed electric field, that is created by the charged nucleus and the core electrons of the atom. Since the moving electron is charged this induces a magnetic field. However, the electron does not only have charge e, but also an intrinsic spin angular momentum. These two ingredients result in the electron exhibiting a magnetic moment itself. Hence, there is a magnetic moment in a magnetic field, which leads to a change in the energy. Therefore, this spin-orbit coupling results in an additional contribution to the Hamiltonian, that essentially describes how the three p-orbitals couple with each other. This leads to the characteristic structure of the valence

Die approbierte gedruckte Originalversion dieser Dissertation ist an der TU Wien Bibliothek verfügbar.
The approved original version of this doctoral thesis is available in print at TU Wien Bibliothek.
TU Bibliothek Your knowledge hub WIEN

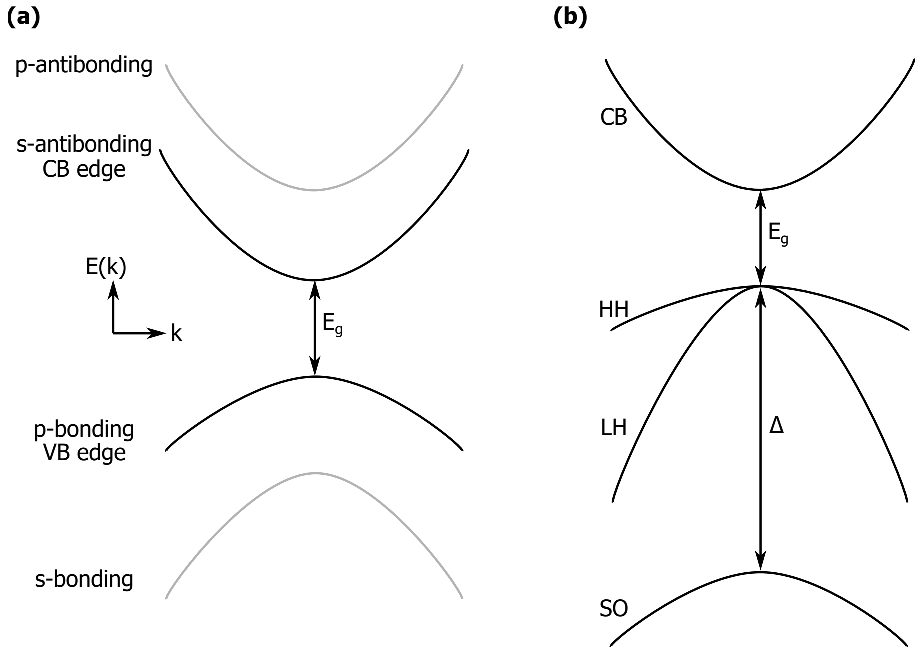

Figure 2.4: (a) The conduction band (CB) edge and the valence band (VB) edge are formed by the s-antibonding and p-bonding states, respectively. The energetically remote bands (p-antibonding and s-bonding), which are located deeper in the conduction band and valence band are depicted in gray. **(b)** When spin-orbit coupling is considered in the calculation of the energy bands in a III-V semiconductor, the valence band degeneracy lifts, resulting in the typical heavy hole (HH), light hole (LH) and split-off (SO) bands. The split-off band is energetically separated by the split-off energy Δ.

band, which exhibits three distinct bands in bulk: the heavy hole, light hole and split-off band (see Fig. 2.4b). Due to the spin-orbit coupling the degeneracy at the Γ-point is lifted for the split-off band, which is energetically separated by the split-off energy Δ, which is a material property. While it is negligibly small for some semiconductors like Si ($\Delta = 0.044$ eV), the effect is large for others like InSb ($\Delta = 0.81$ eV). Heavy and light hole band still share the same energy at $k = 0$. Together with the double degenerate conduction band arising from the symmetric s-orbital, more precisely the s-antibonding states, there are now eight basis functions that are used to describe each individual solution of the eigenvalue problem.

There is still another missing ingredient for the accurate description of the electronic states. So far only the eight bands close to the valence and conduction band edges have been considered. However, bands that are energetically farther away can still influence these bands. Instead of explicitly including these so called remote bands in the model, their contribution is treated by second order perturbation theory, giving rise to additional terms in the Hamiltonian that are proportional to k^2. This approach was first introduced by P. Löwdin and is referred to as Lödwin's

Die approbierte gedruckte Originalversion dieser Dissertation ist an der TU Wien Bibliothek verfügbar.
The approved original version of this doctoral thesis is available in print at TU Wien Bibliothek.
TU Bibliothek, WIEN Your knowledge hub

perturbation theory [52].

The matrix equation for the full eight-band model can then be written as

$$\begin{bmatrix} H_{4\text{x}4} & 0 \\ 0 & H_{4\text{x}4} \end{bmatrix} + H(\mathbf{L}\cdot\mathbf{S}) \begin{bmatrix} |s\uparrow\rangle \\ |p_\text{x}\uparrow\rangle \\ |p_\text{y}\uparrow\rangle \\ |p_\text{z}\uparrow\rangle \\ |s\downarrow\rangle \\ |p_\text{x}\downarrow\rangle \\ |p_\text{y}\downarrow\rangle \\ |p_\text{z}\downarrow\rangle \end{bmatrix} = E_\text{n} \begin{bmatrix} |s\uparrow\rangle \\ |p_\text{x}\uparrow\rangle \\ |p_\text{y}\uparrow\rangle \\ |p_\text{z}\uparrow\rangle \\ |s\downarrow\rangle \\ |p_\text{x}\downarrow\rangle \\ |p_\text{y}\downarrow\rangle \\ |p_\text{z}\downarrow\rangle \end{bmatrix}. \tag{2.18}$$

The block-diagonal first expression includes the coupling between conduction and valence band, which enters via the interband momentum matrix element p_cv that is often also given in terms of the Kane energy $E_\text{P} = 2|p_\text{cv}|^2/m$, with the free-electron mass m [53]. It is treated as a material parameter and not calculated explicitly. In general, the momentum matrix element p_cv describes the coupling strength between the conduction band and the valence band and is given by $\langle u_\text{c}(0,\vec{r})|\,\vec{p}\,|u_\text{v}(\vec{k},\vec{r})\rangle$, with the momentum operator $\vec{p}$ and the basis functions, which are the Bloch functions for the selected bands (in principle the momentum matrix element can be determined for any other two Bloch functions). Furthermore, the influence from remote bands like the p-antibonding and s-bonding states or the d-orbital is included in this part of the Hamiltonian. It is given by

$$H_{4\text{x}4} = \begin{bmatrix} E_\text{g} + \frac{\hbar^2 k^2}{2m}(1+2F) & i\frac{\hbar}{m}k_\text{x}p_\text{cv} & i\frac{\hbar}{m}k_\text{y}p_\text{cv} & i\frac{\hbar}{m}k_\text{z}p_\text{cv} \\ -i\frac{\hbar}{m}k_\text{x}p_\text{cv} & -Lk_\text{x}^2 - M(k_\text{y}^2+k_\text{z}^2) & -Nk_\text{x}k_\text{y} & -Nk_\text{x}k_\text{z} \\ -i\frac{\hbar}{m}k_\text{y}p_\text{cv} & -Nk_\text{x}k_\text{y} & -Lk_\text{y}^2 - M(k_\text{x}^2+k_\text{z}^2) & -Nk_\text{y}k_\text{z} \\ -i\frac{\hbar}{m}k_\text{z}p_\text{cv} & -Nk_\text{x}k_\text{z} & -Nk_\text{y}k_\text{z} & -Lk_\text{z}^2 - M(k_\text{x}^2+k_\text{y}^2) \end{bmatrix}. \tag{2.19}$$

The effect that the remote bands have on the conduction band is described by the parameter F, which is another material parameter. The antibonding p-like states that energetically lie far above the conduction band edge have the largest impact. The parameters L, M and N are valence band material parameters. They relate to another more commonly used set of material parameters, the so called Luttinger parameters γ_1, γ_2, γ_3. In a more tangible fashion the Luttinger parameters describe the heavy m_HH and light hole masses m_LH along different crystal directions

$$m_\text{HH}[001] = \frac{m}{\gamma_1 - 2\gamma_2} \qquad m_\text{LH}[001] = \frac{m}{\gamma_1 + 2\gamma_2} \tag{2.20}$$

$$m_\text{HH}[111] = \frac{m}{\gamma_1 - 2\gamma_3} \qquad m_\text{LH}[111] = \frac{m}{\gamma_1 + 2\gamma_3}, \tag{2.21}$$

where m is the free-electron mass. The spin-orbit coupling, that connects the various

Die approbierte gedruckte Originalversion dieser Dissertation ist an der TU Wien Bibliothek verfügbar.
The approved original version of this doctoral thesis is available in print at TU Wien Bibliothek.

p-orbitals is given by

$$H(\mathbf{L}\cdot\mathbf{S}) = \frac{\Delta}{3}\begin{bmatrix} 0 & 0 & 0 & 0 & 0 & 0 & 0 & 0 \\ 0 & 0 & -i & 0 & 0 & 0 & 0 & 1 \\ 0 & i & 0 & 0 & 0 & 0 & 0 & -i \\ 0 & 0 & 0 & 0 & 0 & -1 & i & 0 \\ 0 & 0 & 0 & 0 & 0 & 0 & 0 & 0 \\ 0 & 0 & 0 & -1 & 0 & 0 & i & 0 \\ 0 & 0 & 0 & -i & 0 & -i & 0 & 0 \\ 0 & 1 & i & 0 & 0 & 0 & 0 & 0 \end{bmatrix}. \tag{2.22}$$

Strain effects

When realizing a heterostructure, the lattice constant of a grown layer can slightly deviate from the lattice constant of the substrate. In general, applying stress σ_{kl} to a crystal results in strain ϵ_{ij}. The proportionality of these properties is described by the elastic constants of the material c_{klij}: $\sigma_{\text{kl}} = \sum_{\text{ij}} c_{\text{klij}}\epsilon_{\text{ij}}$. The strain subsequently effects the material properties like the bandgap, which is described by the deformation potentials a_{c}, l_ϵ, m_ϵ and n_ϵ. The influence of strain can be included in the eight-band model by introducing another term that is added to the Hamiltonian on the left side of Eq. 2.18. It enters in the same block-diagonalized fashion as $\mathbf{H}_{4\text{x}4}$ and reads

$$H_\epsilon = \begin{bmatrix} a_{\text{c}}(\epsilon_{\text{xx}}+\epsilon_{\text{yy}}+\epsilon_{\text{zz}}) & 0 & 0 & 0 \\ 0 & l_\epsilon\epsilon_{\text{xx}}+m_\epsilon(\epsilon_{\text{yy}}+\epsilon_{\text{zz}}) & n_\epsilon\epsilon_{\text{xy}} & n_\epsilon\epsilon_{\text{xz}} \\ 0 & n_\epsilon\epsilon_{\text{xy}} & l_\epsilon\epsilon_{\text{yy}}+m_\epsilon(\epsilon_{\text{xx}}+\epsilon_{\text{zz}}) & n_\epsilon\epsilon_{\text{yz}} \\ 0 & n_\epsilon\epsilon_{\text{xz}} & n_\epsilon\epsilon_{\text{yz}} & l_\epsilon\epsilon_{\text{zz}}+m_\epsilon(\epsilon_{\text{xx}}+\epsilon_{\text{yy}}) \end{bmatrix}. \tag{2.23}$$

When growing III-V heterostructures, the crystal is often grown in [001] direction on substrates like GaSb for ICLs. If the lattice constant of the grown layer does not perfectly match the lattice constant of the substrate, the result is biaxial strain on the cubic Zinc blende crystal. In this case, the non-zero stress components are

$$\sigma_{\text{xx}} = \sigma_{\text{yy}} = c_{11}\epsilon_{\text{xx}} + c_{12}\epsilon_{\text{yy}} + c_{12}\epsilon_{\text{zz}} \neq 0. \tag{2.24}$$

There is no applied stress in growth direction, which means that the behavior of the unit cell along this axis is solely determined by the connection between the in-plane and out-of-plane strain given by the elastic constants. The vanishing stress along the growth axis reads

$$\sigma_{\text{zz}} = c_{12}\epsilon_{\text{xx}} + c_{12}\epsilon_{\text{yy}} + c_{11}\epsilon_{\text{zz}} = 2c_{12}\epsilon_{\text{xx}} + c_{11}\epsilon_{\text{zz}} = 0. \tag{2.25}$$

TU WIEN Bibliothek Your knowledge hub
Die approbierte gedruckte Originalversion dieser Dissertation ist an der TU Wien Bibliothek verfügbar.
The approved original version of this doctoral thesis is available in print at TU Wien Bibliothek.

Using Eqs. 2.24 and 2.25 yields the following relation between out-of-plane ϵ_{zz} and in-plane strain ϵ_{xx}

$$\epsilon_{\mathrm{zz}} = -\frac{2c_{12}}{c_{11}}\epsilon_{\mathrm{xx}}. \tag{2.26}$$

If a layer with lattice constant a is grown on a substrate with lattice constant a_0, the deformed lattice constant along an in-plane axis has to be equal to the substrate lattice constant: $a(1+\epsilon_{\mathrm{xx}}) = a_0$. Hence, the in-plane strain is given by

$$\epsilon_{\mathrm{xx}} = \epsilon_{\mathrm{yy}} = \frac{a_0 - a}{a}. \tag{2.27}$$

in which the unit cell can either expand or shrink depending on the strain:

The change of the material parameters can then be described by the volume change. The conduction band edge is then shifted by $\delta E_{\mathrm{c}} = a_{\mathrm{c}}\frac{\Delta V}{V} = a_{\mathrm{c}}(\epsilon_{\mathrm{xx}} + \epsilon_{\mathrm{yy}} + \epsilon_{\mathrm{zz}})$. This is exactly the corresponding matrix element in Eq. 2.23. The deformation potentials for the valence band can be rewritten and are then called the transformed deformation potentials. They are determined experimentally and are given in Ref. [25] in terms of absolute values, that can then be used for the simulation. The deformation potentials are linked as follows

$$\begin{aligned} a_{\mathrm{v}} &= \frac{l_\epsilon + 2m_\epsilon}{3}, \\ b &= \frac{l_\epsilon - m_\epsilon}{3}, \\ d &= \frac{n_\epsilon}{\sqrt{3}}. \end{aligned}$$

The energetic shift of the valence band edge with volume deformation is quantified by a_{v}. For growth in [001] direction, b describes how the heavy and light hole band split at $k = 0$. This is the case for a layer of GaInSb grown on GaSb, where compressive biaxial strain is introduced ($a > a_0$, $\epsilon_{\mathrm{xx}} < 0$). The band gap increases and the heavy hole band moves energetically above the light hole band.

For the readers left unsatisfied by the here presented description of the $\mathbf{k}\cdot\mathbf{p}$ method, reference [54] is an excellent resource to learn more about useful approximations when employing the $\mathbf{k}\cdot\mathbf{p}$ method.

Ternary alloys

More material parameters are necessary if the band structure of a ternary alloy like $\mathrm{Ga}_{1-\mathrm{x}}\mathrm{In}_{\mathrm{x}}\mathrm{Sb}$ needs to be calculated. According to Vegard's law, also referred to as virtual crystal approximation, the band parameters $P_{\mathrm{AB}}(x)$ can be approximated by a simple average of the band parameters of the two binary compounds A and B that

TU Bibliothek WIEN Your knowledge hub
Die approbierte gedruckte Originalversion dieser Dissertation ist an der TU Wien Bibliothek verfügbar.
The approved original version of this doctoral thesis is available in print at TU Wien Bibliothek.

are being mixed. This is a sufficient approximation for properties like the lattice constant or elastic constants. However, it falls short when looking at the energy gap or the electron mass. A correction term is introduced, which is called the bowing parameter C_{AB}. This yields the following relation, depending on the composition x

$$P_{\mathrm{AB}}(x) = xP_{\mathrm{A}} + (1-x)P_{\mathrm{B}} - x(1-x)C_{\mathrm{AB}}, \tag{2.28}$$

where P_{A} and P_{B} denote the band parameters of the two binary compounds.

2.2.3 Envelope function approximation

So far the descriptions of the concepts to model the electronic bandstructure and transitions between the subbands were only considering one crystalline bulk material where the electrons are located. There is one missing ingredient to describe a heterostructure, where the crystal lattice is not uniform in all directions. There, the electrons are subject to quantum confinement like in QWs or superlattices, which means that the coefficients that are the projections of the solution onto the basis states now need to be evaluated in a spatially dependent manner.

The envelope function theory provides the necessary tools to accurately describe this situation [50]. The underlying assumption is that the wavefunction can be approximated by the Bloch functions multiplied by a slowly changing spatially-dependent function that neglects the quickly-varying potential at each atom in the crystal. The Bloch functions $u_{\mathrm{n}}(\vec{k},\vec{r})$ with band index n are assumed to be the same for the different materials, which can be justified, since the lattice constant of a material layer stack is generally very closely matched. For a heterostructure that is stacked in z-direction the following solution for the wavefunction $\psi(\vec{k},\vec{r})$ is obtained

$$\psi(\vec{k},\vec{r}) = \sum_n \underbrace{\frac{1}{\sqrt{S}} \mathrm{e}^{i(k_{\mathrm{x}}x+k_{\mathrm{y}}y)} \chi_{\mathrm{n}}(z)}_{\text{envelope function}} \, u_{\mathrm{n}}(0,\vec{r}). \tag{2.29}$$

Here, k_{x}, k_{y} are the in-plane wavevectors and S is the in-plane surface area. The envelope function is written by means of a separation ansatz, where it is split up into the z-dependent part $\chi_{\mathrm{n}}(z)$ and a freely-propagating plane-wave part in the in-plane directions $\mathrm{e}^{i(k_{\mathrm{x}}x+k_{\mathrm{y}}y)}$. The Bloch functions are approximated by their values at the Γ-point ($k = 0$). An illustration of the envelope function approximation can be seen in Fig. 2.5 for the case of a simple layer stack consisting of two different materials A and B. Stacked in the order ABA, the difference in the potential leads to the formation of a QW, spatially confining the electron in one dimension.

Die approbierte gedruckte Originalversion dieser Dissertation ist an der TU Wien Bibliothek verfügbar.
The approved original version of this doctoral thesis is available in print at TU Wien Bibliothek.
TU Bibliothek WIEN Your knowledge hub

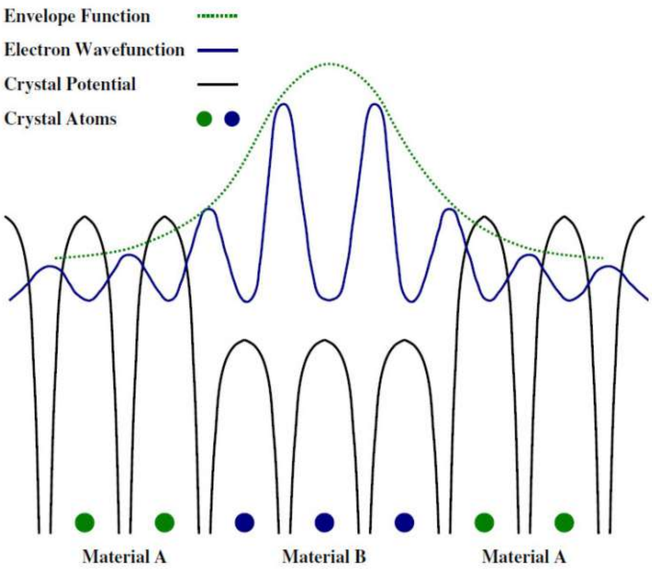

Figure 2.5: The wavefunction in the envelope function approximation can be described by the slowly varying envelope that changes with the material properties and the Bloch functions reflecting the quickly varying potential at the locations of the atoms in the crystal. Figure taken from [51].

2.2.4 Optical transitions

So far all discussions in this chapter were focussed on the electronic properties of semiconductors. In the following, the focus will shift to the optical properties. In general, an optical transition is described as an inelastic scattering process via photon emission or absorption. Therefore, the interaction of electrons with an optical field needs to be described. If the light field is sufficiently weak, not modifying the electronic bandstructure, this can be done using perturbation theory and the dipole approximation. The latter is justified since the spatial dimensions of the electronic wavefunctions are much smaller than the photon wavelength. For optoelectronic heterostructures in the mid-infrared the wavelength in the range of µm is much larger than the QW dimensions on the order of a few nm.

An incident photon upon absorption can energetically lift an electron in the semiconductor from an occupied state to an unoccupied state. The electron and the hole that is left behind can be described as an electric dipole. The interaction between the electric-field vector $\vec{E}$ from the light field and the transition dipole moment $e\vec{r}$ is described by the Hamiltonian

$$H_{\mathrm{ph}} = e\vec{E} \cdot \vec{r}. \tag{2.30}$$

The transition rate (derivative of the probability for the transition to occur with

Die approbierte gedruckte Originalversion dieser Dissertation ist an der TU Wien Bibliothek verfügbar.
The approved original version of this doctoral thesis is available in print at TU Wien Bibliothek.

respect to time) W_{if} between an initial state i and a final state f is given by Fermi's golden rule

$$W_{\mathrm{if}} = \frac{2\pi}{\hbar}|H_{\mathrm{ph}}^{\mathrm{ij}}|^2\delta(E_{\mathrm{i}} - E_{\mathrm{f}} - \hbar\omega), \tag{2.31}$$

with the interaction matrix element $\langle i|\,|H_{\mathrm{ph}}^{\mathrm{ij}}\,|j\rangle$. The energy needs to be conserved during the scattering process. That means that a transition only takes place if the photon energy $\hbar\omega$ equals the energy difference between the initial and final state $(E_{\mathrm{i}} - E_{\mathrm{f}})$. Mathematically this is described by the multiplication with a Dirac δ-function.

The next step will be to obtain a relation between the Hamiltonian H describing the band structure (the eight-band Hamiltonian or any other arbitrary one) and the interaction matrix element $|H_{\mathrm{ph}}|$. Conveniently, the dipole matrix element between two states φ_{ik} and φ_{fk} can be rewritten in terms of the derivative of the Hamiltonian with respect to the wavevector k along the axis in which the light is polarized [25]

$$\langle\varphi_{\mathrm{ik}}|\,\vec{r}\,|\varphi_{\mathrm{fk}}\rangle = -\frac{i}{E_{\mathrm{fk}} - E_{\mathrm{ik}}}\,\langle\varphi_{\mathrm{ik}}|\,\nabla_{\mathrm{k}}H\,|\varphi_{\mathrm{fk}}\rangle\,. \tag{2.32}$$

Using this relation for the interaction Hamiltonian, Eq. 2.30 yields

$$H_{\mathrm{ph}} = \frac{eE_0}{2}\,\langle\varphi_{\mathrm{ik}}|\,\hat{e}\cdot\vec{r}\,|\varphi_{\mathrm{fk}}\rangle = -\frac{ieE_0}{2\,(E_{\mathrm{fk}} - E_{\mathrm{ik}})}\,\langle\varphi_{\mathrm{ik}}|\,\hat{e}\cdot\nabla_{\mathrm{k}}H\,|\varphi_{\mathrm{fk}}\rangle\,, \tag{2.33}$$

where E_0 is the amplitude of the optical field and the unit vector $\hat{e}$ denotes the axis along which the light is polarized. In practice this means that as long as the Hamiltonian that describes the electronic eigenstates is known and the eigenstates can be retrieved, the dipole matrix element $\langle\varphi_{\mathrm{ik}}|\,\vec{r}\,|\varphi_{\mathrm{fk}}\rangle$, and ultimately the absorption between the electronic states, can be calculated.

Next, an expression for the absorption within the envelope function approximation will be tackled. As discussed earlier, one electronic state is defined by the coefficients that quantify the contribution from each basis state to this state. The indices for the basis states are m, n. This results in a double sum over these two indices when evaluating the interaction matrix element. In practice, an integral over the z-direction needs to be calculated as well for the spatially varying envelope in the direction of the confinement when evaluating the interaction matrix element.

The optical susceptibility χ_{if} between an initial state i and final state f, which describes the response of the medium to light, is given by

$$\chi_{\mathrm{if}} = \frac{e^2}{\epsilon_0}\sum_{\mathrm{k}}\frac{f_{\mathrm{fk}} - f_{\mathrm{ik}}}{(E_{\mathrm{fk}} - E_{\mathrm{ik}})^2}\frac{1}{\hbar\omega - (E_{\mathrm{fk}} - E_{\mathrm{ik}}) - i\gamma}|\sum_{\mathrm{m,n}}\langle\chi_{\mathrm{f,m}}|\,\hat{e}\cdot\nabla_{\mathrm{k}}H\,|\chi_{\mathrm{i,n}}\rangle|^2. \tag{2.34}$$

Die approbierte gedruckte Originalversion dieser Dissertation ist an der TU Wien Bibliothek verfügbar.
The approved original version of this doctoral thesis is available in print at TU Wien Bibliothek.

While the χ on the left side is the susceptibility, it should not be confused with the two χ in the matrix element that relate to the coefficients of the envelope functions on the right side of Eq. 2.34. The probability of occupation of a particular electronic state enters the equation via the Fermi factors of the initial f_{ik} and final state f_{fk}. The linewidth of the transition is quantified by γ, which is assumed to be independent of k. Note, that there is only one value of the wavevector k appearing in Eq. 2.34, which relates to the necessity that the transition of the electron from the initial to the final state is vertical.[1]

The absorption coefficient α is obtained by the following relation to the imaginary part of the susceptibility

$$\alpha(\omega) = -\frac{\omega}{n_{\mathrm{r}} c_0} \mathfrak{Im} \left\{ \sum_{\mathrm{i}} \sum_{\mathrm{f>i}} \chi_{\mathrm{if}} \right\}. \tag{2.35}$$

Here, n_{r} denotes the refractive index of the material and c_0 the vacuum speed of light. To obtain the absorption coefficient at a particular photon wavelength, the sum over all possible initial and final states needs to be computed. The second sum $f > i$ avoids counting the same transitions twice. It should be noted that χ_{if} depends on ω according to Eq. 2.34, and hence the photon wavelength does not just enter linearly into the absorption as could be assumed from Eq. 2.35. The dependence on ω when looking at one single transition is roughly $\propto 1/(\hbar\omega + \gamma)$, because $E_{\mathrm{fk}} - E_{\mathrm{ik}} >> \gamma$. This yields a Lorentzian profile of the absorption. The electronic band structure determines the dipole, thus, it can lead to different absorptive resonances between various subbands. The careful evaluation of the matrix elements in dependence on k on the right side of Eq. 2.34 is of utmost importance. The matrix elements need to be evaluated for a 2D k-space. It is important to note, that the description given in this chapter is very general and does not distinguish between interband and intersubband transitions, but simply takes all possible electronic transitions into account that can lead to the absorption of a photon. The other important dependence of the absorption to consider is the polarization of the light. It enters Eq. 2.34 in the form of $\hat{e}$, which is the unit vector denoting the polarization of the light along which the Hamiltonian needs to be differentiated with respect to the wavevector k. For more details on the derivation of a general expression for the momentum matrix elements within the envelope-function approximation and the description of optical properties of type-II ICLs, the reader is referred to Refs. [56] and [57].

Die approbierte gedruckte Originalversion dieser Dissertation ist an der TU Wien Bibliothek verfügbar.
The approved original version of this doctoral thesis is available in print at TU Wien Bibliothek.
TU WIEN Bibliothek Your knowledge hub

---

[1] This is not true, when looking at another intriguing phenomenon - the Bloch gain, which has been proven to be essential for frequency comb formation in QCLs [55].

Die approbierte gedruckte Originalversion dieser Dissertation ist an der TU Wien Bibliothek verfügbar.
The approved original version of this doctoral thesis is available in print at TU Wien Bibliothek.

CHAPTER 3

INTERBAND CASCADE LASERS AND DETECTORS

Two classes of devices were the focus of attention for this thesis: ICLs and ICIPs. The purpose of this chapter is to introduce the working principles of these devices in a sufficiently detailed way, laying the basis for the following chapter 4 covering the design of the ICL active region and chapter 6 discussing the high-speed performance of ICIPs.

Following a brief historical overview, the current state of the art including relevant performance limitations for ICLs will be highlighted. Although ICLs have been established as reliable laser sources in the mid-infrared, a variety of questions regarding the underlying physical mechanisms and working principles still remain unanswered. Moreover, some experimental observations still elude current theoretical explanations.

For further details on ICLs, the reader is kindly referred to the following sources of information to start their journey: Ref. [58] provides a comprehensible description of the operating principles and physics of this device class, which is further expanded to include growth and fabrication aspects in Ref. [59]. The latest review paper, Ref. [60], further aims at bridging both underlying concepts as well as specialized laser architectures, representing the most granular all-encompassing source. A short book-style introduction to ICLs is given in Ref. [25], which represents an excellent reference for band structures and optical transitions within quantum devices, including recommended material parameters to employ in simulations.

In the second part of the chapter, the working principle for ICIPs is described. The

Die approbierte gedruckte Originalversion dieser Dissertation ist an der TU Wien Bibliothek verfügbar.
The approved original version of this doctoral thesis is available in print at TU Wien Bibliothek.
TU WIEN Bibliothek Your knowledge hub

state-of-the-art performance is briefly reviewed, including a discussion of different III-V material combinations used as absorber sections for these devices.

For a general introduction from a more recent perspective on antimonide-based infrared detectors, the reader might consider Ref. [61], which provides a comparison between the two most relevant superlattice material combinations for ICIPs: InAs/GaSb and InAs/InAsSb. Furthermore, among the different device concepts covered, ICIPs are contained as well. Another valuable source of information is a review paper on ICIPs from 2022 that shows a partial overlap in the author list [62].

3.1 Interband cascade lasers

Historically, the first proposal of a cascaded infrared laser relying on type-II interband transitions between an electron state located in an InAs well and a hole state in a GaSb well, dates to 1995 by Rui Yang [63]. The name ICL was not yet used, and the injector region existed only as an unspecified concept. However, it already suggested the modification of the emission wavelength by changing the InAs and GaSb layer thicknesses and overcoming the limitation of short ps-lifetimes in intersubband lasers, i.e., QCLs, caused by phonon-assisted depopulation of the upper lasing state. Owing to the interband nature of the radiative transition, significantly lower threshold current densities in comparison to the one year earlier realized QCL [64] were proposed.

The following year, Jerry Meyer, Igor Vurgaftman, Rui Yang and L. Ramdas Ram-Mohan together suggested a more specific structure that involved a second h-QW in order to block direct tunneling from the upper lasing state to the electron injector and a digitally graded InAs/AlSb superlattice as electron injector [65]. Furthermore, type-I ICLs were proposed and for both cases, a type-II interband tunneling mechanism was advocated to recycle the carriers from the valence band of one cascade to the conduction band of the next. In 1995 the ’W’-QW - an active QW design consisting of a $Ga_{0.7}In_{0.3}Sb$ h-QW encompassed by two InAs layers was suggested by Jerry Meyer et al. [66], although then not embedded in an ICL, but a multiple-QW diode laser. It was later theoretically analyzed by Vurgaftman et al. in 1998 [67] implemented in an interband cascade active region of a vertical-cavity surface-emitting laser to increase the overlap of the electron and hole wavefunctions resulting in a larger optical matrix element. Since 2004, the W-QW is a common trait of almost all ICL designs [60].

Experimentally, electroluminescence of an interband cascade device was first achieved in 1996 [68] and followed shortly after by the first successful demonstration of lasing

Die approbierte gedruckte Originalversion dieser Dissertation ist an der TU Wien Bibliothek verfügbar.
The approved original version of this doctoral thesis is available in print at TU Wien Bibliothek.
TU Bibliothek WIEN Your knowledge hub

for an ICL, which was operating at 3.8 µm [69]. Substantial performance improvement led to an ICL emitting more than one photon (∼1.3) per injected electron at a wavelength of 3 µm [70]. Together with [71], these were the first experimental implementations of the W-QW. Considering that these early devices employed 20 or more stages, the external differential quantum efficiency (EDQE) per stage - even after achieving slight improvement [72] - was rather low, amounting to 9.3 % at a temperature of 80 K.

In 1998, two important design changes were featured in an ICL lasing at 3.5 µm that was the first to get close to room temperature operation in pulsed mode, reaching an operating temperature of 286 K [73]. Firstly, an additional 4 nm-thick $Ga_{0.7}In_{0.3}Sb$ h-QW was introduced to enhance the blocking of the leakage path from the upper lasing state to the electron injector resulting in this first realization of a two-well hole injector, with the other well consisting of a 6 nm-thick GaSb layer. Secondly, the length of the electron injector region was reduced, which in retrospect has been suspected to more dominantly contribute to the observed performance improvement [60]. Nevertheless, these results (albeit potentially unjustifiably) led to the employment of the two-QW hole injector in almost all ICL designs that followed.

Low-temperature performance improvement resulted in an EDQE per stage of about 20 % [74], while the operating temperatures continued to rise, reaching up to 142 K for cw operation, owing to improved device fabrication [75]. Pulsed operation at room temperature was finally achieved in 2002, even though the threshold current density under these conditions amounted to as much as 6.9 kA/cm^2 [76]. Subsequently, the pulsed threshold current density was significantly reduced to approximately 1 kA/cm^2 at room temperature and 3.3 µm [77]. Moreover, distributed feedback (DFB) ICLs to achieve single-mode emission started to emerge [78, 79].

The goal of reaching cw room temperature operation, was enabled by a series of design advances. Prevention of mode leakage into the GaSb substrate was facilitated by the introduction of a thicker bottom cladding (2.7 µm compared to previously 2.1 µm) for a 12-period ICL emitting at 3.3 µm [80]. The number of stages was further reduced to 5 [81] in the attempt of lowering the threshold power density, as the operating voltage is directly proportional to the number of cascades. Although the shortening of the electron injector to a reduced length of 20-25 nm is not specified in publications of that time [82], it helped in reducing the carrier density in the electron injector in favor of a higher occupation in the active QW, resulting in a pulsed threshold current density of 1.15 kA/cm^2 [60]. In 2008, a design that employed 5 active stages for a wavelength of 3.75 µm introduced two 200 nm-thick GaSb separate-confinement layers (SCLs) sandwiching the active region to enhance

Die approbierte gedruckte Originalversion dieser Dissertation ist an der TU Wien Bibliothek verfügbar.
The approved original version of this doctoral thesis is available in print at TU Wien Bibliothek.

the confinement of the mode within [83]. Furthermore, the doping there and in the surrounding layers of the cladding directly next to the SCLs was lowered to $n = 1.5 - 2.0 \times 10^{17}$ cm^{-3} in favor of lower absorption losses. The design featured a thicker AlSb barrier at the semimetallic interface (SMI) between electron and hole injector (2.0 compared to previously 1.5 nm). These adaptations jointly led to a reduced pulsed threshold current density of around 400 A/cm^2 at room temperature, enabling the first demonstration of a cw ICL at room temperature.

The next major design advancement was the employment of carrier rebalancing in the active region by heavy n-type doping in the electron injectors leading to significantly reduced threshold current densities [84]. The imbalance towards a higher hole density stems from inefficient electron transfer, leaving a large number of electrons to reside in the electron injector, whereas nearly all of the holes transfer to the active W-QW. Applying the carrier rebalancing concept to ICLs emitting at longer wavelengths, subsequently, led to improved performances at wavelengths between 4.7-5.6 µm [85].

To date, ICLs are especially valued due to their low threshold current densities and low power consumption, ultimately reaching values below 100 A/cm^2 in pulsed operation at 20 °C for a wavelength of 3.6 µm [86] and requiring input powers of as low as 29 mW to reach cw operation at room temperature [84]. This qualifies them for a large variety of applications aiming for portable, miniaturized sensing systems for trace gases and ICLs have been employed to detect sulfur dioxide, formaldehyde, methane and ethane among others [3]. Wall-plug efficiencies of up to 18 % [87] have been achieved in cw operation, which does not fall far behind the latest achievement of 22 % by a QCL [88]. Furthermore, light emission in a single mode has been reported to reach 55 mW at room temperature [2]. For a 22 µm-wide and 4.5 mm-long ridge employing corrugated sidewalls, the maximum output power at room temperature reached 500 mW, while still exhibiting comparably high beam quality ($M \leq 2.5$) [87]. The highest cw operating temperature amounted up to 118 °C [89]. With the option of heterogeneous integration of these lasers on silicon substrates [90] to benefit from CMOS technology, there is a huge drive towards further reduction of the system footprint and cutting costs of sensing solutions going towards photonic integrated circuits [91].

While the performance sweet spot, with lowest threshold current densities and highest external efficiencies, resides around 3-4 µm [2, 92, 93], in the GaSb material system cw operation has been demonstrated for a wavelength range of 2.8-5.6 µm at room temperature [94, 85] and up to 6 µm [95, 96] on InAs substrate. However, ICL performance notably deteriorates outside of the sweet spot and extending the long

Die approbierte gedruckte Originalversion dieser Dissertation ist an der TU Wien Bibliothek verfügbar.
The approved original version of this doctoral thesis is available in print at TU Wien Bibliothek.
TU Bibliothek WIEN Your knowledge hub

wavelength limit for cw operation has proven to be highly challenging. The longest reported wavelength for a GaSb-based DFB ICL has been 5.2 µm in cw [97], whereas pulsed broad area devices were presented at up to 6.9 µm [98]. While the increasing thickness of the InAs/AlSb superlattice cladding layers required for mode confinement at longer wavelengths on GaSb, due to the longer optical decay length, limit heat dissipation from the active region, plasmon waveguides [99] have been employed on InAs substrates. Hence, broad area InAs-based ICLs were demonstrated in cw operation at 10.4 µm at 166 K [100], 11 µm at 97 K [101] and in pulsed operation up to 13.2 µm at 120 K [102].

3.1.1 State-of-the-art active region

To date, state-of-the-art ICLs consist of 5 to 12 active stages, which is adapted to the performance requirements and emission wavelength of the structure. The principle of cascading, first used in QCLs [64], allows the recycling of carriers from one active stage to the next, and provides a means of efficiently reducing the threshold current density.

The principle of cascading

The following introduction to the fundamentals of cascading is based on Refs. [103] and [58]. In any functioning semiconductor laser, the active region needs to provide sufficient gain to overcome the total losses, including mirror and waveguide losses. Gain media composed of QWs provide carrier confinement within the active region and result in a quasi-two-dimensional density of states, increasing the gain in comparison to bulk material [19]. However, one single QW might not offer enough gain, especially going towards longer wavelengths, where the width of the guided mode increases, leading to a reduced overlap with the QW. To increase the gain in a device, using multiple QWs, two concepts are possible: a parallel or in-series connection. In the following, conceptual differences regarding the required voltage, current and power density to reach the lasing threshold will be highlighted.

In conventional diode lasers, where electrons and holes are injected from opposite sides of a *pn*-junction, multiple QWs are often employed to enhance the gain. They are separated by barriers, that are chosen thick enough to limit the coupling of the individual wave functions, maintaining their two-dimensional characteristics, effectively establishing a parallel connection of the QWs. The voltage at threshold V_{th} is identical to the case of a single QW, where the photon energy $\hbar\omega$ is given by the energy gap E_{g} and an additional contribution ΔE, which correlates to the differential

Die approbierte gedruckte Originalversion dieser Dissertation ist an der TU Wien Bibliothek verfügbar.
The approved original version of this doctoral thesis is available in print at TU Wien Bibliothek.
TU WIEN Bibliothek Your knowledge hub

gain and the internal losses, resulting in

$$V_{\text{th}} = \frac{E_{\text{g}} + \Delta E}{e}, \tag{3.1}$$

where e denotes the electron charge. Assuming ideal conditions, the current is distributed equally over the number of QWs, and each QW has to be supplied with the same current density J_{th} to reach the threshold. Thus, the individual currents add up, resulting in MJ_{th} for the entire device featuring a number of M QWs. To approximate the situation in a real structure, an additional series resistance ρ_{s} needs to be considered, which could be caused by the contacts, transition layers between different device regions, the optical cladding or the active region itself. The required threshold power density amounts to

$$\begin{aligned} P_{\text{th}}^{(\text{parallel})} &= \left(V_{\text{th}} + \rho_{\text{s}} M J_{\text{th}}\right) M J_{\text{th}} \qquad (3.2) \\ &= \frac{\left(E_{\text{g}} + \Delta E\right) M J_{\text{th}}}{e} + \rho_{\text{s}} M^2 J_{\text{th}}^2. \qquad (3.3) \end{aligned}$$

There is a direct relation between the lasing wavelength λ and the applied voltage, due to $E_{\text{g}} = hc/\lambda$, where h represents Planck's constant and c the speed of light. Hence, a longer wavelength translates to a smaller voltage drop. Moreover, J_{th} and M, generally increase towards longer wavelengths in the mid-infrared. This results in a relative increase of the second parasitic term in Eq. 3.3 compared to the first term, which is responsible for photon emission.

In contrast, the principle of cascading, relies on a series connection of multiple QWs. Hence, the threshold current density J_{th} supplies all stages and the total voltage drop at threshold is the sum of V_{th} for each cascade, MV_{th}. This yields a dissipated power density at lasing threshold of

$$\begin{aligned} P_{\text{th}}^{(\text{series})} &= \left(M V_{\text{th}} + \rho_{\text{s}} J_{\text{th}}\right) J_{\text{th}} \qquad (3.4) \\ &= \frac{\left(E_{\text{g}} + \Delta E\right) M J_{\text{th}}}{e} + \rho_{\text{s}} J_{\text{th}}^2. \qquad (3.5) \end{aligned}$$

While the first term in Eqs. 3.3 and 3.5 is identical, the parasitic second term does not scale with the number of QWs in a cascaded active region, which leads to a reduced threshold power density for any device employing more than one QW ($M > 1$). The implementation of a cascaded active region in ICLs, allows the recycled carriers to theoretically generate a maximum of one photon per stage. Thus, ICLs easily reach total EDQEs of more than 100 % [70, 72, 74].

The materials, which make up these heterostructure lasers, in general need to be

Die approbierte gedruckte Originalversion dieser Dissertation ist an der TU Wien Bibliothek verfügbar.
The approved original version of this doctoral thesis is available in print at TU Wien Bibliothek.

lattice matched to prevent the buildup of strain in the structure. An alternative concept is to balance the strain resulting from layers that have larger and smaller lattice constants compared to the used substrate. The layers, which typically go into the thousands, are grown using molecular beam epitaxy (MBE). The established material system for ICLs combines InAs, Ga(In)Sb and AlSb grown on either GaSb or InAs substrates.

Each of the cascades in an ICL is composed of the following building blocks: active W-QW, hole injector, SMI and electron injector. A typical ICL active region design is displayed in Fig. 3.1 for an emission wavelength of 3.7 µm. In the following, the purpose, functioning principle and applicable design guidelines of each segment will be discussed.

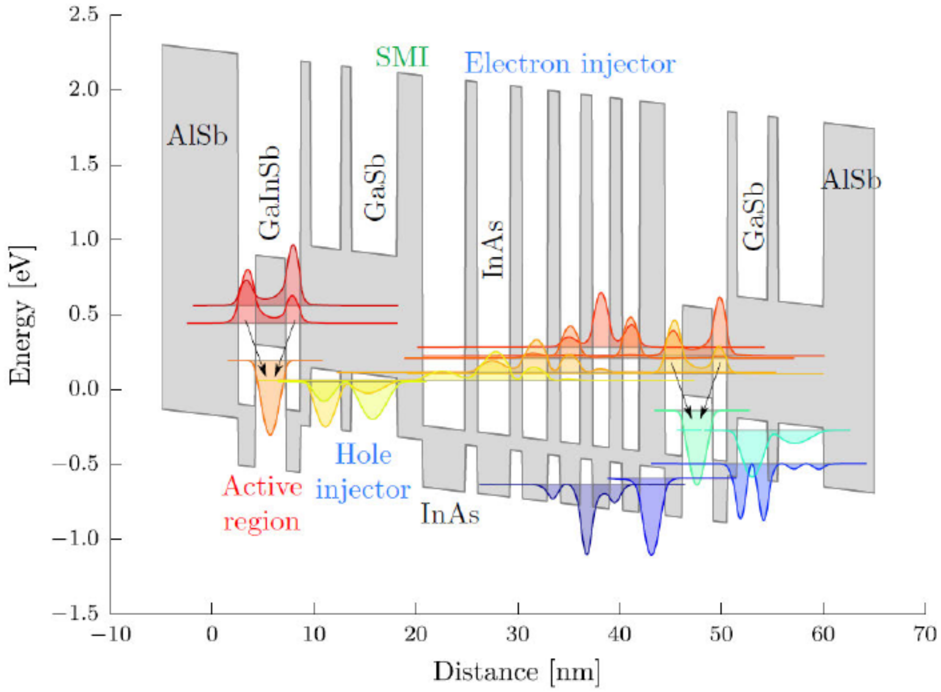

Figure 3.1: Band diagram of 1.5 stages of an ICL active region showing relevant probability densities depicted at the energy levels as well as conduction and valence band edges. Each stage is composed of the same building blocks: active W-QW, two-well hole injector, SMI and electron injector. The heterostructure design is stated in [59] and the figure was reproduced from [1].

W-quantum well

A central element of each cascade of a type-II ICL is the commonly employed W-QW [66], where the lasing transition takes place, providing the gain medium. Compared to a single type-II transition, the spatial overlap between the electron

Die approbierte gedruckte Originalversion dieser Dissertation ist an der TU Wien Bibliothek verfügbar.
The approved original version of this doctoral thesis is available in print at TU Wien Bibliothek.

and hole wavefunctions is enhanced. It is composed of a $Ga_{1-x}In_xSb$ layer, the h-QW, sandwiched between two asymmetric InAs layers, where the electrons in the upper lasing level are localized. A typical W-QW for a lasing wavelength of 4.7 µm is shown in Fig. 3.2 under an applied electric field of 90 kV/cm. The recombination

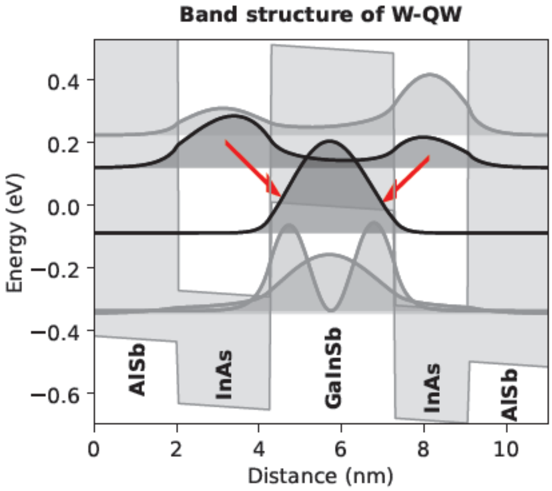

Figure 3.2: Band diagram of a typical W-QW showing the lasing transition in an ICL emitting at around 4.7 µm. The structure consists of 2.00 nm AlSb/2.25 nm InAs/3.00 nm $Ga_{0.65}In_{0.35}Sb$/1.80 nm InAs/2.00 nm AlSb. Probability densities are plotted at the corresponding energy levels. The optical transition, indicated by the red arrows, takes place between the upper lasing level predominantly localized in the two InAs QWs and the heavy hole-like lower lasing level situated in the GaInSb h-QW.

between the electrons in the conduction band and the holes in the valence band under the emission of a photon is indicated by the red arrows. Due to the applied field, the right InAs well is designed to be thinner than the left one, to align the position of the lasing energy level in the two wells, resulting in a more even carrier distribution compared to symmetric InAs layers. Caused by the coupling of the two InAs QWs the electron state splits into a symmetric (black) and an anti-symmetric (gray) energy level, which can be seen in Fig. 3.2. For this structure, the anti-symmetric state lies more than 100 meV above the energy of the symmetric state. Therefore, at and below room temperature the electron population of the anti-symmetric state will be very low [66], as the energy separation is more than $3k_\mathrm{B}T$, with k_B denoting the Boltzmann factor and T the temperature.

Changing the layer thicknesses or the composition of the h-QW allows to adjust the lasing wavelength, although in practice most ICL designs in literature feature an h-QW thickness of 3 nm and a similar $Ga_{1-x}In_xSb$ composition of around $x \approx 0.35$ [60, 96, 102]. The main strategy to select the emission wavelength is to adapt the thickness of the InAs layers, hence, modifying the energy of the up-

Die approbierte gedruckte Originalversion dieser Dissertation ist an der TU Wien Bibliothek verfügbar.
The approved original version of this doctoral thesis is available in print at TU Wien Bibliothek.
TU Bibliothek Your knowledge hub
TU WIEN

per lasing level. While the lower wavelength limit is around ≈ 2 µm for very thin layers, in principle arbitrarily long wavelengths can be achieved [58]. However, a longer wavelength, due to its smaller photon energy, requires the implementation of thicker InAs QWs to reduce the energy gap between electron and hole states. This is accompanied by a reduced spatial overlap of the wavefunctions because the electrons are increasingly localized inside the InAs QWs and the probability density between them, where the h-QW is located, is reduced. For a simplified structure without applied electric field, calculations of the overlap between the envelope functions showed a reduction from 75.5 % for a lasing wavelength of 2.8 µm to 55.1 % for 6 µm [104].

The large In fraction x of the $Ga_{1-x}In_xSb$ layer introduces large compressive strain of more than 2 %, which results in a shift of the heavy hole-like state towards higher energy [58]. In turn, thinner InAs layers can be used to achieve a specific wavelength, in comparison to using a simple GaSb h-QW, which results in a larger wavefunction overlap and increased gain. However, the In fraction x cannot be chosen arbitrarily high due to limitations set by MBE growth, as the $Ga_{1-x}In_xSb$ layer needs to stay below the critical thickness [105, 106].

Moreover, the large compressive strain lowers the effective hole mass near the valence band edge, which according to theory [107] should lead to a reduction of the multi-electron Auger rate. The subband structure of the heavy and light hole levels, which is influenced by the h-QW composition and thickness, should strongly impact the multi-hole Auger rate and internal losses due to hole absorption [22, 108, 109, 44]. These processes are thought to exhibit energetic resonances [31, 109]. However, a non-monotonic correlation between h-QW parameters and the lasing threshold, which is strongly determined by Auger recombination rates, has not been observed for ICLs experimentally [110, 111]. Instead, lower threshold current densities and higher efficiencies were reported with an increase in the indium composition and thickness of the active h-QW, and a 3 nm $Ga_{0.65}In_{0.35}Sb$ layer was suggested as exemplary h-QW in a patent from Vurgaftman et al [112]. The absence of observed resonances is suspected to be due to the large variety of different occurring transitions and broadening effects due to inhomogeneities in the QW thicknesses [113, 30].

In addition, several design adaptations of the W-QW have been proposed and simulated, which rely on the incorporation of arsenic in the h-QW either in the form of a quaternary GaInAsSb [114] or a ternary GaAsSb layer [115]. This allows for an additional degree of freedom regarding valence band engineering or strain compensation [116]. Photoluminescence measurements of structures of five adjacent W-QWs separated by 25 nm-thick GaSb layers, grown on an MBE system, were

Die approbierte gedruckte Originalversion dieser Dissertation ist an der TU Wien Bibliothek verfügbar.
The approved original version of this doctoral thesis is available in print at TU Wien Bibliothek.

Die approbierte gedruckte Originalversion dieser Dissertation ist an der TU Wien Bibliothek verfügbar.
The approved original version of this doctoral thesis is available in print at TU Wien Bibliothek.
TU WIEN Bibliothek Your knowledge hub

conducted in Ref. [114] and [115]. However, these designs have not been employed in an ICL experimentally.

Although the W-QW design is widely used across different research groups working on ICLs, the performance benefit is puzzling, as the larger overlap between electron and hole wavefunctions should in principle lead to an increased non-radiative Auger recombination, in addition to the larger optical matrix element [60]. Nevertheless, ICLs with single type-II active QWs have experimentally shown higher threshold current densities, making the W-QW the preferred choice.

Semi-metallic interface

For an efficient series connection of multiple stages, a recycling mechanism for the carriers from the valence band of one stage back to the conduction band of the next stage needs to be implemented, with a transition time that is much shorter than the recombination lifetime in the W-QW. The SMI between the hole and electron injector in an ICL offers a convenient way to ensure this. The band alignment between GaSb and InAs is unusual, in the sense that the conduction band edge of InAs lies approximately 0.21 eV below the valence band maximum of GaSb at room temperature [117]. This is also known as a type-II broken gap alignment and is schematically depicted in Fig. 3.3. As the materials are employed in the form of QWs, the energetically lowest state will have non-zero eigenenergy (dashed lines). This results in an effective band gap $E_G > 0$ due to the quantum confinement. The two ground states will shift away further from the band edges for thinner QWs,

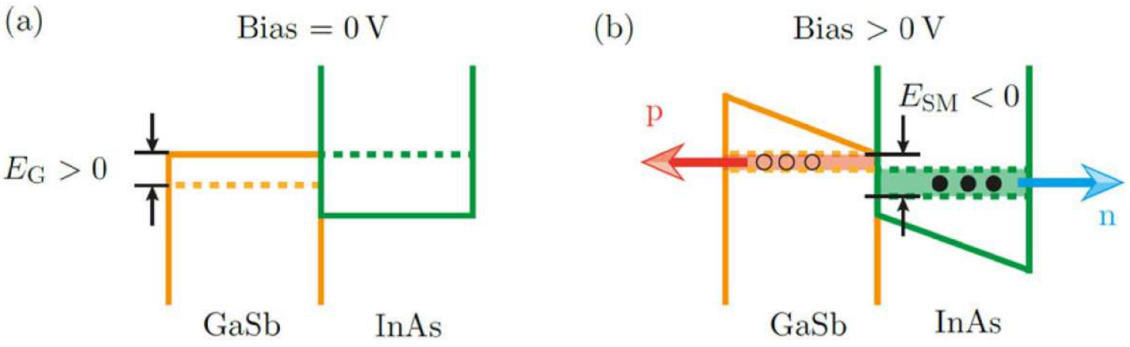

Figure 3.3: a: Band alignment of adjacent GaSb and InAs QWs. Due to the non-zero eigenenergy of the ground state in a QW, an energy gap E_G arises, although GaSb and InAs bulk materials exhibit a semi-metallic band alignment at room temperature. **b**: Upon applying an electric bias, electrons from the GaSb valence band can transfer to the InAs conduction band at the SMI. The generated electrons and holes then move in the direction indicated by the arrows, due to the applied bias. Figure reused from [1], originally adapted from [58].

increasing E_{G}. When applying an electric field E, the semi-metallic band alignment can be reestablished, which is shown in Fig. 3.3b. The energy difference E_{SM} between the electron and hole wavefunctions at the SMI, which quantifies the band overlap, according to

$$E_{\mathrm{SM}} = eE\,(d_{\mathrm{e}} + d_{\mathrm{h}}) - E_{\mathrm{G}}, \tag{3.6}$$

shows a linear dependence on the applied electric field [58]. Here, d_{e} and d_{h} denote the center-of-mass distances from the SMI of the electron and hole probability densities. In order to approximately determine the generated electron and hole densities induced by the band overlap at the SMI, parabolic bands, a two-dimensional density of states $\rho_{\mathrm{2D}} = m_{\mathrm{e}}^*/(\pi\hbar^2)$, where m_{e}^* is the effective electron mass, and a common quasi-Fermi level E_{F} on both sides of the SMI are assumed. In this case E_{F} can approximately be written as $E_{\mathrm{F}} \approx E_{\mathrm{SM}}\, m_{\mathrm{r}}^*/m_{\mathrm{e}}^* + E_{\mathrm{c}}$, where E_{c} is the conduction band minimum [58]. The reduced mass m_{r}^* is defined by the effective electron m_{e}^* and hole masses m_{h}^* according to $m_{\mathrm{r}}^* = m_{\mathrm{e}}^* m_{\mathrm{h}}^*/(m_{\mathrm{e}}^* + m_{\mathrm{h}}^*)$. In order to calculate the carrier density, the density of states and the Fermi function $f(E)$ need to be integrated over the energy interval of interest. Further simplifying the example, by assuming a temperature of $T = 0$ K, where $f(E) = 1$, the electron n and hole densities p induced by the overlap amount to [58]

$$n = p \approx \frac{m_{\mathrm{r}}^*}{\pi\hbar^2} E_{\mathrm{SM}}. \tag{3.7}$$

Thus, the carrier recycling mechanism needed for cascading, is established at the SMI, where the generated carrier densities, according to Eqs. 3.6 and 3.7, can be adjusted by changing the applied electric field and the InAs and GaSb layer thicknesses. Under typical operating voltages, E_{SM} amounts to ≈ 100 meV in ICLs [59].

In an ICL, commonly an AlSb barrier is placed between the GaSb QW of the hole injector and the thickest InAs QW of the electron injector. While it was previously implemented with a thickness of 1.5 nm, a thicker AlSb layer of 2 to 2.5 nm was found to be beneficial for device performance, as it reduces the interband absorption across the SMI, while still enabling sufficient electron transport from the valence to the conduction band [112]. The carrier transport across the SMI via interband tunneling or scattering takes place on a sub-picosecond time scale [118]. Afterwards, the electrons and holes that recombined in the active W-QW, under the emission of a photon or non-radiatively, need to be replenished by the carriers internally generated at the SMI. This task is fulfilled by the electron and hole injectors, which are discussed in the following.

TU Bibliothek Die approbierte gedruckte Originalversion dieser Dissertation ist an der TU Wien Bibliothek verfügbar. WIEN Your knowledge hub The approved original version of this doctoral thesis is available in print at TU Wien Bibliothek.

Die approbierte gedruckte Originalversion dieser Dissertation ist an der TU Wien Bibliothek verfügbar.
The approved original version of this doctoral thesis is available in print at TU Wien Bibliothek.
TU Bibliothek WIEN Your knowledge hub

Hole injector

The hole injector serves two main purposes. It blocks carrier leakage from the upper lasing level to the electron injector, acting as a barrier for this process, and it efficiently transports the generated holes from the SMI to the active h-QW, ensuring population inversion. To date, the most popular design features two GaSb h-QWs, although limited experimental proof for the benefit of implementing the second well has been found. Simulations suggest that a single QW should suffice to disrupt the leakage path from the InAs wells in the W-QW to the electron injector [118].

Due to the applied field, the GaSb QW closer to the SMI should be wider to ensure good transport to the active h-QW, resulting in an alignment of the topmost subband in both wells at threshold and strong coupling of the QWs. Furthermore, the AlSb barrier between the InAs well of the W-QW and the hole injector should be sufficiently thin, to allow adequate hole transport, i.e., 1.0-1.2 nm [59]. Empirically, an energy separation between the topmost subband in the hole injector and the lower lasing level of 80-100 meV was found to be beneficial, ensuring that almost all holes transfer to the active h-QW, yielding very low occupation of the states in the hole injector. Lower threshold power densities for high-temperature operation were reported in this case [58].

The first hole injector was suggested in 1996, which was composed of a 5.8 nm-thick $Ga_{0.7}In_{0.3}Sb$ layer for a structure with a simple active type-II QW employing a 2.5 nm-thick InAs layer and a 3 nm-thick $Ga_{0.7}In_{0.3}Sb$ h-QW [65]. The thought of possible absorption due to intervalence transitions occurred back then but was claimed to be avoided due to the selected thickness of the hole injector QW mitigating resonances between these transitions and the lasing energy. Another study reported, that calculations of valence intersubband absorption in the W-QW and hole injector resulted in non-zero absorption at the lasing wavelength of a simple type-II QW (2.5 nm InAs/3.4 nm $Ga_{0.7}In_{0.3}Sb$) with a hole injector consisting of only one 5.3 nm-thick GaSb QW in the beginning of ICL design [119]. However, apart from the previously stated empirically derived design criteria for the hole injector, valence band engineering has mostly been disregarded in literature.

Electron injector

In order to enable stimulated emission, the quasi-Fermi-levels of electrons and holes in one stage of the ICL have to be separated by more than the photon energy: $E_{\mathrm{Fn}} - E_{\mathrm{Fp}} > \hbar\omega$. In principle this represents the Bernard-Duraffourg condition known from conventional diode lasers [120]. Due to the rapid transport of electrons from the valence to the conduction band of the next stage at the SMI, holes in stage i

share a quasi-Fermi-level with electrons from stage $i + 1$, $E_{\mathrm{Fp,i}} = E_{\mathrm{Fe,i+1}}$. As the carrier lifetimes in the active W-QW are much longer (~ 1 ns) [110], a discontinuity of the quasi-Fermi-levels across the active region of each stage is ensured. In an ideal design the energy difference between the Fermi-levels of consecutive stages exceeds the photon energy only by a small amount, which is on the order of the thermal energy $k_{\mathrm{B}}T$ [19]. Hence, this relation can be written as

$$E_{\mathrm{Fe,i}} - E_{\mathrm{Fe,i+1}} = \hbar\omega + k_{\mathrm{B}}T. \tag{3.8}$$

Recalling the relation established for the overlap at the SMI in dependence on the applied electric field (Eq. 3.6), under ideal conditions at threshold, the applied electric field for the generation of the threshold carrier density n_{th} should equal the field required to fulfill the lasing condition in Eq. 3.8. The electric field is obtained by dividing the energy separation by the total thickness of one stage d and the charge density of an electron e. This results in

$$E_{\mathrm{th}} = \frac{\hbar\omega + k_{\mathrm{B}}T}{ed} = \frac{E_{\mathrm{SM}} + E_{\mathrm{G}}}{e\left(d_{\mathrm{e}} + d_{\mathrm{h}}\right)}. \tag{3.9}$$

Careful design of the electron and hole injectors and the energy levels at the SMI is needed to achieve ideal operating conditions. For one thing, the electron injector is required to have a minimum thickness for a given electric field. The longer the lasing wavelength, the shorter the electron injector can be, following Eq. 3.9. Second, the thickness of the first InAs layer forming the right side of the SMI is critical. If chosen too thin, the band overlap E_{SM} is reduced, and a higher applied field is required to generate a sufficient number of carriers. In contrast, if the thickness is too high, unfavorably high carrier densities increase the threshold due to Auger recombination in the injectors and induce additional losses.

The remaining InAs layers of the electron injector are employed with decreasing thickness towards the active W-QW, and can form a miniband to guide the electrons, which should be designed to align with the upper lasing level. If the miniband is located much higher than the upper lasing state, although most electrons will reside in the active W-QW, an excessive electric field might be required for operation. If it is too low in energy, the carriers will mostly remain in the electron injector.

Instead of using this miniband approach, where the electrons are delocalized over the entire length of the injector, a different design turned out to be advantageous, although the reasons are not completely understood [58]. Here, the electron QWs closest to the W-QW are thinner, which raises the energy levels above the upper lasing level. Although not occupied under quasi-equilibrium conditions, as these

Die approbierte gedruckte Originalversion dieser Dissertation ist an der TU Wien Bibliothek verfügbar.
The approved original version of this doctoral thesis is available in print at TU Wien Bibliothek.

injector states lie several multiples of the thermal energy $k_{\mathrm{B}}T$ above the upper lasing level, they allow effective carrier transport. Experimentally this design showed enhanced performance.

The AlSb barriers between the InAs wells of the injector should be thin (1.2 nm) to guarantee unimpeded transport of the electrons. In contrast, the AlSb barrier separating the injector region from the active W-QW should prevent backfilling of the carriers and hybridization of the upper lasing level and the injector level and should, thus, have a thickness of 2.5 nm [112].

Compared to the historically employed much thicker electron injectors [70], a smaller thickness reduces the carrier density in the electron injector and leads to fewer holes being generated and subsequently injected into the W-QW. As the hole absorption cross section for intervalence transitions tends to be much higher [47] than corresponding cross sections for electrons, an excess number of holes in the active region is undesired. Moreover, thinner electron injectors increase the overlap of the mode with the W-QW under the condition that the mode confinement in the active region stays the same, because they now make up a smaller fraction of the active region. Since the InAs/AlSb layers show a lower refractive index with respect to Ga(In)Sb, a smaller length of the electron injector leads to a higher effective refractive index, and thus, better mode confinement.

Whereas almost all holes generated at the SMI end up in the W-QW, simulations show that a significant amount of the electrons resides in the injector [84]. As the number of electrons and holes generated internally according to Eq. 3.7 is equal, at lasing threshold much more holes than electrons are present in the W-QW. This imbalance of the carrier densities towards holes can be unfavorable, depending on which mechanisms are dominating the device performance. Non-radiative Auger recombination in ICLs is known to govern the threshold current density [121]. If the multi-hole Auger rates are higher than the multi-electron rates, a balance towards higher electron density would be favorable, and vice versa. Internal losses due to various absorption mechanisms may complicate the situation further.

One possibility to increase the number of electrons in the W-QW is presented by heavy n-doping of the InAs layers in the electron injector. By increasing the doping, more electrons will end up in the lasing state despite the inhibited transport. Experiments, investigating the effect on ICL performance under varying doping concentrations at an emission wavelength around 3.7 µm, resulted in an ideal doping of $n = 5 \times 10^{18}$ cm^{-3} compared to previously employed moderate doping of $n = 4 \times 10^{17}$ cm^{-3}, which yielded a simulated carrier ratio of $n_{\mathrm{th}}/p_{\mathrm{th}} \approx 1.2$ [121]. A reduction of the threshold current density and the internal loss was achieved, and

TU Bibliothek, WIEN Your knowledge hub
Die approbierte gedruckte Originalversion dieser Dissertation ist an der TU Wien Bibliothek verfügbar.
The approved original version of this doctoral thesis is available in print at TU Wien Bibliothek.

the Auger rates for multi-electron and multi-hole processes were concluded to be approximately equal, which agrees well with theoretical predictions [22]. This carrier rebalancing approach resulted in a significantly reduced threshold current density from 400 to 167 A/cm^2 and a reduction of the threshold voltage from $V_{\mathrm{th}} \sim 2.5$ V to ~ 2.1 V [84]. Calculations further revealed that for an optimized ICL, the additional voltage drop per stage on top of the photon energy was only ~ 12 meV [84], thus indeed fulfilling Eq. 3.8. The concept of carrier rebalancing by comparably heavy n-doping of the electron injector is now applied in most state-of-the-art ICLs at different wavelengths. A total doping sheet density on the order of 10^{12} cm^{-2}, is suggested in literature for optimum results at room temperature [121].

3.1.2 Waveguide

Although the gain and internal efficiency of an ICL are attributed solely to the active region, for the creation of a well performing device, the waveguide design plays a crucial role. Optical, electrical and thermal properties of the laser need to be considered, most of the times resulting in a trade-off between different aspects, as they cannot be optimized independently.

In general, the waveguide needs to guarantee sufficient overlap of the propagating mode with the active region, while minimizing the internal losses. In ICLs, thick dielectric top and bottom claddings are used for several purposes. The optical mode needs to be separated from the highly n-doped InAs cap layer ($n = 2 \times 10^{19}$ cm^{-3}) and the GaSb substrate to avoid free carrier absorption induced by the electric contacts or high doping concentrations. Furthermore, mode leakage into the substrate needs to be avoided, as GaSb shows a relatively high refractive index [122].

After being reported for a diode laser in 2005 [123], a GaSb layer, which is inserted below the active region, was employed in an ICL [82]. In 2008, another GaSb layer was added on top of the active region [83]. Since then, two GaSb layers known as SCLs are regularly used in ICLs. They encompass the active region, confining the optical mode due to their relatively high refractive index ($n \sim 3.78$) in comparison to the effective refractive index of the active region itself [58].

A schematically assembled ICL structure is displayed in Fig. 3.4 for a wavelength of 6.15 µm. The heterostructure was realized on an MBE system, and subsequently pictures from a cleaved edge were recorded with a scanning electron microscope (SEM). The micrographs of the active region, which includes 9 stages, surrounded by two symmetric 760 nm-thick GaSb SCLs, are shown on the left.

GaSb-based ICLs commonly feature optical claddings composed of an InAs/AlSb superlattice. With a perdiocity of 4.73 nm (2.43 nm InAs/2.3 nm AlSb) these

Die approbierte gedruckte Originalversion dieser Dissertation ist an der TU Wien Bibliothek verfügbar.
The approved original version of this doctoral thesis is available in print at TU Wien Bibliothek.

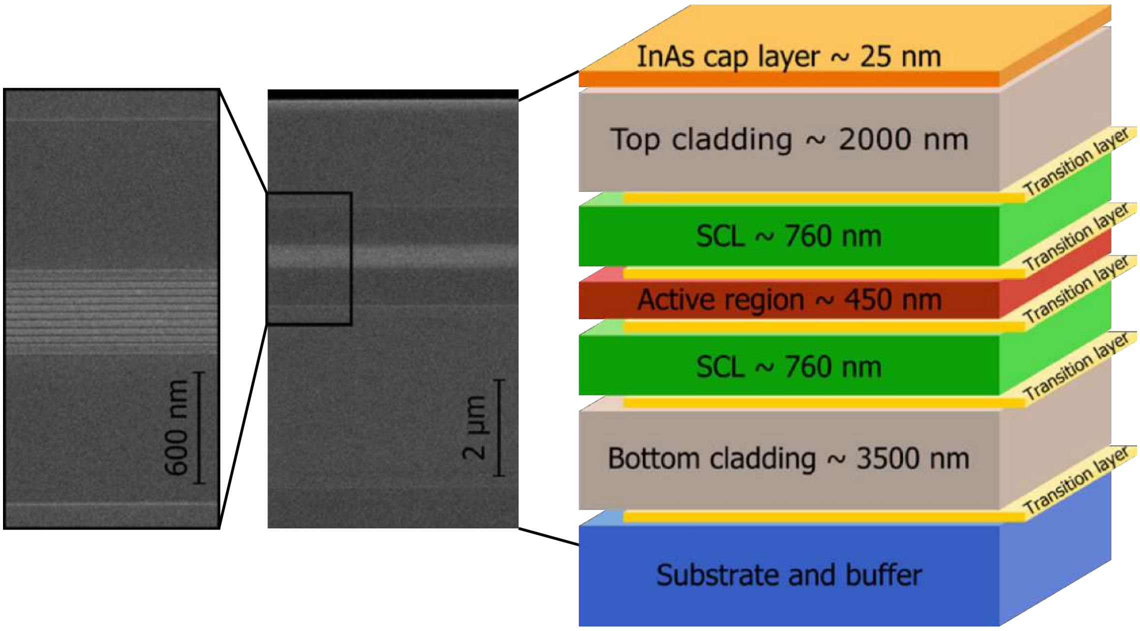

Figure 3.4: Schematic waveguide structure of an ICL designed for a comparably long emission wavelength of around 6.1 µm. Pictures obtained from a SEM show the active region, surrounded by two symmetric GaSb SCLs for mode confinement. The active region comprises 9 stages.

layers are effectively lattice-matched to the GaSb substrate [58]. Due to quantum confinement, the superlattice exhibits an effective bandgap, which corresponds to a wavelength of 1.58 µm [124, 104]. As the lowest realistically possible wavelength for an ICL lies around 2 µm, no absorption due to this effective bandgap should occur in any device. The refractive index of the claddings ($n \sim 3.25$) is significantly lower than that of the active region [58].

The overlap of the propagating light within the waveguide with the active region is quantified by the confinement factor Γ_{AR}

$$\Gamma_{\mathrm{AR}} = \frac{\int_{AR} |E(y,z)|^2 \mathrm{d}y\,\mathrm{d}z}{\int \int_{-\infty}^{\infty} |E(y,z)|^2 \mathrm{d}y\,\mathrm{d}z}, \tag{3.10}$$

where y and z denote the lateral in-plane direction and the vertical in-growth direction, respectively. The propagation inside the waveguide takes place along the x-axis.

Moreover, the confinement factor can be calculated for other functional parts of the ICL, i.e., the cladding, SCL or W-QW. The overlap with the active W-QW is typically around 4 %. The total internal losses arise from the sum of the overlap with a functional part (cladding, SCL and active region) times the material loss in that part, $\alpha_{\mathrm{i}} = \sum_j \alpha_{\mathrm{j}} \Gamma_{\mathrm{j}}$. In literature, the losses in the active region and cladding layers

Die approbierte gedruckte Originalversion dieser Dissertation ist an der TU Wien Bibliothek verfügbar.
The approved original version of this doctoral thesis is available in print at TU Wien Bibliothek.
TU Bibliothek WIEN Your knowledge hub

Die approbierte gedruckte Originalversion dieser Dissertation ist an der TU Wien Bibliothek verfügbar.
The approved original version of this doctoral thesis is available in print at TU Wien Bibliothek.
TU WIEN Bibliothek Your knowledge hub

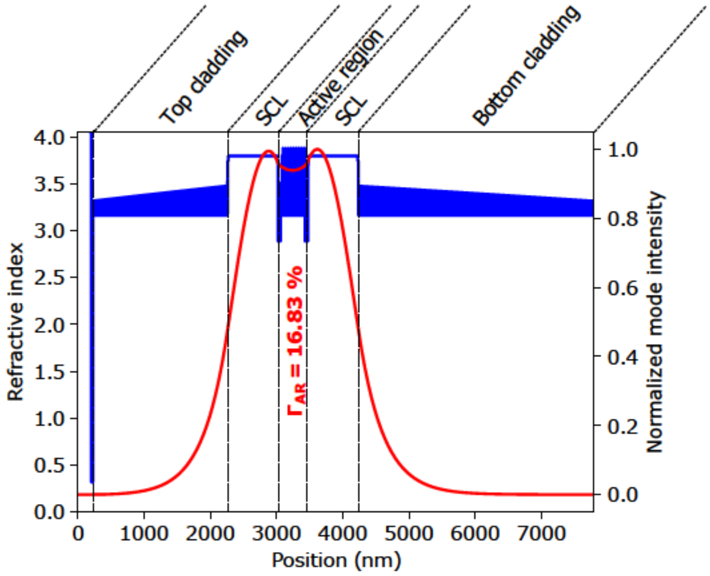

Figure 3.5: Refractive index profile (blue) of the ICL waveguide schematically depicted in Fig. 3.4. As a lot of very thin layers are stacked for the claddings and the active region, the refractive index profile in this plot resembles a blue area instead of a line. For the claddings, the top edge shows the refractive index of InAs, with a graded doping density from $n = 1 \times 10^{18}$ cm^{-3} to $n = 2 \times 10^{17}$ cm^{-3} going towards the SCLs, and the bottom edge corresponds to AlSb. The normalized mode intensity is depicted in red, with a confinement factor of $\Gamma_{\mathrm{AR}} = 16.83\,\%$ within the active region.

are assumed to be much higher than in the SCLs [58]. For the claddings this is due to the higher doping and the large number of interfaces. For the structure shown in Figs. 3.4 and 3.5, the doping of the bulk SCLs is $n = 5 \times 10^{16}$ cm^{-3}, while the doping in the claddings is graded from $n = 1 \times 10^{18}$ cm^{-3} to $n = 2 \times 10^{17}$ cm^{-3} going towards the SCLs, to reduce the doping in the regions with higher mode overlap and, hence, the losses. Thus, maximizing the overlap factor with the SCLs is an effective way to reduce the waveguide losses.

The confinement of the mode in the different functional parts of the ICL can primarily be adjusted by varying the SCL thickness. Going from thin to thick layers, the overlap with the active region first increases due to a stronger modal confinement in the center between the two SCLs and then decreases again, due to the emergence of a minimum in the mode profile within the active region, as can be seen in Fig. 3.5 However, the slightly lower Γ_{AR} is compensated by the much lower losses due to the decreased overlap with the claddings in favor of the SCLs.

Although low doping concentrations are desirable to avoid optical losses, sufficient electric transport needs to be guaranteed for the carriers traversing the waveguide structure on their way from the top to the bottom contact. Moreover, the conduction band edge of the GaSb SCL lies approximately 500-600 meV above the conduction band edges of the active region and the claddings [58]. To avoid excess voltage drops due to arising potential barriers at abrupt interfaces between different functional parts of the ICL, transition layers are placed at all interfaces involving GaSb (the SCL and the substrate) [112]. They are shown in yellow in Fig. 3.4, with thicknesses around 50 nm. The transition layers are comprised of AlSb/InAs barrier/QW pairs, with thinner InAs wells closer to the GaSb parts, in order to increase the energy levels of the electrons due to quantum confinement to smoothen the transition towards the higher conduction band edge. Experimentally, lower voltages at threshold have been observed when employing these transition layers [58]. For the transitions from the SCLs to the active region, GaSb layers can be incorporated in addition to the AlSb barriers to increase the refractive index [104] supporting the mode confinement in the active region. In addition to the transition layers, the voltage drop at the interfaces can be lowered, by layers of higher doping at the edges of the SCLs. In literature doping values of $n = 5 \times 10^{15}$ cm^{-3} for the middle part of the GaSb layers and $n = 1 \times 10^{17}$ cm^{-3} for the 50 nm-thick edges were reported [59].

The waveguide design and the used number of active stages needs to be adapted for ICLs depending on the desired lasing wavelength and required figures of merit, e.g., high output power versus low threshold current density. To minimize the threshold power density, literature suggests 500 nm as optimum thickness for the SCLs of an ICL with 5 stages and an emission wavelength of 3.7 µm [58]. For the same goal, but a wavelength of 3.6 µm and 200 nm-thick SCLs, the optimum number of stages was determined to be 4 [104].

When targeting the same operating voltage for ICLs emitting at different wavelengths, the number of stages needs to be increased with longer wavelength, as the voltage drop across the device scales with the photon energy, according to Eq. 3.9. The addition of stages results in a higher total voltage drop across the device, while providing higher gain and achieving a larger mode overlap with the active region, thus, lowering the threshold current density J_{th}. When trying to minimize the threshold power density P_{th} for one particular wavelength, the ideal number of stages needs to be ascertained by comparison of the lower J_{th} with the additional voltage drop caused by the addition of a stage. If the goal is to maximize the cw output power, a larger number of stages is beneficial [60].

As the mode decay length is larger for longer wavelengths, the waveguide design, in particular the SCL thickness should be modified to reduce the overlap of the mode with the lossy claddings. Hence, thicker SCLs tend to be beneficial for longer wavelengths.

Die approbierte gedruckte Originalversion dieser Dissertation ist an der TU Wien Bibliothek verfügbar.
The approved original version of this doctoral thesis is available in print at TU Wien Bibliothek.

Moreover, alternative approaches to the InAs/AlSb claddings have been demonstrated. Quaternary bulk $Al_{0.85}Ga_{0.15}As_{0.07}Sb_{0.93}$ shows a low refractive index, which is well-fit for confining the mode and can be lattice matched to GaSb [125, 126]. On InAs substrate, plasmon waveguides are used for ICLs at long wavelengths, due to their better thermal conductivity, simplified MBE growth and lower refractive index compared to the superlattice claddings used for GaSb-based ICLs [99, 96, 102]. There, undoped InAs SCLs are used together with n-doped InAs plasmon enhanced claddings. Replacing the outer part of the InAs SCL with an intermediate cladding consisting of a 2.5 nm InAs/2.3 nm AlSb superlattice resulted in enhanced optical confinement [127].

3.1.3 Performance limitations

To date, ICLs cover a wide wavelength range in the mid-infrared, from around 2.8 µm [94] to 13.2 µm [102]. However, their performance metrics differ significantly over this range, with best results reported within 3-4 µm [2]. The reasons for the position of this sweet spot and deteriorating performance toward longer wavelengths appear to be manifold. In general, there is still a variety of open questions regarding the functioning principles and underlying physical mechanisms in ICLs. Moreover, some experimental observations still elude current theoretical explanations, e.g., a decrease in external efficiency with increasing current [128], and the increase of the Auger coefficient and internal loss with decreasing wavelength below 3.2 µm [60]. The ones that are relevant in the context of the results of this thesis, will be highlighted in the following.

Threshold current density

Comparison of the performance of different designs is best approached using broad area devices in pulsed operation, which eliminates the influence due to device fabrication, scattering losses at the etched sidewalls, or heating of the device associated with high duty-cycles. A large set of data was published by Meyer et al. [60], and Fig. 3.6 depicting the threshold current density J_{th} in dependence of emission wavelength, is reprinted from that publication. Two trends are observed for J_{th}, that shows the lowest values in the 3-4 µm region, with a minimum around 3.3 µm. There is a significant increase going towards either shorter (< 3.2 µm) or longer wavelengths. The very thin InAs layers in the W-QW of short wavelength ICLs have been suspected as a contributing factor, inducing higher interface roughness scattering [60]. However, this mechanism is not sufficient to explain the increase

Die approbierte gedruckte Originalversion dieser Dissertation ist an der TU Wien Bibliothek verfügbar.
The approved original version of this doctoral thesis is available in print at TU Wien Bibliothek.
TU WIEN Bibliothek Your knowledge hub

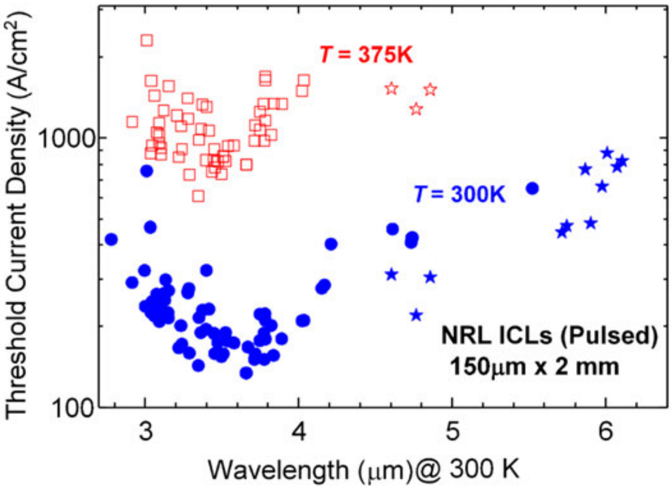

Figure 3.6: Pulsed (250 ns, 3 kHz) threshold current densities for 85 different ICL designs realized at the Naval Research Laboratory, employing 5, 7 or 10 stages. The measured broad area devices were 150 μm wide and 2 mm long. Figure reprinted from [60].

of J_{th}. Some currently unidentified mechanism causes an increase of the internal loss and Auger coefficient with decreasing wavelength in this range [30]. In addition, the efficiency droop discussed in the following section, was reported to be more pronounced for an ICL at 3.1 μm compared to 3.45 μm [128].

The increasing threshold current densities above 4 μm can be rationalized by a multitude of related factors. In ICLs, the threshold current density is mainly determined by the non-radiative Auger recombination [121]. Multi-carrier Auger recombination has been the topic of detailed studies in mid-infrared semiconductor lasers, including type-I InGaAsSb/GaSb QW lasers, with emission wavelengths between 1.7 - 3.2 μm [32] and type-II ICLs [113, 2]. A recent study [30] in the overlapping wavelength region of 2.8 - 3.5 μm of these two types of QW lasers, reported on the influence on threshold current density, which crosses over at around 3.1μm [30]. Below, J_{th} is lower for type-I QW lasers, and above for ICLs. Although non-radiative Auger recombination is suppressed in comparison to bulk materials [110, 111], it is known to increase with longer wavelength, hence, resulting in higher J_{th} [129]. The Auger coefficient extracted from measurements of J_{th} showed 3-4 times higher values at 6 μm compared to a device emitting at 3.5 μm [129]. Increasing free carrier absorption and a reduced overlap due to the thicker InAs layers in the W-QW contribute to this trend.

The threshold at long wavelengths > 4.5 μm was shown to decrease significantly when employing a hybrid bottom cladding [60]. Like in the claddings used for InAs-based ICLs, this hybrid cladding takes advantage of the plasma effect. Below a

Die approbierte gedruckte Originalversion dieser Dissertation ist an der TU Wien Bibliothek verfügbar.
The approved original version of this doctoral thesis is available in print at TU Wien Bibliothek.

1.5 µm-thick standard InAs/AlSb superlattice an $InAs_{0.91}Sb_{0.09}$ layer is placed with high doping density of $n = 4 \times 10^{18}$ cm^{-3}, which shows a low refractive index due to the plasma effect [129]. A hybrid-cladding on both sides of the active region has been demonstrated as well, which employed 0.9 µm-thick intermediate InAs/AlSb superlattice claddings followed by highly doped InAsSb outer claddings with $n = 1.5 \times 10^{19}$ cm^{-3} [130].

Efficiency droop

Another figure of merit is the EDQE, which is a measure for the number of photons emitted per injected electron. It is extracted from the slope of the experimentally determined light-current characteristic and commonly given per stage, yielding

$$\eta_\mathrm{e} = \frac{1}{M}\frac{dP}{dI}\frac{\lambda e}{hc}, \tag{3.11}$$

where M denotes the number of cascades in the active region. Typical values between 3-4 µm lie within 40-50 %, with the highest reported one being 56 %, and decrease to 25-30 % for wavelengths within 4.5-5 µm [60]. What is striking in ICLs is a significant decrease in EDQE with increasing current [128]. This so called 'efficiency droop', is surprising as it occurs even in the absence of device heating, during pulsed operation [59]. It also seems to be too large to be explained by carrier heating [129]. In an ideal laser diode, the carrier density is pinned as soon as the threshold is reached, and the increasing current neither influences the losses nor the internal efficiency, thus, resulting in linearly increasing photon output. Experimentally, indications for the absence of carrier pinning have been discerned. The spontaneous emission was observed to still increase with rising current above threshold at temperatures above 180 K for ICLs emitting at 4.1 µm [131]. When assuming carrier pinning, it should, however, stay constant in favor of the lasing process. This behavior indicates rising carrier densities in the active W-QWs, which will lead to higher losses due to any mechanism dependent on the carrier density. These measurements were conducted by collecting the out of plane emission through a milled window in the substrate of a fabricated laser chip, which is then solely composed of spontaneously emitted photons. It should be noted that evidence for the absence of carrier pinning has also been gathered for type-I mid-infrared diode lasers [132, 15].

Moreover, length-dependent measurements for two ICL designs at 3.1 µm and 3.45 µm implied rising internal losses rather than decreasing internal efficiencies to be the causative underlying mechanism for the decreasing EDQE with increasing current [128]. The rising losses might be, at least partly, due to the rising carrier

Die approbierte gedruckte Originalversion dieser Dissertation ist an der TU Wien Bibliothek verfügbar.
The approved original version of this doctoral thesis is available in print at TU Wien Bibliothek.
TU Bibliothek Your knowledge hub WIEN

densities above threshold [60]. Furthermore, degradation of the EDQE with rising temperature was concluded to be mostly due to a substantially decreasing internal efficiency and only moderately due to increasing internal losses [128]. To date, no design variations have succeeded in eliminating this efficiency droop and the mechanisms surrounding it are not sufficiently understood [133].

3.2 Interband cascade infrared photodetectors

Following the epxerimental realization of ICLs, the first demonstration of the concept for light detection instead of generation from this device architecture was reported in 2005 [134]. Only the year before the first QCD had been demonstrated by slightly modifying the active region of a QCL [135]. In QCDs, the intersubband selection rule in the conduction band limits the optical transitions to light polarized along the growth-direction. Hence, a suitable light coupling mechanisms is required for QCDs. Among the most popular choices are a 45° facet used in a double-pass geometry [136] or diffraction gratings [137]. In contrast, in interband cascade detectors (ICDs) the light can simply be detected under normal incidence, either through the substrate side or via top illumination, due to the interband nature of the optical transition. No additional mechanism is necessary for the light detection, which is very convenient for practical applications.

The functioning principle of ICIPs is tightly linked to ICLs. Unsurprisingly, there is a huge overlap when looking at research groups investigating these two device categories, since many of them are working on both topics [60]. In literature, the terms ICIP and ICD are often used interchangeably, since neither gives indication about the nature of the absorption region, which can for example either be a single absorbing W-QW, when using an ICL without applied bias for light detection, or a type-II superlattice. The first realization of an ICIP making use of a type-II superlattice as active region was demonstrated in 2010 [138], setting the foundation for this relatively new and promising detector technology.

3.2.1 Functioning principle

The integral building blocks of this type of detector are the same as for their laser counterpart, the ICL, which was extensively discussed in the previous section. While ICL active regions consist of the W-QW for photon generation, the electron and hole injector, the latter two bear slightly different labels in ICIPs. The electron barrier, which prevents the electrons from moving in one direction, essentially corresponds to the hole injector in ICLs. It consists of digitally graded GaSb/AlSb QWs. The hole

TU Bibliothek Your knowledge hub WIEN Die approbierte gedruckte Originalversion dieser Dissertation ist an der TU Wien Bibliothek verfügbar. The approved original version of this doctoral thesis is available in print at TU Wien Bibliothek.

barrier on the other hand corresponds to the electron injector, featuring InAs/AlSb QWs. Upon generation of an electron-hole pair via photon absorption the carriers diffuse through the absorber. The direction of the current flow in the device is dictated by the electron and hole barriers, blocking the moving carriers in one direction. The two types of carriers then recombine at the interface of electron and hole barriers of adjacent stages. This functioning principle is schematically depicted in Fig. 3.7.

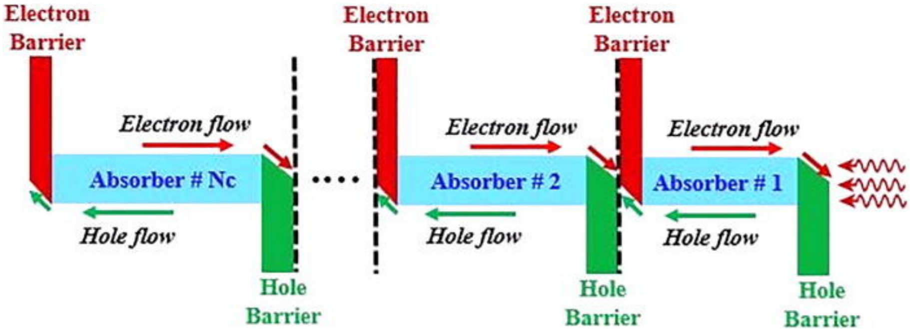

Figure 3.7: Illustration of the functioning principle of an ICIP with reverse-illumination configuration and increasing lengths of the absorbers from stage 1 to stage Nc for current-matching. Each superlattice absorber is encompassed by an electron and a hole barrier. Reprinted from [139], with the permission of AIP Publishing.

Hence, an essential mechanism of both ICLs and ICIPs is the cascading principle discussed in section 3.1.1. While one electron can yield multiple generated photons in an ICL, in the corresponding detector scheme multiple photons are needed for the extraction of one single electron. At first glance this reduction in responsivity seems to be undesirable for a detector, with the responsivity as performance metric indicating the amount of generated current or voltage per incident optical power, given in A/W or V/W. However, this has far-reaching implications when looking at the sensitivity of the detector, often characterized by the detectivity. The detectivity is the reciprocal of another figure of merit, the noise equivalent power (NEP). The NEP, as its name suggests, quantifies the amount of incident power that is necessary to generate a signal that equals the noise output. Hence, at this power level, the signal to noise ratio (SNR) is 1. Therefore, since multiple photons are necessary to generate one electron, the noise is significantly suppressed proportional to the number of stages in comparison to a device using a single absorber section. As a result, the specific detectivity D^* of an ICIP has been shown to be proportional to the square root of the number of stages N_c in a first order approximation, $D^* \propto \sqrt{N_c}$ [140]. The individual absorbers featured in each section are commonly designed to be shorter than the diffusion length, resulting in efficient extraction of the carriers.

Die approbierte gedruckte Originalversion dieser Dissertation ist an der TU Wien Bibliothek verfügbar.
The approved original version of this doctoral thesis is available in print at TU Wien Bibliothek.
TU WIEN Bibliothek Your knowledge hub

The diffusion length in type-II InAs/GaSb superlattice absorbers was experimentally determined to lie between 0.6 µm and 1.0 µm for temperatures between 250 K and 300 K [141]. Recently, the ultimate detectivity achievable in multi-stage ICIPs has been investigated analytically [142]. Even for the limit of infinite diffusion length, for which all generated carriers could be extracted in a single stage absorber long enough to absorb all incident light, the detectivity of a multiple-stage device is about 11 % higher than for this optimized single-absorber detector. This value is only a lower limit for the improvement of the detectivity achievable by using a cascaded device. In real devices, the finite diffusion length limits the maximum absorber length that can be implemented to still efficiently collect the photogenerated carriers, which allows the ICIP to outperform single stage absorbers in terms of detectivity even by a larger amount than the theoretical limit of 11 % [142].

In literature so called current-matching is employed for these devices, in order to maximize the responsivity of an ICIP [143]. If light only passes through the device in one direction, the light intensity will exponentially decrease along the length of the absorbers due to absorption. Hence, the last absorber will be passed by lower intensity light compared to the absorber located in the first stage. If all absorbers feature the same length, more carriers will be generated in the first stage. However, since an ICIP essentially is an in-series arrangement of cascades, the current through each stage is required to be the same. Thus, even though more carriers are generated in the first stage, the current is limited by the carriers generated in the last stage. Current-matching describes gradually increasing absorber lengths from the first to the last stage to account for the attenuation of the light, resulting in an equal amount of carriers generated per stage. While the concept has experimentally been confirmed to result in optimized responsivity, the detectivity did not show significant improvement [143]. Depending on the direction of the current flow with respect to the direction of the incoming light, devices are distinguished into regular- and reverse-illumination configurations [141]. In the latter configuration the light first impinges onto the hole barrier, which is the side of the device where the electrons are ultimately extracted at the contact after traversing the cascades. This reverse-illumination configuration is preferred for *p*-doped absorbers, where electrons are minority carriers [141].

3.2.2 State-of-the-art performance

In comparison to traditional mercury cadmium telluride (MCT) detectors, which constitute one of the most important detector types available in the infrared, ICIPs show intriguing technological advantages like suppressed Auger recombination, re-

Die approbierte gedruckte Originalversion dieser Dissertation ist an der TU Wien Bibliothek verfügbar.
The approved original version of this doctoral thesis is available in print at TU Wien Bibliothek.
TU Bibliothek WIEN Your knowledge hub

duced tunneling currents and high uniformity in their growth [141]. Especially the latter is one of the most critically viewed properties of the otherwise excellently performing MCT detectors, since growth stability is essential for the realization of focal plane arrays.

Tweaking the layer thicknesses of the type-II superlattice absorbers modifies the cutoff wavelength of the detector by shifting the energy of the minibands in the absorber section. Hence, ICIPs can cover a large range of the infrared spectrum. Looking at the transmissivity of earth's atmosphere, the infrared can be classified into so-called transmission windows, which show low absorption by molecules present in the terrestrial atmosphere. Water vapour is the main reason for light attentuation at wavelengths between these windows, that can roughly be divided into the short-wavelength infrared at 1-3 µm, the mid-wave at 3-5 µm, the long-wave at 8-12 µm and the very long wave infrared >14 µm [144]. ICIPs featuring InAs/GaSb type-II superlattices have been demonstrated in all of these wavelength ranges from 2.9 µm up to 16 µm, demonstrating the huge flexibility of this technology [144, 141, 145, 146]. Room temperature operation has so far been demonstrated up to a cutoff wavelength of 10.7 µm, where the detectivity of these devices was reported to outperform commercially available uncooled MCT detectors [145].

Although most reports of ICIPs so far have relied on InAs/GaSb superlattices, or the related InAs/GaAsSb combination with GaAsSb grown lattice-matched to the InAs substrate, other material combinations are emerging and have been reported. Among them, the most notable and promising ones seem to be InAs/InAsSb type-II superlattices [147]. One of the main arguments for using InAs/InAsSb instead of InAs/GaSb is to avoid Ga in the superlattice, which induces short minority carrier lifetimes due to SRH recombination, which is associated with native defects in Ga [148]. This negatively influences device dark current and quantum effciency. Moreover, since the InAs/InAsSb layers have two common elements, In and As, the superlattice shows a rather uncomplicated interface structure simplifying the growth [147]. This comes at the expense of smaller spectral tuneability and weaker optical absorption [147]. The experimental reports of ICIPs based on InAs/InAsSb superlattices are very limited and have only been emerging very recently [149]. However, in this demonstration the interband tunneling mechanism at the interface between hole and electron barriers used in the common ICIP architecture is replaced by a p^+/n^+ tunneling junction between the superlattice absorbers as connecting regions. InAs/InAsSb based ICIPs were further reported by A. Bader from the University of Würzburg at the Mirsens conference in July 2022 [150].

Moreover, an ICIP employing a quaternary GaInAsSb bulk absorber region has

Die approbierte gedruckte Originalversion dieser Dissertation ist an der TU Wien Bibliothek verfügbar.
The approved original version of this doctoral thesis is available in print at TU Wien Bibliothek.
TU WIEN Bibliothek Your knowledge hub

been experimentally realized [151]. The reported detectivity of a three stage detector was comparable to type-II superlattice ICIPs with similar cutoff wavelengths [151]. The advantages lie in the even distribution of electrons and holes and the subsequently larger spatial overlap resulting in an increased absorption coefficient. To achieve the same responsivity, a much shorter absorption region can be realized compared to a superlattice, where electrons and holes are spatially separated. The shorter absorption length could be beneficial for high-speed applications, where fast extraction of the carriers is of utmost importance.

The potential for high-speed applications has only recently experienced a rise in research attention resulting in a number of publications investigating the bandwidth of ICIPs [152, 153, 154, 155]. A 3-dB bandwidth of more than 7 GHz was reported for a cascaded device featuring an InAs/GaSb superlattice absorber with an optical cutoff wavelength around 5 µm [154]. The emergent competing InAs/InAsSb superlattice devices might offer even more favorable properties for high-speed detectino. The 3-dB cutoff of a device featuring this material combination (although not cascaded) was demonstrated to be 12.8 GHz in 2022 [156].

Morover, there is a huge potential for monolithic integration and systems comprising both ICLs and ICIPs for high-frequency applications such as dual-comb spectrometry [157, 158]. High-speed performance and applications of ICIPs will be discussed in chapter 6. Until then the focus will now shift back to light-emitting devices, the ICLs.

TU Bibliothek WIEN Your knowledge hub
Die approbierte gedruckte Originalversion dieser Dissertation ist an der TU Wien Bibliothek verfügbar.
The approved original version of this doctoral thesis is available in print at TU Wien Bibliothek.

Die approbierte gedruckte Originalversion dieser Dissertation ist an der TU Wien Bibliothek verfügbar.
The approved original version of this doctoral thesis is available in print at TU Wien Bibliothek.
TU WIEN Bibliothek Your knowledge hub

CHAPTER 4

ACTIVE REGION DESIGN OF INTERBAND CASCADE LASERS

This chapter is dedicated to the advances in active region design of interband cascade lasers made during the course of this thesis, reporting observations both from a modeling and experimental point of view. The employed theoretical methods were introduced in section 2.2, allowing efficient calculation of the band structure and subsequently absorption between subbands. The general building blocks of ICLs, which are under detailed investigation here, were established in section 3.1.1. Each investigated design modification was triggered by experimental observations, followed by theoretical studies aiming to understand the underlying physical phenomena to give guidance on optimized designs. Subsequently, results obtained from modeling were in turn investigated experimentally with an intent to corroborate the predictions. The common set goal of this approach was to enhance various aspects of ICL device performance.

First, resonant valence intersubband absorption is identified as causative underlying mechanism for a performance degradation in the 4-5 µm region. Changing the thickness of the $Ga_{1-x}In_xSb$ h-QW is proposed as a mitigating strategy. Experimentally, employing this approach leads to an improvement of the laser's characteristic temperature T_0, threshold current density J_{th}, slope efficiency η, and output power. Furthermore, extracted waveguide losses determined from length-dependent measurements confirm the pivotal role of the valence intersubband absorption. Subsequently, this absorption is briefly studied at longer wavelengths, enabling high-performance cw operation above 6 µm. Following, other parts of the active region, i.e., the hole injector and the thickest QW of the electron injector are studied and first insights on possible adaptations of the active region design are discussed.

The findings within the chapter regarding the valence intersubband absorption in ICL W-QWs were in large parts published by H. Knötig, J. Nauschütz et al. in "Mitigating valence intersubband absorption in ICLs", Laser & Photonics Reviews 2022, 2200156 [159]. They furthermore lie the basis for the subsequent publication entitled "Pushing the room temperature continuous-wave operation limit of GaSb-based interband cascade lasers beyond 6 µm" by J. Nauschütz, H. Knötig et al., which explores the application of the established design guidelines among other design improvements above 6 µm [160].

4.1 Motivation

The performance of ICLs is known to notably degrade outside of the sweet spot 3-4 µm region, as is discussed in section 3.1.3. However, various gases exhibit strong absorption features in the 4-5 µm range and, hence, this spectral region is of great importance for spectroscopic applications. In recent years, ICLs have been employed in numerous gas detection systems, i.e., quantifying CO in biogas [4], analyzing dissolved CO_2 in seawater [5], isotopic abundance analysis of CO_2 [6] and measuring SO_2 [7] and N_2O concentrations [8]. Enhancing performance metrics of the laser source, such as increasing the output power or reducing the required driving current, enables the development of more compact and sensitive systems for these trace gases. Thus, an initial goal was to improve the device performance for emission wavelengths in the range of the most dominant absorption feature of CO_2 at 4.35 µm.

Before delving deep into the active region design, the search for clues hinting at possible physical phenomena responsible for the performance degradation begins with the analysis of available data. The performance metrics of 30 different ICL structures previously grown at the University of Würzburg are reviewed below. Although J_{th} is significantly influenced by a variety of parameters, e.g., etch depth, doping for carrier rebalancing and number of grown active stages, the presented data is comparable. The same etch depth and device dimensions of 2.0 mm x 150 µm were selected and carrier rebalancing was employed for all structures. A quick standard process when characterizing structures grown by MBE is the fabrication of shallowly etched broad area ridges. The utilization of broad area ridges reduces the influence of fabrication imperfections on the measured performance, e.g., due to losses introduced by sidewall roughness. For better comparability, light-current-voltage (LIV) characteristics are then determined in pulsed operation to avoid heating the device.

Die approbierte gedruckte Originalversion dieser Dissertation ist an der TU Wien Bibliothek verfügbar.
The approved original version of this doctoral thesis is available in print at TU Wien Bibliothek.
TU WIEN Bibliothek Your knowledge hub

Figure 4.1 shows the pulsed threshold current density J_{th} as a function of emission wavelength.

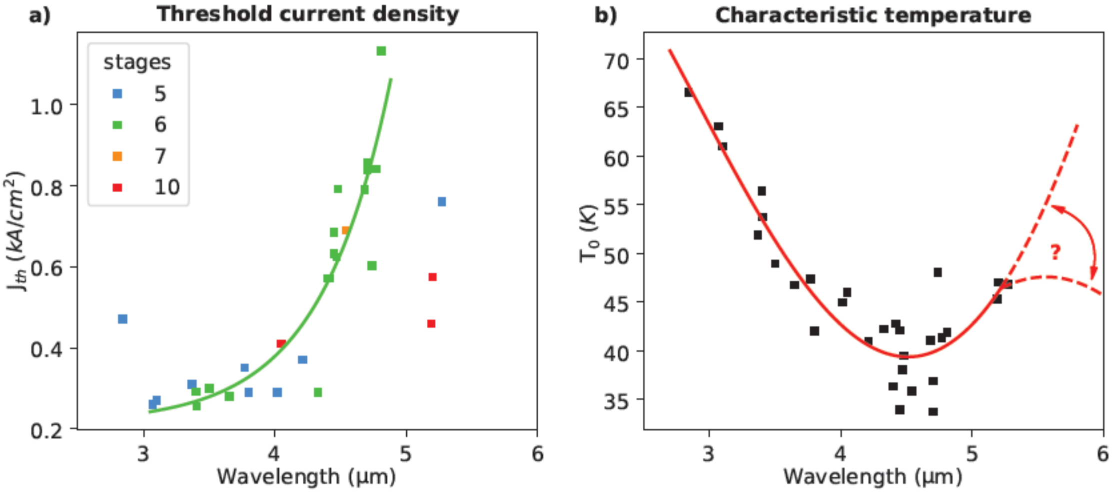

Figure 4.1: ICL performance metrics in dependence on emission wavelength. **a:** Pulsed threshold current densities J_{th} for shallowly etched broad area ICLs at 20 °C with 5 to 10 active stages. **b:** Characteristic temperature T_0 for operating temperatures between 10 and 80 °C. All devices feature a 3 nm $\mathrm{Ga_{0.65}In_{0.35}Sb}$ h-QW. The red line indicates the observed trend for the wavelength dependency of T_0, with two dashed red lines suggesting potential continuations of the trend at longer wavelengths. Data published in [159].

Some of this data was previously published in Ref. [59], however, those devices were etched through the active region. The reason to investigate shallowly etched devices here, is the higher volume of available data, which is essential when trying to identify wavelength dependent trends. However, the reported absolute values of the threshold current densities in Fig. 4.1 are higher in comparison to values reported in literature (see e.g., Fig. 4 in Ref. [60]) due to current spreading and a therefore effectively larger area that is being pumped. The number of active stages significantly influences J_{th}, rationalizing to compare the performance of ICLs with identical number of stages. A clear trend is best seen for structures employing 6 active stages, depicted in green, where the green line is meant as a guide to the eye. With increasing wavelength J_{th} significantly rises, especially above 4 µm. This is a known phenomenon [129, 60] due to several contributing effects: a wavelength dependent rise of non-radiative recombination due to Auger scattering, internal losses due to free carrier absorption, and a reduced overlap of the electron and hole wave functions in the W-QW. The reduced overlap is a result of the thicker InAs electron QWs used for longer wavelengths in the W-QW, as changing their thickness is the main strategy for tuning the energy of the lasing transition. Hence, the thicker wells lead to an increased localization of the electrons inside the InAs QWs and a

Die approbierte gedruckte Originalversion dieser Dissertation ist an der TU Wien Bibliothek verfügbar.
The approved original version of this doctoral thesis is available in print at TU Wien Bibliothek.

reduced probability density between them, where the h-QW is located, which acts as a barrier for the electrons in the upper lasing level. In addition, the fact that this wavelength range has received considerably lower attention regarding device optimization compared to the 3-4 µm range, e.g., with regard to optimizing carrier rebalancing [84, 85] might additionally contribute to the deteriorated performance, and fewer structures have been reported in literature (see e.g., wavelength gap of reported devices between 4.2 and 4.6 µm in Fig. 4 of Ref. [60]).

For most spectroscopic applications cw operation of the laser is required. Bearing that in mind, the temperature dependence of the threshold current density J_{th}, empirically described by the characteristic temperature T_0, is particularly relevant. The exponential temperature dependence is described by

$$J_{th} = J_0 \exp\left(\frac{T}{T_0}\right). \tag{4.1}$$

Thus, a strong temperature dependence of J_{th} corresponds to a low value of T_0, which limits the achievable maximum performance under cw operation. The importance of this parameter becomes evident when looking at QCLs, which exhibit comparably modest temperature sensitivity. There, various active-region design changes resulted in improved values of T_0 of 200 up to above 500 K [161], i.e., employing shallower wells and shorter barriers in the active region to avoid carrier leakage from the upper lasing state to unwanted states energetically directly above [162, 163, 164] and meticulous design of the transition from the last injector well to the upper laser state, leading to suppressed electron populations in the injectors [165]. Moreover, investigations concerning T_0 can elucidate important device characteristics, as was the case for electron leakage contributions to J_{th} in QCLs [166]. ICLs typically exhibit T_0 values of 45-55 K for emission wavelengths between 3 and 4 µm, which further decrease at longer wavelengths [59, 60]. The related T_0 values of the ICL structures under investigation are shown in Figure 4.1b. Remarkably, T_0 does not simply decrease with increasing wavelength, but the values seem to recover at around 5 µm. The data suggests a minimum around 4.6 µm, possibly hinting at another mechanism responsible for an additional temperature dependence specifically in this wavelength region. With the strive towards cw operating ICLs at long wavelengths (> 6 µm) another question is *how this behavior continues*. Do the T_0 values continue to rise as indicated by the top red dashed line or do they drop again?

From a general point of view, an effect that either increases the losses or decreases the gain with increasing temperature with a resonance around 4.6 µm could explain the observed minimum of T_0. In the following, we will revisit effects that have

Die approbierte gedruckte Originalversion dieser Dissertation ist an der TU Wien Bibliothek verfügbar.
The approved original version of this doctoral thesis is available in print at TU Wien Bibliothek.

been introduced in section 2.1, this time with regard to their influence on ICL performance and more precisely to illuminate whether they could be causing the observed behavior of T_0.

- Free carrier absorption (see section 2.1.2) is anticipated to increase towards longer wavelengths, therefore contributing to the increasing J_{th} shown in Figure 4.1a. However, it should be independent of temperature and can be excluded to be the causative effect of the minimum.
- Auger recombination (see section 2.1.1) decreases T_0, inducing a general wavelength dependent trend [113]. Multi-hole Auger processes show a strong dependence on the valence subband structure, exhibiting energetic resonances according to theory [31, 109]. However, experimentally this has not been observed for ICLs [110, 111].
- With increasing temperature, the carriers are distributed over a broader energy range according to the Fermi distribution. Hence, a larger carrier density is required to reach the lasing threshold. This is due to the opposite curvature of the conduction and valence band and represents an inherent effect in interband lasers. Therefore, it is valid for any ICL independent of the wavelength and cannot cause a minimum in T_0. Generally, this higher presence of carriers, in turn, amplifies the Auger effect.
- A resonant absorptive transition between valence subbands could be a potential explanation for the minimum, which will be discussed subsequently.

Looking at intersubband transitions, their behavior differs significantly in the conduction compared to the valence band (see discussion in section 2.1.2). While they are thoroughly studied in the conduction band, especially because of the success of QCLs, the situation is more intricate in the valence band. The conduction band dominantly arises from the highly symmetric s-orbital, resulting in the well-known polarization selection rule. Put simply: interaction (absorption or amplification) of light polarized perpendicular to the growth direction, as it is the case in ICLs, is much weaker compared to light with polarization in growth direction. In contrast, the valence band consists of non-parabolic p-orbitals, thus altering the polarization selection rules to a large extent. Hence, intersubband absorption is partly possible for the typical polarization in ICLs [167]. Under the assumption of thermally distributed carriers with a fixed Fermi level above both levels, the valence intersubband absorption is expected to increase with temperature, giving a possible explanation for the observed minimum in T_0.

Die approbierte gedruckte Originalversion dieser Dissertation ist an der TU Wien Bibliothek verfügbar.
The approved original version of this doctoral thesis is available in print at TU Wien Bibliothek.

All former considerations led to the assumption that a resonant valence intersubband absorption might occur within the active region of the ICL itself more precisely, within the h-QW of the lasing transition. Section 4.2 will be dedicated to a meticulous investigation of exactly this phenomenon.

4.2 W-quantum well

As a first step, calculations of the wavelength-dependent valence intersubband absorption in the W-QW of the ICL were conducted using numerical simulations. More specifically, the electronic band structure was determined using an eight-band $\mathbf{k} \cdot \mathbf{p}$ method [168, 169, 170] (see section 2.2.2). Subsequently, a generalized momentum matrix element model [56, 57] (see section 2.2.4) was employed, which can calculate all contributions regardless of the type of transition to the absorption in the W-QW [25]. It is of utmost importance to evaluate the optical matrix element for a particular valence intersubband transition in a two-dimensional k-space, since effective mass theory falls apart in the valence band. This is due to the non-parabolicity and varying contributions from the heavy hole, light hole and split-off valence bands to one particular valence subband. If not denoted otherwise, all subsequently presented simulations were performed for a temperature of 300 K and an applied electric field of 90 kV/cm.

To confirm the hypothesis, a design showing a particularly low T_0 value was chosen from the epitaxially grown structures presented in Fig. 4.1. The device experimentally showed an emission wavelength of 4.7 µm. The electronic band structure of the W-QW featuring a 3 nm thick $\mathrm{Ga_{0.65}In_{0.35}Sb}$ h-QW is shown in Fig. 4.2a at the Γ-point.

While the red subband has dominant heavy hole contributions, the black subband is light hole-like. The same valence subbands are shown in Fig. 4.2b in dependence on the in-plane wave vector, utilizing the same colors. A potential intersubband transition is indicated by the red arrow, which for this design matches the experimental lasing wavelength. However, the strength of the actual absorption is determined by the optical matrix element between the participating subbands.

Subsequently, we calculated the intersubband absorption in the valence band for this ICL design. The Fermi level was fixed to the uppermost subband energy of the valence band at $k = 0$, which represents the situation in the structures under investigation here reasonably well. The obtained simulation result of the absorption is presented in blue in Fig. 4.3 depending on the wavelength.

While the absorption between 3 and 4 µm is negligible, a pronounced absorption

Die approbierte gedruckte Originalversion dieser Dissertation ist an der TU Wien Bibliothek verfügbar.
The approved original version of this doctoral thesis is available in print at TU Wien Bibliothek.
TU WIEN Bibliothek Your knowledge hub

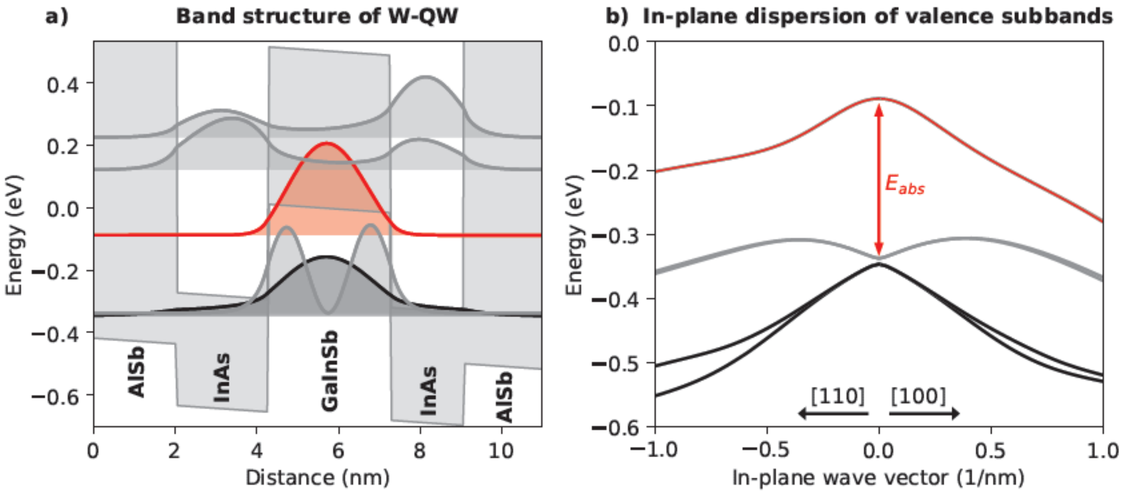

Figure 4.2: Electronic band structure for one particular W-QW. **a:** Band structure calculated at the Γ-point. Probability densities are plotted at the corresponding energy levels. Red denotes the heavy hole-like and black the light hole-like subband. The W-QW consists of 2.00 nm AlSb/2.25 nm InAs/ 3.00 nm $Ga_{0.65}In_{0.35}Sb$/1.80 nm InAs/2.00 nm AlSb. **b:** Dependence of the relevant valence subbands on the in-plane wave vector k. A potential intersubband transition close to the Γ-point between the red and black subbands is suggested by the red arrow. The data was published in [159].

peak occurs at 4.6 µm, indisputably confirming the presence of valence intersubband absorption in this device, as it emits light at a wavelength close to the absorption peak. All structures, including this one, presented in Figure 4.1 employ an active region design with a 3.0 nm thick $Ga_{0.65}In_{0.35}Sb$ layer as h-QW. Changing the thickness of the two InAs layers, in order to define the lasing wavelength, only marginally influences the valence band structure. Hence, the degraded T_0 (Fig. 4.1b) is explained directly by the wavelength dependence of the valence intersubband absorption reported here. For better comparison, T_0 is additionally shown in Fig. 4.3 with reverse y-axis. Hence, where the lasing wavelength coincides with the absorption wavelength, lower T_0 values are obtained. The rising absorption towards even longer wavelengths yields an answer to the previously raised question regarding the continuation of the trend (red dashed line). As a conclusion, T_0 is expected to be influenced and can potentially be enhanced by avoiding valence band resonances via design changes.

Temperature dependence and doping concentration

By simulating the same W-QW design for varying temperatures, the dependence of the valence intersubband absorption on temperature is confirmed. A W-QW design with slightly differing InAs layer thicknesses was used in this case: 2.00 nm AlSb/

Die approbierte gedruckte Originalversion dieser Dissertation ist an der TU Wien Bibliothek verfügbar.
The approved original version of this doctoral thesis is available in print at TU Wien Bibliothek.

Die approbierte gedruckte Originalversion dieser Dissertation ist an der TU Wien Bibliothek verfügbar.
The approved original version of this doctoral thesis is available in print at TU Wien Bibliothek.
TU WIEN Bibliothek Your knowledge hub

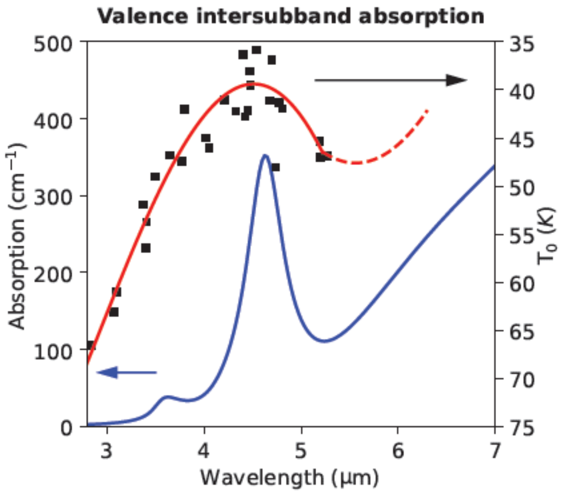

Figure 4.3: Calculated intersubband absorption in the valence band (blue) of the W-QW depicted in Fig. 4.2. A strong absorption peak is observed in the same wavelength range as low T_0 values for several ICL designs. As all depicted devices rely on the same h-QW design, a connection begs to be drawn. Bearing this in mind, another degradation of T_0 is expected towards even longer wavelengths (red dashed line) as the absorption rises again.

2.25 nm InAs/3.00 nm $Ga_{0.65}In_{0.35}Sb$/1.85 nm InAs/2.00 nm AlSb. The temperature was varied between 50 K and 500 K in steps of 50 K and the result is shown in Fig. 4.4, with the black line denoting the absorption at 300 K.

In general, the absorption increases with increasing temperature, hence, the impact on T_0 is evident. This temperature behavior is not surprising since the carrier distribution smears out at higher temperatures according to the Fermi distribution and a higher absolute value of the number of holes is required to reach the lasing threshold. Hence, a higher temperature will automatically result in an increased hole density and thus higher valence intersubband absorption. Moreover, a redshift of the dominant absorption peak is observed, indicated by the dark blue arrow.

Due to the dependence of the valence intersubband absorption on hole density, modifying the approach for the optimization of the doping in the electron injector for carrier rebalancing might be necessary for structures or at wavelengths, where valence intersubband absorption takes place. The optimization should then not only result in reduced non-radiative Auger recombination, but the absorption should be decreased as well due to the lower hole density. However, the most favorable doping density to achieve balanced carrier densities of electrons and holes might be concealed, as increasing the n-doping beyond this optimal point, might still reduce the valence intersubband absorption, resulting in better device performance. In literature, the need for higher sheet doping densities for optimized carrier rebalancing

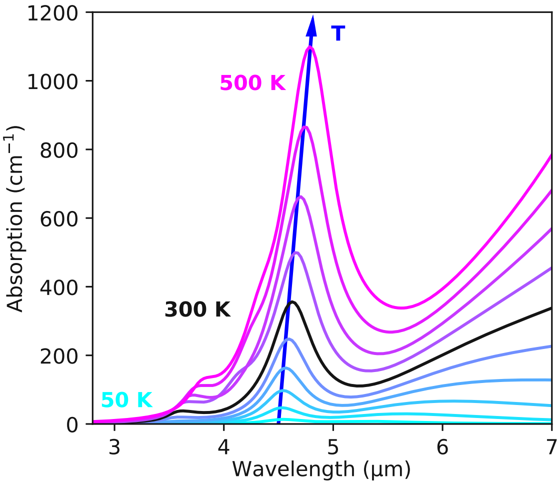

Figure 4.4: Calculated valence intersubband absorption for a W-QW at varying temperatures from 50 K to 500 K. The dark blue arrow illustrates the increase and redshift of the absorption peak around 4.6 µm with rising temperature.

has been suggested for wavelengths > 4 µm due to an observed rise of the internal loss [121]. For best results, mitigating hole absorption should be attempted before optimization of the doping. For structures not implementing strategies to reduce the valence intersubband absorption, higher n-doping, achieving a reduced hole density instead of a truly balanced ratio between electrons and holes is expected to be favorable.

4.2.1 Design variations of the hole-QW

Having identified valence intersubband absorption as a causative phenomenon for the reduced T_0 values of ICLs around 4.6 µm, the next step is the investigation of how the absorption losses can be mitigated by adapting the design of the active W-QW. The predominant design in literature was so far employing a $\mathrm{Ga}_{1-x}\mathrm{In}_x\mathrm{Sb}$ layer thickness of 3 nm with an alloy composition of $x \approx 0.35$. A variation of the valence band structure can intuitively be achieved by modifying the h-QW of the active region. That offers two possibilities that will be explored in the following:

(a) varying the layer thickness

(b) changing the $\mathrm{Ga}_{1-x}\mathrm{In}_x\mathrm{Sb}$ alloy composition.

However, modifications to the h-QW need to be made with care. For very thin $\mathrm{Ga}_{1-x}\mathrm{In}_x\mathrm{Sb}$ layers, e.g., below 2.5 nm, the confinement of the valence band state of the optical transition needs to be evaluated, as carriers could accumulate in the neighboring GaSb hole injector [171] (see Fig. 3.1 for complete band structure of

Die approbierte gedruckte Originalversion dieser Dissertation ist an der TU Wien Bibliothek verfügbar.
The approved original version of this doctoral thesis is available in print at TU Wien Bibliothek.
TU Bibliothek WIEN Your knowledge hub

one cascade of the active region). An upper limit to the thickness is set by the introduction of excessive compressive strain when growing $Ga_{1-x}In_xSb$ with high indium content, due to the lattice constant mismatch between InSb and the GaSb substrate. In addition, varying the composition and thickness of the h-QW changes the lasing wavelength and spatial overlap of the electron and hole wave functions.

Thickness variation

Variations of the thickness of the $Ga_{1-x}In_xSb$ h-QW were explored within a reasonable range (2 - 4 nm) in the simulation and the intersubband absorption in the valence band was determined. The result is presented in Fig. 4.5.

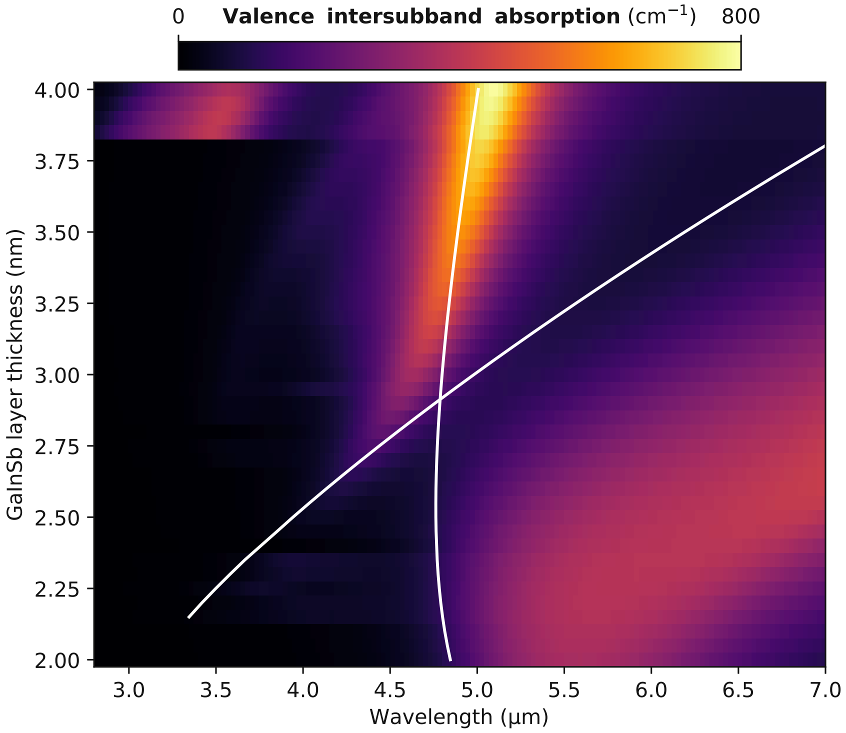

Figure 4.5: Calculated valence intersubband absorption in the W-QW in dependence on the $Ga_{0.65}In_{0.35}Sb$ layer thickness. The two white lines indicate the wavelengths determined by the energy difference at the Γ-point between the valence subbands (red-black and red-gray in Fig. 4.2). At h-QW widths below 2.2 nm, some subbands are not bound anymore, hence, the left white line ends there. Data published in [159].

The two white lines in Fig. 4.5 indicate the transition energies at the Γ-point between the simulated subbands (red-black and red-gray in Fig. 4.2). As the picture painted by the actual calculation of the valence intersubband absorption differs strongly from the position of the Γ-point transition energies, this acts as confirmation of the non-trivial nature of the optical matrix elements and selection rules in the

Die approbierte gedruckte Originalversion dieser Dissertation ist an der TU Wien Bibliothek verfügbar.
The approved original version of this doctoral thesis is available in print at TU Wien Bibliothek.
TU WIEN Bibliothek Your knowledge hub

valence band. Hence, it is not sufficient to only look at the Γ-point. Dominant absorption can arise at non-zero k values, i.e., leading to the absorptive feature above 5 µm and thin h-QWs in the lower right corner.

What is most striking, is that within the parameter space, spanned by the GaInSb thickness and the absorption wavelength, there are regions where negligible absorption is present. First and foremost, the wavelength region between 3 and 4 µm, which coincides with the sweet spot of ICL performance shows close to zero absorption. Between 4 and 5 µm insignificant absorption is present for h-QWs thinner than 2.75 nm, whereas for longer wavelengths, thicker h-QWs result in low absorption. The most prominent absorption arises around 4.6 µm, increases and slightly redshifts going towards thicker h-QWs. Another absorption feature, which is much broader than the first one, occurs at wavelengths above 5 µm and thin h-QWs. In conclusion, the practical relevance for ICLs lies in the possibility to use these results as a guideline, employing a $\mathrm{Ga}_{1-x}\mathrm{In}_x\mathrm{Sb}$ thickness in the active region design that lies within a region of low absorption for the desired lasing wavelength. Hence, the simulations suggest that using a thinner h-QW, compared to the standard 3 nm thick one, should result in enhanced performance for ICLs lasing at around 4.5 µm.

The absorption feature in the upper left corner at small wavelengths ($<$ 4.7 µm) and large h-QW thickness ($>$ 3.8 nm) is due to transitions involving electronic states that are unbound at smaller well widths. A recently demonstrated ICL design, using InAsP layers [102], could potentially lead to better control over these quasi-bound valence band states because of the larger band offset.

Moreover, it should be noted that in the early days of ICL development, valence intersubband transitions were considered to be a potential source of losses, however, calculations at that time resulted in negligible loss at the lasing wavelength of 3.9 µm for a type-II transition not yet employing a W-QW active region [167]. Comparing the simulation results presented here to previously reported observations in literature [110] yields an excellent fit. The studied active regions by Bewley et al. all fall into regions with comparably low absorption, hence, most likely no influence of the thickness and composition of the $\mathrm{Ga}_{1-x}\mathrm{In}_x\mathrm{Sb}$ on the device performance could have been observed.

Alloy composition

Next, the influence of the $\mathrm{Ga}_{1-x}\mathrm{In}_x\mathrm{Sb}$ alloy composition on the valence intersubband absorption will be investigated. Qualitatively, varying the composition within the range relevant for ICL design ($x \in [0.30, 0.40]$) results in a similar picture comparable to Fig. 4.3, when altering the h-QW thickness. Conducted simulations are shown in

Die approbierte gedruckte Originalversion dieser Dissertation ist an der TU Wien Bibliothek verfügbar.
The approved original version of this doctoral thesis is available in print at TU Wien Bibliothek.

Fig. 4.6.

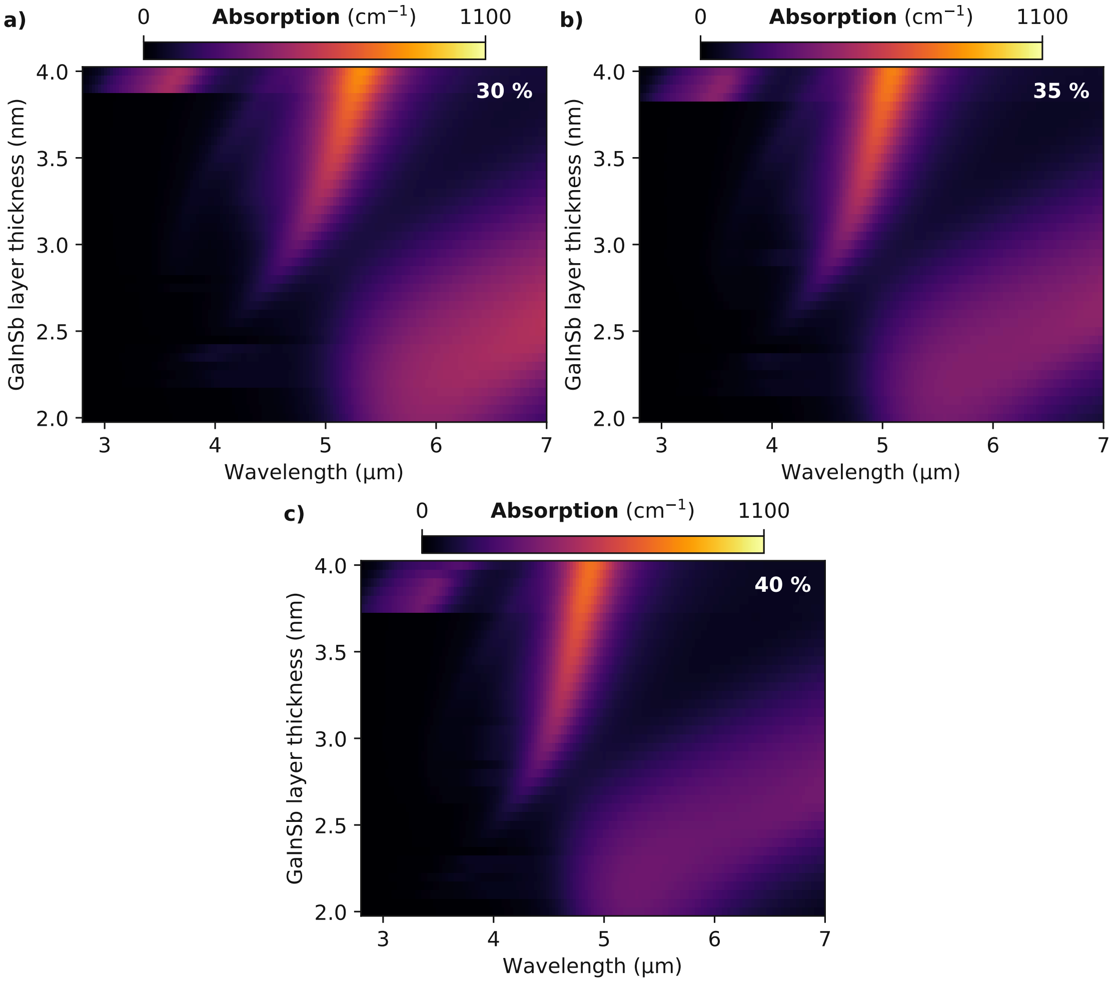

Figure 4.6: Influence of the $Ga_{1-x}In_xSb$ composition on the absorption. Results are shown for the same W-QW structure given in Fig. 4.4 for varying compositions of $x \approx$ **a**: 0.30, **b**: 0.35 and **c**: 0.40.

The most significant differences induced by the variation of the composition are summarized below:

- The quasi-bound states corresponding to the absorption feature in the upper left corner are still bound at slightly smaller h-QW thicknesses for higher indium content.
- A blueshift is induced to the dominant absorption feature around 4.6 µm, mitigating the dependence of the absorption peak wavelength on the GaInSb width.
- Going towards higher indium content, the absorption for thin h-QWs and long wavelengths (bottom right corner) is reduced, possibly making this region

Die approbierte gedruckte Originalversion dieser Dissertation ist an der TU Wien Bibliothek verfügbar.
The approved original version of this doctoral thesis is available in print at TU Wien Bibliothek.
TU WIEN Bibliothek Your knowledge hub

attractive for long wavelength ICLs.

To better investigate the blueshift of the dominant absorption peak, line plots for a $Ga_{1-x}In_xSb$ thickness of 3 nm are displayed in Fig. 4.7.

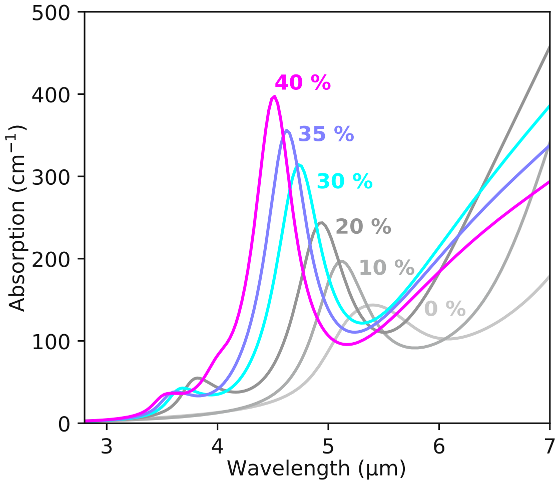

Figure 4.7: Comparison of line plots for an h-QW thickness of 3 nm from the results of the alloy variation shown in Fig. 4.6. An extended range of indium contents is depicted in gray ranging from 0 % to 20 %. A blueshift of the absorption peak with increasing indium content is evident. Data published in Supplement of [159].

The alloy variation is extended to indium contents realistically achievable with MBE between 0 - 20% in gray to give further insight into how the composition of the h-QW influences the valence intersubband absorption. In addition to the evident blueshift of the prominent peak, the absorption increases with higher indium content. Indium contents deviating from 30 - 40 % are expected to degrade device performance substantially. In general, a higher indium content reduces the height of the barrier between the two InAs electron QWs, allowing for an increased spatial overlap of the electron and hole wave function. However, high-quality layer growth becomes increasingly challenging above a composition of $x \approx 0.35$. The higher indium content results in the introduction of defects upon relaxation of the grown layers. This is due to the increasingly large lattice constant deviating further from the smaller lattice constant of the GaSb substrate, which leads to excessive compressive strain. For InAs substrates, this is even more critical because of the smaller lattice constant (6.058 Å) compared to GaSb (6.096 Å), as the lattice constant of the GaInSb layer is larger for higher indium compositions, going towards the lattice constant of InSb (6.479 Å). In literature, ICLs based both on GaSb and InAs substrates predominantly report an indium content of the GaInSb layer close to 35 % [60, 96, 102].

Die approbierte gedruckte Originalversion dieser Dissertation ist an der TU Wien Bibliothek verfügbar.
The approved original version of this doctoral thesis is available in print at TU Wien Bibliothek.
TU WIEN Bibliothek Your knowledge hub

Material parameters

The growth of antimonide based materials used in ICLs is less mature in comparison to exhaustively investigated material systems such as GaAs/AlGaAs used for QCLs. Hence, some uncertainties with respect to the knowledge of the precise band parameters of antimonide materials prevail. The effect of the material parameters was thoroughly investigated, and for all presented simulations the recommended values from Ref. [25] were implemented unchanged. In order to allow for a modification of the heavy m_{HH} and light hole mass m_{LH}, the Luttinger parameters γ_1 and γ_2 (see section 2.2.2), which are used in the simulation, are calculated from the chosen masses according to

$$\gamma_1 = \frac{m}{2}\left(\frac{1}{m_{LH}} + \frac{1}{m_{HH}}\right) \tag{4.2}$$

$$\gamma_2 = \frac{m}{4}\left(\frac{1}{m_{LH}} - \frac{1}{m_{HH}}\right), \tag{4.3}$$

derived from Eq. 2.20. In Fig. 4.8 the in-plane dispersion of the relevant valence subbands is shown for a variation of the heavy and light hole mass by ± 20 %. The behavior seems increasingly unphysical for larger values of the light hole mass (bottom right), where an upwards bending of the valence subbands is observed at higher k-values. This is a known issue, particularly for InAs and InSb, due to the material parameters having to fulfill specific constraints [169, 170]. Hence, results for an increased light hole mass are excluded from Fig. 4.9, depicting the impact of a discrepancy of the heavy and light hole mass of $\mathrm{Ga}_{1-x}\mathrm{In}_x\mathrm{Sb}$ with a fixed composition of $x \approx 0.35$ on the valence intersubband absorption in a W-QW containing a 3 nm thick h-QW. Although a deviation of the parameters by 20 % is highly unlikely, exploring the influence of these changes gives insight into the investigated phenomenon. Going from reduced to increased heavy hole mass (pink to blue in Fig. 4.9a) results in a redshift of the absorption peak at 4.6 µm, an increase in absorption at that wavelength range, and a reduction at longer wavelengths. Fig. 4.9b displays an almost negligible redshift and reduction of the absorption peak, as well as reduced absorption at longer wavelengths when scaling down the light hole mass. In conclusion, an error in the used material parameters might result in a slight over- or underestimation of the absorption between 4 and 5 µm or above 5 µm. However, the established design guideline should qualitatively be unaffected.

Die approbierte gedruckte Originalversion dieser Dissertation ist an der TU Wien Bibliothek verfügbar.
The approved original version of this doctoral thesis is available in print at TU Wien Bibliothek.

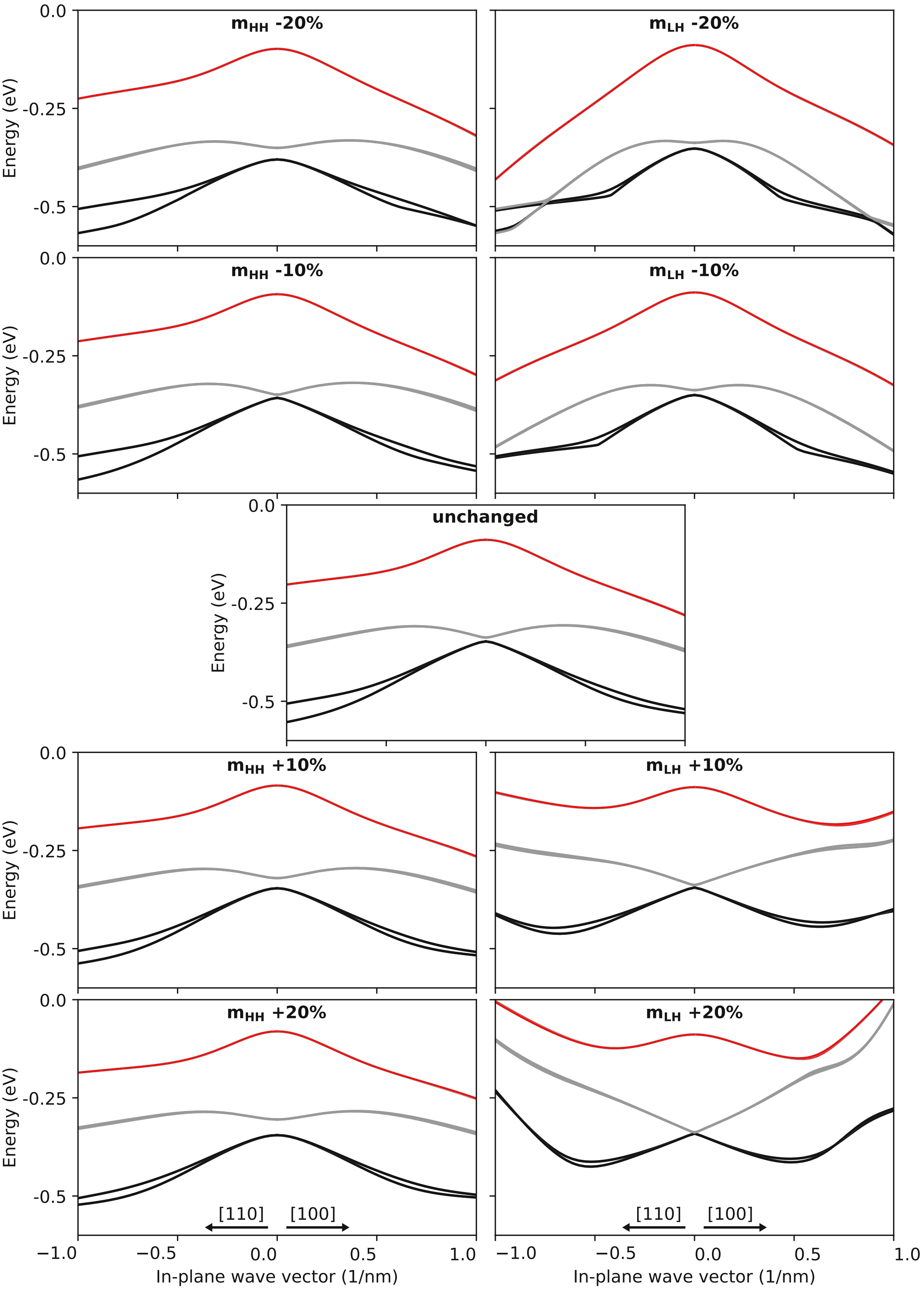

Figure 4.8: In-plane dispersion of the valence subbands depending on a change in **left column**: heavy hole m_{HH} or **right column**: light hole mass m_{LH} of a W-QW employing a 3 nm thick $\mathrm{Ga_{0.65}In_{0.35}Sb}$ layer.

Die approbierte gedruckte Originalversion dieser Dissertation ist an der TU Wien Bibliothek verfügbar.
The approved original version of this doctoral thesis is available in print at TU Wien Bibliothek.

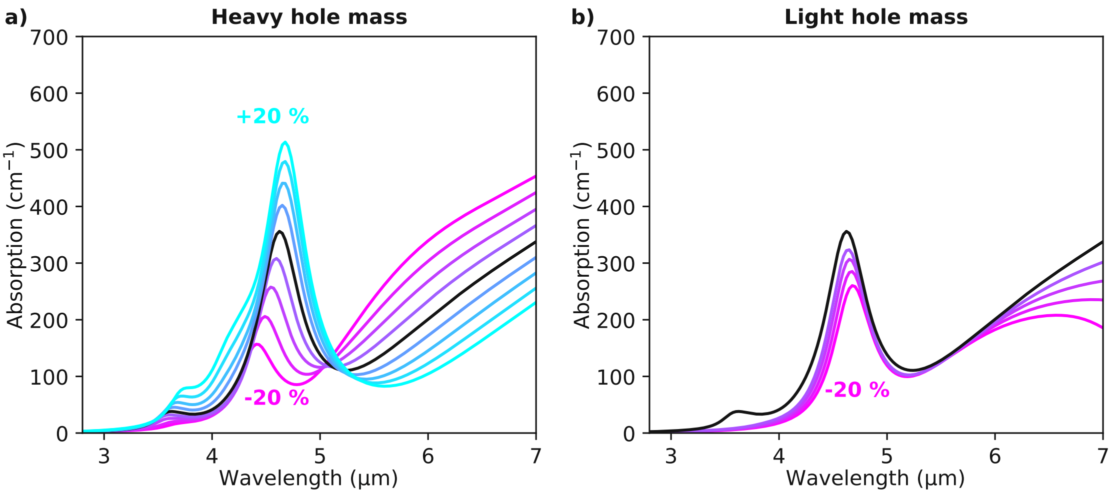

Figure 4.9: Simulated valence intersubband absorption for a variation of the **a**: heavy and **b**: light hole mass of $Ga_{0.65}In_{0.35}Sb$ for a 3 nm thick h-QW. Larger heavy hole mass induces a redshift and increases the dominant absorption peak, while at longer wavelengths the absorption is reduced. A smaller light hole mass leads to an almost insignificant redshift and reduction of the absorption around 4.6 µm. Data published in [159].

InAs substrate

All previous simulations shown were conducted assuming GaSb as substrate material. However, the influence of valence intersubband absorption on device performance should be present independent of the used substrate material. To confirm the relevance of the findings for ICL design and to demonstrate the general applicability, additional simulations for InAs-based ICLs were conducted. Due to the smaller lattice constant of InAs in comparison to GaSb, an epitaxial layer of $Ga_{0.65}In_{0.35}Sb$ commonly results in higher strain. As depicted in Fig. 4.10a for a 3 nm thick h-QW, a change of substrate from GaSb (solid pink) to InAs (blue) leads to a blueshift and increase of the absorption peak for the same alloy composition. Hence, the behavior resembles the case of additionally introduced strain on GaSb by changing the $Ga_{1-x}In_xSb$ alloy composition towards larger x values. A comparison of the lattice constants yielded a composition of $x \approx 0.45$ on GaSb (dashed pink) to most closely resemble a $Ga_{0.65}In_{0.35}Sb$ h-QW on InAs. However, this alloy composition is incompatible with the goal of high-quality layer growth on GaSb. Repeating the simulations of valence intersubband absorption in dependence on $Ga_{0.65}In_{0.35}Sb$ layer thickness, this time employing an InAs substrate, yields Fig. 4.10b. The comparably small redshift of the strongest absorption with increasing h-QW thickness, and the low absorption in the bottom right corner both resemble the case of high indium content on GaSb substrate (Fig. 4.6c). Hence, the same design principles should be

Die approbierte gedruckte Originalversion dieser Dissertation ist an der TU Wien Bibliothek verfügbar.
The approved original version of this doctoral thesis is available in print at TU Wien Bibliothek.

Die approbierte gedruckte Originalversion dieser Dissertation ist an der TU Wien Bibliothek verfügbar.
The approved original version of this doctoral thesis is available in print at TU Wien Bibliothek.

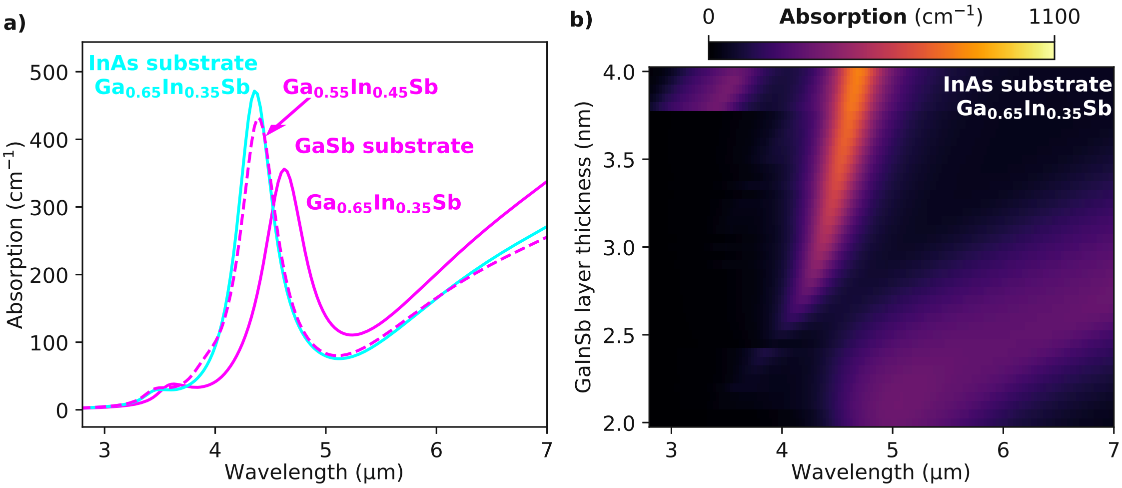

Figure 4.10: Results of valence intersubband absorption simulations assuming InAs as substrate material. **a**: Changing the substrate from GaSb (solid pink) to InAs (blue) results in a blueshift and rise of the absorption peak for an identical composition of $x \approx 0.35$ of the $\mathrm{Ga}_{1-x}\mathrm{In}_x\mathrm{Sb}$ layer. The result on InAs is comparable to a higher indium content of 45 % on GaSb (dashed pink). **b**: Valence intersubband absorption dependent on the thickness of the $\mathrm{Ga}_{0.65}\mathrm{In}_{0.35}\mathrm{Sb}$ layer for the assumption of an InAs substrate. Data published in [159].

applicable for GaSb- and InAs-based ICLs.

Electric field

Apart from the temperature dependence of the valence intersubband absorption, the impact of the electric field is investigated. In Fig. 4.11 the applied electric field is varied between 90 and 180 kV/cm in steps of 30 kV/cm. While $E = 90$ kV/cm represents the typical operating conditions of the presented structures, the idea was to investigate whether an increase in the absorption was potentially occurring at higher electric field and, hence, at higher operating voltages. An occurring efficiency droop (see section 3.1.3), meaning a reduction of the external efficiency with rising operating current, could be caused by increasing internal losses [128]. The results shown in Fig. 4.11, however, show the reverse trend: the absorption peak at 4.6 µm is reduced with higher electric field. Thus, a contributing effect to the efficiency droop seems to be unlikely.

4.2.2 Experimental investigation at 4.35 µm

Previous subsections pinpointed the valence intersubband absorption as causative underlying mechanism behind the performance degradation of ICLs in the 4-5 µm region. This subsection aims at confirming the benefit of using a modified W-QW

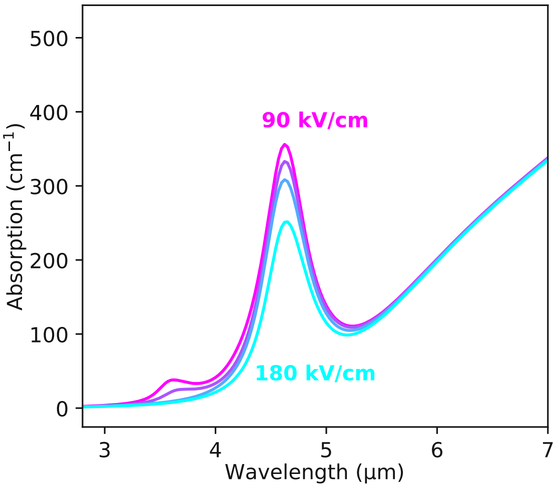

Figure 4.11: Influence of the applied electric field on the valence intersubband absorption in a W-QW with a standard 3 nm $Ga_{0.65}In_{0.35}Sb$ layer. Increasing the electric field reduces the absorption around 4.6 µm.

thickness to avoid this absorption experimentally. With the goal to achieve superior performance at 4.35 µm close to the strongest CO_2 absorption feature, three W-QW designs were explored:

(A) 2.19 nm InAs / **2.50 nm $Ga_{0.60}In_{0.40}Sb$** / 1.79 nm InAs

(B) 2.23 nm InAs / **3.00 nm $Ga_{0.60}In_{0.40}Sb$** / 1.83 nm InAs

(C) 2.26 nm InAs / **3.50 nm $Ga_{0.60}In_{0.40}Sb$** / 1.87 nm InAs

From the simulations, the best performance is anticipated for the thinnest h-QW (A). The thicker wells of 3.0 (B) and 3.5 nm (C) are considered as reference structures. A $Ga_{1-x}In_xSb$ alloy composition of $x \approx 0.40$ was chosen for the realization of all structures to increase the dipole moment between the lasing subbands (see section 4.2.1 for discussion). The neighboring AlSb barriers were grown with thicknesses of 2.5 and 1.0 nm, whereas 2.0 nm were chosen symmetrically in the simulations for simplicity. In the conducted simulations the AlSb barrier thickness showed no evidence of significantly influencing the valence intersubband absorption. The calculated electronic band structure at the Γ-point and the valence subband energies depending on the in-plane wave vector k are depicted in Fig. 4.12. Several changes in the valence subband structure are observable when going from thin (2.5 nm) to thick (3.5 nm) $Ga_{0.60}In_{0.40}Sb$ QW. The two lower valence subbands (black and gray) switch positions, as the well width changes. The energy difference between the energetically lowest heavy hole-like and the light hole-like subband stays approximately the same at the Γ-point when varying the thickness, while the energy of the second

Die approbierte gedruckte Originalversion dieser Dissertation ist an der TU Wien Bibliothek verfügbar.
The approved original version of this doctoral thesis is available in print at TU Wien Bibliothek.
TU Bibliothek WIEN Your knowledge hub

Die approbierte gedruckte Originalversion dieser Dissertation ist an der TU Wien Bibliothek verfügbar.
The approved original version of this doctoral thesis is available in print at TU Wien Bibliothek.
TU Bibliothek WIEN Your knowledge hub

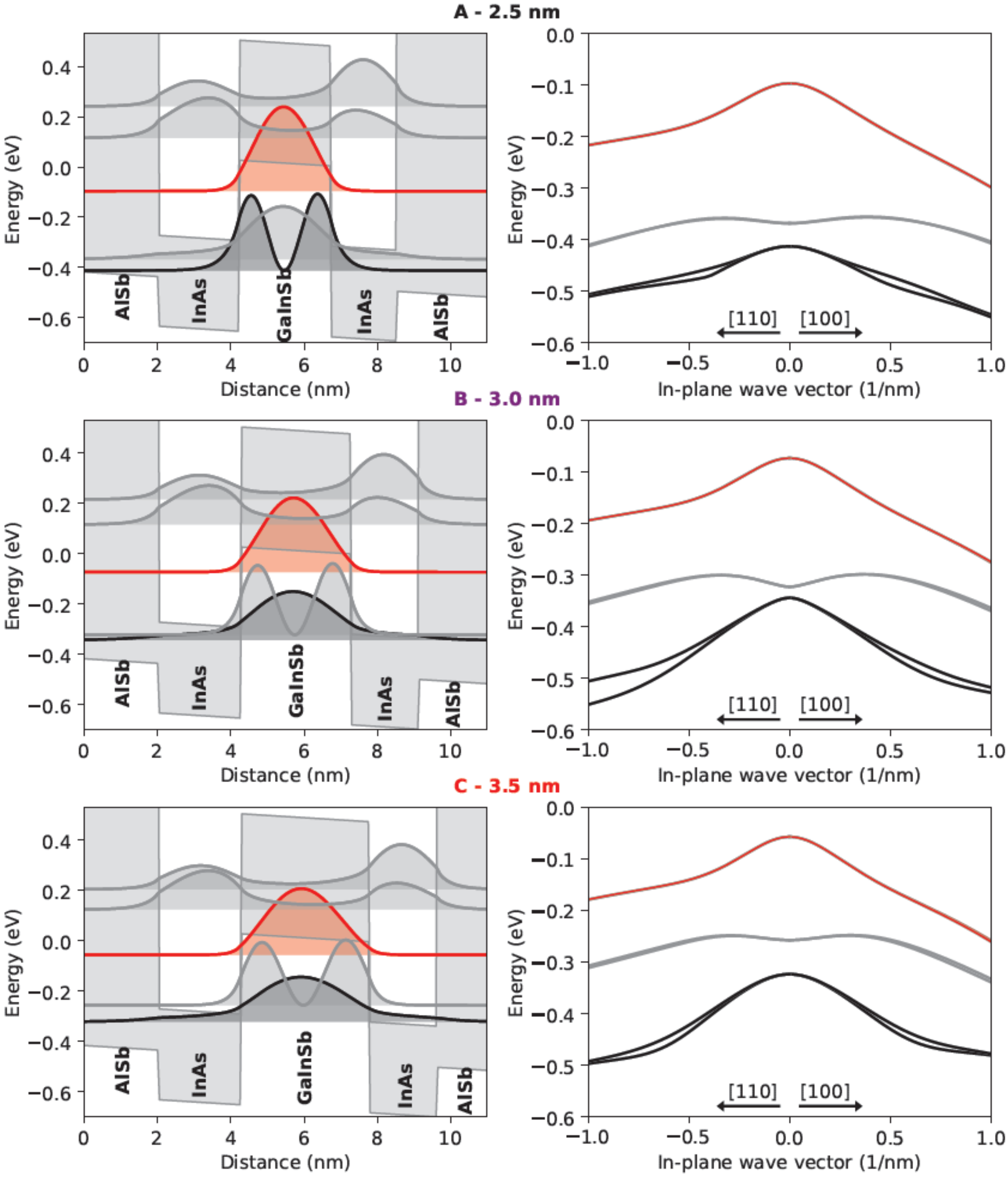

Figure 4.12: left column: Electronic band structure at the Γ-point of three different W-QWs employing different thicknesses of the h-QW. The black and gray valence subbands change positions going from 2.5 nm (A) to 3.5 nm (C). **right column**: Valence subbands depending on k. Data published in [159].

heavy hole-like subband is influenced much stronger upon thickness variation (see two white lines in Fig. 4.5). Moreover, when the gray and black subbands are in vicinity to each other energetically, the subbands influence each other. Hence, the dip seen for $k = 0$ in the dispersion of the gray subband (right column) is largest for design B. Once more, attention should be paid to the intricate nature of the valence band and its selection rules, making the evaluation of the momentum matrix elements for the two-dimensional k-space and the exact calculation of the intersubband absorption a necessity.

All simulation results shown before are considering light propagation exclusively within the simulated W-QW. However, only a fraction of the light propagating within the cavity will overlap with the active region in an ICL. Hence, to estimate the actual losses induced by the W-QW, the entire grown layer stack needs to be considered. The building blocks, which allow waveguiding in a typical ICL, were introduced in section 3.1.2. All three realized structures (A, B and C) were grown by MBE on n-GaSb (100) substrates, employing 6 active stages with a doping of $n = 6 \times 10^{18}$ cm^{-3} for carrier rebalancing. The active region was then encompassed by two 400 nm thick GaSb SCLs. The upper and lower superlattice cladding were grown with thicknesses of 2000 nm and 3300 nm, respectively, and suitable transition layers were inserted between both sides of the active region and the SCLs, as well as between the SCLs and the claddings. The vertical mode profile and the refractive index of the layer stack are displayed in Fig. 4.13 for design A. Moreover, only a part of the light overlapping with the active region, quantified by the confinement factor Γ_{AR}, is overlapping with the active W-QW considered in the simulations. Hence, the fraction of the entire active region composed of the simulated structure $d_{\mathrm{WQW}}/d_{\mathrm{AR}}$ needs to be evaluated, yielding the confinement factor within the W-QW

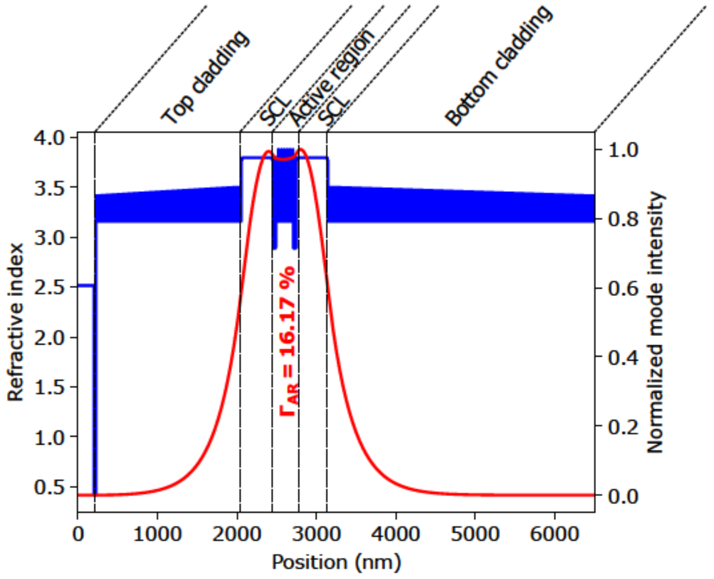

Figure 4.13: Refractive index profile (blue) of the ICL waveguide for structure A. The claddings employ a graded doping density from $n = 1 \times 10^{18}$ cm^{-3} to $n = 1 \times 10^{17}$ cm^{-3} going towards the SCLs. The normalized mode intensity is shown in red, yielding a confinement factor of $\Gamma_{\mathrm{AR}} = 16.17\,\%$ in the active region.

TU Bibliothek WIEN Your knowledge hub
Die approbierte gedruckte Originalversion dieser Dissertation ist an der TU Wien Bibliothek verfügbar.
The approved original version of this doctoral thesis is available in print at TU Wien Bibliothek.

$\Gamma_{\mathrm{WQW}} = \Gamma_{\mathrm{AR}}\, d_{\mathrm{WQW}}/d_{\mathrm{AR}}$. Table 4.1 summarizes the determined values for all three designed structures. The confinement factor of the lasing mode within the W-QW for structure A amounts to approximately 4.6 %. The simulated absorption taking the modal overlap into account, $\alpha = \alpha_{\mathrm{WQW}}\,\Gamma_{\mathrm{WQW}}$, is shown in Fig. 4.14a for all three designs. The most dominant absorption peak is observed for the widest h-QW (C).

	A	B	C
Γ_{AR} (%)	16.17	16.44	16.76
$d_{\mathrm{WQW}}/d_{\mathrm{AR}}$	0.286	0.298	0.306
Γ_{WQW} (%)	4.62	4.89	5.13

Table 4.1: Calculated confinement factor of the mode within the active region Γ_{AR}, the fraction of the active region consisting of the simulated W-QW (Γ_{WQW}) and the confinement factor within the W-QW for all three realized structures (A, B and C).

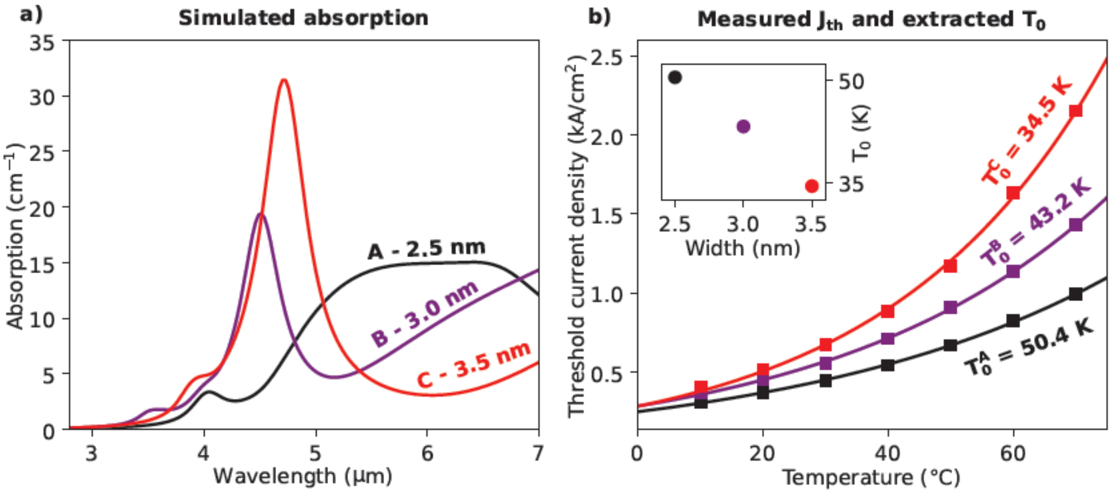

Figure 4.14: **a**: Valence intersubband absorption in the W-QW simulated for three experimentally realized structures with varying $Ga_{0.60}In_{0.40}Sb$ widths. **b**: Characteristic temperature T_0 experimentally determined from low duty-cycle measurements of shallowly etched broad area devices. The T_0 values were extracted from the exponential fit to the measured J_{th} data (squares) according to Eq. 4.1. Data published in [159].

The value of the absorption loss in the ICL, however, depends on the exact lasing wavelength.

The first experiments were designed to determine whether the characteristic temperature was indeed influenced by changing the h-QW width. Thus, particular emphasis was put on maintaining identical growth and fabrication conditions during device processing. To achieve good experimental comparability, the broad area devices for determination of the characteristic temperature in pulsed mode were

Die approbierte gedruckte Originalversion dieser Dissertation ist an der TU Wien Bibliothek verfügbar.
The approved original version of this doctoral thesis is available in print at TU Wien Bibliothek.
TU Bibliothek Your knowledge hub

Die approbierte gedruckte Originalversion dieser Dissertation ist an der TU Wien Bibliothek verfügbar.
The approved original version of this doctoral thesis is available in print at TU Wien Bibliothek.
TU Bibliothek WIEN Your knowledge hub

fabricated analogously, with etch depths between 1.5 - 1.7 µm into the 2 µm upper superlattice cladding. The experimentally determined lasing wavelengths of the devices were 4.38 µm for design A, 4.36 µm for B and 4.35 µm for C. Measured threshold current densities for temperatures between 10 - 70 °C and extracted T_0 values are presented in Fig. 4.14b. The thickness reduction of the h-QW from 3.5 to 2.5 nm resulted in reduced temperature sensitivity, quantified by a significantly increased T_0 of 50.4 K (A) from 34.5 K (C). Furthermore, the absolute value of J_{th} at 20 °C was lowered from 516 to 370 A/cm^2. Thus, performance similar to the 3 - 4 µm sweet spot region was achieved.

Following these promising results, the performance dependence at 4.35 µm on the $\mathrm{Ga}_{1-x}\mathrm{In}_x\mathrm{Sb}$ width was further investigated. For that purpose, 100 µm broad ridges were fabricated from all three grown structures with varying lengths (1.0, 1.2, 1.4, 1.8, and 2.2 mm), this time etched through the active region to reduce current spreading. The facets were left uncoated. Measurements of the LIV characteristics were performed in pulsed operation at low duty-cycle (1 kHz repetition frequency, 500 ns pulse length) at 20 °C using an integrating sphere and a MCT detector for light collection. The LIV data is shown for at least two devices of each length in the left column of Fig. 4.15. Performance metrics, i.e., J_{th}, the peak output power at $J = 2$ kA/cm^2, and the slope efficiency η close to lasing threshold are depicted for each device in the right column of Fig. 4.15. A clear performance enhancement can be seen for all resonator lengths due to the reduction of the h-QW width. For a length of $L = 1.8$ mm reducing the width from 3.5 nm to 2.5 nm culminated in decreased J_{th} by 34 % from 372 (C) to 247 A/cm^2 (A), increased output power by 63 % from 268 (C) to 436 mW (A), and increased slope efficiency by 63 % from 108 (C) to 176 mW/A (A), indicated by the blue arrows.

What is important to acknowledge at this point, is that although a correlation between the h-QW width and the device performance is unequivocally observed, the explanation presented and supported by the simulations is still challenged by another explanation. The cause for the enhanced performance could be either a mitigation of the valence intersubband absorption or a reduction of the Auger effect resulting in an increased internal efficiency. Nevertheless, varying the width of the h-QW represents a control knob, which clearly influences the device performance. In the following, arguments indicating that the valence intersubband absorption plays a larger role than the Auger effect for the device performance at 4.35 µm, are presented, although an influence of the latter, when changing the W-QW design, cannot be completely excluded.

From the LIV data presented on the left side of Fig. 4.15, the best performing

Die approbierte gedruckte Originalversion dieser Dissertation ist an der TU Wien Bibliothek verfügbar.
The approved original version of this doctoral thesis is available in print at TU Wien Bibliothek.
TU Bibliothek Your knowledge hub WIEN

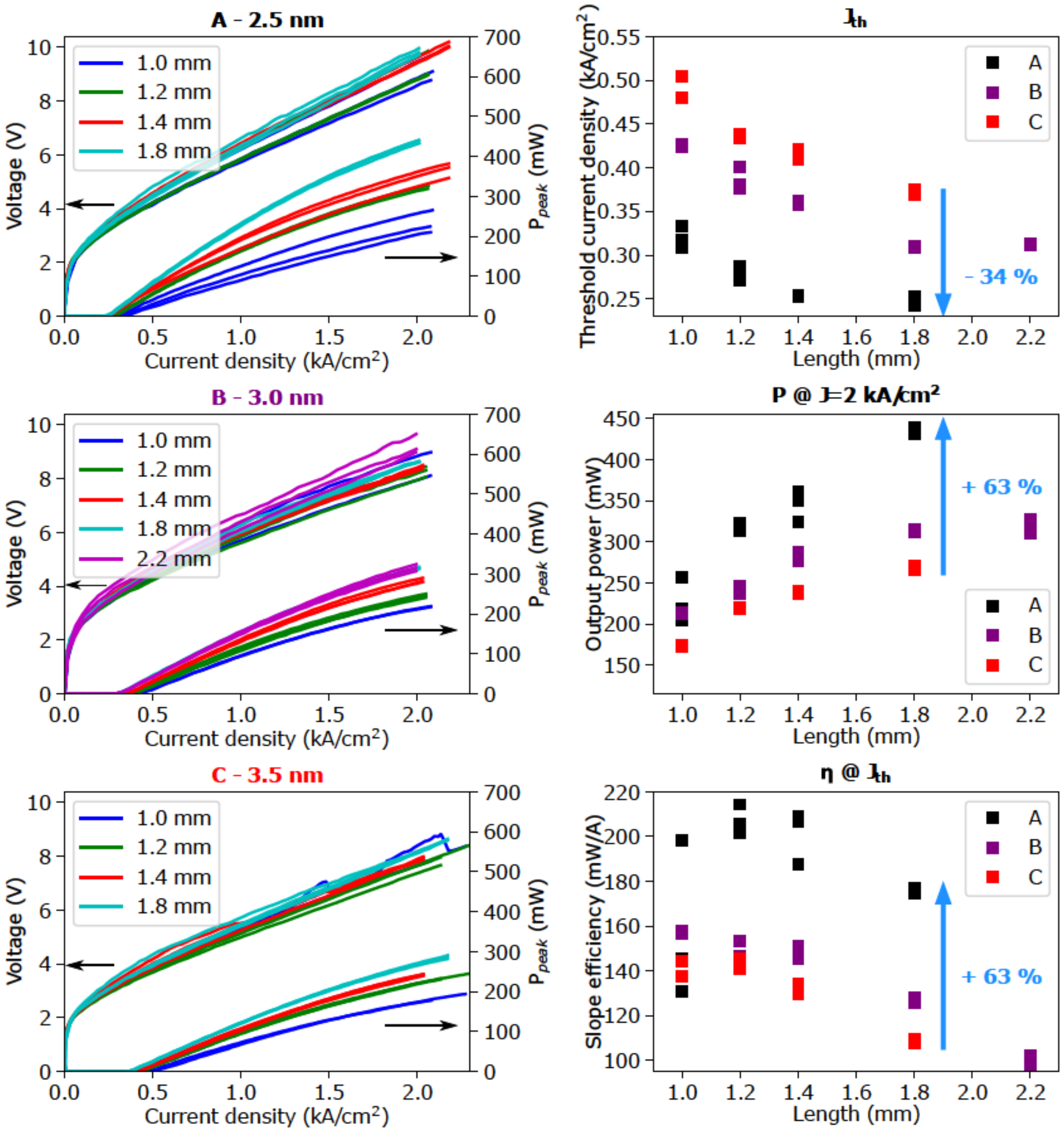

Figure 4.15: left column: Measured LIV data from ICL structures A, B and C in pulsed operation at 20 °C. **right column**: Comparison of deduced performance indicators for all devices: J_{th}, output power P at $J = 2\,\mathrm{kA/cm}^2$ and slope efficiency η close to J_{th}. The improvement for a device length of 1.8 mm is additionally quantified in blue. Data published in [159].

device with respect to the maximum output power at $J = 2$ kA/cm^2 is selected for each length in an attempt to alleviate device-to-device fluctuations, e.g., due to defects introduced during growth or fabrication. Subsequently, the EDQE per stage is calculated using Eq. 3.11 in dependence on the current density and shown in Fig. 4.16 (fine lines in left column). The data appears to be rather noisy, because output power and current, determining the EDQE via the derivative dP/dI, are

Die approbierte gedruckte Originalversion dieser Dissertation ist an der TU Wien Bibliothek verfügbar.
The approved original version of this doctoral thesis is available in print at TU Wien Bibliothek.

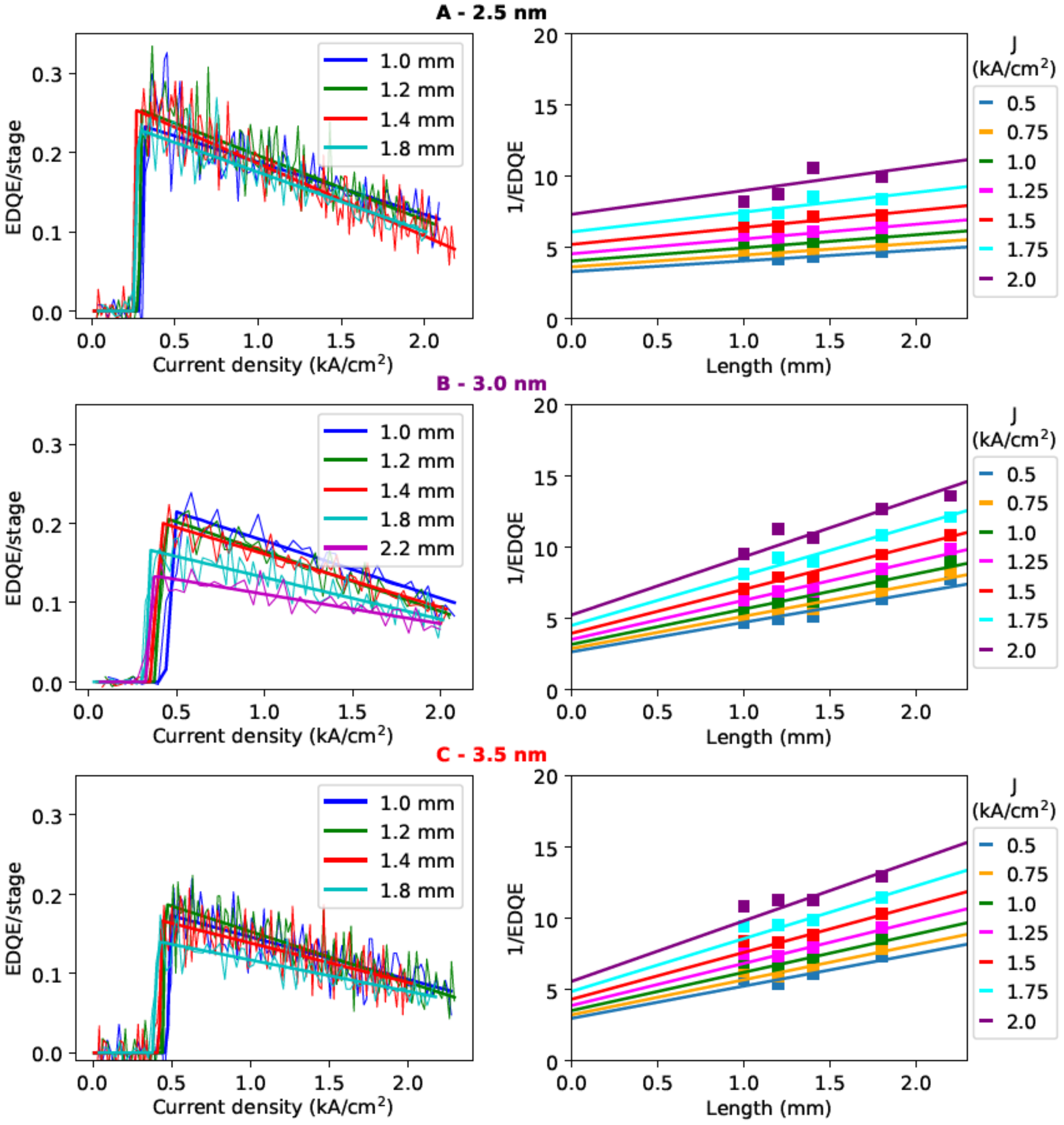

Figure 4.16: left column: Deduced EDQE per stage for the best device at each length showing an efficiency droop with increasing current. The fine lines represent the EDQE directly deduced from the measured data, while the thicker lines, showing a negative linear slope were obtained from a second order polynomial fit to the light-current characteristic. **right column**: Fit (lines) to experimental data (squares) of the inverse EDQE for varying J according to Eqs. 4.4, 4.5 and 4.6. Data published in [159].

both measured variables. Using a second order polynomial fit to the light-current characteristic yields excellent agreement with the data. Hence, all devices exhibit a notable efficiency droop with increasing J (see section 3.1.3), which is connected to a decreasing internal efficiency or increasing losses with rising J [128]. The derivative of the second order polynomial fit, yielding a linear slope, is shown in Fig. 4.16

(lines on left side) and used for subsequent analysis. Design A shows the highest EDQE, which does not come as a surprise as it is directly connected to the already investigated output power. The internal efficiency η_i and the waveguide losses α_w can directly be assessed from the dependence of the inverse EDQE per stage on device length L, as described by

$$\frac{1}{EDQE} = \frac{1}{\eta_\mathrm{i}}\left(1 + \frac{\alpha_\mathrm{w} L}{\ln \frac{1}{R}}\right). \tag{4.4}$$

This relation assumes equal facet reflectivity R for both sides of the cavity. In the following a reflectivity of $R = 0.31$ will be employed, in accordance with Ref. [128], yielding an upper limit for the losses. On the right side of Fig. 4.16, EDQE^{-1} is depicted depending on L for varying J within a range of 0.5 - 2.0 kA/cm^2. According to Eq. 4.4 the internal efficiency η_i can be extracted from the intercept of the fit and the y-axis at $L = 0$, whereas the waveguide losses α_w can be assessed from the slope. To account for the observed efficiency droop, a linear dependence of the losses and the internal efficiency on the current density was defined as fitting parameters,

$$\eta_\mathrm{i} = \eta_\mathrm{i}^{(0)} - \eta_\mathrm{i}^{(1)}\, J \tag{4.5}$$

$$\alpha_\mathrm{w} = \alpha_\mathrm{w}^{(0)} + \alpha_\mathrm{w}^{(1)}\, J. \tag{4.6}$$

Parameters $\eta_\mathrm{i}^{(1)}$ and $\alpha_\mathrm{w}^{(1)}$ were restricted to positive values and the fit was performed to the data presented for each design (A, B and C) independently. The experimentally determined values (squares) on the right side of Fig. 4.16 for the shortest devices with $L = 1$ mm, particularly for design C, do not align nicely with the results from longer devices. This is a known issue, arising from higher mirror losses at short cavity lengths. All devices with $L = 1$ mm were thus excluded from the fit. In Fig. 4.17a the best achieved fit is compared for the three designs for one particular current density $J = 1$ kA/cm^2. The significantly smaller slope for design A (black) directly translates to lower waveguide losses. For all designs, the fit yielded a decreasing internal efficiency, while the losses were unchanged with current density, implying that for the investigated structures the efficiency droop is connected to an increasing internal efficiency and not to rising waveguide losses with J. The results are depicted in Fig. 4.17b and c for η_i and α_w, respectively. Design A and C show slightly diminished internal efficiencies in comparison to the standard 3 nm design of B, potentially implying that additional design modifications, such as an adjustment of the energy levels in the hole injector, might be beneficial when manipulating the h-QW design. The extracted fitting parameters for α_w

Die approbierte gedruckte Originalversion dieser Dissertation ist an der TU Wien Bibliothek verfügbar.
The approved original version of this doctoral thesis is available in print at TU Wien Bibliothek.
TU WIEN Bibliothek Your knowledge hub

Die approbierte gedruckte Originalversion dieser Dissertation ist an der TU Wien Bibliothek verfügbar.
The approved original version of this doctoral thesis is available in print at TU Wien Bibliothek.

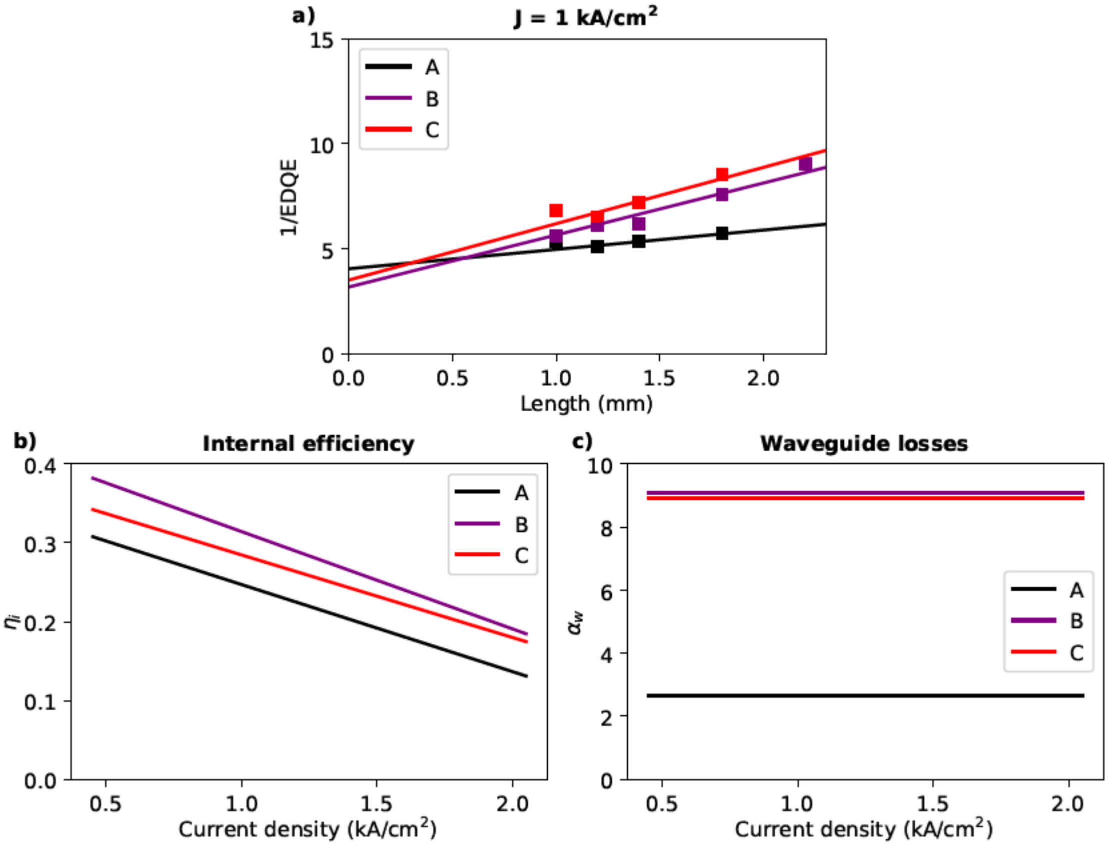

Figure 4.17: **a**: Data and fit of EDQE^{-1} over L for all three designs, indicating lower waveguide losses for the optimized design A, connected to the flatter slope. **b**: Internal efficiency η_i extracted from the fit to EDQE^{-1} over L according to Eq. 4.4 with η_i depending on J as stated in Eq. 4.5. The observed decrease in external efficiency seems to be due to this decrease of the internal efficiency with increasing J. **c**: The extracted waveguide losses α_w for all devices are constant over J. The optimized design A resulted in waveguide losses amounting to only a third of the other investigated designs. Data published in [159].

yield significantly reduced waveguide losses for the optimized design A (2.7 cm^{-1}) compared to B (9.1 cm^{-1}) and C (8.9 cm^{-1}). They amount to less than a third of the value. In general, the waveguide losses are composed of losses not exclusively induced within the active region, but include, i.e., absorption losses in the cladding α_Clad, the SCLs α_SCL or scattering losses caused by side-wall roughness. The total internal loss α_i, which does not include, e.g., the geometry of the laser resonator or fabrication imperfections, is defined as [58]

$$\alpha_\mathrm{i} = \alpha_\mathrm{Clad}\Gamma_{Clad} + \alpha_\mathrm{SCL}\Gamma_{SCL} + \alpha_\mathrm{AR}\Gamma_{AR}, \tag{4.7}$$

where Γ_Clad and Γ_SCL denote the confinement factor in the claddings and the SCLs, respectively. In the presented experimental proof, the same waveguide structure and

Die approbierte gedruckte Originalversion dieser Dissertation ist an der TU Wien Bibliothek verfügbar.
The approved original version of this doctoral thesis is available in print at TU Wien Bibliothek.

fabrication scheme (broad area devices) was employed for all active W-QW designs. As Γ_{AR} is approximately the same for all three designs (see Table 4.1), the only parameter in Eq. 4.7 affected by the design change is α_{AR}. These active region losses can further be divided into losses induced in the different functional parts of the active region, i.e., the electron injector $\alpha_{\mathrm{e-inj}}$, the hole injector $\alpha_{\mathrm{h-inj}}$ and the W-QW α_{WQW},

$$\alpha_{\mathrm{AR}}\Gamma_{\mathrm{AR}} = \alpha_{\mathrm{e-inj}}\Gamma_{\mathrm{e-inj}} + \alpha_{\mathrm{h-inj}}\Gamma_{\mathrm{h-inj}} + \alpha_{\mathrm{WQW}}\Gamma_{\mathrm{WQW}}, \tag{4.8}$$

with the corresponding confinement factors $\Gamma_{\mathrm{e-inj}}$ and $\Gamma_{\mathrm{h-inj}}$ for the electron and hole injector. However, the only adaptation introduced is the different h-QW width affecting the losses in the W-QW α_{WQW}, while leaving the confinement factor Γ_{WQW} almost unaffected (see Table 4.1). Thus, this presents strong proof that the difference in the total waveguide losses α_{w} can be traced back to this change. A summary of the presented experimental results is given in Fig. 4.18. Reducing the non-radiative Auger recombination, would result in an increased internal efficiency. Experimentally, this is not observed for the optimized design A. The internal efficiency even seems to be slightly reduced compared to the reference designs. Instead, the waveguide losses appear to be significantly lower, which is traced back to reduced valence intersubband absorption. Thus, this absorption seems to play a vital role outside the sweet spot 3-4 µm region, potentially even acting as an explanation for the position of the wavelength region of the sweet spot itself.

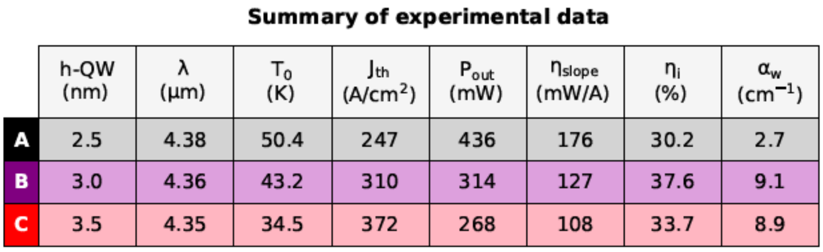

Summary of experimental data

	h-QW (nm)	λ (µm)	T_0 (K)	J_{th} (A/cm^2)	P_{out} (mW)	η_{slope} (mW/A)	η_i (%)	α_w (cm^{-1})
A	2.5	4.38	50.4	247	436	176	30.2	2.7
B	3.0	4.36	43.2	310	314	127	37.6	9.1
C	3.5	4.35	34.5	372	268	108	33.7	8.9

Figure 4.18: Experimental data summarized: thickness of the h-QW, measured lasing wavelength λ, extracted T_0 (from shallowly etched devices), J_{th}, peak output power P_{out} at $J = 2$ kA/cm^2 and slope efficiency η_{slope} close to threshold for a device length of $L = 1.8$ mm, extracted internal efficiency η_{i} for $J = 0.5$ kA/cm^2 and waveguide losses α_{w}. All performance metrics testify the superiority of design A. Data published in [159].

Although experimentally the relevance of adapting the h-QW design to mitigate losses from valence intersubband absorption was demonstrated for a specific waveguide structure with the active region comprising a particular number of stages at a wavelength of 4.35 µm, the simulation results are not limited to this case. The general applicability was shown for substrates composed of both InAs and GaSb and subsequently, results of designs targeting wavelengths around 6.1 µm will be presented.

4.2.3 Experimental investigation beyond 6 µm

At longer wavelengths, QCLs [64] are still often the preferred choice for a coherent laser source. Extending the cw operation range at room temperature above 6 µm has proven difficult for ICLs. As discussed in the preceding section, a performance degradation towards longer wavelengths is directly related to an increase in the intersubband absorption in the valence band, as the predominantly used design was so far employing a $Ga_{1-x}In_xSb$ layer thickness of 3 nm.

An extended wavelength range for the calculated valence intersubband absorption in a W-QW composed of 2.00 nm AlSb/2.70 nm InAs/2.00 - 4.00 nm $Ga_{0.60}In_{0.40}Sb$/ 2.25 nm InAs/2.00 nm AlSb is presented in Fig. 4.19. Depending on the desired emission wavelength, modifying the thickness of the h-QW towards wider or thinner wells should benefit the device performance. In contrast to the behavior observed at 4.35 µm in section 4.2.2, higher absorption for thinner $Ga_{1-x}In_xSb$ wells seems to

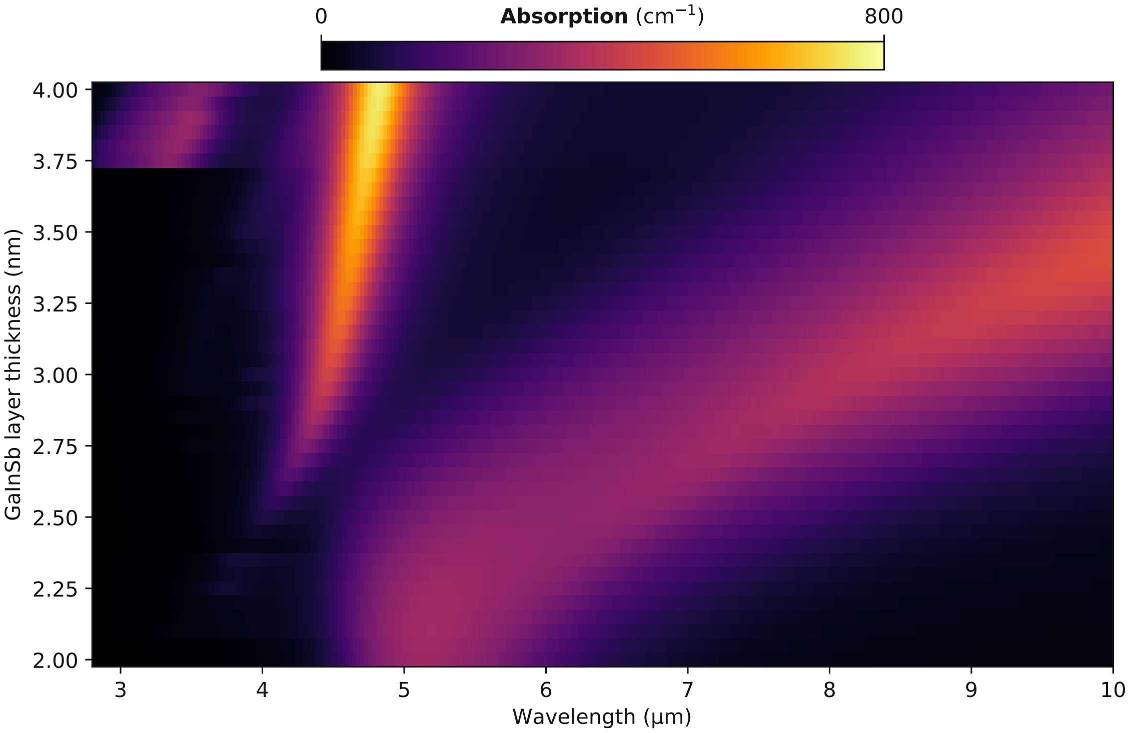

Figure 4.19: Simulated valence intersubband absorption for an extended wavelength range, illuminating the behavior above 6 µm.

Die approbierte gedruckte Originalversion dieser Dissertation ist an der TU Wien Bibliothek verfügbar.
The approved original version of this doctoral thesis is available in print at TU Wien Bibliothek.

occur at around 6 µm. While a region of insignificant absorption exists for thick hole wells at this wavelength, for even higher wavelengths (> 7 µm) this region eludes experimental realization due to the increasing strain. There, switching to the other side of the absorption feature and, hence, to thinner wells below 2.5 nm appears to be more feasible and beneficial.

Three active region designs aiming at a lasing wavelength of 6.14 µm were experimentally realized, once more varying the thickness of the h-QW between 2.5 and 3.5 nm:

(D) 2.77 nm InAs / **2.50 nm $\mathbf{Ga_{0.60}In_{0.40}Sb}$** / 2.31 nm InAs

(E) 2.71 nm InAs / **3.00 nm $\mathbf{Ga_{0.60}In_{0.40}Sb}$** / 2.26 nm InAs

(F) 2.68 nm InAs / **3.50 nm $\mathbf{Ga_{0.60}In_{0.40}Sb}$** / 2.24 nm InAs

With the goal to target the same emission wavelength, the layer thicknesses of the two InAs films were reduced going towards larger $Ga_{0.60}In_{0.40}Sb$ thickness to compensate for the redshift. Measured wavelengths at 20 °C amounted to 6.18 (D), 6.33 (E) and 6.12 µm (F). Since the target wavelength is significantly longer than 4.35 µm, a larger number of periods (see discussion in section 3.1.2) and thicker SCLs were employed, to provide sufficient mode confinement despite the longer optical mode decay length due to the longer wavelength. All structures were realized with 9 active stages and 760 nm thick SCLs. Furthermore, the doping for carrier rebalancing was lowered to $n = 3\times10^{18}$ cm^{-3}. Upper and lower superlattice cladding were chosen to be 2000 nm and 3500 nm thick.

The confinement factors of the mode within the active region Γ_{AR}, the fraction of the entire active region composed of the simulated structure $d_{\mathrm{WQW}}/d_{\mathrm{AR}}$, and the resulting confinement factor within the W-QW Γ_{WQW} for the three structures are given in Table 4.2.

	D	**E**	**F**
Γ_{AR} (%)	16.47	16.59	16.87
$d_{\mathrm{WQW}}/d_{\mathrm{AR}}$	0.290	0.297	0.306
Γ_{WQW} (%)	4.77	4.92	5.16

Table 4.2: Calculated confinement factor of the mode within the active region Γ_{AR}, the fraction of the active region consisting of the simulated W-QW (Γ_{WQW}) and the confinement factor within the W-QW for the three realized structures around 6.15 µm (D, E and F).

Results from simulations for the realized W-QW designs are depicted in Fig. 4.20a. For this wavelength, superior performance is anticipated for structure F (red) due to

Die approbierte gedruckte Originalversion dieser Dissertation ist an der TU Wien Bibliothek verfügbar.
The approved original version of this doctoral thesis is available in print at TU Wien Bibliothek.
TU Bibliothek WIEN Your knowledge hub

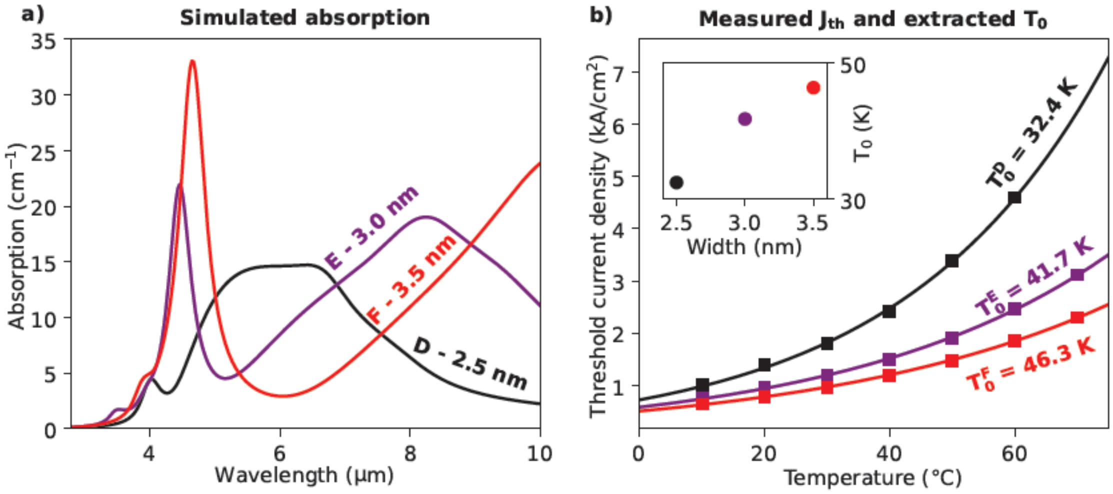

Figure 4.20: a: Simulated valence intersubband absorption for three experimentally realized structures at wavelengths around 6.1 µm. An opposite trend is visible compared to 4.35 µm (designs A-C). b: J_{th} and T_0 data of shallowly etched broad area devices.

reduced absorption. In analogy to the results for 4.35 µm, pulsed measurements were performed on shallowly etched broad area devices, which are shown together with the extracted values of the characteristic temperature in Fig. 4.20b. At a temperature of 20 °C, a significantly lower threshold current density of 790 kA/cm^2 is observed for design F, compared to 1385 kA/cm^2 for D and 960 kA/cm^2 for E. Evidently J_{th} is higher compared to the structures at 4.35 µm owing to other contributing wavelength dependent effects. Nevertheless, the improvement due to the W-QW adaptation is compelling. The sensitivity to temperature was additionally reduced, leading to a T_0 of 46.3 K. Experimentally the opposing trend with changing h-QW thickness is clearly observed at this wavelength with respect to 4.35 µm thicker vs. thinner h-QW yields superior results undeniably linking the performance improvement to the studied valence intersubband transitions.

Coming back to the aim of extending the wavelength range of cw performance of ICLs at room temperature, the best performing structure (F) with a reasonable low J_{th} and high T_0 is further investigated. Narrow ridges with a width of 7.7 µm were fabricated, and cw emission at room-temperature was indeed feasible for devices with electro-plated gold contacts for good thermal dissipation, mounted epi-side up. LIV characteristics at varying operating temperatures and the spectrum of a typical 1.2 mm-long device are depicted in Figure 4.21. The maximum output power of 3.6 mW at 20 °C is more than ten times higher compared to the ICL at the so far highest reported wavelength of 6.01 µm in cw at room temperature, which was based on an InAs substrate [95]. The presented study provides an insight into ICL

Die approbierte gedruckte Originalversion dieser Dissertation ist an der TU Wien Bibliothek verfügbar.
The approved original version of this doctoral thesis is available in print at TU Wien Bibliothek.
TU WIEN Bibliothek Your knowledge hub

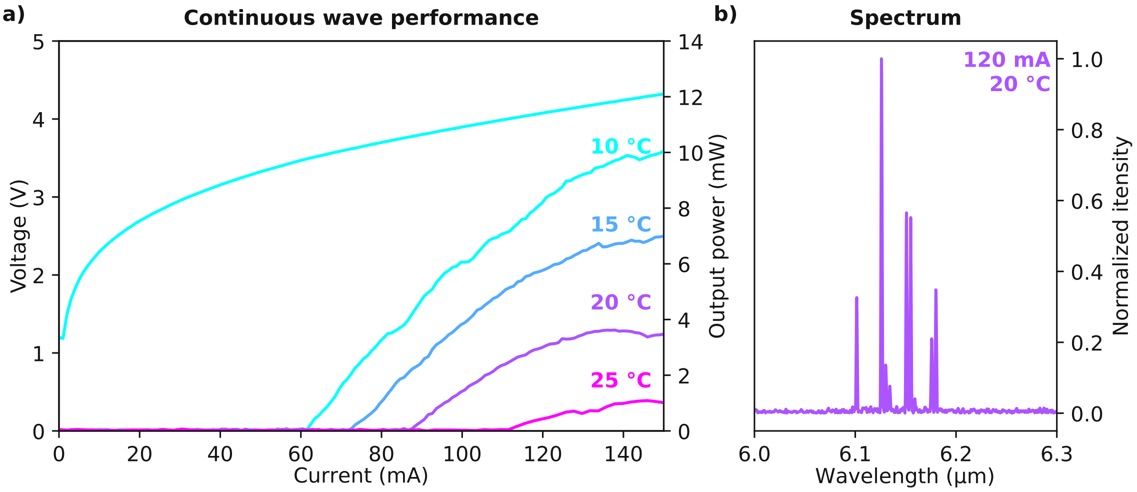

Figure 4.21: a: Performance results of epi-up mounted electro-plated narrow ridges fabricated from design F in cw emission. LIV characteristics are displayed for temperatures ranging between 10 - 25 °C. **b**: Emission spectrum at a driving current of 120 mA and T = 20 °C, displaying a wavelength of 6.12 µm for the dominant intensity peak.

active region design, offering a practical and valuable guideline to improve device performance, especially in the strive for cw room-temperature emission at longer operating wavelengths.

4.3 Prospects on absorption in the active region

When talking about valence intersubband absorption, the W-QW is not the only section of the ICLs active region where substantial absorption could occur. The hole injector constitutes another factor that should be considered in careful band structure engineering to enhance device performance, which will be discussed in the following.

4.3.1 Absorption in the hole injector

Including the hole injector (see section 3.1.1) in calculations of valence intersubband absorption was assessed to result in non-zero absorption at the lasing wavelength of a simple type-II QW (2.5 nm InAs/3.4 nm $Ga_{0.7}In_{0.3}Sb$) with a hole injector consisting of only one 5.3 nm thick GaSb QW in the beginning of ICL design [119]. Subsequently, a short investigation of the influence of the hole injector on the valence intersubband absorption, which was extensively studied in the W-QW in section 4.2, is presented.

Die approbierte gedruckte Originalversion dieser Dissertation ist an der TU Wien Bibliothek verfügbar.
The approved original version of this doctoral thesis is available in print at TU Wien Bibliothek.
TU WIEN Bibliothek Your knowledge hub

Die approbierte gedruckte Originalversion dieser Dissertation ist an der TU Wien Bibliothek verfügbar.
The approved original version of this doctoral thesis is available in print at TU Wien Bibliothek.

First, the difference in absorption will be investigated for design B, which is defined here again for the sake of convenience: 2.23 nm InAs/3.00 nm $Ga_{0.60}In_{0.40}Sb$/ 1.83 nm InAs. In order to be able to approximately compare the absolute values, the simulated structure was extended by a 9.6 nm thick AlSb barrier (Fig. 4.22 (left)) to account for the later subjoined length of the hole injector. For the calculation of the valence intersubband absorption, shown on the right side of Fig. 4.22, the subbands arising due to the thick AlSb barrier (bottom right in gray) were excluded. Hence, the result unsurprisingly resembles the absorption presented in the previous section. The employed hole injector comprises two GaSb QWs of thicknesses 2.8 and 4.8 nm separated by 1.0 nm-thick AlSb barriers and followed by a slightly thicker AlSb barrier (2.5 nm) at the SMI, separating the wider h-QW from the thickest InAs layer of the electron injector. In Fig. 4.23 this part of one active stage is depicted, showing a multitude of confined states in the valence band arising from the three coupled h-QWs. The simulated absorption (bottom) was calculated for all depicted subbands in the valence band (colored). Evidently, the additionally occurring subbands and the modification of the already investigated ones due to the coupling of the wells leads to a broadening of the reported absorption peaks. However, the resonant peak around 4.3 µm is still within the same wavelength range as before. The peak at shorter wavelengths is traced back to subband transitions involving the lowest states visible in the rightmost GaSb QW.

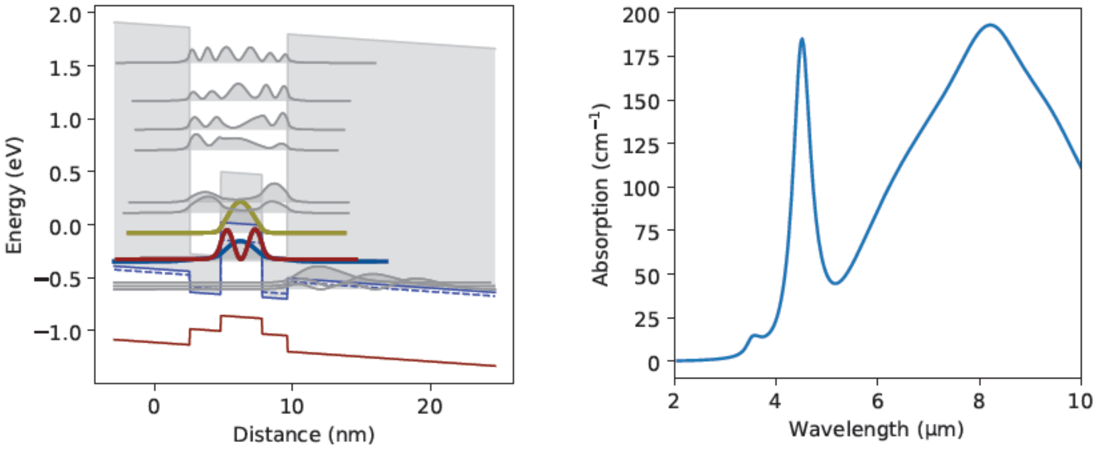

Figure 4.22: left: Subbands at the Γ-point of W-QW design B including an extension of the GaSb barrier by 9.6 nm on the right side to achieve better comparability between the absorption shown here, on the right, and the one considering the influence of the hole injector of that length, displayed in Fig. 4.23 (bottom). **right**: Calculated valence intersubband absorption between the colorfully depicted subbands on the left.

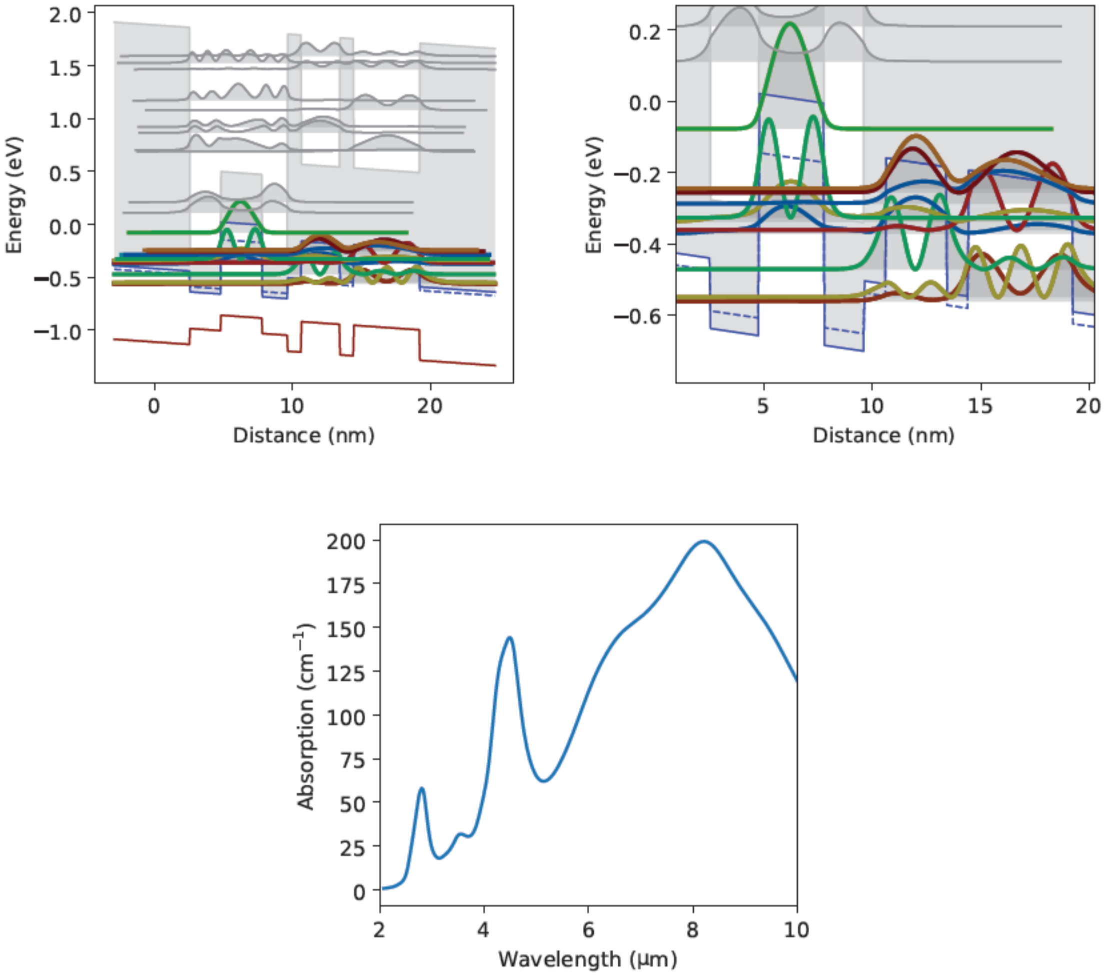

Figure 4.23: top left: Subbands depicted for the W-QW and the hole injector of design B, showing a variety of emerging states in the valence band (colored). **top right**: Magnified picture of the valence subband structure. **bottom**: Simulated absorption within the valence band.

Historically, the hole injector has predominantly undergone adaptations based on empirically deduced design principles, first implementing one and then two GaSb QWs and choosing the layer widths to achieve an energy separation of 80-100 meV between the lower lasing state in the GaInSb h-QW and the injection state in the adjacent GaSb well (section 3.1.1) [60]. Thus, this building block of the active region might still offer room for potential improvement of the device performance if investigated carefully. In the following, four different designs featuring adaptations of the hole injector and the first InAs QW of the electron injector will be presented. All of them have been experimentally realized. The reference structure (subsequently denoted G) considered is an ICL with a W-QW targeting an emission wavelength of 3.4 µm (1.63 nm InAs/3.00 nm $Ga_{0.60}In_{0.40}Sb$/1.28 nm InAs) featuring the already

Die approbierte gedruckte Originalversion dieser Dissertation ist an der TU Wien Bibliothek verfügbar.
The approved original version of this doctoral thesis is available in print at TU Wien Bibliothek.
TU WIEN Bibliothek Your knowledge hub

introduced double GaSb-QW hole injector employed in design B. The electron injector, which was additionally considered in the simulations is made up of five InAs wells with widths of 4.3/3.1/2.28/1.6/1.6 nm separated by 1.2 nm-thick AlSb barriers. The simulated band structure is depicted in Fig. 4.24. The multitude of

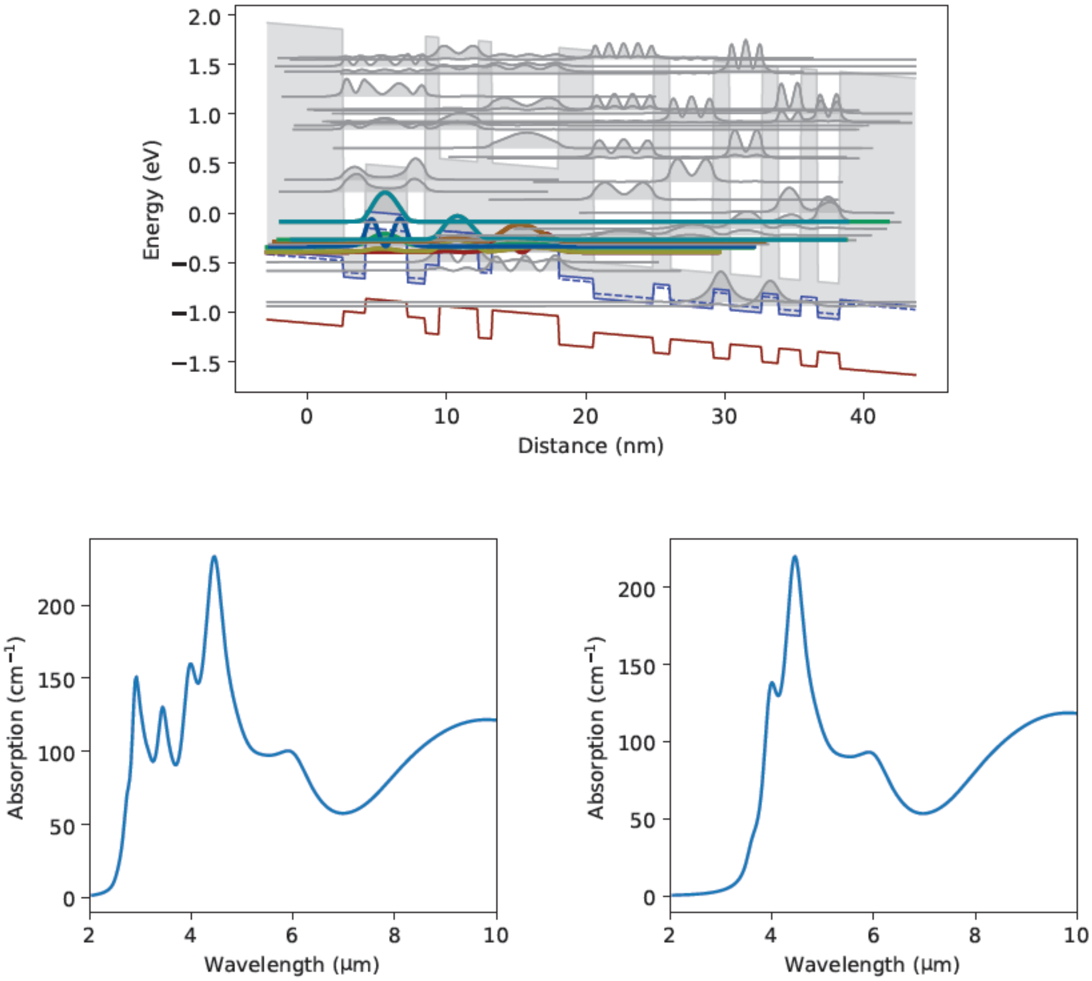

Figure 4.24: top: Simulated subbands for one active stage of reference structure G, showing the W-QW, hole- and electron injector from left to right. **bottom**: Calculated valence intersubband absorption for all valence band states present in the W-QW and the hole injector (left). The right side shows the same result, however, only including the colored subbands shown in the band structure calculation. This clearly demonstrates that transitions involving the lowest two states in the hole injector cause the two absorption peaks at shorter wavelengths. These transitions might not actually occur, as these states are potentially not fully bound in the actual structure.

emerging valence subbands possibly rationalizes the empirically established energy separation of 80-100 meV between the lower lasing level and the adjacent hole injec-

Die approbierte gedruckte Originalversion dieser Dissertation ist an der TU Wien Bibliothek verfügbar.
The approved original version of this doctoral thesis is available in print at TU Wien Bibliothek.

tor level. This design feature results in an expected hole concentration within the hole injector that is considerably lower than in the GaInSb h-QW. The lower hole concentration should result in reduced absorption within the hole injector, which would benefit the device performance. However, the situation might change further away from the threshold, since the carrier distribution within the cascade might differ significantly due to the dependence of the scattering rates on the applied bias voltage.

In contrast to all simulation results showing valence intersubband absorption before, where the Fermi level was fixed to the topmost valence subband, here, the position of the Fermi level is roughly deduced from the calculated band structure. However, the results shown here are not meant to provide a critical analysis in terms of absolute values but should give a qualitative idea and insight into possibly occurring transitions and serve as a relative comparison between the structures investigated in this section. The calculated absorption between the valence subbands is shown for all subbands (left) and excluding the lowest two states in the hole injector (right) in Fig. 4.24. Hence, the two features at low wavelengths are due to those lowest two states, which are potentially not fully bound in the actual structure. These results serve as a baseline for the comparison of the adaptations made in the following.

The first investigated adaptation (design H) was a simplification of the hole injector to one single GaSb well with a width of 4.8 nm. Although not new as a concept per se, the goal was to investigate whether this modification would lead to a significant change in device performance, e.g., due to potentially reduced valence intersubband absorption. The subbands at the Γ-point are depicted on the left side of Fig. 4.25. The simulation result of the valence intersubband absorption between the colored subbands is presented on the right. Due to the modification the resulting calculated valence intersubband absorption differs substantially from reference structure G. However, both seem to show negligible absorption at the lasing wavelength of 3.4 µm if the lowest two subbands in design G are disregarded. At longer wavelengths (6 - 10 µm) the design only employing a single GaSb well displays significantly higher absorption, which might make the implementation unfeasible for ICLs emitting above 6 µm.

Next, the single QW hole injector was modified to employ a strained 2.5 nm-thick $Ga_{0.60}In_{0.40}Sb$ layer. The band structure, as well as the calculated valence intersubband absorption are depicted in Fig. 4.26 for this design denoted I. Qualitatively, the simulated wavelength-dependent absorption looks similar as for design H, showing large absorption above 6 µm. The absorption at the lasing wavelength around

Die approbierte gedruckte Originalversion dieser Dissertation ist an der TU Wien Bibliothek verfügbar.
The approved original version of this doctoral thesis is available in print at TU Wien Bibliothek.
TU WIEN Bibliothek Your knowledge hub

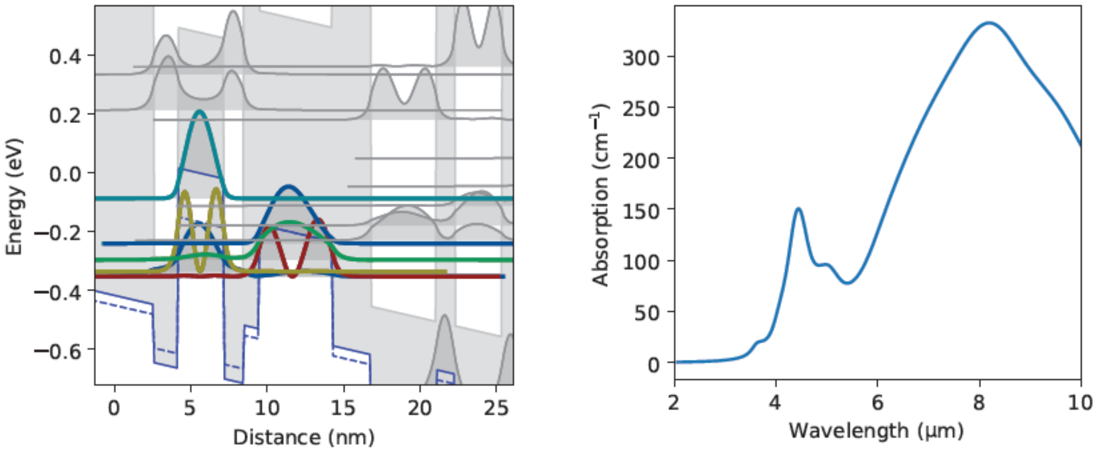

Figure 4.25: left: Simulated subbands shown for the simplified hole injector of design H. The subbands are depicted for the W-QW, the single GaSb-QW hole injector and the first two QWs of the electron injector. **right**: Calculated valence intersubband absorption between the colored subbands.

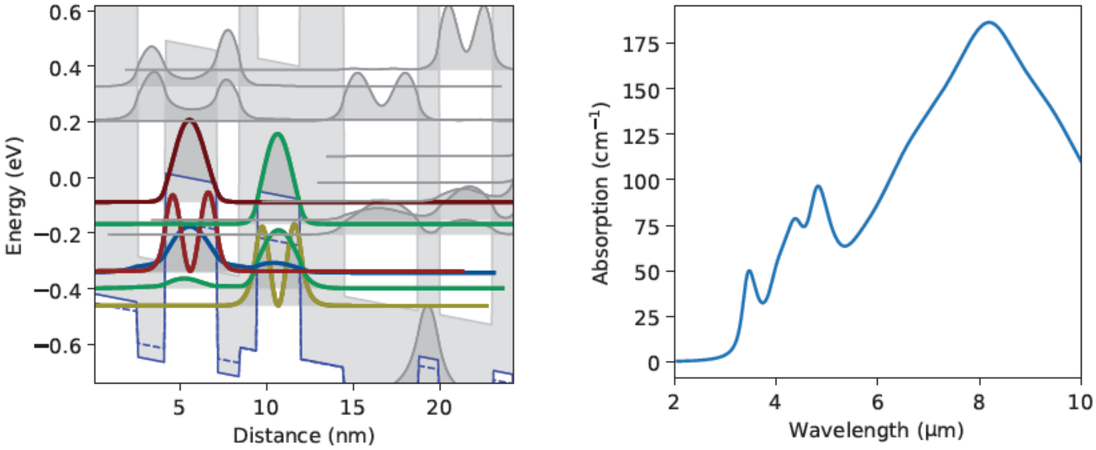

Figure 4.26: left: Calculated subbands for design I, employing a 2.5 nm-thick $Ga_{0.60}In_{0.40}Sb$ well as hole injector. **right**: Calculated valence intersubband absorption between all colored subbands.

3.4 µm still appears to be insignificant. However, in this design the energy difference between the lower lasing state and the topmost hole injector state was adjusted to amount to approximately 80 meV, compared to 180 meV and 160 meV for designs G and H, respectively. Apart from potentially occurring absorption in the hole injector, transitions within the first well of the electron injector were considered additionally.

Die approbierte gedruckte Originalversion dieser Dissertation ist an der TU Wien Bibliothek verfügbar.
The approved original version of this doctoral thesis is available in print at TU Wien Bibliothek.
TU WIEN Bibliothek Your knowledge hub

4.3.2 Absorption in the electron injector

Although the polarization of the light in ICLs is highly unfavorable for absorptive transitions to occur between subbands of the conduction band, the probability for this is non-zero due to the coupling between the conduction and valence band. Going back to design H the single GaSb hole injector absorption within the first QW of the electron injector was examined. The result is shown in Fig. 4.27 for light polarized perpendicular to (X - as in ICLs) and parallel to growth direction (Z). The transition is extremely favorable for Z polarization; however, the absorption is still finite for light polarized in X-direction between 3 and 4 µm, which is shown again separately in blue on the right side for better comparison. The idea was to avoid this potential source of losses by decreasing the width of the first well of the electron injector from 4.3 to 3.7 nm. The band structure of this design named J, is pictured in Fig. 4.28. Due to the smaller thickness of the well the lower energy levels (red and orange) are energetically farther separated from the higher state (turquoise) resulting in a blueshift of the absorption peak away from the lasing wavelength of the structure. Generally speaking, adaptations of the active region design do not only potentially influence the absorption looked at in the simulations. Instead, changes in the band structure can lead to performance improvement or degradation likewise, when unconsidered effects dominate the device dynamics, e.g., misalignment of the band structure or inefficient transport in the injectors. Hence, the most conclusive way to assess the potential of an aspired design modification is an experimental

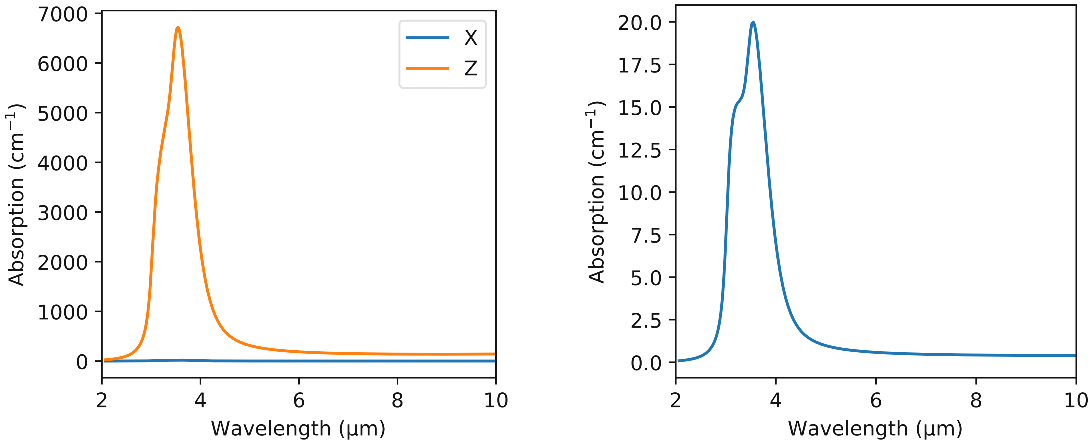

Figure 4.27: left: Simulated absorption between the subbands localized in the first InAs QW of the electron injector of design H for polarization of the light perpendicular to (X) and in growth direction (Z). **right**: Result for X-polarization for better comparison of the wavelength position.

Die approbierte gedruckte Originalversion dieser Dissertation ist an der TU Wien Bibliothek verfügbar.
The approved original version of this doctoral thesis is available in print at TU Wien Bibliothek.

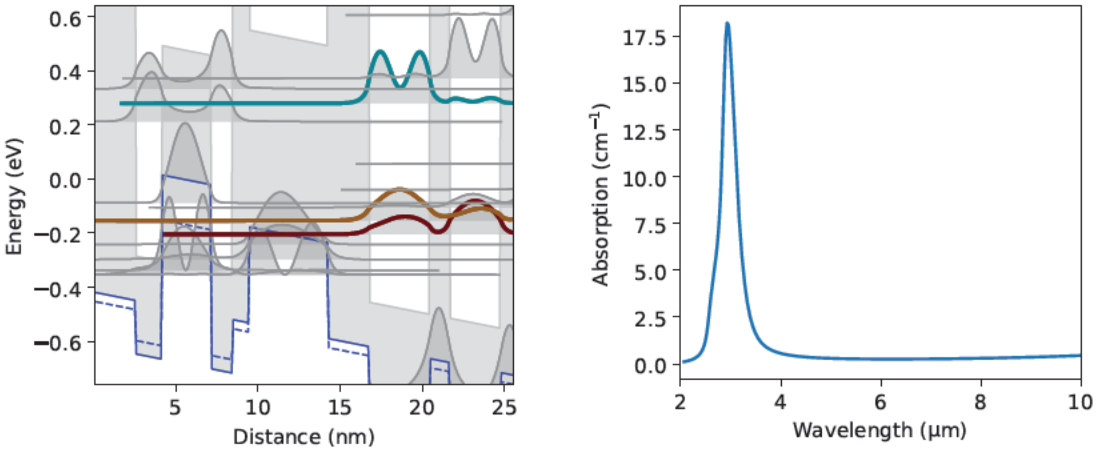

Figure 4.28: left: Band structure of design J featuring a thinner InAs layer as first QW of the electron injector. **right**: Calculated absorption for X-polarization between the subbands localized within this InAs layer.

realization of the structure.

4.3.3 Experimental indications

All four designs analyzed in the previous two sections were experimentally realized by MBE and the performance was assessed in pulsed operation (1 kHz, 500 ns) for 2 mm-long ridges with a width of 100 µm. The measured wavelength λ, threshold current density J_{th} at 20 °C as well as the characteristic temperature T_0 are stated in Tab. 4.3 and subsequently discussed. While the first three designs show approximately the same current-voltage characteristics, design J featuring the reduced InAs QW thickness showed a significantly higher operating voltage by approximately 0.5 V. The band structures shown in the previous two sections were all simulated for an applied electric field of 120 kV/cm. Employing the same hole injector as in design H but shifting the electron level upwards leads to a higher required voltage to align the states at the SMI. This situation can be seen on the left side of Fig. 4.28,

	λ (µm)	J_{th} (A/cm^2)	T_0 (K)	Description
G	3.56	243	50.0	2 GaSb QWs
H	3.43	240	54.2	1 GaSb QW
I	3.49	295	59.9	1 GaInSb QW
J	3.38	242	69.3	1 GaSb QW & thinner InAs QW

Table 4.3: Description and experimental results of the four realized designs, including the wavelength, threshold current density and characteristic temperature.

Die approbierte gedruckte Originalversion dieser Dissertation ist an der TU Wien Bibliothek verfügbar.
The approved original version of this doctoral thesis is available in print at TU Wien Bibliothek.

where the red state is energetically still separated from the state in the neighboring hole injector. This behavior was anticipated and accepted in favor of not introducing too many modifications at once, i.e., by additionally further modifying the hole injector to correct for the energy shift in the InAs QW.

Comparison of the LIV characteristics of the four designs indicated that an efficiency droop is more pronounced for design J. Apart from that, the EDQE seems to be similar for all investigated structures. The same can be said for the observed maximum output power. None of the designs showed any distinct improvement for all performance indicators, as was the case for the optimization of the W-QW presented in section 4.2.

Neither did the reduction of the hole injector from two to one QW lead to any noticeable performance deterioration. This supports the claim of Ref. [60] that the need for the incorporation of a second QW in the hole injector is questionable, since a single well should already efficiently suppress the leakage of electrons from the active W-QW to the electron injector.

The threshold currents extracted at 20 °C do not differ largely for the different designs. Although a slightly increased J_{th} is observed for design I, this structure shows an improved T_0, making it difficult to deduce any meaningful design guidelines without further investigation. The most significant improvement is achieved for structure J, which shows a compelling increase in the value of T_0, implying enhanced insensitivity towards temperature variations. However, these results still remain largely inconclusive, as no significant trend implying overall performance improvement was demonstrated by any of the experimentally investigated design modifications. In conclusion, the design of the hole injector appears not to be crucial at least at the investigated lasing wavelength of 3.4 µm, serving as justification to first only investigate the W-QW design to achieve enhanced ICL performance.

Die approbierte gedruckte Originalversion dieser Dissertation ist an der TU Wien Bibliothek verfügbar.
The approved original version of this doctoral thesis is available in print at TU Wien Bibliothek.
TU WIEN Bibliothek Your knowledge hub

Die approbierte gedruckte Originalversion dieser Dissertation ist an der TU Wien Bibliothek verfügbar.
The approved original version of this doctoral thesis is available in print at TU Wien Bibliothek.

Die approbierte gedruckte Originalversion dieser Dissertation ist an der TU Wien Bibliothek verfügbar.
The approved original version of this doctoral thesis is available in print at TU Wien Bibliothek.
TU WIEN Bibliothek Your knowledge hub

CHAPTER 5

RING INTERBAND CASCADE LASERS

Performance enhancement via suitable modifications of the active region, such as the ones established in chapter 4, are just one step — albeit a fundamental and important one — on the road that leads to the actual implementation of a device in real-world applications. Device design and fabrication are equally important, because no matter how well-performing the ICL epi-structure realized via MBE growth is, an inadequate fabrication scheme can greatly diminish the ultimate performance outcome, in the worst case rendering the structure useless.

This chapter aims at equipping the reader with an understanding of the basic principles of several topics relevant for the realization of ring ICLs preceding the presentation of the achieved results. First, a discussion of different cavity geometries, i.e., Fabry-Pérot and ring-shaped cavities, will be given. In view of the requirements for a vast majority of sensing applications — cw emission at room temperature in a single spectral mode — an introduction to different single mode mechanisms will be provided, followed by a discussion of the implemented strategies for ICLs. Furthermore, the state-of-the art and merits of vertical light emission will be highlighted, both in general and for interband cascade devices, putting the results described afterwards into perspective. The main part of this chapter will focus on the fabrication and performance of one particular device class, ring ICLs, which constitutes one of the topics explored during the course of this thesis.

The DFB gratings employed for the presented ring ICLs have been the subject of study of a large number of PhD theses and publications, that have extensively dealt with the theoretic description of said gratings. Since the focus of this work was on the experimental realization and performance enhancement of these devices, the reader is kindly referred to the following suggested resources for a more detailed description of DFB gratings for ring ICLs and QCLs. The PhD theses conducted at TU Wien on ring QCLs are listed in the reverse order of appearance. M. Holzbauer worked on ring QCLs and was the first to transfer the concept to ICLs [1]. R. Szedlak studied the light emission from ring QCLs in detail, including various modifications of the farfield by grating phase shifts and fabricated meta-material lenses on the substrate [172]. Before him, C. Schwarzer realized a polarizer on the substrate of a ring QCL and investigated the changing fraction of surface- and substrate-emitted light upon variation of the grating duty-cycle [173]. E. Mujagić started the work on ring QCLs in the research group of G. Strasser [174]. This chapter, thus, represents the continuation of their work. The theoretic description of DFB gratings is based on the coupled mode theory by Kogelnik and Shank [175], that is applicable for small modulations of the refractive index. N. Finger extended this description to strongly coupling grating structures, like complex coupled metal gratings, and developed a numerically stable Floquet-Bloch theory within his PhD thesis [176, 177]. W. Schrenk around that time experimentally realized the first vertically emitting DFB QCLs in the AlGaAs/GaAs material system [178, 179].

The results on ring ICLs presented here are mostly based on the publication "Continuous-wave operation of vertically emitting ring interband cascade lasers at room temperature" by H. Knötig et al. in Appl. Phys. Lett. 116, 131101 (2020) [180].

5.1 Cavities

Light confinement in a cavity has so far only been discussed in the vertical (in-growth) direction, where in ICLs the GaSb SCLs and InAs/AlSb cladding layers play a crucial role (see section 3.1.2). In a laser resonator the light ultimately is confined in the other two directions as well. Lateral mode confinement is often achieved by removal of the semiconductor material by etching procedures and subsequent layer deposition, i.e., electrical insulation and metallization. Other methods employ ion implantation or regrowth. The two most common resonator geometries are displayed in Fig. 5.1 - a Fabry-Pérot ridge and a ring waveguide.

5.1.1 Fabry-Pérot cavity

In a Fabry-Pérot resonator the light confinement in longitudinal direction is provided by the finite length of the cavity. In the simplest case the gain medium is located between two mirrors that are formed at the inferface of the semiconductor material and the surrounding air due to the refractive index difference. These laser facets are

Die approbierte gedruckte Originalversion dieser Dissertation ist an der TU Wien Bibliothek verfügbar.
The approved original version of this doctoral thesis is available in print at TU Wien Bibliothek.

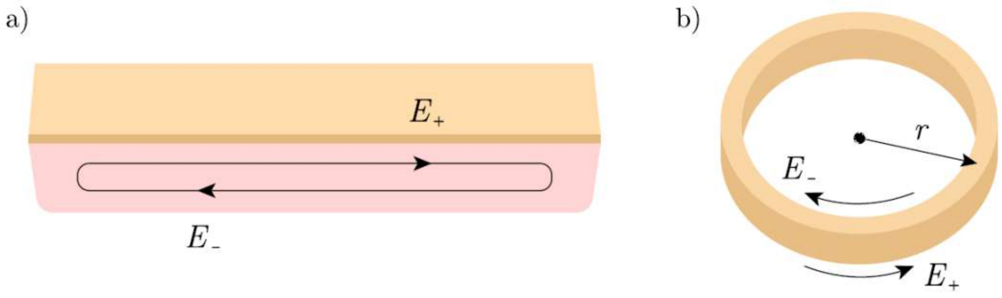

Figure 5.1: Illustrations of two common geometries for semiconductor laser cavities. **a)** Fabry-Pérot resonator with counterpropagating field components $E_\pm$ **b)** Ideal ring resonator, where the field propagates either clockwise or counterclockwise. Figure taken with permission from [181].

formed by cleaving the material along the crystallographic directions, resulting in a high quality interface. The reflectivity R for normal incidence is then given by the refractive index difference between the two materials

$$R = \left(\frac{n_1 - n_0}{n_1 + n_0}\right)^2 \xRightarrow{n_1 = n_{\text{eff}}, n_0 = 1} \left(\frac{n_{\text{eff}} - 1}{n_{\text{eff}} + 1}\right)^2, \tag{5.1}$$

where n_{eff} denotes the effective refractive index in the semiconductor and air is assumed for n_0. For ICLs, n_{eff} is on the order of 3.5, resulting in a reflectivity of R=0.31, which was already used in section 4.2.2. With two cleaved facets, the light is partially outcoupled on both sides of the waveguide, which is quantified by the mirror losses α_{m}

$$\alpha_{\text{m}} = \frac{1}{2L} \ln\left(\frac{1}{R_1 R_2}\right), \tag{5.2}$$

where L denotes the length of the laser ridge and $R_{1,2}$ the two mirror reflectivities. It is important to note that the mirror losses are inversely proportional to the cavity length. If the cavity length is chosen too short, lasing can be inhibited. For some applications modifications of the facet reflectivities can be beneficial or even required. For high power applications, emission from a single facet is desired. In that case, one of the cleaved facets can be covered with a high-reflectivity (HR) coating often composed of a metal. This can alternatively be achieved during the fabrication process if the facet is etched instead of cleaved when defining the waveguide geometry, and subsequently covered with the electric passivating layer and the metallization. However, this reduction of fabrication effort is achieved at the expense of the facet quality. Another example is the use of a laser in an external cavity (EC) configuration, where the feedback provided by one of the facets is substituted by an external mechanism, hence, requiring one facet to be anti-reflection (AR) coated.

For amplification of the light to occur, the gain provided within the resonator

Die approbierte gedruckte Originalversion dieser Dissertation ist an der TU Wien Bibliothek verfügbar.
The approved original version of this doctoral thesis is available in print at TU Wien Bibliothek.
TU WIEN Bibliothek Your knowledge hub

needs to exceed the total losses, composed of the mirror losses α_m and the internal losses α_i, causing an exponential attenuation of the light. Hence, the gain at threshold g_th given by the material gain g and the modal overlap of the propagating electric field with this gain region, i.e., the W-QWs in an ICL, exactly compensates the losses

$$g_\mathrm{th} = \Gamma g = \alpha_\mathrm{m} + \alpha_\mathrm{i}. \tag{5.3}$$

Internal loss mechanism were generally introduced in section 2.1.2 and further differentiated by their occurrence in different functional parts of ICLs in Eq. 4.7. Chapter 4 dealt with one particular internal loss mechanism in detail, valence intersubband absorption in the h-QW of the active region.

The Fabry-Pérot cavity exhibits resonances, determined by the condition for standing waves

$$m\lambda = 2 n_\mathrm{eff} L, \tag{5.4}$$

with the mode number m being a positive integer. Taking the wavelength dependence of the refractive index into account, the group refractive index is defined as

$$n_\mathrm{g} = n_\mathrm{eff} - \lambda \frac{\delta n_\mathrm{eff}}{\delta \lambda} = n_\mathrm{eff} + \nu \frac{\delta n_\mathrm{eff}}{\delta \nu}, \tag{5.5}$$

in terms of wavelength and wavenumber $\nu = 1/\lambda$. The spacing between two neighbouring eigenmodes, also referred to as the free spectral range (FSR), is given by

$$\Delta\lambda = \frac{\lambda^2}{2 n_\mathrm{g} L}, \tag{5.6}$$

$$\Delta\nu = \frac{1}{2 n_\mathrm{g} L}. \tag{5.7}$$

For ICLs, typical cavity lengths are on the order of a few millimeters, resulting in a mode spacing of $\Delta\nu = 0.71\ \mathrm{cm}^{-1}$, assuming $L = 2$ mm and neglecting dispersion $n_\mathrm{g} \approx n_\mathrm{eff} = 3.5$. Reducing the cavity length results in a wider spacing of the modes. The longitudinal modes and emission spectrum of a Fabry-Pérot cavity are schematically depicted in Fig. 5.2. Without the implementation of further wavelength discriminating mechanisms, multi-mode emission is obtained from Fabry-Pérot ICLs, as the gain profile is typically broad enough to support a multitude of possible longitudinal modes away from threshold.

While the experimental results in chapter 4 were obtained by the realization of broad-area Fabry-Pérot cavities, which feature a multitude of longitudinal as well as lateral modes and, thus, exhibit multi-mode spectra, the geometry that will be the focus of this chapter is the ring shape.

Die approbierte gedruckte Originalversion dieser Dissertation ist an der TU Wien Bibliothek verfügbar.
The approved original version of this doctoral thesis is available in print at TU Wien Bibliothek.

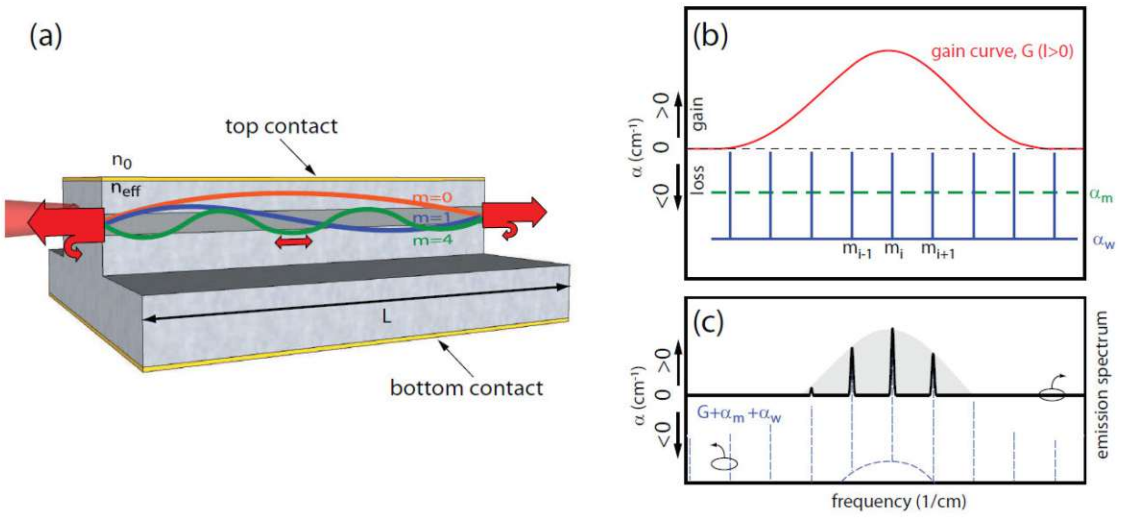

Figure 5.2: **(a)** Fabry-Pérot resonator supporting a variety of longitudinal modes. **(b)** The active region determines the gain profile, while the cavity geometry dictates the mode spacing. **(c)** The modes within the gain spectrum are amplified sufficiently to reach lasing threshold. Figure taken from [173].

5.1.2 Ring-shaped cavities

While the electromagnetic field propagating in a Fabry-Pérot cavity undergoes reflections at the two facets, an ideal ring waveguide does not provide an optical feedback mechanism. Hence, the field either propagates in the clockwise or counter-clockwise direction, if no backscattering mechanisms or strong optical feedback is present [182, 183]. The light inside a ring cavity can be guided, if the angle of incidence at the circular interface is larger than the critical angle $\theta_{\text{crit}} = arcsin(n_2/n_1)$, where the cavity shows a refractive index n_1 larger than that of the surrounding material n_2. Translating that into geometrical constraints requires the radius of the cavity to be larger than the wavelength. Under these conditions, the light impinging on the outer sidewalls of the cavity is totally reflected internally, leading to the formation of whispering gallery modes. The name dates back to the first observations of these modes in acoustics, for example by Lord Rayleigh in St. Paul's cathedral in London [184]. The sounds are described to be clinging to a concave surface. In analogy, the intensity maxima of the modes in semiconductor lasers with circular shapes are shifted towards the outer sidewall of the cavity, compared to a ridge waveguide. However, this effect depends on the curvature. The larger the cavity diameter is, the more closely the situation resembles the conditions in a straight waveguide.

Besides ring-shaped lasers, semiconductor lasers can moreover be realized in the shape of thin disks. The first experimental realization was reported for optically pumped InGaAs QWs in 1992 [185]. Since then, they have been demonstrated with

TU Bibliothek Your knowledge hub WIEN
Die approbierte gedruckte Originalversion dieser Dissertation ist an der TU Wien Bibliothek verfügbar.
The approved original version of this doctoral thesis is available in print at TU Wien Bibliothek.

QCLs in the mid-infrared [186] and the THz spectral region [187]. They are applied in biosensing applications [188] and are featured in the realization of ultrafast short pulse generation with high output powers [189]. In contrast to electrically pumped semiconductor disk lasers, for ring cavities the active area is significantly smaller leading to reduced power consumption, for diameters of the same size. Moreover, ring lasers due to their reduced waveguide width offer the possibility for the selective suppression of higher order lateral modes. Since the losses for higher order modes increase due to the higher modal overlap with the sidewalls with decreasing waveguide width, the fundamental mode showing the lowest waveguide losses can be excited exclusively in a sufficiently narrow waveguide (see section 5.4.2).

Calculations of the waveguide modes in a ring laser can be performed by employing the conformal transformation method [190, 191]. The cylindrical coordinates of the ring (r, θ, z) can be mapped onto a straight ridge geometry (u, v, z) using the following transformation [173]

$$u = r_{\text{out}} \ln\left(\frac{r}{r_{\text{out}}}\right), \tag{5.8}$$

$$v = r_{\text{out}}\theta. \tag{5.9}$$

The ring is described by the radial coordinate r, the azimuthal angle θ and the outer radius r_{out}. The transformation further affects the refractive index profile in lateral direction ($r \to u$). In the new coordinate system the refractive index increases towards the outer ring radius r_{out} according to $n_{\text{t}}(u) = \exp(u/r_{\text{out}})$. An intuitive understanding can be gained by considering the optical path for light propagating within the cavity. Closer to the outer sidewall the optical path is longer, which relates to a lower phase velocity and thus a higher refractive index $n = c/v_{\text{phase}}$.

The mode profile for the fundamental (orange) and the first higher order lateral mode (green) is calculated for an ICL waveguide, composed of the epitaxial structure described later on in this chapter in section 5.5. It is laterally sandwiched between 250 nm of Si_3N_4 and 650 nm of Au. In order to explore the effects of the ring shape on the propagation of the light, ridge and ring waveguides were simulated with two different waveguide widths w = 4 µm and 10 µm and two different outer ring diameters of D_{out} = 400 µm and 800 µm. The results are shown in Fig. 5.3. Several conclusions can be drawn from the simulations. The second order mode exhibits two intensity antinodes. The antinode with the higher maximum intensity is always found to be closer to the inner radius. The asymmetry between the antinodes of the higher order modes decreases when the waveguide width is reduced. While the whispering gallery modes in the 10 µm wide ring waveguides are located closer

Die approbierte gedruckte Originalversion dieser Dissertation ist an der TU Wien Bibliothek verfügbar.
The approved original version of this doctoral thesis is available in print at TU Wien Bibliothek.
TU WIEN Bibliothek Your knowledge hub

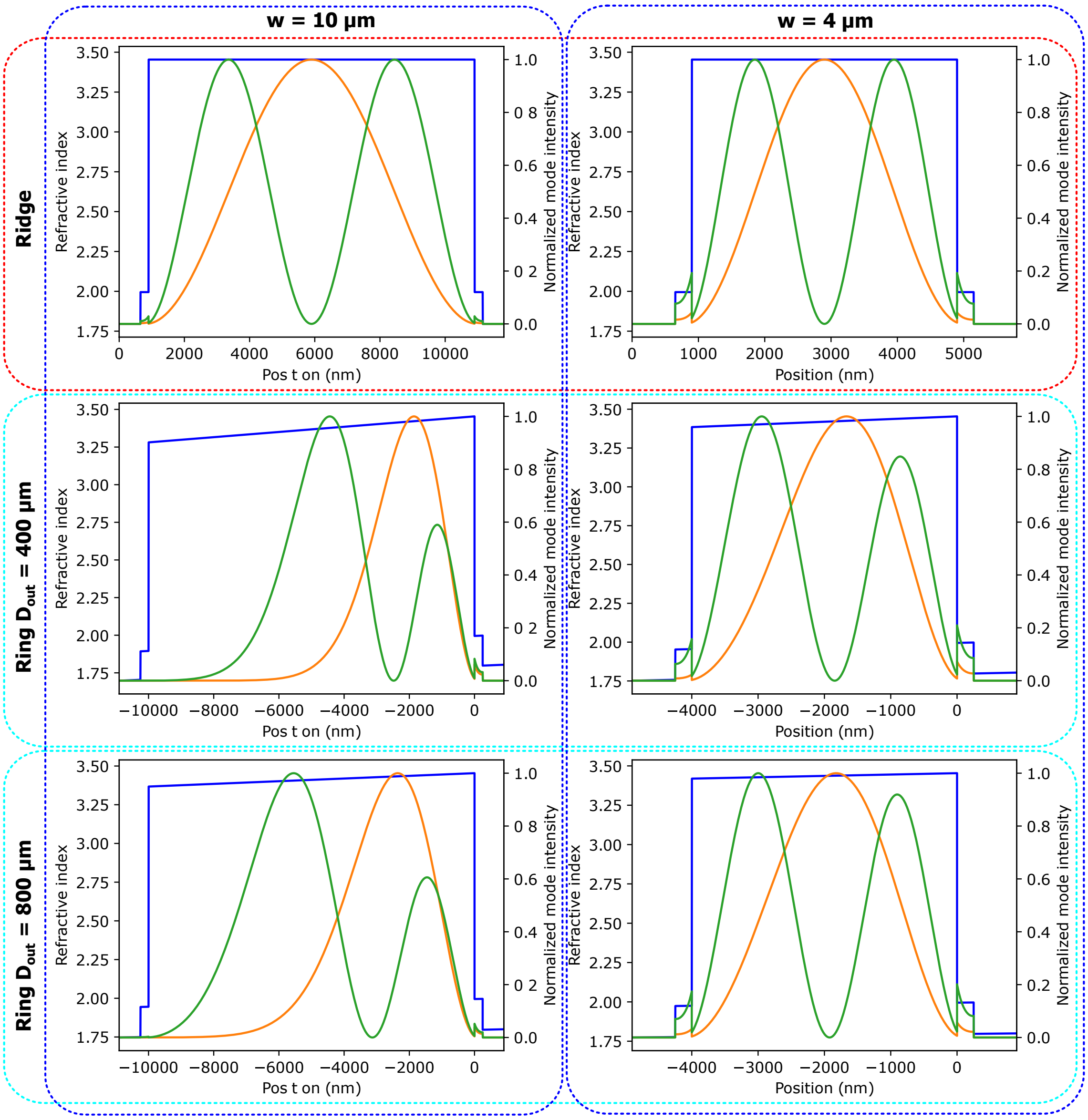

Figure 5.3: Calculations of the lateral modes in ridge and ring ICL waveguides for a wavelength of 3.85 µm. The calculations for the rings are performed with the conformal transformation method, hence, the refractive index increases towards the outer ring diameter, which in this coordinate system is defined at $x = 0$. The highest peak of the first-order lateral mode (green) is located closer to the inner sidewall compared to the fundamental modes of the ring cavities. The effect of a reduction of the waveguide width from 10 µm to 4 µm is additionally explored.

to the outer sidewall, this behavior is almost suppressed for the small waveguide width. For larger outer diameters, the behavior increasingly resembles that of the ridge waveguides. Especially the narrow ridge (top right) and the narrow ring with large diameter (bottom right) show very similar lateral mode profiles.

Die approbierte gedruckte Originalversion dieser Dissertation ist an der TU Wien Bibliothek verfügbar.
The approved original version of this doctoral thesis is available in print at TU Wien Bibliothek.

Die approbierte gedruckte Originalversion dieser Dissertation ist an der TU Wien Bibliothek verfügbar.
The approved original version of this doctoral thesis is available in print at TU Wien Bibliothek.
TU Wien Bibliothek Your knowledge hub

The eigenmodes in a circular cavity need to fulfill the condition

$$m\lambda = n_{\text{eff}} L_{\text{eff}}, \tag{5.10}$$

where m denotes the index of the azimuthal (lateral) mode and the effective cavity length $L_{\text{eff}} = 2\pi r_{\text{eff}}$ relates to the circumference of the effective radius r_{eff}. The center of mass of the mode is commonly used as r_{eff}. The spacing between two adjacent modes that can in principle be supported by the circular cavity is given by

$$\Delta\lambda = \frac{\lambda^2}{n_{\text{g}} L_{\text{eff}}}, \tag{5.11}$$

$$\Delta\nu = \frac{1}{n_{\text{g}} L_{\text{eff}}}. \tag{5.12}$$

This condition only holds for different longitudinal modes from the same order of the lateral mode m. The relation is similar to the one developed in the preceding section for the Fabry-Pérot resonator (Eq. 5.6), differing only by a factor of 2.

The interest in ring cavities for lasers has gained new momentum in recent years, especially since frequency combs have been experimentally realized in ring QCLs in the mid-infrared [192, 193] and the THz-region [194]. The rich physics and multimode dynamics giving rise to the formation of free-running combs in ring QCLs without any additionally implemented defects are beautifully described from a theoretical point of view in [195] and [181].

Light extraction

The absence of facets positively impacts the performance of circular cavities. However, the outcoupled light intensity is comparably weak without the implementation of adequate extraction mechanisms and the emission is uniform for all angles θ, if the outer sidewalls are left uncoated. One approach is to bring a second waveguide, for example a ridge, in contact or close proximity to the ring laser [196, 197, 198]. The evanescent field leaking outside of the ring can then couple to this adjacent output coupler and the light can be emitted through the facets. Since the evanescent field decays exponentially with distance, the gap between the two waveguides determines the coupled light intensity and hence, the extraction efficiency. Another approach is to abandon the circularly symmetric shape of the cavity and use a distorted geometry influencing the whispering gallery modes in the cavity, either in the form of a spiral [199] or other deformations of the shape like ellipses [200]. This improves both the output power and directionality of the light.

The ring cavities of importance in the context of this thesis, are employing a second-order DFB grating on top of the waveguide, which enables efficient outcoupling of the light from the ring cavity, either through the surface or the substrate. It additionally offers a mechanism for wavelength selection. These single-mode devices have been realized both for QCLs [201] and ICLs [202].

5.2 Single mode devices

The mid-infrared spectral region is of great interest for gas spectroscopy, due to a large variety of gases that exhibit their fundamental absorption lines there [203]. Although frequency combs [204] are gaining momentum, offering possibilities for alternative sensors, i.e., employing dual comb spectroscopy [205, 206, 207, 208, 209], for the vast majority of sensitive sensing schemes lasing in a single spectral mode is an essential prerequisite [210, 3].

Single-mode emission can be achieved by increasing the losses of all other modes selectively. Different concepts can be used to accomplish this goal, including geometrical constraints, coupled cavities or gratings.

5.2.1 Short cavities

If the separation between the longitudinal cavity modes is large enough, the laser can be inherently single mode, if only a single mode lies within the gain profile. Since the mode spacing is inversely proportional to the cavity length, as established in Eq. 5.6, this can be achieved by using a very short cavity. However, since the mirror losses are increasing when reducing the cavity length (see Eq. 5.2), the gain needs to be high enough to compensate for them. Bandgap lasers show high enough gains to still overcome the losses, achieving single mode emission with cavity lengths on the order of only tens of micrometers [211].

5.2.2 External cavity lasers

Integrating a diffraction grating in the beam path of an EC, that can be realized by suppressing the Fabry-Pérot modes upon the deposition of an AR coating on one of the laser facets, constitutes another popular method for wavelength selection. The tuning is achieved by either tilting the grating (Littrow configuration) or by tilting an additional mirror (Littman-Metcalf configuration) that is positioned opposite of the grating to back reflect the light onto it [212]. In both configurations, the light impinges under a varying angle onto the grating. Due to their exceptionally broad wavelength tuning range of up to several hundreds of wavenumbers, as an

Die approbierte gedruckte Originalversion dieser Dissertation ist an der TU Wien Bibliothek verfügbar.
The approved original version of this doctoral thesis is available in print at TU Wien Bibliothek.
TU Bibliothek WIEN Your knowledge hub

exemplary representative of this device class, EC-QCLs are especially attractive for sensing applications [213, 214].

5.2.3 Distributed Bragg reflectors

Distributed Bragg reflectors (DBRs) can be used to realize wavelength-selective mirrors. They are formed by alternating stacks of two different materials with thicknesses d_1 and d_2 and refractive indices n_1 and n_2. At the interfaces between these two materials, a plane wave is partly transmitted and partly reflected with a reflectivity according to Eq. 5.1. A scheme of this structure is depicted in Fig. 5.4. The green arrows indicate the incoming and reflected wave, which experiences a phase shift of $\pi/2$ while propagating through each of the layers with a thickness of $d_{1,2} = \frac{1}{4}\lambda_\mathrm{B}/n_{1,2}$, where λ_B is the Bragg wavelength in free-space. The reflection at the interfaces from a medium with lower to a medium with higher refractive index ($n_{0,1} \rightarrow n_2$) leads to an additional phase shift of π. Hence, a plane wave coming from a material with refractive index n_0 undergoes a total phase shift of $m\pi$, where m is an odd integer, leading to constructive interference of the reflections of the wave at each interface. This is a direct consequence of the thickness of the layers

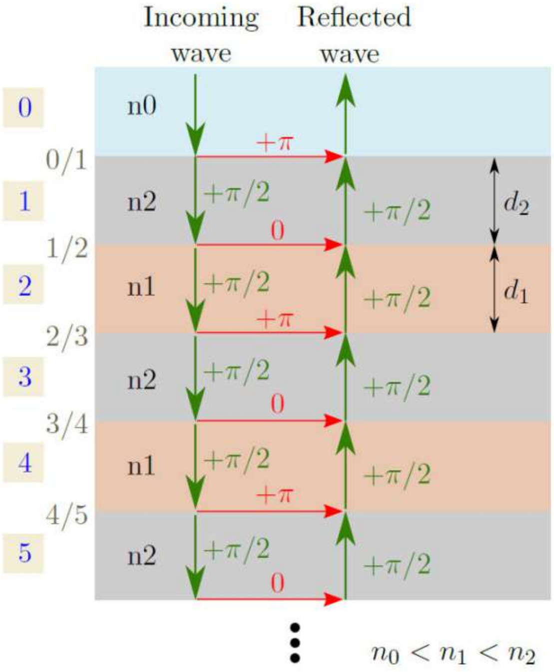

Figure 5.4: Depiction of the functioning principle of a distributed-Bragg reflector composed of alternating layers of differing refractive index. The experienced phase shifts for light propagating through layers of thicknesses $d_{1,2} = \frac{1}{4}\lambda_B/n_{1,2}$ and upon reflection on an interface going from lower to higher refractive index ($n_{0,1} \rightarrow n_2$) is annotated. Reproduced from [1], where it was based on [215].

Die approbierte gedruckte Originalversion dieser Dissertation ist an der TU Wien Bibliothek verfügbar.
The approved original version of this doctoral thesis is available in print at TU Wien Bibliothek.

being one quarter of the wavelength in the material for a first order grating. The structure is providing wavelength-dependent feedback due to the periodic variation of the refractive index. The grating period Λ_g is then defined as the sum of the two layers

$$\Lambda_\mathrm{g} = d_1 + d_2 = \frac{\lambda_\mathrm{B}}{2}\left(\frac{1}{2n_1} + \frac{1}{2n_2}\right) = \frac{\lambda_\mathrm{B}}{2}\frac{1}{n_\mathrm{eff}}, \tag{5.13}$$

where the effective refractive index is defined as the average $n_\mathrm{eff} = 2/(1/n_1 + 1/n_2)$. Subsequently, the following equation can be used to determine the Bragg wavelength λ_B,

$$m\lambda_\mathrm{B} = 2n_\mathrm{eff}\Lambda_\mathrm{g}, \tag{5.14}$$

where m is the diffraction order ($m = 1, 2, 3, ...$) and the propagation constant at the Bragg wavelength is defined as $\beta_\mathrm{B} = 2\pi n_\mathrm{eff}/\lambda_\mathrm{B}$. For small variations of the refractive indices, the coupled-mode theory is applicable as described by Kogelnik and Shank [175]. Within a small wavelength range around the Bragg wavelength λ_B, the so called stop band, the DBR shows very high reflectivities. Propagation of light with wavelengths within the stop band is highly suppressed, which is where the name derives from. The deviation from the Bragg wavelength is usually described in terms of the detuning of the wavelength $\Delta\beta = \beta - \beta_\mathrm{B}$ with the propagation constant $\beta = 2\pi/\lambda$.

Vertical cavity surface emitting lasers

A prominent device class employing DBRs are vertical cavity surface emitting lasers (VCSELs) [216, 217]. They take advantage of the short cavity approach, since the cavity lengths are usually on the order of only a few times the wavelength. These power-efficient and compact devices rely on epitaxially grown and/or deposited high-quality DBRs above and below the gain material [218, 219]. Although inherently single-mode, the mirror losses need to be reduced by increasing the reflectivity of the mirrors with this approach. The first experimental demonstration of a VCSEL featuring an interband cascade active region was reported in 2016 by Bewley et al. [217]. The design is schematically depicted in Fig. 5.5, featuring a GaSb/AlAsSb mirror on the bottom and a dielectric Ge/$\mathrm{Al_2O_3}$ reflector on top of the active region. Depending on the desired wavelength and the used substrate other material combinations are used for the epitaxial mirrors, e.g., AlGaAs/GaAs (600-1300 nm) or AlGaAs/InP (1300-1800 nm) [220], as well as the dielectric mirrors, e.g., ZnS/Ge [221]. The total reflectivity of the grating in the simplified description of the plane-wave approximation is defined by the refractive index contrast $\gamma = n_1/n_2$

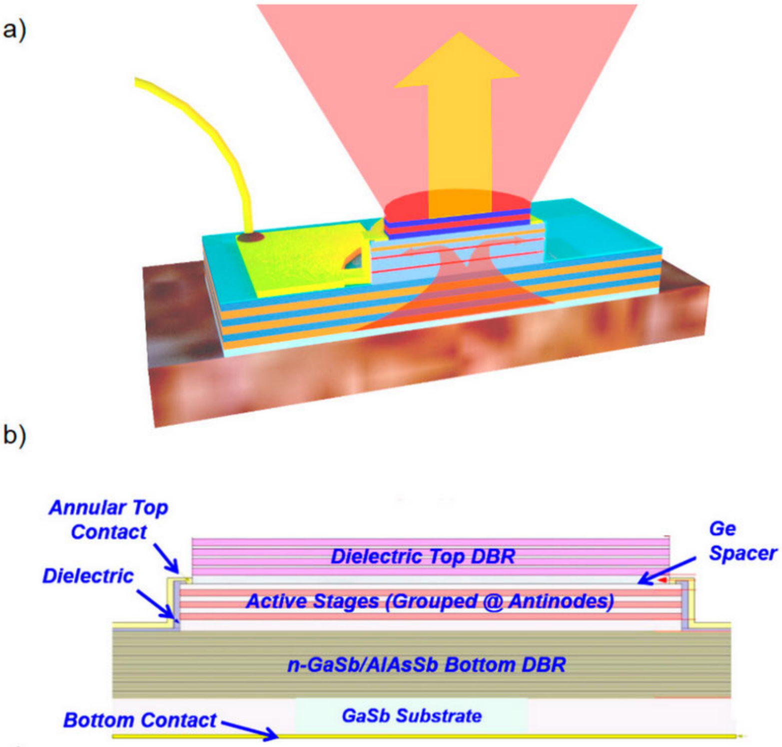

Figure 5.5: a: Schematic device architecture of the VCSEL published in [217] with **b**: the vertical layering. The 15 active stages are located in three spatially separated groups placed at the antinodes of the resonator. The epitaxially grown bottom mirror consists of GaSb/AlAsSb pairs, while a dielectric Ge/Al_2O_3 is deposited on top. Figure taken from [60].

($n_1 < n_2$) and the number of layer pairs as per [222]

$$R_{\mathrm{DBR}} = \left(\frac{1-\gamma^{2N}}{1+\gamma^{2N}}\right)^2 . \tag{5.15}$$

Thus, a high index contrast and large number of layers benefit the reflectivity.

5.2.4 Distributed feedback gratings

In contrast to DBRs, that are spatially separated from the active region of the laser, DFB gratings are integrated along the entire waveguide of the laser. They rely on periodic perturbations of the refractive index and/or the gain (or loss) of the active region itself [175],

$$n(z) = n + \Delta n \cos\left(2\beta_{\mathrm{B}} z\right) , \tag{5.16}$$

$$\alpha(z) = \alpha + \Delta\alpha \cos\left(2\beta_{\mathrm{B}} z\right) . \tag{5.17}$$

Die approbierte gedruckte Originalversion dieser Dissertation ist an der TU Wien Bibliothek verfügbar.
The approved original version of this doctoral thesis is available in print at TU Wien Bibliothek.
TU WIEN Bibliothek Your knowledge hub

Here, the average values of the refractive index and the gain constant are denoted by n and α, respectively, and Δn and $\Delta\alpha$ describe the amplitudes of the spatial modulations. The strength of the coupling between the forward and backward propagating light within the coupled mode theory is described by the coupling constant κ given by [175]

$$\kappa = \frac{\pi \Delta n}{\lambda_\mathrm{B}} + i\frac{\Delta\alpha}{2}. \tag{5.18}$$

It indicates how much feedback (per unit length) is provided by the grating structure. The working principle of the DFB grating is, like in DBRs, the coupling of the forward and backward propagating waves via Bragg scattering, where constructive interference is only achieved for certain wavelengths. Depending on whether the coupling constant is real, imaginary or complex, DFB gratings are distinguished into index coupled, gain/loss coupled or complex coupled, respectively. Their characteristic behavior as yielded by the coupled mode theory is schematically displayed in Fig. 5.6. For index coupling, due to the periodic nature of the modulation of the refractive index a stop band occurs, which is centered around the Bragg wavelength

(a) Index coupling: $\Delta n \neq 0$, $\Delta\alpha = 0$ (b) Gain coupling: $\Delta n = 0$, $\Delta\alpha \neq 0$

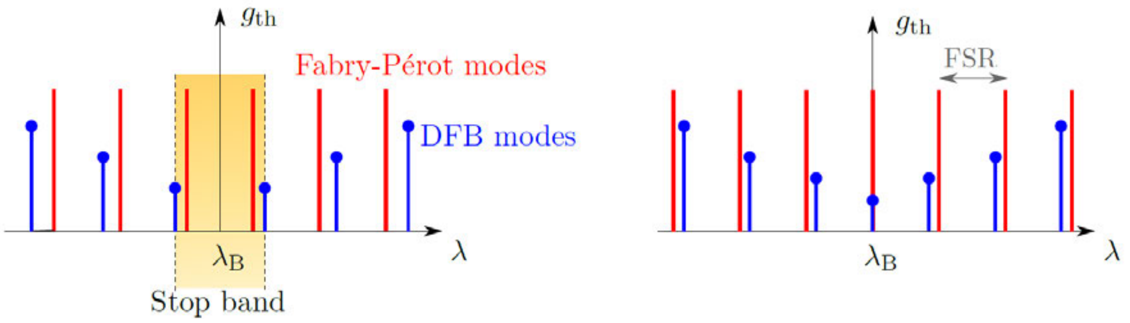

(c) Complex coupling: $\Delta n \neq 0$, $\Delta\alpha \neq 0$

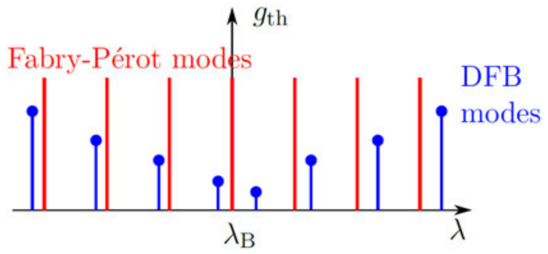

Figure 5.6: Different coupling regimes of DFB gratings as obtained within the coupled mode theory. **(a)** Index coupling shows the lowest threshold gain for two modes that are located on the edges of the arising stop band around the Bragg wavelength. **(b)** Gain coupled DFB devices show the lowest threshold gain at the Bragg wavelength. **(c)** Complex coupling leads to asyemmtrically located resonance frequencies around the Bragg wavelength. Figure taken and adapted from [1].

Die approbierte gedruckte Originalversion dieser Dissertation ist an der TU Wien Bibliothek verfügbar.
The approved original version of this doctoral thesis is available in print at TU Wien Bibliothek.
TU Bibliothek Your knowledge hub

λ_B, prohibiting the propagation of frequencies within this range. With larger κ the width of the stop band increases. The two lowest threshold gains are experienced by the two DFB modes on the edges of the stop band. Due to imperfections the threshold gain required for one or the other of the two modes will in most devices be lower. However, a prediction of which of these modes will start to lase cannot be made, which leaves an uncertainty regarding the wavelength of the device. By implementing a $\lambda/4$ shift in the middle of the grating, the mode degeneracy can be lifted, and a mode at λ_B then shows the lowest theshold gain [223, 224]. A gain coupled DFB grating results in the lowest threshold gain at the Bragg wavelength. For the mixed case of complex coupling the arising DFB modes are no longer spaced symmetrically around λ_B. For strong modulations of the index and gain, like they occur in DFB metal gratings, a more general approach based on the *Floquet-Bloch theory*, instead of the coupled-mode theory, has to be applied [176, 177].

Recalling the Bragg condition (Eq. 5.14) that has to be fulfilled for DFB gratings in order to provide feedback at the Bragg wavelength λ_B, different diffraction orders ($m_{\mathrm{DFB}} = 1, 2, 3, ...$) can be designed. Each of them comes with a unique set of properties. The emission angles and feedback provided by different DFB gratings can be analyzed by looking at the propagation vectors at the interface of two media. The angles of the ingoing and outgoing waves α_{i} and α_{o} are defined with respect to the grating normal, and n_{i} and n_{o} are the refractive indices of the two considered media. The diffraction order is given by m_{diff}, limited to positive integers. In the general case, valid for any diffraction grating, the horizontal components of the vectors, obtained by the projections of the propagation vectors onto the surface, need to fulfill

$$|\vec{\beta}'|\sin(\alpha_{\mathrm{o}}) = |\vec{\beta}|\sin(\alpha_{\mathrm{i}}) - m_{\mathrm{diff}}|\vec{G}|. \tag{5.19}$$

The grating vector is fixed and defined by the grating period Λ_g according to $|\vec{G}| = 2\pi/\Lambda_g$. Hence, it is half the length for a second order DFB grating compared to a first order grating, according to Eq. 5.14. The propagating vectors of incoming and scattered light are $\vec{\beta} = n_{\mathrm{i}}\vec{k_0}$ and $\vec{\beta}' = n_{\mathrm{o}}\vec{k_0}$, with $|\vec{k_0}| = 2\pi/\lambda$.

For a DFB grating, the incoming light travels within the resonator showing an effective refractive index $n_{\mathrm{i}} = n_{\mathrm{eff}}$ and is parallel to the grating, meaning perpendicular to the grating normal, hence $\alpha_{\mathrm{i}} = 90°$. The outgoing light can either exit the cavity and subsequently propagate in air (surface emission → $n_{\mathrm{o}} = 1$), be refracted in the direction of the substrate or stay within the laser cavity ($n_{\mathrm{o}} = n_{\mathrm{eff}}$). If Eq. 5.14 is not fulfilled and the resulting horizontal component of $\vec{\beta}'$ is within the light cone for propagation in air, i.e., $|\vec{\beta}'|\sin(\alpha_{\mathrm{o}}) < |\vec{k_0}|$, the light can be diffracted from the surface under an angle α_{o}. The emission angle can be conveniently written

Die approbierte gedruckte Originalversion dieser Dissertation ist an der TU Wien Bibliothek verfügbar.
The approved original version of this doctoral thesis is available in print at TU Wien Bibliothek.

as

$$\alpha_\mathrm{o} = \arcsin\left(\frac{m_\mathrm{diff}\lambda}{n_\mathrm{o}\Lambda_\mathrm{g}} - \frac{n_\mathrm{eff}}{n_\mathrm{o}}\right). \tag{5.20}$$

Light scattering towards the substrate is possible without restrictions. This case can be seen in Fig. 5.7(a). In the figure the emission angle is defined as $\phi = 90° - \alpha_\mathrm{o}$.

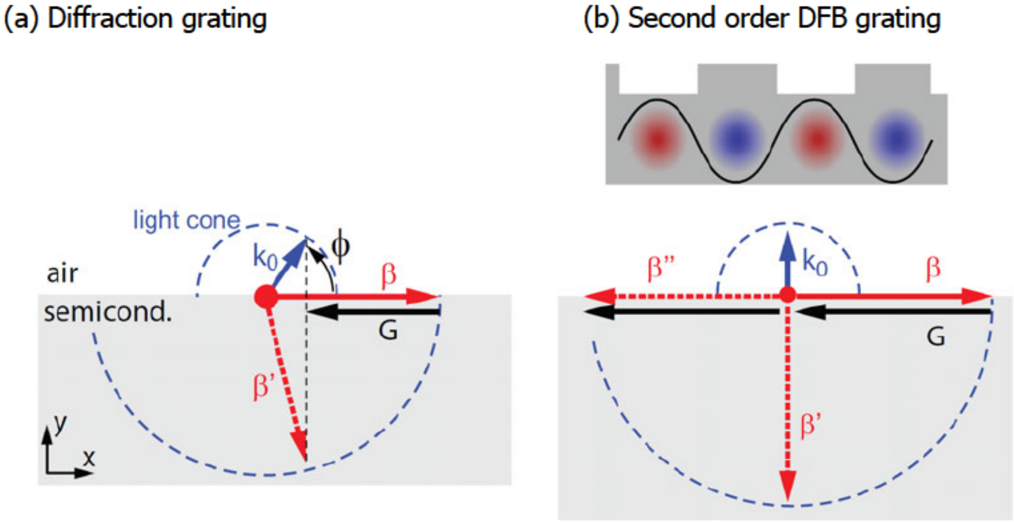
(a) Diffraction grating

(b) Second order DFB grating

Figure 5.7: **(a)** Scattering of light within a cavity at a diffraction grating not meeting the Bragg condition. Under these conditions the light can either be scattered toward the substrate (red dashed arrow) or the light is extracted into the surrounding air (blue arrow) under an angle ϕ. **(b)** Functioning principle of a second order DFB grating enabling optical feedback within the cavity ($\vec{\beta''}$) as well as vertical light emission from the substrate ($\vec{\beta'}$) and the surface ($\vec{k_0}$). Figure taken from [173].

If the light fulfills the Bragg condition, Eq. 5.20 can be rewritten in terms of the DFB order m_DFB using Eq. 5.14, resulting in

$$\alpha_\mathrm{o} = \arcsin\left[\frac{n_\mathrm{eff}}{n_\mathrm{o}}\left(\frac{2m_\mathrm{diff}}{m_\mathrm{DFB}} - 1\right)\right]. \tag{5.21}$$

Under the assumption of a first order DFB grating $m_\mathrm{DFB} = 1$, the only physical solutions are obtained for $m_\mathrm{diff} = 1$ and $n_\mathrm{o} = n_\mathrm{eff}$, resulting in $\alpha_\mathrm{o} = \arcsin(1) = \pm 90°$. This results in optical feedback in the inplane direction, which is for example exploited in edge emitting ridge devices. For a second order DFB grating, diffraction orders $m_\mathrm{diff} = 1$ and 2 are possible. The first case yields the solution $\alpha_\mathrm{o} = \arcsin(0) = 0°, \pm 90°$. Due to the multiplication with zero, $n_\mathrm{o} = n_\mathrm{eff}$ and $n_\mathrm{o} = 1$ are both possible in vertical direction, making substrate and surface emission equally probable. Hence, this diffraction order accomplishes the task of vertical light outcoupling from the cavity. The solution obtained for the second diffraction order is $\alpha_\mathrm{o} = \pm 90°$ as obtained for the first order grating, thus providing optical feed-

Die approbierte gedruckte Originalversion dieser Dissertation ist an der TU Wien Bibliothek verfügbar.
The approved original version of this doctoral thesis is available in print at TU Wien Bibliothek.

back for the light in the cavity. A second order DFB grating is shown in Fig. 5.7(b), where $m_{\mathrm{diff}} = 1$ results in $\vec{\beta}'$ and $\vec{k_0}$. The second diffraction order $m_{\mathrm{diff}} = 2$ yields $\vec{\beta}''$. This concept is employed for the ring ICLs presented in this chapter.

5.2.5 Single-mode interband cascade lasers

Various single-mode concepts have been applied to ridge ICLs and the realized devices have found application in numerous chemical sensing schemes [3]. The most popular choice for wavelength selection are DFB gratings, which can be applied to the laser in different geometries.

Corrugated sidewall gratings [225, 226], which are etched into both sidewalls of the ridge haven been realized as fourth-order gratings. Since the grating period is proportional to the order of the grating, it is technologically simpler to realize a fourth order grating compared to a first order one, due to restrictions imposed by the lithography and the subsequent etching step. However, due to a relatively weak coupling, the yield for single-mode devices is inadequate [227].

The limitations concerning reproducibility observed for vertical side wall gratings can be circumvented by employing a germanium top grating approach [228]. First demonstrated in 2007 up to a temperature of 180 K [229], room-temperature operation was reported in 2012 [227]. The increased stability in manufacturing is achieved at the cost of higher introduced losses. To guarantee sufficiently high coupling of the mode to the high-index first-order germanium grating deposited on top of the ridge, the thickness of the top InAs/AlSb superlattice cladding needs to be significantly reduced. A thickness of 700 nm thick is reported in literature [227], which compared to a more often employed thickness of 2 µm leads to an increased overlap of the mode with the highly doped contact layer and metallization and thus, additional losses. Nevertheless, single-mode output powers of 27 mW were achieved at 40 °C with HR/AR facet coatings and an emission wavelength around 3.8 µm. The losses can be significantly reduced by minimizing the area, where the top contact is in actual contact with the epi-structure, which resulted in a reduced threshold current density by a factor of 2 [230]. The duty-cycle of the metallized area was adjusted by selectively removing the top passivation layer, showing the lowest threshold single-mode emission of this device for a fraction of 14 %.

Top and sidewall gratings can be used in a combined approach, as demonstrated by Thorlabs [231]. While the top grating was targeting the Bragg wavelength, the period of the sidewall corrugation did not, and was used to suppress higher order lateral modes. The two gratings were spatially separated along the ridge and output powers of 42 mW were shown at 25 °C and around 3.3 µm.

TU Bibliothek WIEN Your knowledge hub
Die approbierte gedruckte Originalversion dieser Dissertation ist an der TU Wien Bibliothek verfügbar.
The approved original version of this doctoral thesis is available in print at TU Wien Bibliothek.

An alternative approach is the deposition of metal gratings next to the laser ridge in immediate proximity to the active region [232]. First demonstrated on InGaAs/AlGaAs diode lasers [233], this concept is now very successfully applied to ICLs over the entire available spectral range of cw GaSb-based devices [234, 94, 10]. During fabrication of these devices the etching depth for the definition of the waveguide is crucial, as it determines the coupling strength [234]. For best performance results, the etching needs to be precisely stopped in the upper part of the lower GaSb SCL, just below the active region. This ensures good overlap of the evanescent field of the mode with the complex-coupled grating as well as reduced current spreading.

Single-mode ICLs have also been realized using an EC approach [235, 236] with tuning ranges of more than 100 nm. More recently, single mode devices based on two V-coupled ICL cavities of slightly different lengths have been demonstrated [237]. No grating is needed for this approach that exploits the Vernier effect and has been demonstrated up to a temperature of 120 K in a proof-of-principle realization. Vertically emitting single-mode ICLs, i.e., VCSELs and ring cavities, will be discussed in the subsequent section.

5.3 State-of-the-art vertical light emission

In comparison to edge emitting devices, surface emitters offer numerous advantages. Firstly, no cleaved facet is needed for light emission. The cleaving procedure can potentially introduce inhomogeneities degrading the performance, posing a risk at the very end of device fabrication. In addition, depending on the position of the cleave edge with respect to an existing grating implemented for a ridge device, an additional phase difference is introduced, which influences the mode selection (see section 5.2.4). For surface emitters, avoiding the cleave edge, results in a more deterministic procedure for mode selection.

While multiple edge emitting devices can only be arranged side by side in one dimension, e.g., targeting various emission wavelengths on the same chip, surface emission allows for a two-dimensional arrangement, as has been demonstrated for ring QCLs [238]. In addition, if the emission is facilitated via the substrate, the integration of other optical elements, i.e., simple polarizers [239], or more sophisticated structures like meta-material lenses [240], is possible. This monolithic approach represents an appealing option for reducing the size of the foot-print when thinking about sensing systems, while broadening the field of applications, for example, allowing the integration of fluidic cells directly on the substrate side, bringing the

Die approbierte gedruckte Originalversion dieser Dissertation ist an der TU Wien Bibliothek verfügbar.
The approved original version of this doctoral thesis is available in print at TU Wien Bibliothek.
TU Bibliothek, WIEN Your knowledge hub

analyte into close contact with the light source.

One of the most appealing aspects about vertical light emission, is the possibility for wafer-level testing of these devices [218, 220]. What is often smiled at by researchers, for example at universities and research centers, for its apparent simplicity compared to more fundamental research and device development, and, thus, sometimes even disregarded, is the need for back-end processing. Dicing, wire-bonding, packaging and testing are essential steps in the full fabrication process of many semiconductor devices, requiring a substantial amount of resources. Light sources are no exception to this. If the device performance is unknown until the back-end processing is almost completed, potential resources might already be wasted up to this point. This is the case for edge-emitting devices, since the mirrors forming the laser cavity are only achieved upon cleaving the sample. Here lies the appeal of surface emitting devices to industry and for volume manufacturing. There, testing on VCSELs is regularly done at different points in the manufacturing cycle, e.g., after epitaxial growth and wafer processing, at the wafer level [220]. Measurements of the LIV characteristics, emission spectra and optical beam shape can be performed this way. Not only does it save costs for flawed devices, it also allows to quickly react to variations in the manufacturing process, enabling prompt trouble shooting, yield control and guaranteeing compliance to data sheet values.

The most prominent and well established class of vertically emitting semiconductor lasers are VCSELs (see section 5.2.3). With the first prototype realized in 1979 [241], they now constitute a multibillion-dollar global industry [220]. The commercial interest for VCSELs is driven by the growing demand for low-cost data communication, applications in optical sensing and imaging for consumer electronics (facial recognition in the iPhone X), the automotive industry (light detection and ranging (lidar)) and other industrial markets [220]. Commercial VCSELs are emitting in a wavelength range of 650 nm to 1500 nm and are mostly manufactured on GaAs (600-1300 nm) and InP (1300-1800 nm) substrates, employing direct bandgap III-V semiconductors for the optical transition [220]. At longer and shorter wavelengths, they are still at an experimental stage of development, with GaSb-based buried tunnel junction-VCSELs covering the spectral region from 2.7 µm to 4 µm, either employing type-I GaInAsSb/AlGaInAsSb multiple-QW [242, 219] or non-cascaded type-II multiple-QW active regions [221]. Furthermore, a microelectromechanical system (MEMS)-tunable device with a tuning range of 70 nm has been demonstrated at 3.35 µm with a type-I AlGaInAsSb optically pumped gain region and a suspended ZnSe/ThF_4 top mirror [243].

Removing the top mirror from a VCSEL and replacing it by an external component

Die approbierte gedruckte Originalversion dieser Dissertation ist an der TU Wien Bibliothek verfügbar.
The approved original version of this doctoral thesis is available in print at TU Wien Bibliothek.
TU Bibliothek WIEN Your knowledge hub

leads to another vertically emitting device class, the vertical external cavity surface emitting laser (VECSEL). These commonly optically pumped semiconductor lasers, achieve multi-watt level optical output powers while maintaining high beam quality, with applications spanning laser cooling, telecommunications and spectroscopy among others [244]. While these devices often suffer from significant heat accumulation in the active region due to the optical pumping, this issue is addressed in the membrane external cavity surface emitting laser (MECSEL) [245], which sandwiches the very thin semiconductor gain membrane between two transparent heat spreaders, for example made of diamond.

Edge emitting ICLs based on GaSb are typically operating in cw mode at room-temperature and above [59], and single mode devices are readily available between 2.8 µm and 6.5 µm [10]. In contrast, before the publication discussed in this chapter [180], vertical light emission from interband cascade gain material had been restricted to low duty-cycles [217, 202] or below room temperature operation [221]. A VCSEL based on a single active stage employing type-II QWs was reported to work in cw mode at 4 µm up to -7 °C [221], while devices based on type-I QWs at 3 µm reached cw operating temperatures of up to 5 °C [242].

In retrospect, reaching cw emission at room temperature turned out to be a neck-and-neck race between ring ICLs and interband cascade VCSELs. After a VCSEL based on two spatially separated active regions, employing five ICL periods was reported to work in cw at a wavelength of 3.35 µm up to a temperature of 18.5 °C in 2019 [246], the ring ICLs realized within the scope of this thesis reached room temperature with a maximum operating temperature of 38 °C and were submitted for publication in November 2019 [180]. Now only realizing in retrospect, it seems that the results on both of these devices were reported at the same conference - CLEO Europe in Munich, June 2019. Shortly afterwards, a structurally identical VCSEL was reported to lase up to a temperature of 26 °C, showing a threshold current of 5 mA and a maximum optical output power of around 47 µW at 20 °C [243].

5.4 Device fabrication

The device concept of ring ICLs prior to this thesis was not new, with the first experimentally realized devices being reported in 2017 by Holzbauer et al. [202]. However, this first generation of ring devices was limited to operation at low duty-cycles. Hence, a primary goal was to enhance the device performance in a way that would enable vertical light emission in cw mode at room temperature, to increase the practicability of employing ring ICLs for spectroscopic applications.

Die approbierte gedruckte Originalversion dieser Dissertation ist an der TU Wien Bibliothek verfügbar.
The approved original version of this doctoral thesis is available in print at TU Wien Bibliothek.
TU WIEN Bibliothek Your knowledge hub

This section will deal with the device fabrication, which was a major factor in achieving the performance improvements. The most important changes, that were implemented, are an optimized dry etching procedure, subsequent wet-etchant based smoothing of the sidewalls, and epi-side down mounting.

The early stages of the work done on this new generation of ring ICLs coincided with the move of the used cleanroom facilities to a new location. This included the acquisition of a new inductively coupled plasma (ICP) reactive ion etching (RIE) machine. Hence, the process parameters for the dry etching step, which in this machine is performed in a Cl/Ar-chemistry, had to be adjusted accordingly. The former process, relying on $SiCl_4$/Ar-chemistry resulted in a negative slope of the etched sidewalls. The new process yields vertical slightly positively sloped sidewalls. Results of these two dry etching processes, performed on ICL material, are shown as SEM images in Fig. 5.8 for comparison. The imaged structures feature etched ring waveguides, a SiN passivation layer, etched grating on top of the waveguide and Ti/Au top contacts. While the left image depicts a cleaved edge of the sample through the ring waveguide, which is the reason the softer Au contact that ripped off during cleaving is overhanging in front, the right side is a FIB cut, with leftover material, that was not completely milled, in front of the waveguide. The process is used for the definition of the waveguide and the etching of the grating structure, thus, it is one of the most crucial steps within the entire ICL fabrication process. The importance is not limited to the fabrication of substrate-emitting rings, but applies to all ICL waveguides, such as ridges.

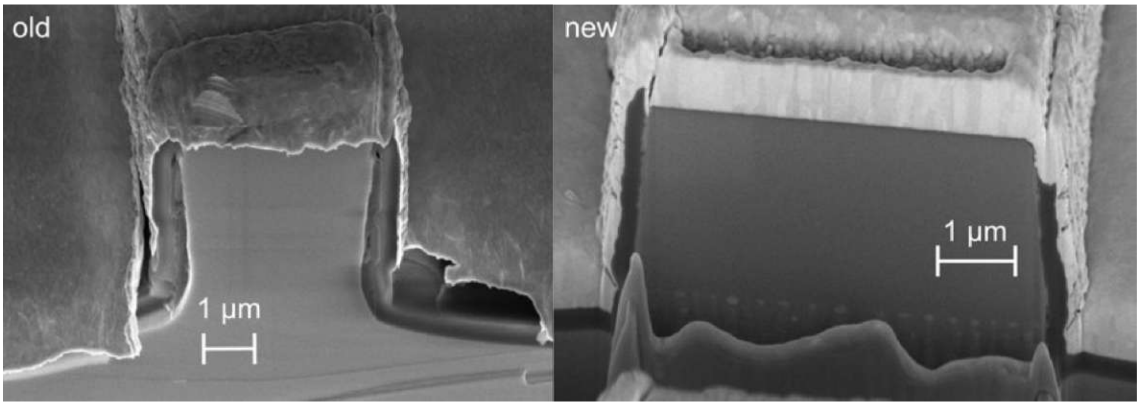

Figure 5.8: SEM images of etched ICL structures. The result of the previously used etching recipe ($SiCl_4$/Ar) is shown on the left side. On the right side a focussed ion beam (FIB) cut through an ICL ridge defined using the newly developed Cl/Ar-recipe is depicted.

Especially in the case of narrow ridge devices, surface roughness can induce significant waveguide losses. To further smoothen the surface after the mostly physical

Die approbierte gedruckte Originalversion dieser Dissertation ist an der TU Wien Bibliothek verfügbar.
The approved original version of this doctoral thesis is available in print at TU Wien Bibliothek.

etching process performed in the RIE system, additional chemical surface treatments were investigated for their suitability to reduce surface inhomogeneities. The tests comprised dips in wet etchant compositions containing phosphoric acid (H_3PO_4), KOH and two different compositions containing citric acid ($C_6H_8O_7$), which are listed below:

(A) $H_3PO_4 : H_2O_2 : H_2O = 3\text{ ml} : 2\text{ ml} : 40\text{ ml}$

(B) KOH (30%)

(C) $C_6H_8O_7 : H_3PO_4 : H_2O_2 : H_2O = 18\text{ g} : 2\text{ ml} : 2\text{ ml} : 39\text{ ml}$

(D) $C_6H_8O_7 : H_3PO_4 : H_2O_2 : H_2O = 9\text{ g} : 2\text{ ml} : 3.5\text{ ml} : 25\text{ ml}$

The results of these tests are shown in Fig. 5.9, where the SEM images of various samples are pictured. Whereas dipping in the phosphoric acid-based mixture (A) and the second composition containing citric acid (D) showed promising results, dipping in KOH (B) showed significant selectivity when etching the individual layers of the ICL structure, especially looking at the upper cladding layer (where the grating is etched into). The surface roughness greatly influenced the performance of the tested devices, which can be seen in a set of ridge devices with different widths of 5, 6 and 7 µm. The optical mode guided in the smallest ridge (for a lasing wavelength around 4.45 µm) will experience the highest losses due to sidewall roughness. Hence, the point where the gain equals the losses and lasing can start will be met only at higher gain, associated with a higher lasing threshold. LIV characteristics of the three devices are shown in Fig. 5.10. With increasing waveguide width the losses induced by sidewall roughness scattering are reduced, which manifests in a lower threshold current and higher optical output power. Moreover, higher operating temperatures can be reached. While the 5 µm-wide ridge lased only at 14 °C and below, the 6 µm-wide one lased up to 16 °C and the 7 µm-wide one up to 18 °C. Clearly, KOH is a poor choice for a wet etching dip meant to decrease surface roughness, as it selectively etches half of the superlattice layers.

For the first used composition containing citric acid (C), remnants of the etchant could be observed on the surface, visible as small white dots. In addition, a faster etch rate for the layers of the active region of the ICL structure, lead to a visible step. In comparison the changed composition (D) resulted in a very smooth surface without the aforementioned white remnants. The wet etching is extremely sensitive to the exact conditions, i.e., the temperature (which for these experiments was not stabilized, but they were simply performed under ambient conditions) and used composition, and not moving the sample while submerged in the solution was observed to lead to more homogeneous results.

Die approbierte gedruckte Originalversion dieser Dissertation ist an der TU Wien Bibliothek verfügbar.
The approved original version of this doctoral thesis is available in print at TU Wien Bibliothek.
TU WIEN Bibliothek Your knowledge hub

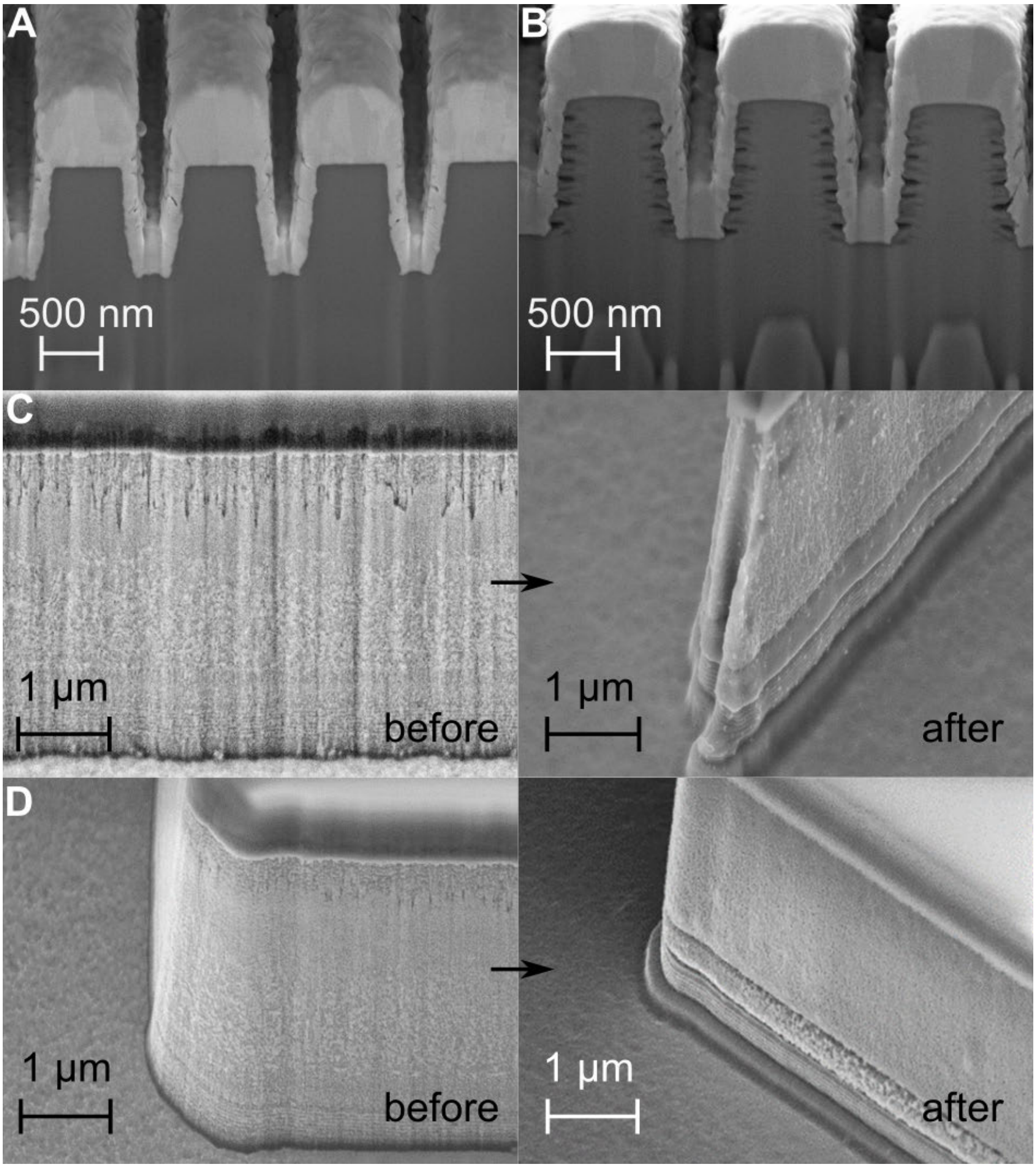

Figure 5.9: SEM pictures of the different smoothing etch results. An etched grating structure after a full ring ICL process run with Ti/Au top contacts **A:** treated with the H_3PO_4-based mixture and **B:** KOH as smoothing etchant. The structures were revealed by FIB cuts through the ring waveguides. **C:** RIE etched ICL structures before and after treating the surface with a composition containing citric acid. The RIE etching is stopped directly in the lower GaSb SCL below the active region. The layers of the active region between the two GaSb SCLs is etched faster, resulting in a step. In, addition white remnants are visible on the surface. **D:** Modification of the composition of the citric acid mixture resulted in a smoother sidewall profile.

Die approbierte gedruckte Originalversion dieser Dissertation ist an der TU Wien Bibliothek verfügbar.
The approved original version of this doctoral thesis is available in print at TU Wien Bibliothek.
TU WIEN Bibliothek Your knowledge hub

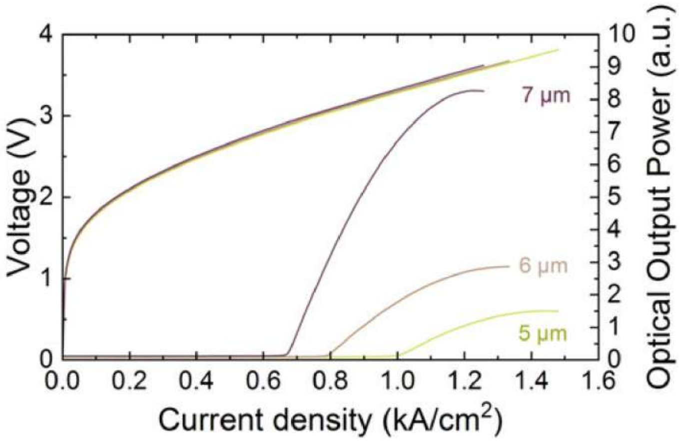

Figure 5.10: Performance comparison of three ICL ridges, that were dipped in KOH following the RIE etching of the waveguides. Due to the losses induced by considerable sidewall roughness, the broadest devices (7 µm) outperform the narrower ones (5 and 6 µm).

5.4.1 Ring interband cascade laser fabrication

In the following, the full fabrication process for ring ICLs will be discussed, stating all individual processing steps. Schematics of all fabrication stages are shown in Fig. 5.11 for reference. As a first step of the fabrication process, the 10 mm x 11.5 mm sample surface is cleaned (A) by means of ultrasound in acetone and isopropyl alcohol to remove the cleaving dust and oxygen plasma to eliminate organic residues. The asymmetric size of the samples is chosen in order to keep track of the crystal orientation during the fabrication process. The long side is oriented parallel to the major flat. The ridges, which are processed together with the ring ICLs for performance comparison are then oriented parallel to the major flat, achieving good cleaving of the facets for light extraction.

After cleaning, a layer of Si_3N_4 is deposited as a hardmask (B) using plasma enhanced chemical vapor deposition (PECVD). The thickness of this layer is selected according to the desired etching depth of the waveguide, which depends on the grown epitaxial design. It therefore differs for varying wavelengths and other purposes, e.g., if a doped bottom contact is grown that needs to be hit for contact deposition. The desired waveguide geometry is then defined using optical contact lithography (C). Extra care should be taken during this first lithography step, because any inhomogeneities in the resist defining the waveguide geometry will ultimately be transferred to the waveguide itself, posing a potential risk for the introduction of waveguide losses. Subsequently, the hard mask is etched (D) by an ICP RIE process in CHF_3/O_2-chemistry. This leads to straight and vertical sidewalls of the hardmask. The photoresist is subsequently removed (E) using

Die approbierte gedruckte Originalversion dieser Dissertation ist an der TU Wien Bibliothek verfügbar.
The approved original version of this doctoral thesis is available in print at TU Wien Bibliothek.

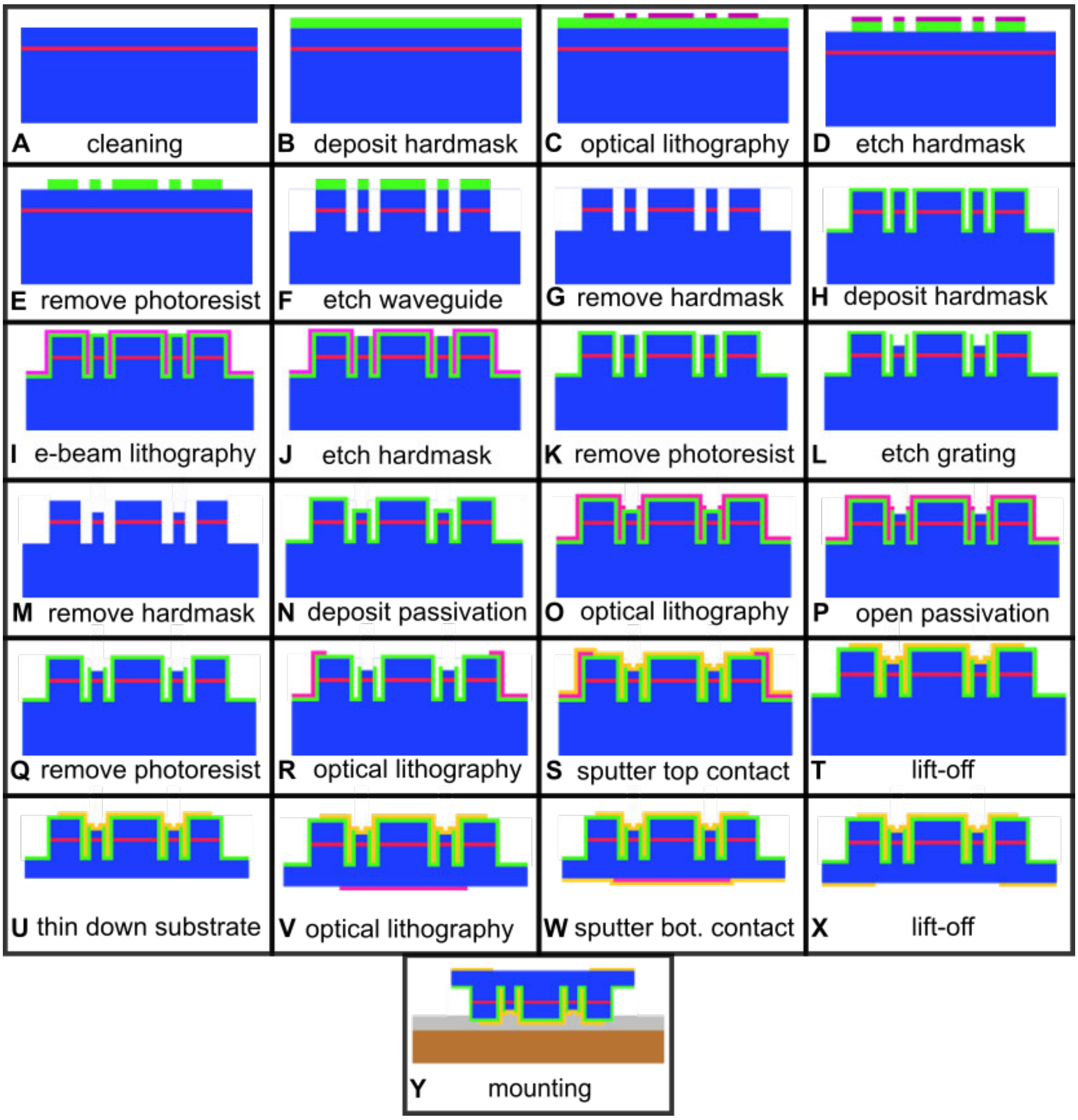

Figure 5.11: a: The multitude of individual processing steps required for the manufacturing of ring ICLs is depicted schematically. The ring waveguide is defined in a double trench geometry, with a trench width of 10 µm. The schematic images represent cuts along the diameter of one ring, with the active region symbolized by the red area. Si_3N_4 is imaged in light green, photoresist in purple, and the metallization in gold. All fabrication steps are performed in a cleanroom, with the exception of the thinning and polishing of the substrate (U) and the cleaving and mounting of the finished ring devices (Y).

Die approbierte gedruckte Originalversion dieser Dissertation ist an der TU Wien Bibliothek verfügbar.
The approved original version of this doctoral thesis is available in print at TU Wien Bibliothek.

O_2-plasma and dissolving it in acetone. Then, the waveguide etch is performed (F) in a Cl/Ar-chemistry with the ICP-RIE process discussed above. The etching is stopped in the GaSb SCL below the active region. Subsequently, an appropriate wet etch (phosphoric-acid or citric-acid based) is performed in order to smoothen the sidewalls and reduce surface-roughness induced absorption losses. Afterwards, the Si_3N_4 hardmask is completely removed (G) by RIE in SF_6-chemistry.

After the definition of the waveguide geometry, the fabrication of the second order DFB grating is performed. Hence, another Si_3N_4-hardmask is deposited (H) with appropriate thickness depending on the desired etching depth of the grating structure. Due to its sub-µm size the second order DFB grating is defined via electron-beam lithography (I) (details on the alignment procedure can be found in [1]). The fabrication then proceeds using the same fabrication steps as for the waveguide (etching of hardmask with CHF_3 (J), removal of the photoresist (K), etching of the upper cladding layer with Cl/Ar (L), subsequent smoothing of the surface and removal of the remaining hardmask with SF_6 (M)). We use a grating etch depth of ∼1 µm into the upper cladding layer. The grating period is selected depending on the desired wavelength.

For electrical passivation a 250 nm Si_3N_4 layer is deposited on the entire sample (N) and selectively removed (O-Q) from a contact window on top of the ring (e.g., 3.9 µm wide for a 4 µm wide waveguide). A two-step process (P) (CHF_3 and SF_6 plasma anisotropic and isotropic, respectively) allows to efficiently remove the dielectric layer from within the grating grooves. The devices were metallized via sputtering of 10 nm/650 nm Ti/Au layers (S), defining the desired contact structure via a lift-off process (R, T). To facilitate single device cleaving and reduce the attenuation of the extracted radiation, the GaSb substrate is thinned down (U) to a thickness of roughly ∼150 µm and consecutively polished using a 0.1 µm-diamond lapping film to reduce scattering of the emitted light at the substrate surface. Ti/Au bottom contacts (10 nm/200 nm) are sputtered on the backside (W) leaving an uncovered circular area with a diameter of 1.2 mm for the substrate emission (V, X). The required lift-off lithography needs to be aligned to the fabricated structures on the epi-side by measuring the distances from the sample edges to the structures, since the GaSb substrate is not transparent in the visible spectral range.

A SEM image of a finished device is shown in Fig. 5.12. The top right inset shows a FIB cut through the grating, revealing its periodic structure. The grooves are not fully filled with gold, which is due to the directional sputtering of the metallization.

The previous generation of ring ICLs suffered from insufficient thermal dissipation. The epi-side up mounting of the devices is suspected to have been the primary

Die approbierte gedruckte Originalversion dieser Dissertation ist an der TU Wien Bibliothek verfügbar.
The approved original version of this doctoral thesis is available in print at TU Wien Bibliothek.

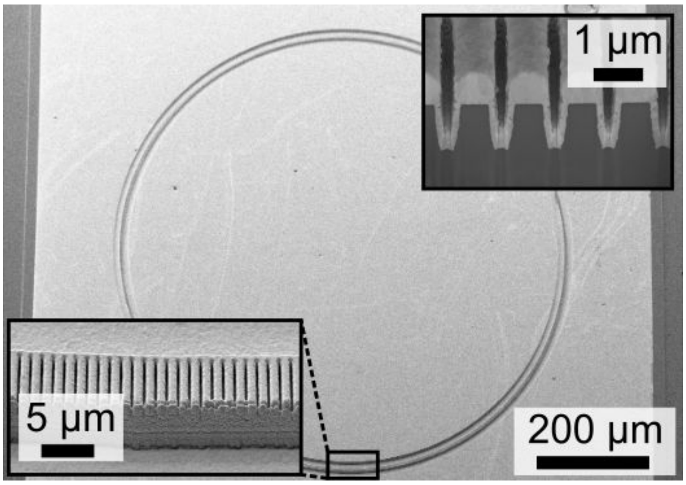

Figure 5.12: SEM images of a fabricated ring ICL with a diameter of ∼ 800 µm. The metallized second order DFB grating, etched into the upper superlattice cladding and covered with Ti/Au is depicted in a close-up on the bottom left corner of the figure. A FIB cut through the middle of the waveguide shows the etched grating structure in the top right inset. Figure taken from [180].

cause of the limitation to pulsed operation. As the ring devices are designed for substrate emission, a multiple mm-wide hole in a copper heat sink was used to allow for collection of the emitted light. This is schematically shown in Fig. 5.13. The devices above this drilled hole in the middle of the mounted chip are on both sides surrounded by air, which is known to be a poor heat conductor.

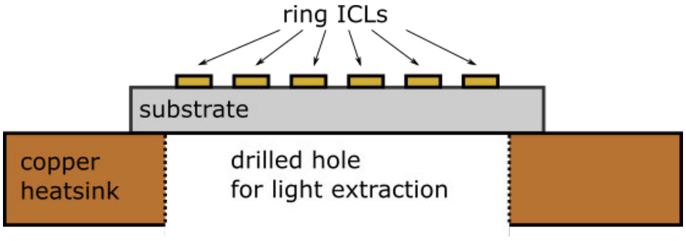

Figure 5.13: Epi-side up mounting scheme for substrate emission from ring ICLs. In order to avoid blocking of the light due to the heat sink on the substrate side of the devices, a hole in the heat sink needs to be realized, resulting in poor thermal dissipation.

To mitigate this shortcoming, epi-side down mounting was established for the ring ICLs that are reported in [180]. First, individual rings are cleaved from the processed chip. Then each ring is picked up via a vacuum tip and placed epi-side down on a copper plate with a thin layer of indium solder (see Fig. 5.11Y). The double trench geometry of the waveguide is essential for the epi-down mounting procedure. Since a large area in the middle of the ring and outside of it has the same height, the applied force during the mounting is distributed over a large area, reducing the pressure on

Die approbierte gedruckte Originalversion dieser Dissertation ist an der TU Wien Bibliothek verfügbar.
The approved original version of this doctoral thesis is available in print at TU Wien Bibliothek.

the waveguide itself and additionally increasing the area that is in contact with the heatsink, for improved thermal dissipation. A hotplate is used to heat up the indium to 150 °C, melting it in order to bond it to the sputtered gold of the top contact of the ring ICL. Although the etched grating grooves are not fully filled with gold, this does not pose an issue when using a soft solder like indium, as they get filled up during the soldering process in an epi-side down configuration. Epi-side down mounting allows for superior heat extraction compared to epi-up soldering, as the active region, where the heat is created during operation, is in close proximity to the heat sink. In Fig. 5.14 an epi-side down mounted ring (A) and the water-cooled stage (B) for optical characterization of the ring ICLs can be seen.

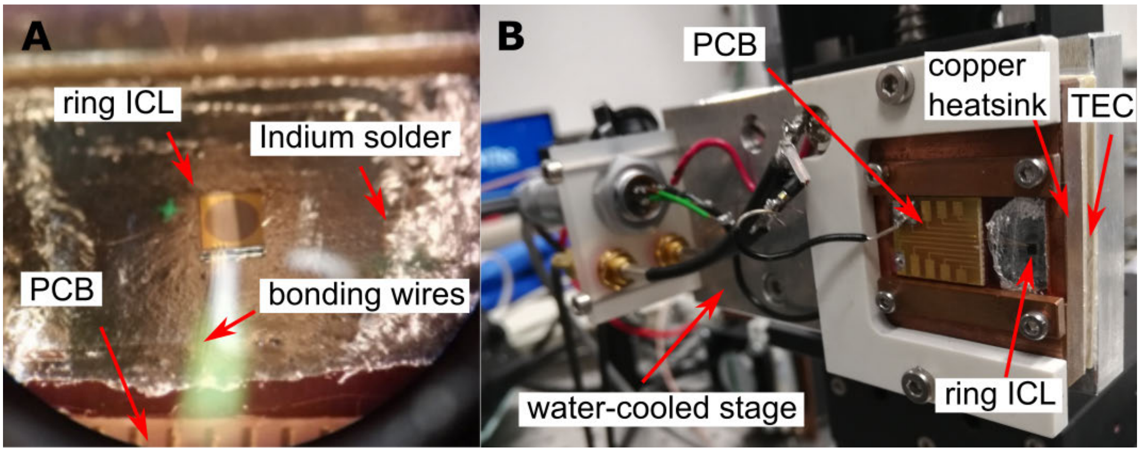

Figure 5.14: A: Epi-side down mounted ring ICL on top of the indium solder on the copper heatsink. Bonding wires are connecting the back contact of the ring with a printed circuit board (PCB) for electrical connection. The circular opening in the backside contact for light extraction can be seen. **B:** Copper heatsink with mounted device attached to the water-cooled stage with thermoelectric cooler (TEC) for temperature control and electric contacts for device characterization.

5.4.2 Geometric considerations

Besides the improved fabrication scheme, the waveguide geometry was changed from the first generation of devices. Since single mode emission as well as cw operation are important requirements for practicable sensing solutions, another shortcoming of the first generation was tackled. These devices were exhibiting a second mode in their spectra when operated above 20 °C [202]. This additional mode was attributed to multiple lateral modes that could co-exist in the broad ridge with a width of 10 µm, compared to the lasing wavelength of 3.75 µm. In order to suppress lasing of higher order lateral modes, the width of the waveguide is reduced to 4 µm [247]. In contrast to VCSELs, that emit limited maximum output power due to their relatively small

TU WIEN Bibliothek Your knowledge hub
Die approbierte gedruckte Originalversion dieser Dissertation ist an der TU Wien Bibliothek verfügbar.
The approved original version of this doctoral thesis is available in print at TU Wien Bibliothek.

gain volume, the output power of ring ICLs scales with the width and diameter of the chosen waveguide [202]. Hence, this modification would result in a reduction of the optical output power. To balance the smaller gain area due to the reduction in width, the outer ring diameter was almost doubled from 400 µm to ∼799 µm. This yields an active volume that is comparable to a 2.5 mm long ridge device with the same waveguide width.

In order to further investigate the suitability of these choices to suppress parasitic higher order lateral modes, optical simulations of the ring waveguide were performed using COMSOL [248]. Varying waveguide widths between 3 µm and 12 µm were simulated and the waveguide losses were deduced from the imaginary part of the effective refractive index yielded by the simulation. The results for a wavelength of ∼3.8 µm are given in Fig. 5.15. Waveguides with larger widths can support an

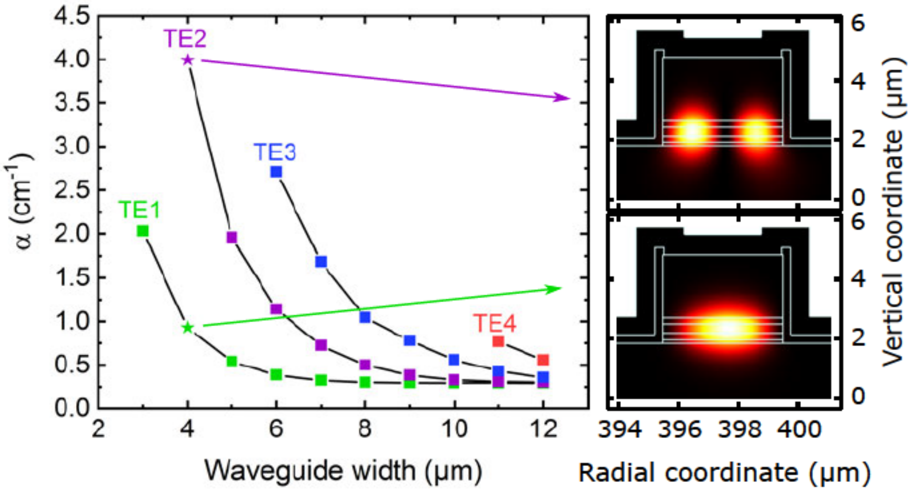

Figure 5.15: Simulated waveguide losses depending on the waveguide width for a wavelength of 3.8 µm and an outer ring diameter of ∼800 µm. The two images on the right depict the profile of the time-averaged power flow for the fundamental and second order radial mode for a 4 µm-wide ring ICL waveguide. Figure adapted from [180].

increasing amount of different lateral modes. While at a width of 3 µm only the fundamental lateral mode is guided within the waveguide, above 10 µm up to four modes can in principle be present at the same time, that show similar waveguide losses. In general, the losses for all modes increase with decreasing waveguide width, the difference is at which width this behavior sets in. For the fundamental mode the losses start to rise below a waveguide width of 5 µm, while for the second order lateral mode this is already observed for an 8 µm wide waveguide. For the experimentally realized width of 4 µm the losses serve as a discriminator between the higher order lateral modes and the fundamental mode, as the losses for the second order mode

Die approbierte gedruckte Originalversion dieser Dissertation ist an der TU Wien Bibliothek verfügbar.
The approved original version of this doctoral thesis is available in print at TU Wien Bibliothek.

are more than four times as high as for the fundamental mode.

The profiles of the time-averaged power flow are shown on the right side of Fig. 5.15 for the two modes that can be supported in a 4 µm-wide waveguide. The two antinodes of the second-order lateral mode are situated farther towards the outside of the waveguide, with a node in the middle. Thus, the higher order mode suffers greater from surface roughness induced losses, that are unavoidably introduced during device fabrication, i.e., the sidewall etching and interfaces of different layers on top of the surface (SiN electric passivation, Ti/Au top contact). These losses are additive, hence, contributing to the selectivity in favor of the fundamental mode. In general, a further reduction of the waveguide width would completely eradicate the possibility of occurring higher order radial modes, but at the expense of higher losses for the fundamental mode. As this would result in a higher lasing threshold, or if taken to an extreme even prevent lasing operation at all, 4 µm appears to be a reasonable choice.

5.5 Performance of ring interband cascade lasers

Although different MBE grown ICL designs were fabricated in a ring geometry during the course of this thesis, the following discussion will be limited to the best achieved results, which were published in [180]. The active region of that particular ICL features six stages. The W-QW targeting a lasing wavelength of 3.8 µm, is composed of 2.50 nm AlSb/1.90 nm InAs/2.40 nm $Ga_{0.68}In_{0.32}Sb$/1.47 nm InAs/ 1.00 nm AlSb. The GaSb SCLs encompassing the active region are 200 nm thick and the upper and lower InAs/AlSb superlattice claddings have thicknesses of 2100 nm and 3500 nm, respectively. All layers were realized by MBE growth on a single-side polished n-GaSb (100) substrate.

The geometry was chosen according to the discussion in section 5.4.2 (outer ring diameter D=799 µm, waveguide width w=4 µm). The fabrication proceeded as described in section 5.4.1 with an etch depth of 3 µm for the waveguide etch. The phosphoric acid-based wet etch was chosen for the chemical treatment of the sidewalls. The second-order DFB grating featured an etch depth of 910 nm into the upper cladding, an effective grating duty-cycle of $\sigma \sim 60\%$ measured at half the etch depth and the middle of the waveguide, and a grating period of $\Lambda_g = 1.41$ µm. Here, the grating duty-cycle quantifies the fraction of the etched groove with respect to the grating period Λ_g.

For the measurement of the emitted optical output power, a power meter (Thorlabs S401C) is put in close proximity of the substrate-side of the laser. All subse-

Die approbierte gedruckte Originalversion dieser Dissertation ist an der TU Wien Bibliothek verfügbar.
The approved original version of this doctoral thesis is available in print at TU Wien Bibliothek.
TU WIEN Bibliothek Your knowledge hub

quently reported measurements are performed in cw operation. The LIV characteristics of the device are shown in Fig. 5.16 with operating temperatures from 14 °C to a maximum of 38 °C with a step size of 2 °C. Since the device is not packaged under

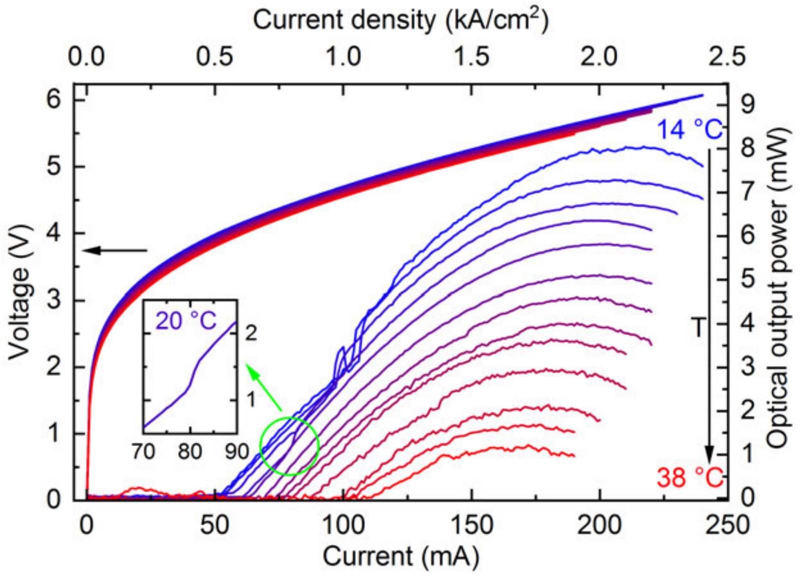

Figure 5.16: LIV characteristics of the ring ICL at different operating temperatures from 14 °C to 38 °C in cw operation. The light intensity of the device emitting around 3.8 µm is measured with a power meter. The inset shows a jump in optical output power at 20 °C. Figure taken from [180].

nitrogen atmosphere or placed under vacuum, i.e., in a cryostat, but operated under ambient conditions, at lower temperatures water would start to condense on the sample surface. The maximum optical output power amounted to 8 mW at 14 °C and 6.4 mW at 20 °C. The lasing threshold is observed at 60 mA, which corresponds to a threshold current density of 0.60 kA/cm^2. The green circle in Fig. 5.16 marks a small jump in the optical output power at 20 °C, which is shown in the magnified inset. The jump at I=81 mA, separates two distinct operating regimes, that are explored in the subsequent spectral characterization.

The threshold current densities J_{th} and slope efficiencies η are obtained from the measured LIVs and the characteristic temperatures T_0 and T_1 are extracted from exponential fits to these values according to Eq. 4.1 for J_{th} and $\eta = \eta_0 \exp(-T/T_1)$ for η. Data and fits are displayed in Fig. 5.17, resulting in characteristic temperatures of T_0=30 K and T_1=22 K. In comparison, state-of-the-art broad area ICLs exhibit T_0 values of 45-55 K for emission wavelengths between 3 and 4 µm [59]. The higher thermal load due to cw operation results in a lower T_0 value. At 20 °C, the values for η before and after the jump in optical output power, are 59 mW/A and 70 mW/A. Thus, this point and values obtained at even lower temperatures are

Die approbierte gedruckte Originalversion dieser Dissertation ist an der TU Wien Bibliothek verfügbar.
The approved original version of this doctoral thesis is available in print at TU Wien Bibliothek.

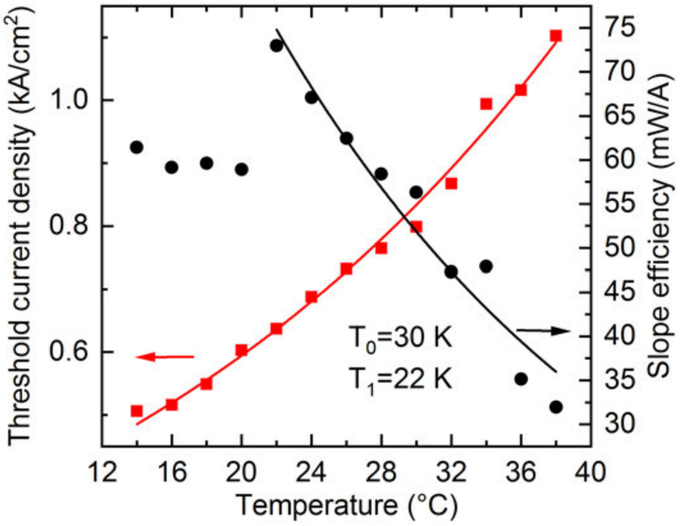

Figure 5.17: Measured threshold current densities (red squares) and differential slope efficiencies (black circles) at different operating temperatures between 14 and 38 °C. Exponential fits (red and black lines) to the data yield characteristic temperatures of T_0=30 K and T_1=22 K.

excluded from the fit for T_1. From the differential slope efficiency of 73 mW/A at 22 °C, an EDQE of 23 % is obtained. Even when comparing this cw value of the slope efficiency to the reported pulsed value of ~52 mW/A at 20 °C for a 15-stage interband cascade VCSEL [217], the slope efficiency is higher. In general, when going from pulsed to cw operation the inevitable increased thermal load is expected to result in a performance degradation. Even when assuming optimal heat extraction, this will at best result in the same slope efficiency as in pulsed operation. A very rough estimation of the slope efficiency of the cw VCSEL in [243] yields a maximum value of 50 mW/A at 20 °C from the data provided in Fig. 7. Hence, the ring ICL performs comparably well in terms of efficiency.

To characterize the emitted light spectrally, a BF$_2$ (f=50 mm) lens is used for collimation. The light is directed towards a Bruker Equinox 55 Fourier transform infrared spectrometer (FTIR) spectrometer, and measured by the internal wide-range deuterated triglycine sulfate (DTGS) detector. The standard rapid-scan mode of the FTIR is sufficient for these measurements. The measured spectra for varying temperatures from 15 °C to 35 °C are depicted in Fig. 5.18. At an operating current of I=140 mA single-mode operation is achieved over the entire explored temperature range, at a lasing wavelength of ~3.84 µm and a spectral range of 7 nm. The wavelength shift is caused by a temperature induced change of the refractive index, which for this device relates to a linear temperature tuning coefficient of $\Delta\lambda/\Delta T$= 0.37 nm/K ($\Delta\nu/\Delta T$=-0.25 cm^{-1}/K). In general, this tuning mechanism happens on a rather long timescale, also depending on the employed heat sink geometry

Die approbierte gedruckte Originalversion dieser Dissertation ist an der TU Wien Bibliothek verfügbar.
The approved original version of this doctoral thesis is available in print at TU Wien Bibliothek.
TU Bibliothek WIEN Your knowledge hub

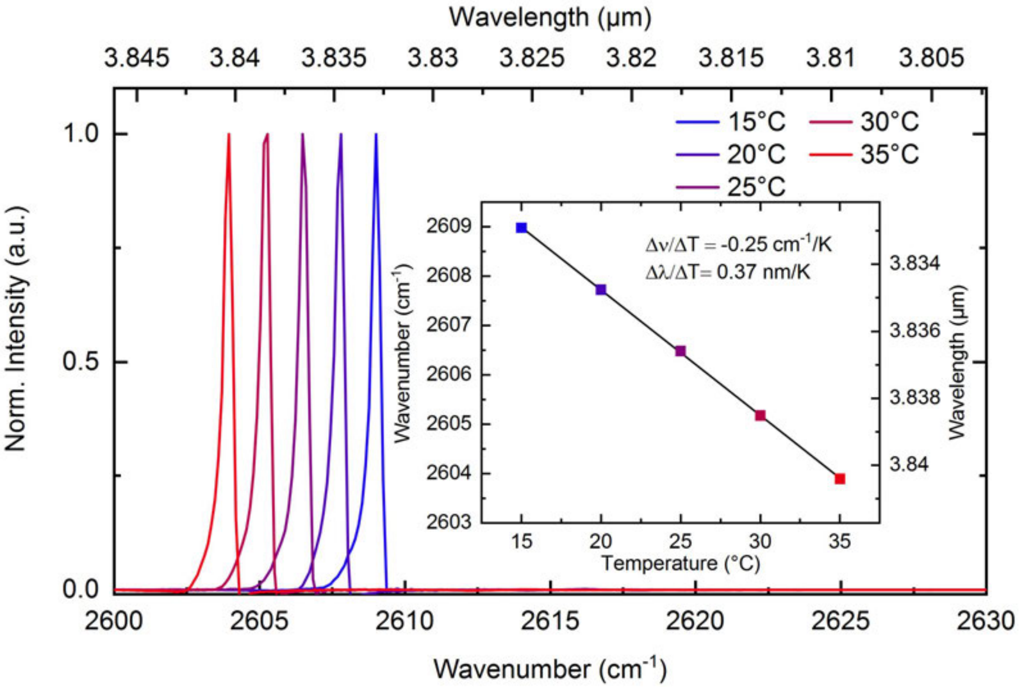

Figure 5.18: Normalized spectral emission of the ring ICL measured at varying operating temperatures and constant current of I=140 mA. The temperature tuning is shown in the inset, resulting in an extracted linear temperature tuning coefficient of $\Delta\lambda/\Delta T$=0.37 nm/K, which corresponds to $\Delta\nu/\Delta T$=-0.25 cm^{-1}/K. Figure taken from [180].

and temperature control. In comparison, tuning the wavelength by modifying the driving current, is a faster possibility, and, hence, an essential method for spectroscopic applications. Current tuning is investigated for an operating temperature of 20 °C from the lasing threshold at I=60 mA up to a maximum injected current of 220 mA with a step size of 1.5 mA, which is shown in Fig. 5.19. The device exhibits single-mode emission over the entire operating range, apart from a limited transition region around 81 mA, where the laser shows a spectral jump from ν=2643 cm^{-1} to 2613 cm^{-1}. This coincides with the jump in optical output power, shown in Fig. 5.16. Thus it is likely that the gain differs for these different wavelengths, resulting in the changing output power. The second jump in wavelength at 180 mA, however, is not connected to a change in the output power. It seems plausible, that because the wavelengths are in close proximity to each other, the value of the gain is comparable. The jumps in optical output power occurring at lower temperatures (14-18 °C), which can be seen in Fig. 5.16 around 100 mA, are possibly attributed to other mode jumps, although they were not studied experimentally.

The linear current tuning coefficient is extracted for all three wavelength regions at 20 °C, which is shown in Fig. 5.20. Starting from the lowest current region, the

Die approbierte gedruckte Originalversion dieser Dissertation ist an der TU Wien Bibliothek verfügbar.
The approved original version of this doctoral thesis is available in print at TU Wien Bibliothek.
TU WIEN Bibliothek Your knowledge hub

Die approbierte gedruckte Originalversion dieser Dissertation ist an der TU Wien Bibliothek verfügbar.
The approved original version of this doctoral thesis is available in print at TU Wien Bibliothek.

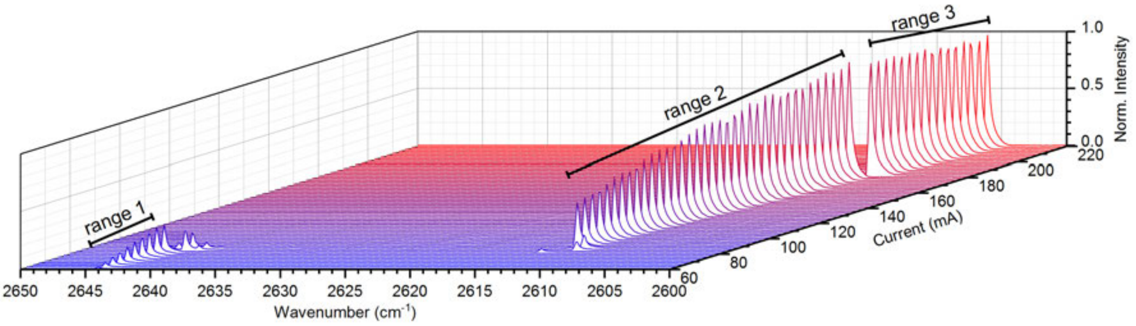

Figure 5.19: Current tuning of the ring ICL at an operating temperature of 20 °C between 60 and 220 mA. Three distinct ranges are identified, which are separated by two jumps in the wavenumber of the emitted light. They reproducibly occur around 81 mA and 180 mA. The largest part (range 2) of the operating current range shows continuous tuning, spanning 3.7 cm^{-1} (4.4 nm) from 90 to 180 mA. Figure reproduced from [180].

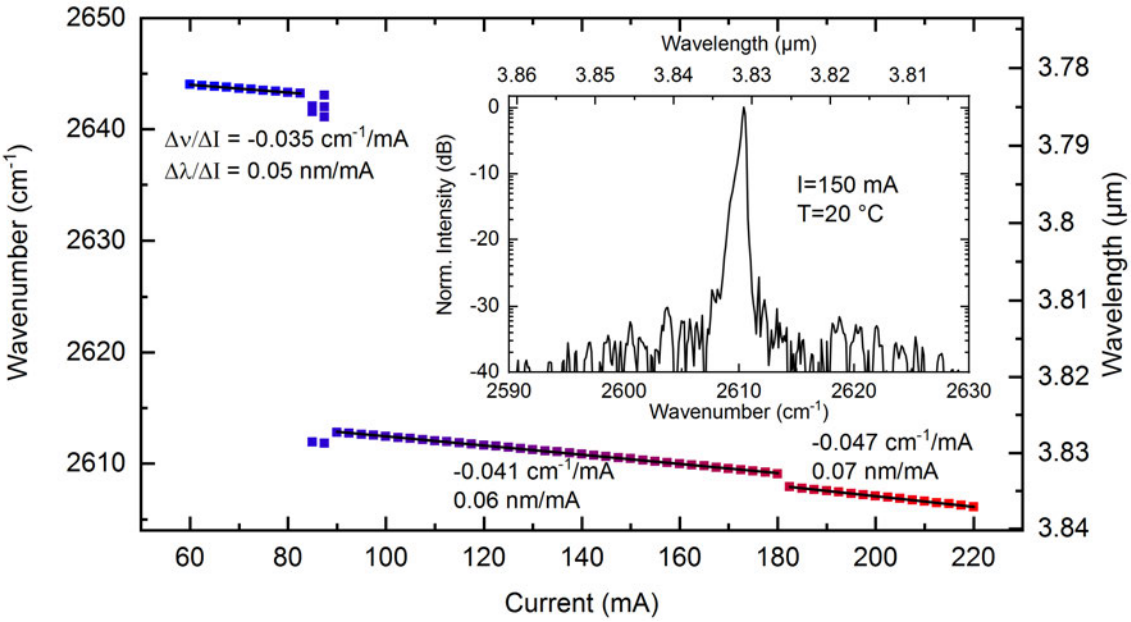

Figure 5.20: Current tuning coefficients for the ring ICL at 20 °C. The emitted spectrum at I=150 mA is presented on a semi-logarithmic scale with a side mode suppression ratio (SMSR)>25 dB. Figure taken from [180]

linear current tuning coefficient increases slightly from 0.05 nm/mA to 0.07 nm/mA ($\Delta\nu/\Delta I$=-0.035 cm^{-1}/mA to -0.047 cm^{-1}/mA).

In an attempt to gain more insight into the different operating regimes of the device, the farfield at currents within each range (I=65 mA, 150 mA and 200 mA) was recorded at 20 °C. The measurements where conducted with an MCT detector mounted on a translational xy-stage, which was placed in a distance of 20 cm to the ring ICL. The intensity is then recorded in a step-wise scan over an area of 76.8 mm x 76.8 mm, using a step size of 0.6 mm. The data is corrected for an intensity loss according to $1/r^2$, with r denoting the distance of the measurement point to the ring, and transformed into angle-dependent values. Since ring lasers show much lower divergence angles compared to their edge-emitting counterparts [240], even without achieving additional focusing by implementing a collimating meta-substrate, using a translational stage instead of a rotational stage is justifiable. The results of the farfield measurement are shown in Fig. 5.21. The farfield pattern is circularly symmetric, as is expected from the device geometry. This is in contrast to the almost Gaussian shaped beam profile reported for interband-cascade VCSELs [217]. The angle under which the maximum light intensity is emitted is determined by the geometry of the waveguide and the grating [249]. The observed inhomogeneities in the intensity distribution can be caused by defects and imperfections arising from the device fabrication, i.e., the etching of the waveguide and the grating. For the lowest current region (range 1 in Fig. 5.19) two rings of the same intensity are observed in the farfield (left side of Fig. 5.21). Recalling the lateral mode distribution of the second higher order mode in Fig. 5.15 could provide an explanation, if, for example, the losses for the fundamental mode due to the grating are higher under these operating conditions. In any case, there is potential for improvement of the grating parameters. However, the farfield remains the same above the first mode

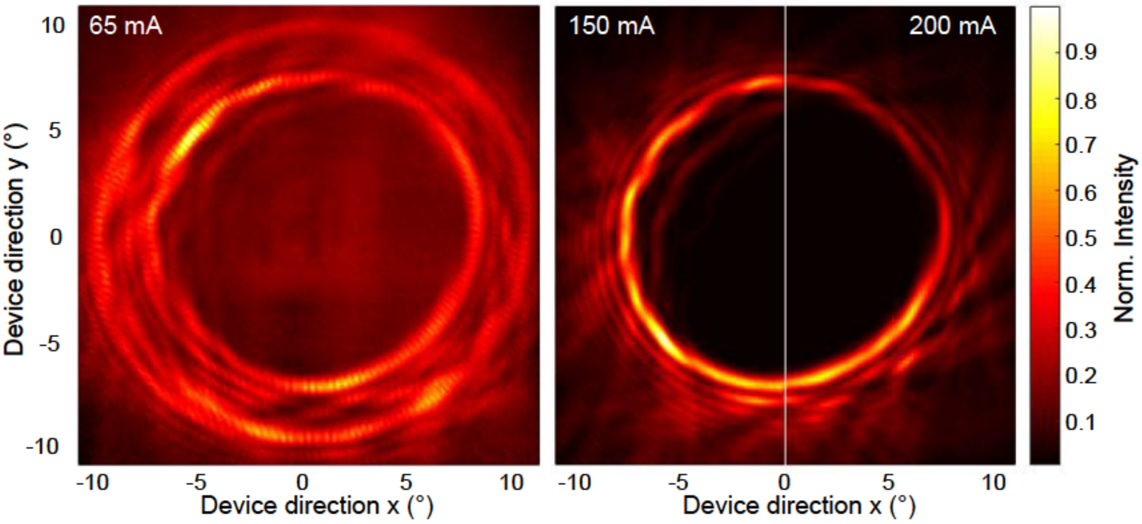

Figure 5.21: Measured farfield of the ring ICL at three different currents to investigate the spectral mode hopping behavior. The measurements at I=65 mA, 150 mA and 200 mA were performed ar 20 °C and normalized individually. Figure adapted from [180].

Die approbierte gedruckte Originalversion dieser Dissertation ist an der TU Wien Bibliothek verfügbar.
The approved original version of this doctoral thesis is available in print at TU Wien Bibliothek.

hop for spectral ranges 2 and 3, shown on the right side. Deliberate modifications of the farfield have been extensively studied in QCLs [239, 240, 250] and show the potential there is for ring ICLs.

Further ongoing work on ring ICLs is dedicated to improving the thermal transport from the devices by implementing electro-plating of µm-thick gold on top of the waveguide after sputtering of the top contact, ensuring that the grating grooves are filled up completely, and an advanced mounting scheme. This is expected to lead to even higher output power and a lower lasing threshold. The devices realized during the course of this thesis were restricted to epi-down mounting using indium as solder due to the low melting temperature. Attempts of using AuSn heat sinks that require much higher temperatures of up to 310 °C resulted in diffusion of the Au from the top contact into the epi-structure. This led to significant current leakage, manifesting in a lowered device resistance and a flatter onset of the voltage visible in the current-voltage characteristics. One way to circumvent this is by integrating a diffusion barrier like nickel or platinum between the adhesion promoting titanium layer and the gold contact. Other possibilities to increase the optical output power would be the MBE growth of the ICL on compensation doped GaSb substrate to reduce the free carrier absorption for the extracted light on its path through the substrate or the deposition of an anti-reflection coating on the substrate surface, that could be realized by depositing a $\lambda/4$ layer of Si_3N_4.

In addition, the reverse statement to what is said at the beginning of this chapter is equally true. In short: no matter how well-performing the ICL epi-structure realized via MBE growth is, an inadequate fabrication scheme can render it useless. Conversely, no matter how well established the fabrication scheme is, if the base material is of poor quality, the final device will still be performing unsatisfactorily, if at all. Depending on the desired wavelength, the active region modifications introduced in chapter 4 can contribute to superior ring ICL performance.

Die approbierte gedruckte Originalversion dieser Dissertation ist an der TU Wien Bibliothek verfügbar.
The approved original version of this doctoral thesis is available in print at TU Wien Bibliothek.

Die approbierte gedruckte Originalversion dieser Dissertation ist an der TU Wien Bibliothek verfügbar.
The approved original version of this doctoral thesis is available in print at TU Wien Bibliothek.

Die approbierte gedruckte Originalversion dieser Dissertation ist an der TU Wien Bibliothek verfügbar.
The approved original version of this doctoral thesis is available in print at TU Wien Bibliothek.
TU WIEN Bibliothek Your knowledge hub

CHAPTER 6

INTERBAND CASDCADE INFRARED PHOTODETECTORS

For a vast variety of applications employing mid-infrared semiconductor lasers for light emission, the detection of light is a crucial requirement. Photodetectors are essential components for spectroscopy, optical communication, and are also imperative for seemingly simple tasks such as laser characterization. Thus, for many applications, an often encountered task is the identification of a suitable detector.

While broad spectral bandwidth and high sensitivity are often sought after performance indicators of a detector, some applications require detectors to work at high frequencies up to several GHz. Therefore, high-speed performance will be the focus of this chapter, which summarizes the work on ICIPs that was done during the course of this thesis. The general working principle and state-of-the-art performance was already discussed in section 3.2. Here, after a section highlighting the underlying motivation for the work on this device class, the realized structures are described, including their active region design and fabrication. Subsequently, the results on some important performance metrics like the dark current and responsivity are discussed. The main focus however, is set on the high-speed properties of these detectors. Finally, two application scenarios currently employing the realized ICIPs will be illuminated, clearly demonstrating the value and potential of this only rather recently emerging detector class.

6.1 Motivation

Emerging areas such as high-precision frequency comb spectroscopy [205, 251], free-space optical communication [252, 253] and lidar [254, 255] demand for high-speed detectors in the mid-infrared. Instead of measuring the round-trip delay of an electromagnetic wave at radio-frequencies, lidar relies on wavelengths in the optical spectrum to estimate the distance to objects. These different distance measurements are then used to reconstruct a 3D point cloud. Employing a shorter wavelength compared to radar offers better resolution for 3D imaging. Dual-comb spectroscopy offers the possibility to detect multiple chemical species over a broad spectral range with high temporal resolution that can even enable the real-time monitoring of chemical reactions [256, 257]. High-speed detectors are essential to detect the multi-heterodyne beatings between individual comblines in the mid-infrared. Moreover, fast detectors have proven to be invaluable tools for frequency comb research, where they are being used to reconstruct the waveform of mode-locked lasers and measure the phase-coherence and timing jitter of frequency combs [204, 258].

Although commercially available MCT detectors offer high sensitivity and wide spectral range, cooling is still often employed to reduce thermal noise. Moreover, long carrier lifetimes and a high dielectric constant result in a frequency response limited to around 1 GHz [259, 260]. Alternatively, photoconductive QWIPs [261] are based on a biased superlattice structure, with an optical transition between a bound electron state in a QW and a quasi-bound state close to resonance with the conduction band edge of the employed barrier. They exhibit very short carrier lifetimes on the order of picoseconds [262]. Hence, they are well suited for high-speed applications, and heterodyne detection was reported up to 110 GHz at 300 K [263]. However, considerable dark current limits their signal-to-noise ratio at elevated temperatures. The QCD, another widely used type of detector, also relies on intersubband transitions for light detection, exhibiting picosecond lifetimes as well. At room temperature, a frequency response up to 21 GHz was recently demonstrated [136]. One disadvantage of QCDs is their narrow spectral bandwidth, arising due to the intersubband nature of the optical transition. It is exactly this limitation, that ignited the work on ICIPs during the course of this thesis to push the research on ICL frequency combs within our group. The broad spectral bandwidth of these detectors allows to characterize ICLs at various wavelengths, eliminating the need to acquire or fabricate QCDs or QWIPs at the desired emission wavelengths.

TU Bibliothek WIEN Your knowledge hub
Die approbierte gedruckte Originalversion dieser Dissertation ist an der TU Wien Bibliothek verfügbar.
The approved original version of this doctoral thesis is available in print at TU Wien Bibliothek.

6.2 Realized devices

In the following, the results on the performance of ICIPs based on a type-II InAs/GaSb superlattice are presented. The goal was to study the limitations of the high-speed performance by employing varying superlattice absorber thicknesses. In addition to the fundamental carrier transport time scales, parasitic electronic components can further limit the detector speed.

6.2.1 Design and growth

All three realized ICIP structures were grown by MBE on a compensation-doped GaSb substrate. This is achieved by Te-doping, which is used to compensate for the intrinsic doping of GaSb resulting in a carrier concentration of $n \leq 5 \times 10^{16}$ cm^{-3}. The low carrier concentration reduces the free carrier absorption in the substrate, benefiting the performance for the chosen device configuration. Since the conductivity of the substrate is significantly reduced by the compensation doping, a 500 nm-thick GaSb bottom contact was grown with a doping of $n = 1 \times 10^{18}$ cm^{-3}. For the active region, the hole absorber was grown first and is thus located closest to the substrate. The devices were illuminated from the substrate side, hence, this resembles the reverse-illumination configuration (see section 3.2). However, since the top is completely metallized, in principle a double-pass geometry is realized. Consequently, current matching of the device is (at least in a first approximation) dispensable. The light is attenuated on its way through the detector from the substrate to the top contact, where it is reflected and travels back. This means that the first absorber stage is passed first by the light showing full intensity and then by the most attenuated light at the very end of its journey through the device. In comparison the last stage is traversed by the light that is mid-way through the device both before and after being reflected. This difference in light intensity in both directions should effectively result in a similar number of photons being absorbed in each stage.

The absorbers consist of a superlattice of 1.5 nm GaSb/0.8 nm AlSb/1.5 nm GaSb/2.7 nm InAs, which is a design previously reported by Lei et al. [141]. The 0.8 nm-thin AlSb barriers inserted between the GaSb layers are included in order to reduce the dependence of the miniband energy on possible variations of the thickness due to MBE growth. The higher barrier in the conduction band additionally reduces the width of the miniband, leading to a sharper onset of the absorption coefficient near the cutoff wavelength. In order to balance the strain in the structure very thin InSb layers were grown at the InAs interfaces, which were measured to

Die approbierte gedruckte Originalversion dieser Dissertation ist an der TU Wien Bibliothek verfügbar.
The approved original version of this doctoral thesis is available in print at TU Wien Bibliothek.

be 0.15 nm in width. This modification of the design leads to a redshift of the cutoff wavelength of about 500 nm compared to the original design. There, cutoff wavelengths between 4.2 µm and 4.5 µm were demonstrated [141]. The entire active region was left undoped in contrast to the *p*-doping employed in [141]. The electron barrier consists of four GaSb/AlSb pairs with a constant thickness of 1.5 nm for the AlSb barriers and varying thicknesses of 7.3/5.8/4.3/3.3 nm for the GaSb h-QWs. The hole barrier was modified in comparison to the original design and extended by four InAs wells to a total of 11 QWs, consisting of InAs wells (3.1/3.3/3.5/3.9/4.0/4.3/4.5/4.8/5.2/5.9/6.8 nm) separated by AlSb barriers (7 x 1.8/1.6/1.4/1.3/1.2/1.2 nm). The thicknesses of the layers in the last hole barrier connecting the absorber to the top contact layer were slightly adjusted and the last three InAs QWs were additionally doped with a concentration of $n = 2 \times 10^{18}$ cm^{-3} to avoid potential barriers at the interface and allow for a smooth transition of the carriers. The highly doped ($n = 2 \times 10^{18}$ cm^{-3}) top contact was realized as a lattice matched $InAs_{0.91}Sb_{0.09}$ layer of 50 nm thickness. Transition layers were furthermore inserted between the bottom contact layer and the first electron barrier consisting of three InAs/GaSb pairs, followed by seven InAs QWs separated by AlSb barriers. The ICIPs exhibit good crystal quality as determined by x-ray diffraction and a surface defect density of ∼300 cm^{-2}. The superlattice is perfectly lattice-matched to the substrate and the corresponding peaks are narrow.

Three different designs were realized in order to investigate the high-speed performance in dependence on the absorber length. All three devices share the design components described above and feature three cascades of the active region. They differ in the number of absorber superlattice periods as follows:

ICIP1: 54 x absorption section → 351 nm

ICIP2: 18 x absorption section → 117 nm

ICIP3: 18 x absorption section → 117 nm & modified hole barrier

Simulations of the bandstructure of ICIP1 are shown in Fig. 6.1. At zero bias the simulation of the structure results in a potential barrier that the carriers need to overcome before being extracted from the superlattice absorber. This is unfavorable for high-speed performance. The absorber thicknesses of ICIP2 and ICIP3 are one third of the absorber in ICIP1. Simulations of the bandstructures of these two designs are shown in Fig. 6.2. In addition, for ICIP3 the third InAs QW of each hole barrier was doped with a concentration of $n = 5 \times 10^{18}$ cm^{-3} and the thicknesses of the QWs were adjusted accordingly to achieve good carrier transport. The influence on the conduction band edge is clearly seen in the simulation in Fig. 6.2b. The idea

Die approbierte gedruckte Originalversion dieser Dissertation ist an der TU Wien Bibliothek verfügbar.
The approved original version of this doctoral thesis is available in print at TU Wien Bibliothek.
TU WIEN Bibliothek Your knowledge hub

Die approbierte gedruckte Originalversion dieser Dissertation ist an der TU Wien Bibliothek verfügbar.
The approved original version of this doctoral thesis is available in print at TU Wien Bibliothek.

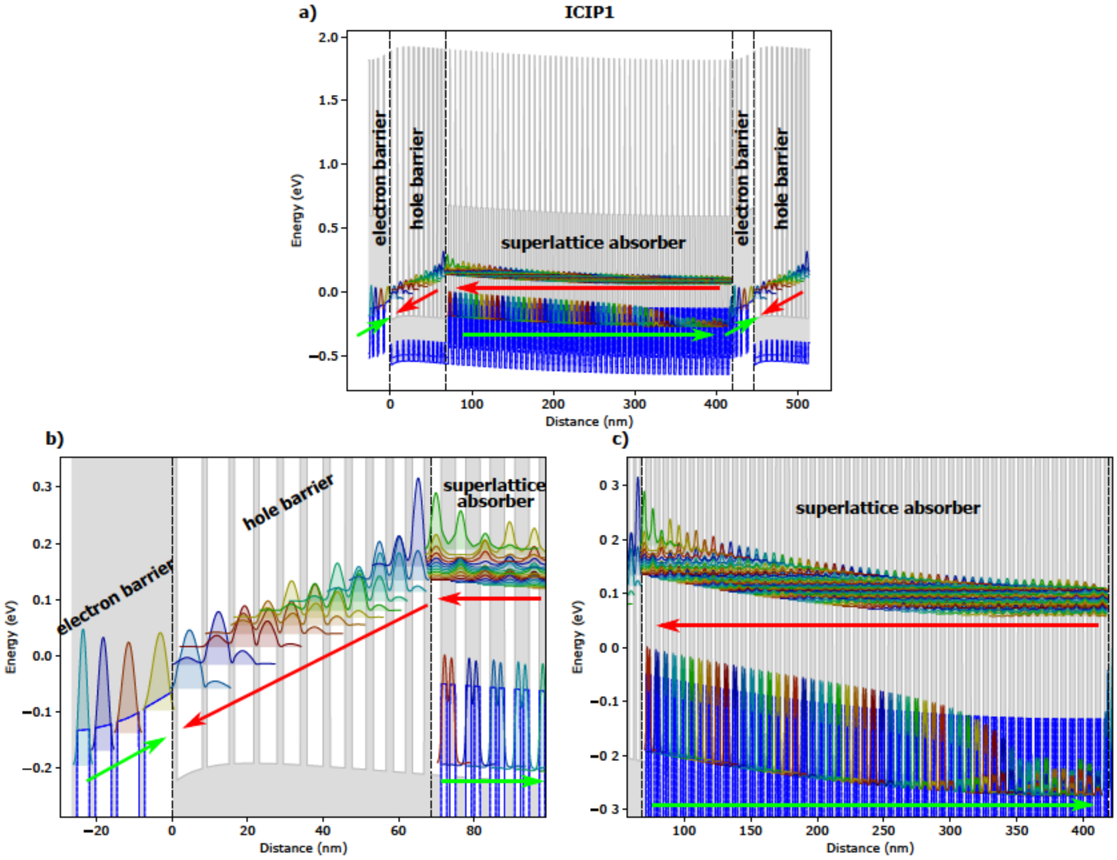

Figure 6.1: **a)** Simulated bandstructure of ICIP1. The directions of carrier transport are indicated by red and green arrows for electrons and holes respectively. **b)** Zoom for better visibility of the electron and hole barrier. After extraction from the superlattice absorber in opposite directions, the carriers recombine at the interface between two adjacent cascades. **c)** Magnification of the superlattice absorber showing the miniband forming in the conduction band.

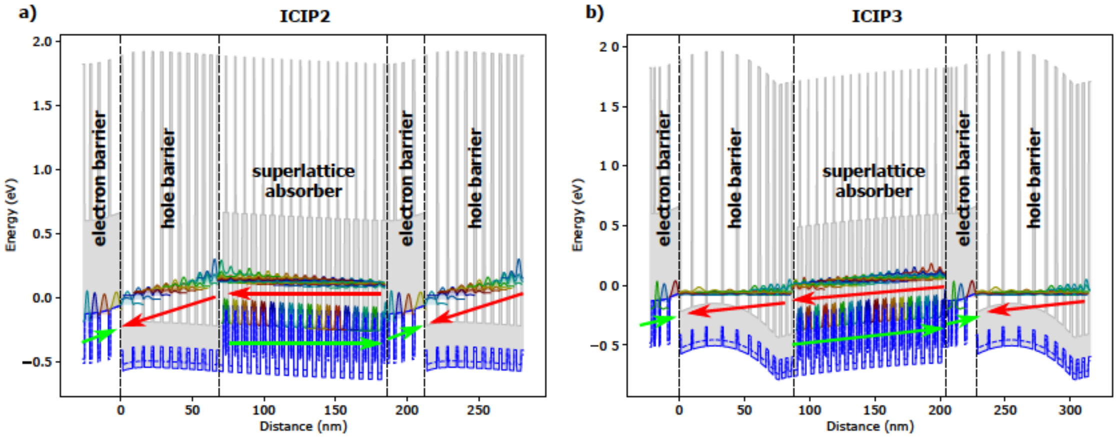

Figure 6.2: **a)** Simulated bandstructure of ICIP2 picturing the reduced length of the superlattice absorber. **b)** Band structure of ICIP3, featuring a modified hole barrier, where the third well from the right is additionally highly n-doped.

behind this was to create an inherent forward bias and allow for improved high-speed operation at zero bias.

6.2.2 Fabrication

Micrographs taken with an SEM of two of the three MBE grown structures, ICIP1 and ICIP2, are shown in Fig. 6.3. The three stages, consisting of the electron barrier (dark), the hole barrier (almost homogeneously bright) and the absorber (bright superlattice structure) can be identified. The two insets in the middle are plotted at the same scale, clearly showing the reduced length of the absorber of ICIP2 (right) to one third of the length of the absorber of ICIP1 (left). The fabrication succeeding the growth was performed similarly to the process described for ring ICLs in section 5.4.1. Looking at Fig. 5.11, the circular detector mesas (A-G) are etched with diameters of different sizes of between 20 µm and 200 µm. The etching process is stopped in the highly n-doped GaSb layer grown on the substrate. Subsequently, a Si_3N_4 passivation layer is deposited, which is selectively removed on top of the mesa and for the bottom contact (N-Q). A 60 s dip in $HCl{:}H_2O = 1{:}3$ is performed before contact deposition to remove the native oxide from GaSb. In order to form an ohmic contact to the n-GaSb bottom contact layer [264], Ge/Au/Ni/Au (14/30/14/200 nm) is sputter-deposited. A lift-off process is employed for structuring and the contact is annealed using rapid thermal annealing (RTA) at a temperature of 310 °C for one minute. Since the Ti/Au top contact did not include a diffusion barrier like Ni or Pt, it was deposited (R-T) only after the annealing of the bottom contact. The devices were then cleaved and mounted on small copper

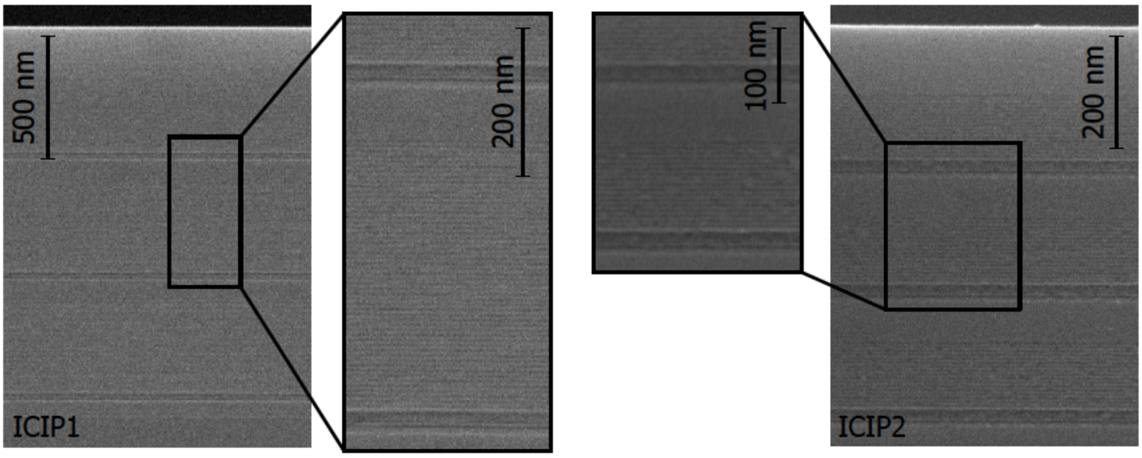

Figure 6.3: SEM images of the MBE grown structures ICIP1 and ICIP2. The reduced length of the superlattice absorber from design 2 to 1 is visible when comparing the two magnified images in the middle.

Die approbierte gedruckte Originalversion dieser Dissertation ist an der TU Wien Bibliothek verfügbar.
The approved original version of this doctoral thesis is available in print at TU Wien Bibliothek.

Die approbierte gedruckte Originalversion dieser Dissertation ist an der TU Wien Bibliothek verfügbar.
The approved original version of this doctoral thesis is available in print at TU Wien Bibliothek.
TU WIEN Bibliothek Your knowledge hub

plates with drilled holes to facilitate backside illumination. The devices used for the characterization were contacted using ground-source-ground (GSG) probes to reduce the losses at high frequencies. The processed chip can be seen in Fig. 6.4a. For easier integration of the fabricated detectors in applications, 100 µm diameter mesas were fully packaged and connected to coplanar waveguides and subsequently to end-launch connectors, which is shown in Fig. 6.4b.

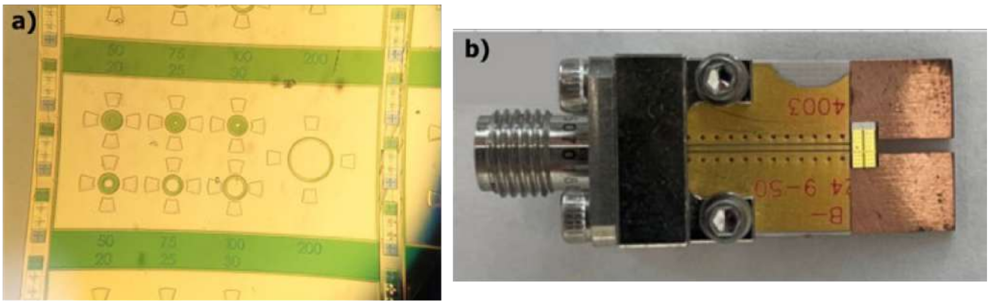

Figure 6.4: **a)** Processed chip of ICIP1 with different mesa sizes. The area of the bottom contact (big gold pad around the seven mesas) is designed to reduce the series resistance by upsizing the area. The four small pads around each of the mesas are designed for level placement of the GSG probes. **b)** Photograph of a fully packaged 100 µm ICIP1 mesa connected to a 50 Ω coplanar waveguide mounted on a copper substrate. The mesa is contacted using short wire bonds and attached to a 2.92 mm end-launch connector.

6.2.3 Performance

The responsivity of ICIP1 and 2 was characterized using devices that were fabricated with a mesa diameter of 1 mm. The large mesas guarantee that all incident light from a laser can be focused on the detector facilitating the measurement of the responsivity. The spectral response was recorded with a mid-infrared globar source from an FTIR and corrected for the spectrally varying intensity of the source. Therefore, the globar spectrum was recorded with a thermal detector showing a flat response. To determine the absolute values of the responsivity, the photocurrent generated by the incident light from an ICL of known output power (measured with a power meter) was measured. The measured responsivity is shown in Fig. 6.5 for ICIP1 and in Fig. 6.6 for ICIP2. The values for design 1 compare well with the reported values of around 200 mA/W from Lei et al. [141] where the design was adapted from. What is interesting is that the responsivity is not as much reduced as it would be expected from a reduction of the absorber length to one third of the original value in ICIP2. However, the measurements of single devices of each design are shown here and no statistical comparison of the responsivity between the two designs was

Die approbierte gedruckte Originalversion dieser Dissertation ist an der TU Wien Bibliothek verfügbar.
The approved original version of this doctoral thesis is available in print at TU Wien Bibliothek.

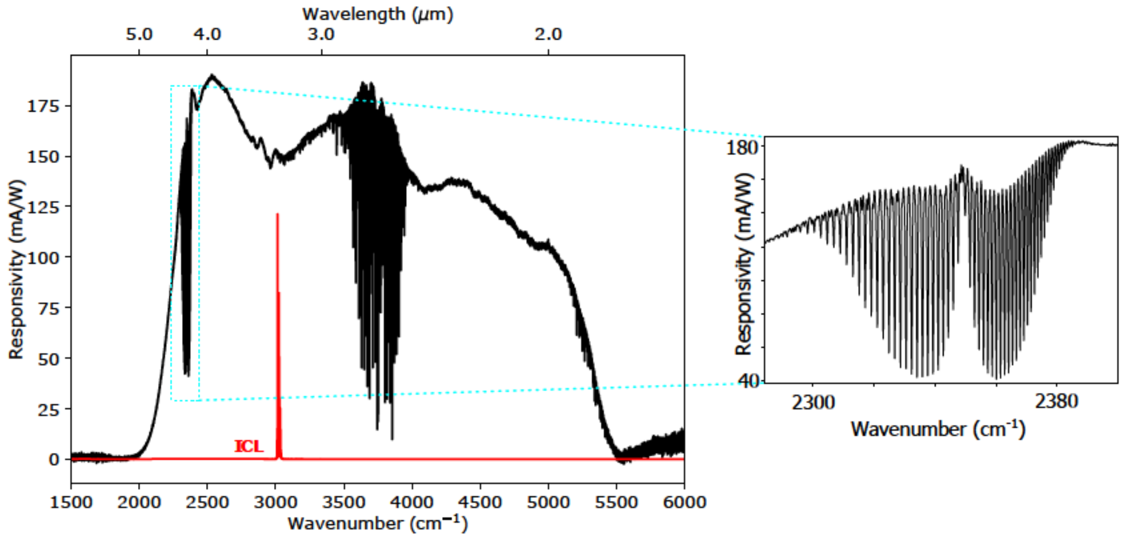

Figure 6.5: Recorded responsivity for a mesa with a diameter of 1 mm of ICIP design 1. The spectrum of the ICL used for characterization is additionally plotted in red. The measurements were performed under ambient conditions and two absorption bands of CO_2 can be seen within this wavelength range. A magnification of the absorption lines between 4 µm and 5 µm is displayed on the right side.

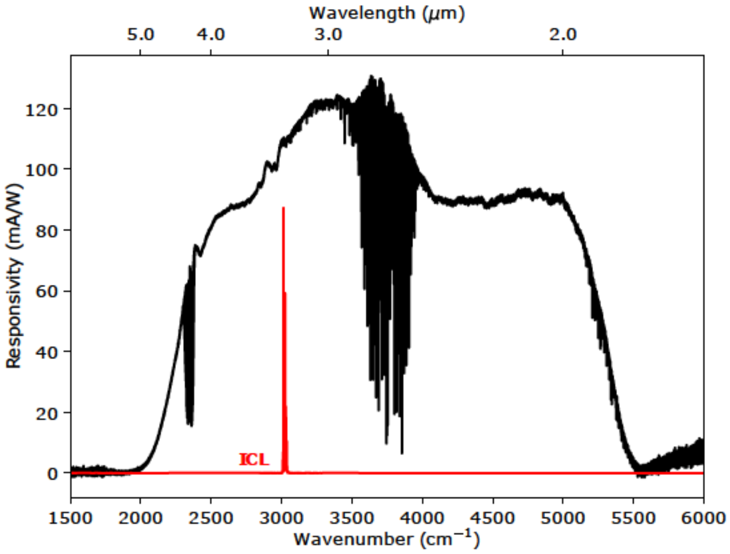

Figure 6.6: Measured responsivity of ICIP design 2. Although the absorber length is reduced to one third compared to ICIP1 the responsivity is still comparably high.

attempted. Since the same superlattice period was employed for both designs a very similar spectral response is achieved spanning the wavelength range between 1.8 µm and 5 µm. Two absorption bands of CO_2 lie within this range, which are seen in the responsivity measurements because they were performed under ambient conditions. One of the main motivations to investigate these detectors was to push the research on ICL frequency combs within the group. Hence, the measured broad spectral response of the ICIP is very beneficial, including ICLs performance sweet spot between 3-4 µm, and allowing the characterization of ICLs emitting at various wavelengths. By changing the superlattice period the cutoff wavelength could easily be extended to slightly above 6 µm in order to facilitate detection of the ICLs emitting above 6 µm presented in section 4.2.3 as well.

The light-current characteristics of the devices were investigated, and are displayed for ICIP1 in Fig. 6.7. The dark current density is plotted on the left side a), whereas b) shows the dark current divided by the circumference for detectors of different sizes. It scales linearly with the circumference which is a clear sign, that it is linked to the sidewalls of the etched mesas, where leakage current is occurring. Reducing the dark current is especially important for detectors with diameters smaller than 100 µm, since their surface to area ratio is higher than for larger detectors. Different passivation techniques for InAs/GaSb superlattice detectors to reduce surface leakage currents have been reported in literature [265, 266]. These include passivation with organic materials like SU-8 or aqueous ammonium sulfide solutions. Special attention should also be dedicated to the remaining process routine, e.g. after employing a sulfide passivation, since high temperature, chemical or physical processes can degrade the passivation.

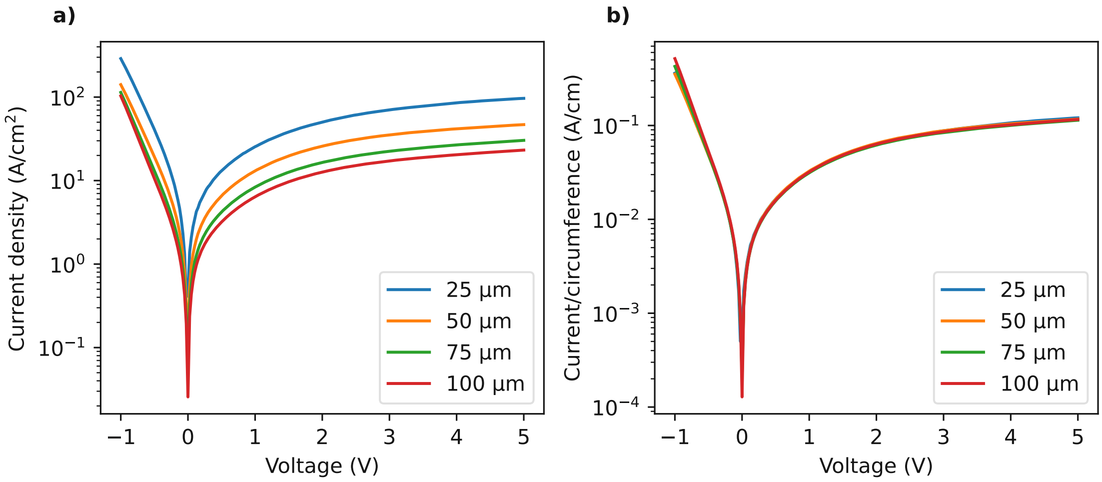

Figure 6.7: Dark current for ICIP design 1 measured for devices with varying diameters from 25 µm to 100 µm divided by the **a)** detector area and **b)** the circumference. The largest contribution to the dark current is surface leakage, resulting in a linear proportionality of dark current to circumference.

Heterodyne beating of two single-mode interband cascade lasers

The first attempt at characterizing the high-speed response of the realized ICIPs was undertaken by employing a heterodyne beating scheme using two single-mode

Die approbierte gedruckte Originalversion dieser Dissertation ist an der TU Wien Bibliothek verfügbar.
The approved original version of this doctoral thesis is available in print at TU Wien Bibliothek.
TU WIEN Bibliothek Your knowledge hub

ICLs at identical emission wavelength. By tuning the wavelength via the current of one of the two lasers away from the other laser, the beating between the two signals shifts towards higher frequencies. The two laser beams are combined via a beam splitter and focussed, using a lens, onto the substrate-side of the ICIP, which is connected to a bias tee. A bias can be applied via the DC port, while the AC signal is fed into a spectrum analyzer, from which the power and spectral position of the beating signal is then read out. The results for ICIP1 are shown in Fig. 6.8 for mesas with diameters of 100 µm, 50 µm and 25 µm and applied bias varied from 0 V to 5 V. Applying a positive bias to the ICIPs results in an improved high-speed

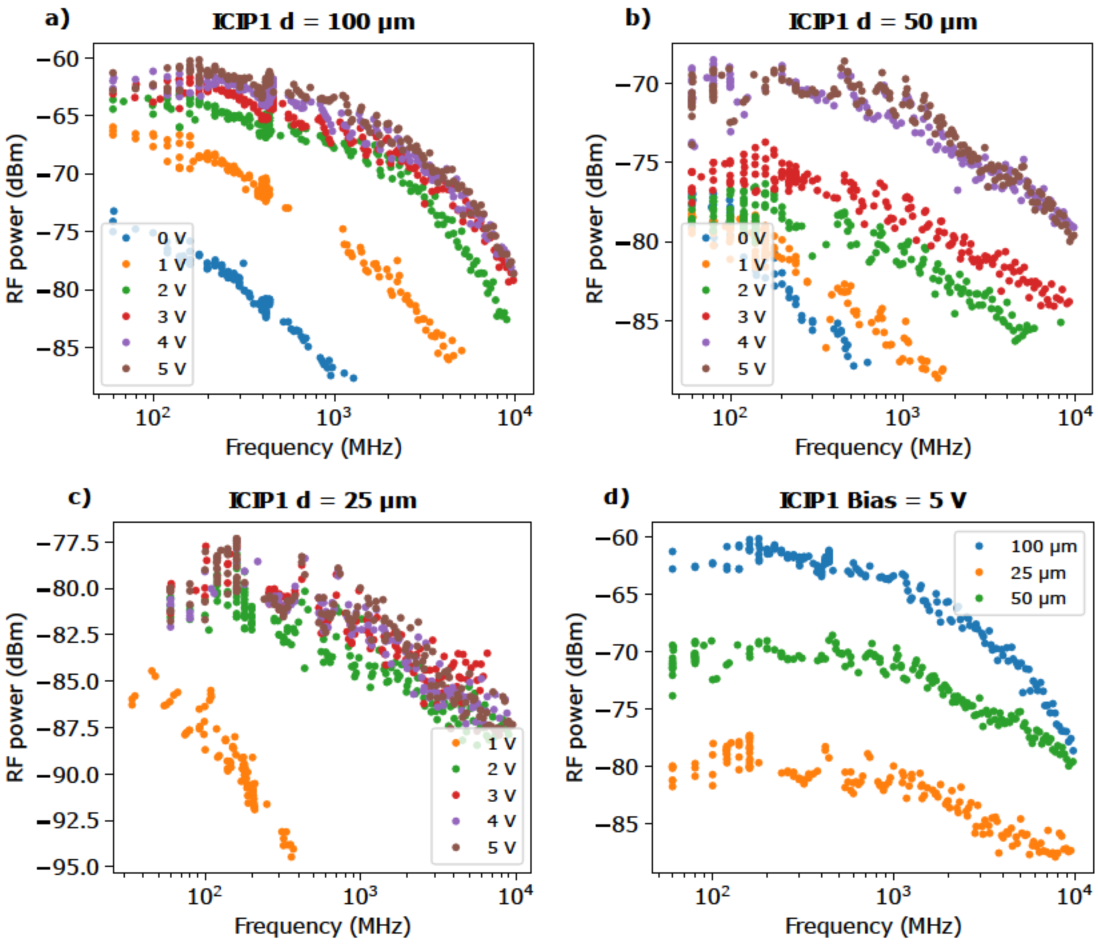

Figure 6.8: Measured frequency response of ICIP1 using a heterodyne beating experiment with two single-mode ICLs measured for different mesa sizes with diameters of **a)** 100 µm, **b)** 50 µm and **c)** 25 µm. A comparison of the different sizes at a bias of 5 V is shown in **d)**.

response. While at zero bias, the signal decays quickly going towards 1 GHz, the heterodyne beating can still be detected effectively up to 10 GHz for a bias of 5 V. Since, the frequency response is similar for 4 V and 5 V, no further improvement

Die approbierte gedruckte Originalversion dieser Dissertation ist an der TU Wien Bibliothek verfügbar.
The approved original version of this doctoral thesis is available in print at TU Wien Bibliothek.

is expected for even higher bias. Interestingly with increasing bias the DC signal is increased as well, which could indicate that the carrier recombination time in the superlattice absorber is significantly smaller than the time it takes for the carriers to move through the superlattice absorber via diffusion. The additional drift due to the applied bias then results in more carriers being extracted. Moreover, the largest mesa with a diameter of 100 µm clearly shows a stronger decrease of the signal at higher frequencies compared to the smaller detectors. This behavior is best seen in Fig. 6.8d, where the three mesa sizes are compared at a bias of 5 V and can be traced back to the higher parasitic capacitance caused by the larger detector area. In an RC circuit, the 3-dB cutoff frequency can be estimated to be $f_{\mathrm{RC}} = 1/(2\pi RC)$, with the resistance R and the capacitance C. For an ICIP the capacitance can be approximated by the formula for a parallel-plate capacitor $C = \epsilon_0\epsilon_{\mathrm{r}}A/d$ of thickness d and area A, where ϵ_0, ϵ_{r} denote the vacuum and relative permittivity, respectively. By using a higher number of cascades, thus increasing d, the cutoff due to the parasitic capacitance could be mitigated for large mesa sizes. Furthermore, a difference in the DC signal between the different detector sizes is observed. This is most probably due to the beam spot being larger than the detector size. The responsivity of different sizes should otherwise be the same.

In comparison to ICIP1, ICIP3 features shorter superlattice absorbers and additional doping in the hole barrier. The results of the measurements are shown in Figs. 6.9 and 6.10 on a linear and a logarithmic frequency scale, respectively. Here, instead of reading out the frequency and power of the beating signal, the trace was recorded at the spectrum analyzer while tuning the current of one of the single-mode lasers. Thus, the individual beatings can be seen, which are still significantly above the noise floor at a frequency of 20 GHz and applied bias of 3 V and 5 V. Applying a bias is, hence, concluded to be essential for high-speed measurements using ICIPs. The shorter absorber length results in a larger capacitance of the detectors compared to ICIP1. The influence of the parasitic capacitance can be seen for a detector diameter of 50 µm for ICIP3, since it shows a much steeper drop of the signal towards higher frequencies than the device with a 20 µm diameter. The recorded frequency response for the smallest mesa size of ICIP3 at a bias of 3 V and 5 V looks intriguingly flat. However, determining the 3-dB cutoff frequency, which is an often reported figure of merit in literature, proved to be quite tricky. The response at low frequencies approaching DC is difficult to assess, because during this experiment the two lasers exhibited optical frequency locking, most probably due to unintentional optical feedback from one laser to the other induced by the measurement setup.

Die approbierte gedruckte Originalversion dieser Dissertation ist an der TU Wien Bibliothek verfügbar.
The approved original version of this doctoral thesis is available in print at TU Wien Bibliothek.
TU WIEN Bibliothek Your knowledge hub

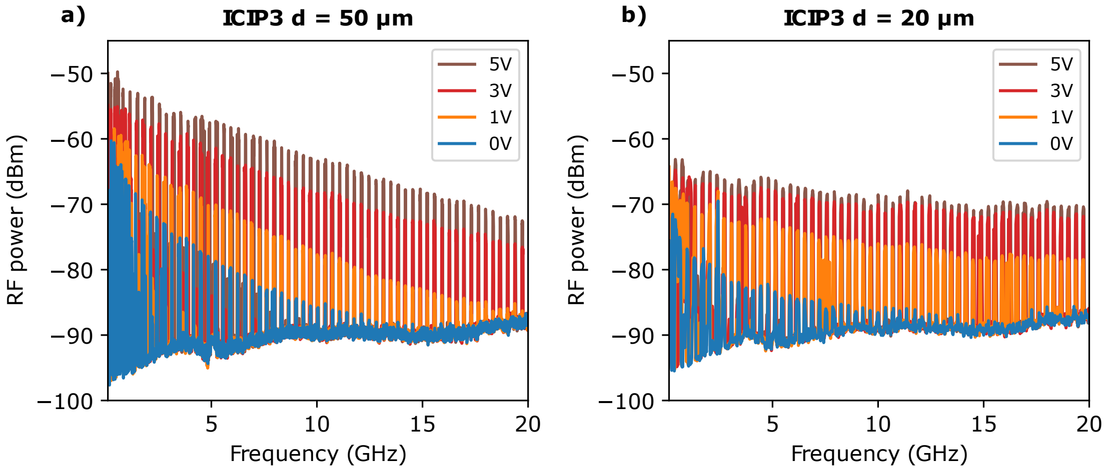

Figure 6.9: Recorded trace at the spectrum analyzer while performing the heterodyning experiment on ICIP3 detectors with diameters of **a)** 50 µm and **b)** 20 µm.

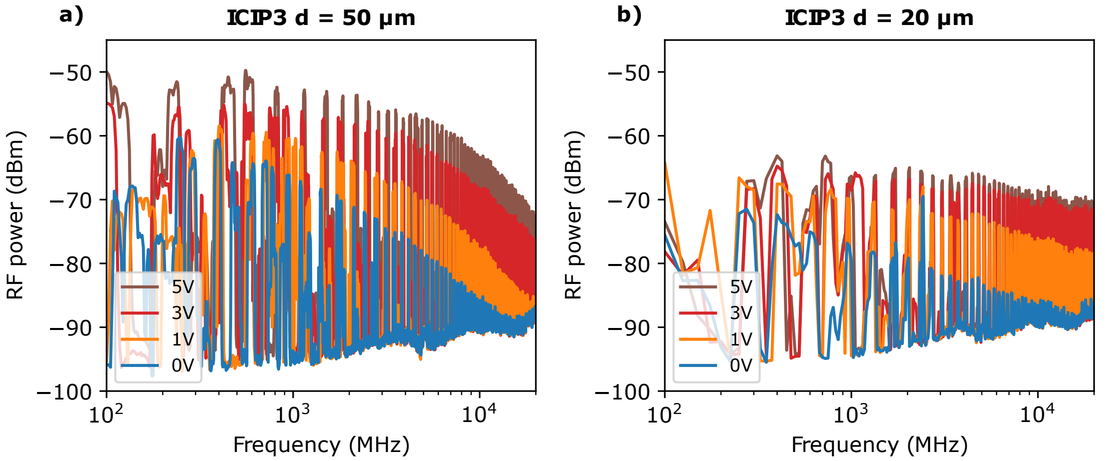

Figure 6.10: The same data as shown in Fig. 6.9 plotted on a logarithmic frequency scale for better comparison with the measured data of ICIP1.

Direct modulation of an interband cascade laser

Due to the unsatisfyingly unreliable measurement results at low frequencies obtained from the heterodyne experiment, another method of determining the frequency response of the ICIP was pursued. Direct modulation of an ICL emitting at a wavelength around 4.3 µm was employed, since the measurement setup in principle promised to be simpler compared to the tedious overlapping of the two beams from the single-mode lasers on the detector as necessary for the heterodyne measurement. First, an radio frequency (RF)-optimized ICL with an emission wavelength within the spectral bandwidth of a detector of known frequency response had to be fabricated. A two section geometry was used, featuring a long gain section and a

Die approbierte gedruckte Originalversion dieser Dissertation ist an der TU Wien Bibliothek verfügbar.
The approved original version of this doctoral thesis is available in print at TU Wien Bibliothek.
TU Bibliothek, WIEN Your knowledge hub

short modulation section. The frequency response of the ICL was characterized by a QCD, which was then subtracted from the measured signal at the ICIP, yielding the net frequency response of the detector. Moreover, a chopper was placed in the beam path between ICL and ICIP. This resulted in side beatings next to the fundamental beating at frequencies separated by the chopper frequency from the modulation frequency. Due to the direct modulation, the fundamental beating was subject to strong electric cross-talk impairing the SNR. The cross-talk and hence, the noise, was efficiently suppressed when recording the power of the side beatings. The results of the measurements for the smallest detectors fabricated from ICIP1 and ICIP2 are shown in Fig. 6.11. The losses from cables and bias tees were subtracted from the recorded frequency response, yielding a 3-dB cutoff frequency of 1.3 GHz for ICIP1 and 1.8 GHz for ICIP2. Unfortunately, at high frequencies the losses from the setup were too high to obtain data that would be reliable enough to extract any meaningful carrier transport times. However, the trend of a flatter frequency response for all applied bias values, when reducing the superlattice thickness is confirmed. This trend can also be observed when comparing ICIP3 to ICIP1 in the heterodyne beating measurement. In conclusion, although the ICIP design is far from optimized, the frequency response of the smallest detectors seems to be unaffected by their electric capacitance. More stages with even thinner absorber lengths are expected to be beneficial for the high-speed behavior, offering fast carrier extraction as well as small capacitance due to the compensation of the reduced absorber thickness by the total number of stages. Moreover, the SNR in the GHz range appears to be sufficiently high for the detectors to be employed in various

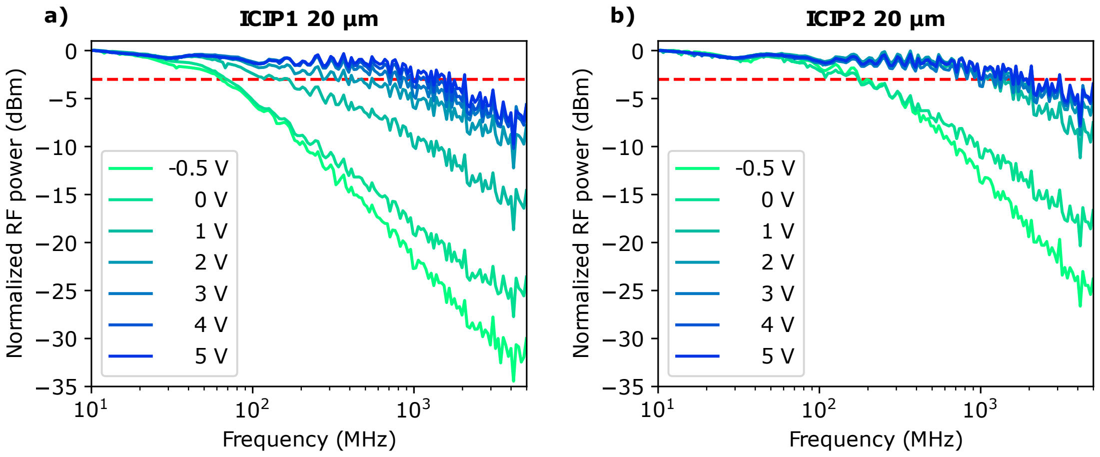

Figure 6.11: Net frequency response of 20 µm diameter detectors from **a)** ICIP design 1 and **b)** design 2, measured by directly recording the AC part of the detector signal under illumination from a directly modulated ICL.

Die approbierte gedruckte Originalversion dieser Dissertation ist an der TU Wien Bibliothek verfügbar.
The approved original version of this doctoral thesis is available in print at TU Wien Bibliothek.
TU Bibliothek WIEN Your knowledge hub

applications already, even without further optimization.

6.3 High-speed applications

In the following, two applications of the ICIP realized during the course of this thesis are highlighted. For both applications devices fabricated from ICIP1 with a diameter of 100 µm were packaged as described earlier and depicted in Fig. 6.4b. Although neither the long superlattice absorbers nor the large detector area are beneficial for the high-speed behavior, the signal at high frequencies is still sufficient, achieving good results for frequency-comb characterization and free-space optical communication.

6.3.1 Frequency-comb characterization

Characterization of the temporal waveform and phase-coherence of semiconductor frequency combs has been demonstrated to be possible with the comparably novel method named shifted wave interference Fourier transform spectroscopy (SWIFTS), that was first introduced by Burghoff et al. in 2015 [267]. Although critically viewed in the research community in the beginning it is now a well established and accepted method that has been experimentally verified numerous times [268, 269]. It relies on the detection of the frequency comb beating at its roundtrip frequency. Depending on the length of the laser, this frequency typically lies around 10 GHz for mid-infrared ICL or QCL frequency combs. Hence, fast detectors are required in order to employ this measurement technique. The here realized ICIPs have been and are successfully implemented in our lab and regularly used for the investigation of ICL frequency combs. The biggest benefits lie in the high signal from the thick superlattice absorbers, facilitating optical alignment, the broad spectral response, allowing to characterize frequency combs with various emission wavelengths and the possibility for room temperature operation, eliminating the need for bulky cryostats. An exemplary measurement of an frequency-modulated (FM) ICL frequency comb, that was performed using an ICIP, is shown in Fig. 6.12. The goal is to measure the amplitudes and phases of the individual intermodal beatings between two neighboring comb lines. This is undertaken by using an FTIR as a frequency discriminator and recording the two quadratures of the beatnote X and Y, and the average intensity as function of the delay, which is equivalent to the mirror displacement (top left). In essence, the quadratures represent the phase and amplitude of the beatnote. From the three interferograms, the intensity and complex SWIFTS spectrum can be obtained by applying a Fourier transformation (top right). This information

Die approbierte gedruckte Originalversion dieser Dissertation ist an der TU Wien Bibliothek verfügbar.
The approved original version of this doctoral thesis is available in print at TU Wien Bibliothek.
TU WIEN Bibliothek Your knowledge hub

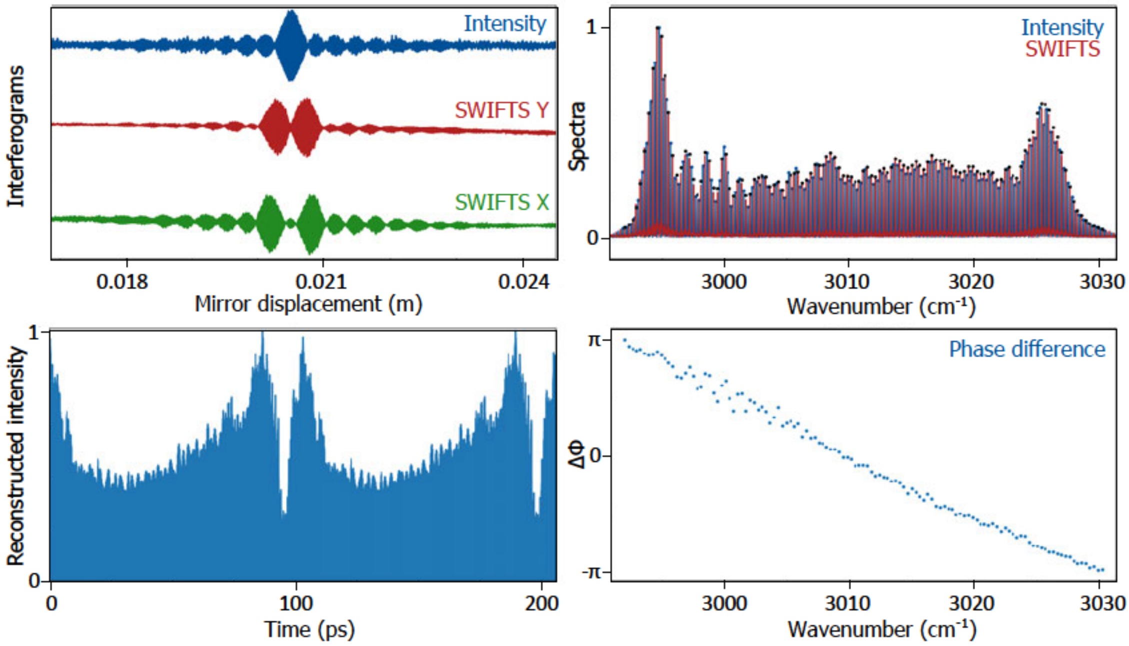

Figure 6.12: SWIFTS measurement of an ICL frequency comb exhibiting FM behavior. The measurement was conducted using an ICIP as fast detector.

allows to reconstruct the temporal intensity waveform (bottom left). The here investigated comb minimizes amplitude modulation, since the phase difference is splayed between a range of 2π. This results in the observed FM type behavior showing almost constant intensity in the time domain.

6.3.2 Free-space optical communication

Recently, one of the ICIPs is employed in a free-space communication experiment [270, 271]. Additionally, the system makes use of a directly modulated ICL emitting at 4.1 µm, that is optimized for RF injection [272], and as such constitutes a full interband system. The bandwidth of the system is heavily influenced by the applied bias on the detector, which is shown in Fig. 6.13a. A 3-dB bandwidth of 1.7 GHz is observed at a bias of 5 V. This value lies at two thirds of the bandwidth of the ICL, which means that the ICIP is the limiting element. Nevertheless, communication at a transmission rate of 12 Gbits/s could be established in a 2 level modulation scheme over a distance of 2 m. The eye diagram obtained using an on-off keying format is displayed in Fig. 6.13b, exhibiting a bit error rate (BER) of 1.5×10^{-2}. The last reported attempt in literature of free-space optical communication using an ICL yielded a maximum transmission rate of 300 Mbits/s [252]. For a QCL at 4.65 µm transmission rates of up to 6 Gbits/s were reported [253]. Hence, the results achieved with the ICIP are very promising, paving the way towards energy-efficient

Die approbierte gedruckte Originalversion dieser Dissertation ist an der TU Wien Bibliothek verfügbar.
The approved original version of this doctoral thesis is available in print at TU Wien Bibliothek.

multi-Gbits/s communication.

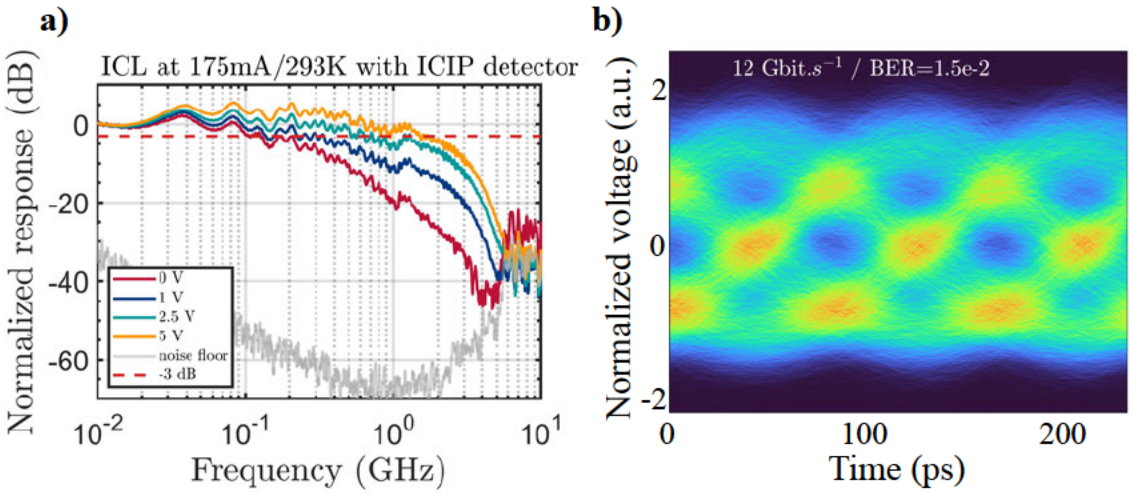

Figure 6.13: a) Frequency response of the interband communication system when applying varying bias up to a maximum of 5 V. b) Eye diagram obtained from a two level communication scheme at a transmission rate of 12 Gbits/s.

Die approbierte gedruckte Originalversion dieser Dissertation ist an der TU Wien Bibliothek verfügbar.
The approved original version of this doctoral thesis is available in print at TU Wien Bibliothek.
TU WIEN Bibliothek Your knowledge hub

Die approbierte gedruckte Originalversion dieser Dissertation ist an der TU Wien Bibliothek verfügbar.
The approved original version of this doctoral thesis is available in print at TU Wien Bibliothek.
TU WIEN Bibliothek Your knowledge hub

CHAPTER 7

CONCLUSION AND OUTLOOK

Interband cascade devices, both lasers and detectors, are rapidly advancing, gaining more and more attention from both researchers and industry, as they constitute an ideal platform for novel integrated photonic sensors. Their unbeatably low power consumption is accelerating the development of portable, compact, and battery-driven trace gas sensors. Moreover, due to their distinctly longer upper state lifetime compared to QCLs, ICLs constitute a promising candidate for future chip-integrated femtosecond sources. Envisioning an integrated supercontinuum source it is necessary to push ICLs to their ultimate performance limit. Hence, additional efforts targeting the performance improvement of ICLs are of the utmost importance to achieve this ambitious goal.

Most notable in today's ICLs is the performance degradation outside of the 3-4 µm sweet spot region, which prohibits the cw operation at longer wavelengths. Since the last breakthrough 10 years ago, with the introduction of carrier rebalancing [84] leading to significantly lower lasing thresholds, no other fundamental design improvements had been reported prior to the findings presented in chapter 4 of this thesis. With the help of both simulations and experiments, the observed performance limitations, like a low characteristic temperature and high threshold current densities, are traced back to resonant absorptive transitions between subbands in the valence band of the W-QW in the ICL active region. Hence, this study fills in one of the missing puzzle pieces in understanding the underlying physical operation principles of ICLs. The intersubband absorption is unambiguously proven to depend on the $\mathrm{Ga_{1-x}In_xSb}$ h-QW thickness and a guideline for mitigating these losses is presented. Improvements were achieved experimentally for figures of merit like the threshold current density, the characteristic temperature, the slope efficiency and output power. While the initial efforts were focusing on the wavelength range of 4-5 µm, it was these results that ultimately resulted in pushing the room temperature cw operation limit of GaSb-based ICLs beyond 6 µm [160].

While these observations constitute the most fundamental breakthrough on ICL technology achieved during this thesis, a lot of the excitement and motivation during my PhD came from pursuing a variety of very different projects from active region design to the realization of actual devices in the cleanroom. During all of these projects room temperature operation was a recurring theme, since it facilitates the implementation of devices in real-life applications. Hence, achieving the first vertically emitting ring ICLs in cw operation at room temperature (see chapter 5) laid a solid foundation for the realization of compact, possibly battery-powered sensors employing these devices. In the near future, applications making use of a ring-in-ring geometry, previously demonstrated for QCLs [273], could either feature emission at two different wavelengths combined on the same optical axis or the on-chip integration of both laser and detector from the same ICL material. Since, vertical light-emission allows for wafer-level testing, this device configuration offers tremendous potential when thinking about taking ICLs towards mass fabrication.

The potential of ICLs for high-speed, low-noise and high-temperature detection is taken to the extreme in ICIPs employing superlattice absorbers, which were studied in chapter 6. These devices combine interband optical transitions with fast intraband transport and their potential for applications like free-space optical communication and the characterization of frequency combs was indisputably demonstrated by implementing fully-packaged ICIPs realized during the course of this thesis for these two use cases. So far the packaging and bonding of these ICIPs was limited to rather big mesa diameters of 100 µm because of the size of the bonding wire. Hence, the high-speed performance is deteriorated by the large parasitic capacitance. By using SU-8 to realize an extended top contact for bonding to small mesas without increasing the capacitance this performance degradation can be circumvented. This is a topic that is currently being investigated.

In general, ICIP technology is rapidly gaining momentum and this rather recent device class aspires to successfully compete with the dominant and widely used MCT detectors in the mid-infrared, offering several distinct technological advantages like suppressed Auger recombination and high growth uniformity. Their main appeal in my opinion, however, lies in their broad spectral coverage while exhibiting promising potential for high-speed applications. Pushing this high-speed performance should be attempted by a careful investigation of the tunneling rates and other fundamental carrier lifetimes within the superlattice absorber. In order to ex-

Die approbierte gedruckte Originalversion dieser Dissertation ist an der TU Wien Bibliothek verfügbar.
The approved original version of this doctoral thesis is available in print at TU Wien Bibliothek.

plore the ultimate speed performance limit possible for these devices, a comparative investigation of the only recently emerging InAs/InAsSb type-II superlattice ICIPs and the so far predominantly realized InAs/GaSb devices should be tackled. One possibility to do this would be to study the electronic impulse response using an optical parametric oscillator, emitting pulses on the order of femtoseconds as has been shown for an ICL used as a detector [155]. There, two distinct decay times could be identified, possibly connected to the different contributions of electrons and holes. The InAs/InAsSb material system holds promising potential since recently a 3-dB cutoff frequency of 12.8 GHz was reported for a detector featuring a single 900 nm thick absorber [156]. Reducing this thickness and employing the superlattice absorber in a cascaded detector could further boost the high-speed characteristics. Most certainly the next years promise to hold an exciting journey for both ICL and superlattice ICIP development, that I am thrilled to be witnessing.

TU Bibliothek WIEN Your knowledge hub
Die approbierte gedruckte Originalversion dieser Dissertation ist an der TU Wien Bibliothek verfügbar.
The approved original version of this doctoral thesis is available in print at TU Wien Bibliothek.

Die approbierte gedruckte Originalversion dieser Dissertation ist an der TU Wien Bibliothek verfügbar.
The approved original version of this doctoral thesis is available in print at TU Wien Bibliothek.

Die approbierte gedruckte Originalversion dieser Dissertation ist an der TU Wien Bibliothek verfügbar.
The approved original version of this doctoral thesis is available in print at TU Wien Bibliothek.

BIBLIOGRAPHY

[1] M. Holzbauer. *Quantum cascade interband and intersubband ring lasers*. Ph.D. thesis, TU Wien (2018) cited on pages 1, 7, 8, 33, 36, 94, 102, 105, and 117.

[2] I. Vurgaftman, W. W. Bewley, C. L. Canedy, C. S. Kim, M. Kim, C. D. Merritt, J. Abell and J. R. Meyer. *Interband cascade lasers with low threshold powers and high output powers*. IEEE Journal of Selected Topics in Quantum Electronics 19 (4): 1200210 1200210 (2013). doi: 10.1109/JSTQE.2012.2237017 cited on pages 2, 30, 45, and 46.

[3] I. Vurgaftman, P. Geiser, W. W. Bewley, C. D. Merritt, C. L. Canedy, M. V. Warren, M. Kim, C. S. Kim and J. R. Meyer. *Sensitive chemical detection with distributed feedback interband cascade lasers*. R. A. Meyers, editor, *Encyclopedia of Analytical Chemistry*, 1 19. John Wiley & Sons, Ltd (2016). doi: 10.1002/9780470027318.a9559 cited on pages 2, 30, 101, and 108.

[4] J. A. Nwaboh, S. Persijn, K. Arrhenius, H. Bohlén, O. Werhahn and V. Ebert. *Metrological quantification of CO in biogas using laser absorption spectroscopy and gas chromatography*. Measurement Science and Technology 29 (9): 095010 (2018). doi: 10.1088/1361-6501/AAD116 cited on pages 2 and 54.

[5] Z. Liu, C. Zheng, T. Zhang, Y. Li, Q. Ren, C. Chen, W. Ye, Y. Zhang, Y. Wang and F. K. Tittel. *Midinfrared sensor system based on tunable laser absorption spectroscopy for dissolved carbon dioxide analysis in the South China Sea: System-level integration and deployment*. Analytical Chemistry 92 (12): 8178 8185 (2020). doi: 10.1021/ACS.ANALCHEM.0C00327 cited on pages 2 and 54.

[6] Z. Wang, Q. Wang, J. Y.-L. Ching, J. C.-Y. Wu, G. Zhang and W. Ren. *A portable low-power QEPAS-based CO_2 isotope sensor using a fiber-coupled*

interband cascade laser. Sensors and Actuators B: Chemical 246: 710 715 (2017). doi: 10.1016/J.SNB.2017.02.133 cited on pages 2 and 54.

[7] P. Geiser. *New opportunities in mid-infrared emission control.* Sensors 15 (9): 22724 22736 (2015). doi: 10.3390/s150922724 cited on pages 2 and 54.

[8] L. Liao, J. Zhang and D. Dong. *The driver design for N_2O gas detection system based on tunable interband cascade laser.* E3S Web Conf 78: 03002 (2019). doi: 10.1051/e3sconf/20197803002 cited on pages 2 and 54.

[9] Z. Du, W. Zhen, Z. Zhang, J. Li and N. Gao. *Detection of methyl mercaptan with a 3393-nm distributed feedback interband cascade laser.* Applied Physics B 122 (4): 100 (2016). doi: 10.1007/s00340-016-6378-z cited on page 2.

[10] *Nanoplus webpage.* `https://nanoplus.com/en/news/icl-2800-6500-nm/`. Accessed: 2022-06-13 cited on pages 2, 109, and 111.

[11] *Vigo webpage.* `https://vigo.com.pl/en/home/`. Accessed: 2022-07-08 cited on page 2.

[12] *Aeris technologies webpage.* `https://aerissensors.com/`. Accessed: 2022-07-08 cited on page 2.

[13] *Neo monitors webpage.* `https://neomonitors.com/`. Accessed: 2022-07-08 cited on page 2.

[14] *Airoptic webpage.* `https://www.airoptic.pl/`. Accessed: 2022-07-08 cited on page 2.

[15] S. J. Sweeney, T. D. Eales and I. P. Marko. *The physics of mid-infrared semiconductor materials and heterostructures.* E. Tournié and L. Cerutti, editors, *Mid-infrared Optoelectronics*, Woodhead Publishing Series in Electronic and Optical Materials, 3 56. Woodhead Publishing (2020). doi: 10.1016/B978-0-08-102709-7.00001-2 cited on pages 6, 9, and 47.

[16] W. Shockley and W. T. Read. *Statistics of the recombinations of holes and electrons.* Physical Review 87 (5): 835 842 (1952). doi: 10.1103/PhysRev.87.835 cited on page 7.

[17] R. N. Hall. *Electron-hole recombination in germanium.* Physical Review 87 (2): 387 387 (1952). doi: 10.1103/PhysRev.87.387 cited on page 7.

Die approbierte gedruckte Originalversion dieser Dissertation ist an der TU Wien Bibliothek verfügbar.
The approved original version of this doctoral thesis is available in print at TU Wien Bibliothek.

[18] C. R. Pidgeon, C. M. Ciesla and B. N. Murdin. *Suppression of non-radiative processes in semiconductor mid-infrared emitters and detectors.* Progress in Quantum Electronics 21 (5): 361 419 (1997). doi: 10.1016/S0079-6727(97)00012-8 cited on page 7.

[19] L. A. Coldren and S. W. Corzine. *Diode lasers and photonic integrated circuits.* Wiley (1995) cited on pages 9, 31, and 39.

[20] P. S. Zory. *Quantum well lasers.* Quantum electronics. Academic Press, Boston (1993) cited on page 9.

[21] H. K. Choi and G. W. Turner. *Antimonide-based strained quantum-well diode lasers.* Physica Scripta T69: 17 25 (1997). doi: 10.1088/0031-8949/1997/t69/003 cited on pages 9 and 10.

[22] C. H. Grein, M. E. Flatté, J. T. Olesberg, S. A. Anson, L. Zhang and T. F. Boggess. *Auger recombination in narrow-gap semiconductor superlattices incorporating antimony.* Journal of Applied Physics 92 (12): 7311 7316 (2002). doi: 10.1063/1.1521255 cited on pages 9, 35, and 41.

[23] J. T. Olesberg and M. E. Flatté. *Theory of mid-wavelength infrared laser active regions: Intrinsic properties and design strategies.* A. Krier, editor, *Mid-infrared semiconductor optoelectronics*, 3 92. Springer London, London (2006). doi: 10.1007/1-84628-209-8 cited on page 9.

[24] T. D. Eales, I. P. Marko, B. A. Ikyo, A. R. Adams, S. Arafin, S. Sprengel, M.-C. Amann and S. J. Sweeney. *Wavelength dependence of efficiency limiting mechanisms in type-I mid-infrared GaInAsSb/GaSb lasers.* IEEE Journal of Selected Topics in Quantum Electronics 23 (6): 1 9 (2017). doi: 10.1109/JSTQE.2017.2687823 cited on page 10.

[25] I. Vurgaftman, M. P. Lumb and J. R. Meyer. *Bands and photons in III-V semiconductor quantum structures.* Oxford University press (2021) cited on pages 10, 13, 14, 21, 24, 27, 58, and 66.

[26] K. S. Gadedjisso-Tossou, S. Belahsene, M. A. Mohou, E. Tournié and Y. Rouillard. *Recombination channels in 2.4-3.2 µm GaInAsSb quantum-well lasers.* Semiconductor Science and Technology 28 (1): 015015 (2012). doi: 10.1088/0268-1242/28/1/015015 cited on page 10.

Die approbierte gedruckte Originalversion dieser Dissertation ist an der TU Wien Bibliothek verfügbar.
The approved original version of this doctoral thesis is available in print at TU Wien Bibliothek.

[27] A. Haug. *Auger recombination in direct-gap semiconductors: band-structure effects*. Journal of Physics C: Solid State Physics 16 (21): 4159 4172 (1983). doi: 10.1088/0022-3719/16/21/017 cited on page 10.

[28] S. Hausser, G. Fuchs, A. Hangleiter, K. Streubel and W. T. Tsang. *Auger recombination in bulk and quantum well InGaAs*. Applied Physics Letters 56 (10): 913 915 (1990). doi: 10.1063/1.103175 cited on page 10.

[29] A. D. Andreev and G. G. Zegrya. *Auger recombination in strained quantum wells*. Semiconductors 31 (3): 297 303 (1997). doi: 10.1134/1.1187132 cited on page 10.

[30] J. R. Meyer, C. L. Canedy, M. Kim, C. S. Kim, C. D. Merritt, W. W. Bewley and I. Vurgaftman. *Comparison of Auger coefficients in type I and type II quantum well midwave infrared lasers*. IEEE Journal of Quantum Electronics 57 (5): 1 10 (2021). doi: 10.1109/JQE.2021.3096219 cited on pages 11, 35, and 46.

[31] C. H. Grein, P. M. Young, M. E. Flatté and H. Ehrenreich. *Long wavelength InAs/InGaSb infrared detectors: Optimization of carrier lifetimes*. Journal of Applied Physics 78 (12): 7143 7152 (1995). doi: 10.1063/1.360422 cited on pages 11, 35, and 57.

[32] T. D. Eales, I. P. Marko, A. R. Adams, J. R. Meyer, I. Vurgaftman and S. J. Sweeney. *Quantifying Auger recombination coefficients in type-I mid-infrared InGaAsSb quantum well lasers*. Journal of Physics D: Applied Physics 54 (5): 055105 (2020). doi: 10.1088/1361-6463/ABC042 cited on pages 11 and 46.

[33] A. Chandola, R. Pino and P. S. Dutta. *Below bandgap optical absorption in tellurium-doped GaSb*. Semiconductor Science and Technology 20 (8): 886 893 (2005). doi: 10.1088/0268-1242/20/8/046 cited on pages 11, 12, and 13.

[34] J. Pankove. *Optical processes in semiconductors*. Dover Books on Physics. Dover (1971) cited on page 11.

[35] M. R. Lorenz, W. Reuter, W. P. Dumke, R. J. Chicotka, G. D. Pettit and J. M. Woodall. *Band structure and direct transition electroluminescence in the* $In_{1-x}Ga_xP$ *alloys*. Applied Physics Letters 13 (12): 421 423 (1968). doi: 10.1063/1.1652500 cited on page 13.

[36] A. R. Adams, M. Asada, Y. Suematsu and S. Arai. *The temperature dependence of the efficiency and threshold current of* $In_{1-x}Ga_xAs_yP_{1-y}$ *lasers related*

Die approbierte gedruckte Originalversion dieser Dissertation ist an der TU Wien Bibliothek verfügbar.
The approved original version of this doctoral thesis is available in print at TU Wien Bibliothek.

to intervalence band absorption. Japanese Journal of Applied Physics 19 (10): L621 L624 (1980). doi: 10.1143/jjap.19.l621 cited on page 13.

[37] G. N. Childs, S. Brand and R. A. Abram. *Intervalence band absorption in semiconductor laser materials.* Semiconductor Science and Technology 1 (2): 116 120 (1986). doi: 10.1088/0268-1242/1/2/004 cited on page 13.

[38] M. Asada, A. Kameyama and Y. Suematsu. *Gain and intervalence band absorption in quantum-well lasers.* IEEE Journal of Quantum Electronics 20 (7): 745 753 (1984). doi: 10.1109/JQE.1984.1072464 cited on page 13.

[39] G. Fuchs, J. Hörer, A. Hangleiter, V. Härle, F. Scholz, R. W. Glew and L. Goldstein. *Intervalence band absorption in strained and unstrained InGaAs multiple quantum well structures.* Applied Physics Letters 60 (2): 231 233 (1992). doi: 10.1063/1.106973 cited on page 13.

[40] H. C. Liu, F. Szmulowicz, Z. R. Wasilewski, M. Buchanan and G. J. Brown. *Intersubband infrared detector with optimized valence band quantum wells for 3-5 μm wavelength region.* Journal of Applied Physics 85 (5): 2972 2976 (1999). doi: 10.1063/1.369062 cited on pages 13 and 14.

[41] H. C. Liu, M. Buchanan and Z. R. Wasilewski. *How good is the polarization selection rule for intersubband transitions?* Applied Physics Letters 72 (14): 1682 1684 (1998). doi: 10.1063/1.121151 cited on page 13.

[42] G. J. Brown and F. Szmulowicz. *Modeling of normal incidence absorption in p-type GaAs/AlGaAs quantum well infrared detectors.* M. Razeghi, Y.-S. Park and G. L. Witt, editors, *Optoelectronic Integrated Circuit Materials, Physics, and Devices*, volume 2397, 461 473. International Society for Optics and Photonics, SPIE (1995). doi: 10.1117/12.206932 cited on page 14.

[43] F. Szmulowicz and G. J. Brown. *Calculation and photoresponse measurement of the bound-to-continuum infrared absorption in p-type GaAs/*$Al_xGa_{1-x}As$ *quantum wells.* Physical Review B 51 (19): 13203 13220 (1995). doi: 10.1103/PhysRevB.51.13203 cited on page 14.

[44] W. W. Bewley, I. Vurgaftman, C. L. Felix, J. R. Meyer, C.-H. Lin, D. Zhang, S. J. Murry, S. S. Pei and L. R. Ram-Mohan. *Role of internal loss in limiting type-II mid-IR laser performance.* Journal of Applied Physics 83 (5): 2384 2391 (1998). doi: 10.1063/1.366997 cited on pages 14 and 35.

TU WIEN Bibliothek Your knowledge hub
Die approbierte gedruckte Originalversion dieser Dissertation ist an der TU Wien Bibliothek verfügbar.
The approved original version of this doctoral thesis is available in print at TU Wien Bibliothek.

[45] Y. Chang and J. N. Schulman. *Modification of optical properties of GaAs-*$Ga_{1-x}Al_xAs$ *superlattices due to band mixing.* Applied Physics Letters 43 (6): 536–538 (1983). doi: 10.1063/1.94410 cited on page 14.

[46] H. H. Chen, M. P. Houng, Y. H. Wang and Y.-C. Chang. *Normal incidence intersubband optical transition in GaSb/InAs superlattices.* Applied Physics Letters 61 (5): 509–511 (1992). doi: 10.1063/1.107870 cited on page 14.

[47] D. Teng, C. Lee and L. F. Eastman. *Strain effects on normal incidence hole intersubband absorption in a p-type semiconductor quantum well.* Journal of Applied Physics 72 (4): 1539–1542 (1992). doi: 10.1063/1.351722 cited on pages 14 and 40.

[48] Y.-C. Chang and J. N. Schulman. *Interband optical transitions in GaAs-*$Ga_{1-x}Al_xAs$ *and InAs-GaSb superlattices.* Physical Review B 31 (4): 2069–2079 (1985). doi: 10.1103/PhysRevB.31.2069 cited on page 14.

[49] Y.-C. Chang. *Bond-orbital models for superlattices.* Physical Review B 37 (14): 8215–8222 (1988). doi: 10.1103/PhysRevB.37.8215 cited on page 14.

[50] G. Bastard. *Wave mechanics applied to semiconductor heterostructures.* Wiley-Interscience (1991) cited on pages 15 and 22.

[51] H. Detz. *Epitaxy of InGaAs/GaAsSb heterostructures for intersubband optoelectronics.* Ph.D. thesis, TU Wien (2018) cited on pages 15 and 23.

[52] P.-O. Löwdin. *A note on the quantum-mechanical perturbation theory.* The Journal of Chemical Physics 19 (11): 1396–1401 (1951). doi: 10.1063/1.1748067 cited on page 19.

[53] E. O. Kane. *Band structure of indium antimonide.* Journal of Physics and Chemistry of Solids 1 (4): 249–261 (1957). doi: 10.1016/0022-3697(57)90013-6 cited on page 19.

[54] M. Willatzen and L. C. Lew Yan Voon. *The k·p method.* Springer Berlin (2009). doi: 10.1007/978-3-540-92872-0 cited on page 21.

[55] N. Opačak, S. Dal Cin, J. Hillbrand and B. Schwarz. *Frequency comb generation by Bloch gain induced giant Kerr nonlinearity.* Physical Review Letters 127 (9): 093902 (2021). doi: 10.1103/PhysRevLett.127.093902 cited on page 25.

Die approbierte gedruckte Originalversion dieser Dissertation ist an der TU Wien Bibliothek verfügbar.
The approved original version of this doctoral thesis is available in print at TU Wien Bibliothek.

[56] F. Szmulowicz. *Derivation of a general expression for the momentum matrix elements within the envelope-function approximation.* Physical Review B 51 (3): 1613 1623 (1995). doi: 10.1103/PhysRevB.51.1613 cited on pages 25 and 58.

[57] Y.-M. Mu and S. S. Pei. *Effects of anisotropic* $\mathbf{k} \cdot \mathbf{p}$ *interactions on energy bands and optical properties of type-II interband cascade lasers.* Journal of Applied Physics 96 (4): 1866 1879 (2004). doi: 10.1063/1.1763243 cited on pages 25 and 58.

[58] I. Vurgaftman, W. W. Bewley, C. L. Canedy, C. S. Kim, M. Kim, J. R. Lindle, C. D. Merritt, J. Abell and J. R. Meyer. *Mid-IR type-II interband cascade lasers.* IEEE Journal on Selected Topics in Quantum Electronics 17 (5): 1435 1444 (2011). doi: 10.1109/JSTQE.2011.2114331 cited on pages 27, 31, 35, 36, 37, 38, 39, 41, 42, 43, 44, and 78.

[59] I. Vurgaftman, R. Weih, M. Kamp, J. R. Meyer, C. L. Canedy, C. S. Kim, M. Kim, W. W. Bewley, C. D. Merritt, J. Abell and S. Höfling. *Interband cascade lasers.* Journal of Physics D: Applied Physics 48: 123001 (2015). doi: 10.1088/0022-3727/48/12/123001 cited on pages 27, 33, 37, 38, 44, 47, 55, 56, 111, and 122.

[60] J. R. Meyer, W. W. Bewley, C. L. Canedy, C. S. Kim, M. Kim, C. D. Merritt and I. Vurgaftman. *The interband cascade laser.* Photonics 7 (3): 75 (2020). doi: 10.3390/PHOTONICS7030075 cited on pages 27, 28, 29, 34, 36, 44, 45, 46, 47, 48, 55, 56, 65, 85, 91, and 104.

[61] A. Rogalski, M. Kopytko and P. Martyniuk. *Antimonide-based infrared detectors: A new perspective.* SPIE Press (2018) cited on page 28.

[62] P. Martyniuk, A. Rogalski and S. Krishna. *Interband quantum cascade infrared photodetectors: Current status and future trends.* Physical Review Applied 17 (2): 027001 (2022). doi: 10.1103/PhysRevApplied.17.027001 cited on page 28.

[63] R. Q. Yang. *Infrared laser based on intersubband transitions in quantum wells.* Superlattices and Microstructures 17 (1): 77 83 (1995). doi: 10.1006/spmi.1995.1017 cited on page 28.

[64] J. Faist, F. Capasso, D. L. Sivco, C. Sirtori, A. L. Hutchinson and A. Y. Cho. *Quantum cascade laser.* Science 264 (5158): 553 556 (1994). doi: 10.1126/science.264.5158.553 cited on pages 28, 31, and 80.

Die approbierte gedruckte Originalversion dieser Dissertation ist an der TU Wien Bibliothek verfügbar.
The approved original version of this doctoral thesis is available in print at TU Wien Bibliothek.
TU WIEN Bibliothek Your knowledge hub

[65] J. R. Meyer, I. Vurgaftman, R. Q. Yang and L. R. Ram-Mohan. *Type-II and type-I interband cascade lasers.* Electronics Letters 32 (1): 45 46 (1996). doi: 10.1049/EL:19960064 cited on pages 28 and 38.

[66] J. R. Meyer, C. A. Hoffman, F. J. Bartoli and L. R. Ram-Mohan. *Type-II quantum-well lasers for the mid-wavelength infrared.* Applied Physics Letters 67 (6): 757 759 (1995). doi: 10.1063/1.115216 cited on pages 28, 33, and 34.

[67] I. Vurgaftman, J. R. Meyer and L. R. Ram-Mohan. *Mid-IR vertical-cavity surface-emitting lasers.* IEEE Journal of Quantum Electronics 34 (1): 147 156 (1998). doi: 10.1109/3.655018 cited on page 28.

[68] R. Q. Yang, C.-H. Lin, P. C. Chang, S. J. Murry, D. Zhang, S. S. Pei, S. R. Kurtz, A.-N. Chu and F. Ren. *Mid-IR interband cascade electroluminescence in type-II quantum wells.* Electronics Letters 32 (17): 1621 1622 (1996). doi: 10.1049/EL:19961049 cited on page 28.

[69] C.-H. Lin, R. Q. Yang, D. Zhang, S. J. Murry, S. S. Pei, A. A. Allerman and S. R. Kurtz. *Type-II interband quantum cascade laser at 3.8 µm.* Electronics Letters 33 (7): 598 599 (1997). doi: 10.1049/EL:19970421 cited on page 29.

[70] C. L. Felix, W. W. Bewley, I. Vurgaftman, J. R. Meyer, D. Zhang, C.-H. Lin, R. Q. Yang and S. S. Pei. *Interband cascade laser emitting >1 photon per injected electron.* IEEE Photonics Technology Letters 9 (11): 1433 1435 (1997). doi: 10.1109/68.634699 cited on pages 29, 32, and 40.

[71] C. L. Felix, W. W. Bewley, E. H. Aifer, I. Vurgaftman, J. R. Meyer, C.-H. Lin, D. Zhang, S. J. Murry, R. Q. Yang and S. S. Pei. *Low threshold 3 µm interband cascade "W" laser.* Journal of Electronic Materials 27 (2): 77 80 (1998). doi: 10.1007/S11664-998-0192-2 cited on page 29.

[72] B. H. Yang, D. Zhang, R. Q. Yang, C.-H. Lin, S. J. Murry and S. S. Pei. *Mid-infrared interband cascade lasers with quantum efficiencies >200%.* Applied Physics Letters 72 (18): 2220 (1998). doi: 10.1063/1.121265 cited on pages 29 and 32.

[73] L. J. Olafsen, E. H. Aifer, I. Vurgaftman, W. W. Bewley, C. L. Felix, J. R. Meyer, D. Zhang, C.-H. Lin and S. S. Pei. *Near-room-temperature mid-infrared interband cascade laser.* Applied Physics Letters 72 (19): 2370 (1998). doi: 10.1063/1.121359 cited on page 29.

Die approbierte gedruckte Originalversion dieser Dissertation ist an der TU Wien Bibliothek verfügbar.
The approved original version of this doctoral thesis is available in print at TU Wien Bibliothek.
TU WIEN Bibliothek Your knowledge hub

[74] R. Q. Yang, J. D. Bruno, J. L. Bradshaw, J. T. Pham and D. E. Wortman. *High-power interband cascade lasers with quantum efficiency > 450%.* Electronics Letters 35 (15): 1254 1255 (1999). doi: 10.1049/EL:19990880 cited on pages 29 and 32.

[75] J. L. Bradshaw, J. T. Pham, R. Q. Yang, J. D. Bruno and D. E. Wortman. *Enhanced CW performance of the interband cascade laser using improved device fabrication.* IEEE Journal on Selected Topics in Quantum Electronics 7 (2): 102 105 (2001). doi: 10.1109/2944.954117 cited on page 29.

[76] R. Q. Yang, J. L. Bradshaw, J. D. Bruno, J. T. Pham, D. E. Wortman and R. L. Tober. *Room temperature type-II interband cascade laser.* Applied Physics Letters 81 (3): 397 (2002). doi: 10.1063/1.1494455 cited on page 29.

[77] C. J. Hill, B. Yang and R. Q. Yang. *Low-threshold interband cascade lasers operating above room temperature.* Physica E: Low-dimensional Systems and Nanostructures 20 (3-4): 486 490 (2004). doi: 10.1016/J.PHYSE.2003.08.064 cited on page 29.

[78] J. L. Bradshaw, J. D. Bruno, J. T. Pham, D. E. Wortman, S. Zhang and S. R. J. Brueck. *Single-longitudinal-mode emission from interband cascade DFB laser with a grating fabricated by interferometric lithography.* IEE Proceedings: Optoelectronics 150 (4): 288 292 (2003). doi: 10.1049/IP-OPT:20030613 cited on page 29.

[79] R. Q. Yang, C. J. Hill, B. H. Yang, C. M. Wong, R. E. Muller and P. M. Echternach. *Continuous-wave operation of distributed feedback interband cascade lasers.* Applied Physics Letters 84 (18): 3699 (2004). doi: 10.1063/1.1738184 cited on page 29.

[80] R. Q. Yang, C. J. Hill and B. H. Yang. *High-temperature and low-threshold midinfrared interband cascade lasers.* Applied Physics Letters 87 (15): 151109 (2005). doi: 10.1063/1.2103387 cited on page 29.

[81] M. Kim, D. C. Larrabee, J. A. Nolde, C. S. Kim, C. L. Canedy, W. W. Bewley, I. Vurgaftman and J. R. Meyer. *Narrow-ridge interband cascade laser emitting high CW power.* Electronics Letters 42 (19): 1097 1098 (2006). doi: 10.1049/EL:20062507 cited on page 29.

[82] C. L. Canedy, W. W. Bewley, M. Kim, C. S. Kim, J. A. Nolde, D. C. Larrabee, J. R. Lindle, I. Vurgaftman and J. R. Meyer. *High-temperature interband*

Die approbierte gedruckte Originalversion dieser Dissertation ist an der TU Wien Bibliothek verfügbar.
The approved original version of this doctoral thesis is available in print at TU Wien Bibliothek.

cascade lasers emitting at $\lambda=3.6$ 4.3 μm. Applied Physics Letters 90 (18): 181120 (2007). doi: 10.1063/1.2736272 cited on pages 29 and 41.

[83] M. Kim, C. L. Canedy, W. W. Bewley, C. S. Kim, J. R. Lindle, J. Abell, I. Vurgaftman and J. R. Meyer. *Interband cascade laser emitting at $\lambda=3.75$ μm in continuous wave above room temperature.* Applied Physics Letters 92 (19): 191110 (2008). doi: 10.1063/1.2930685 cited on pages 30 and 41.

[84] I. Vurgaftman, W. W. Bewley, C. L. Canedy, C. S. Kim, M. Kim, C. D. Merritt, J. Abell, J. R. Lindle and J. R. Meyer. *Rebalancing of internally generated carriers for mid-infrared interband cascade lasers with very low power consumption.* Nature Communications 2 (1): 585 (2011). doi: 10.1038/ncomms1595 cited on pages 30, 40, 41, 56, and 145.

[85] W. W. Bewley, C. L. Canedy, C. S. Kim, M. Kim, C. D. Merritt, J. Abell, I. Vurgaftman and J. R. Meyer. *Continuous-wave interband cascade lasers operating above room temperature at λ = 4.7-5.6 μm.* Optics Express 20 (3): 3235 3240 (2012). doi: 10.1364/OE.20.003235 cited on pages 30 and 56.

[86] R. Weih, M. Kamp and S. Höfling. *Interband cascade lasers with room temperature threshold current densities below 100 A/cm^2.* Applied Physics Letters 102 (23): 231123 (2013). doi: 10.1063/1.4811133 cited on page 30.

[87] M. Kim, W. W. Bewley, C. L. Canedy, C. S. Kim, C. D. Merritt, J. Abell, I. Vurgaftman and J. R. Meyer. *High-power continuous-wave interband cascade lasers with 10 active stages.* Optics Express 23 (8): 9664 9672 (2015). doi: 10.1364/OE.23.009664 cited on page 30.

[88] F. Wang, S. Slivken, D. H. Wu and M. Razeghi. *Room temperature quantum cascade lasers with 22% wall plug efficiency in continuous-wave operation.* Optics Express 28 (12): 17532 17538 (2020). doi: 10.1364/OE.394916 cited on page 30.

[89] W. W. Bewley, C. L. Canedy, C. S. Kim, M. Kim, C. D. Merritt, J. Abell, I. Vurgaftman and J. R. Meyer. *High-power room-temperature continuous-wave mid-infrared interband cascade lasers.* Optics Express 20 (19): 20894 20901 (2012). doi: 10.1364/OE.20.020894 cited on page 30.

[90] A. Spott, E. J. Stanton, A. Torres, M. L. Davenport, C. L. Canedy, I. Vurgaftman, M. Kim, C. S. Kim, C. D. Merritt, W. W. Bewley, J. R. Meyer and J. E. Bowers. *Interband cascade laser on silicon.* Optica 5 (8): 996 1005 (2018). doi: 10.1364/OPTICA.5.000996 cited on page 30.

Die approbierte gedruckte Originalversion dieser Dissertation ist an der TU Wien Bibliothek verfügbar.
The approved original version of this doctoral thesis is available in print at TU Wien Bibliothek.

[91] J.-M. Fedeli and S. Nicoletti. *Mid-infrared (mid-IR) silicon-based photonics*. Proceedings of the IEEE 106 (12): 2302 2312 (2018). doi: 10.1109/JPROC.2018.2844565 cited on page 30.

[92] C. L. Canedy, J. Abell, C. D. Merritt, W. W. Bewley, C. S. Kim, M. Kim, I. Vurgaftman and J. R. Meyer. *Pulsed and CW performance of 7-stage interband cascade lasers*. Optics Express 22 (7): 7702 7710 (2014). doi: 10.1364/OE.22.007702 cited on page 30.

[93] M. von Edlinger, J. Scheuermann, L. Nähle, C. Zimmermann, L. Hildebrandt, M. Fischer, J. Koeth, R. Weih, S. Höfling and M. Kamp. *DFB interband cascade lasers for tunable laser absorption spectroscopy from 3 to 6 µm*. M. Razeghi, E. Tournié and G. J. Brown, editors, *Quantum Sensing and Nanophotonic Devices XI*, volume 8993, 213 221. International Society for Optics and Photonics, SPIE (2014). doi: 10.1117/12.2039734 cited on page 30.

[94] J. Scheuermann, R. Weih, M. von Edlinger, L. Nähle, M. Fischer, J. Koeth, M. Kamp and S. Höfling. *Single-mode interband cascade lasers emitting below 2.8 µm*. Applied Physics Letters 106 (16): 161103 (2015). doi: 10.1063/1.4918985 cited on pages 30, 45, and 109.

[95] S. M. S. Rassel, L. Li, Y. Li, R. Q. Yang, J. A. Gupta, X. Wu and G. C. Aers. *High-temperature and low-threshold interband cascade lasers at wavelengths longer than 6 µm*. Optical Engineering 57 (1): 1 4 (2017). doi: 10.1117/1.OE.57.1.011021 cited on pages 30 and 82.

[96] R. Q. Yang, L. Li, W. Huang, S. M. S. Rassel, J. A. Gupta, A. Bezinger, X. Wu, S. G. Razavipour and G. C. Aers. *InAs-based interband cascade lasers*. IEEE Journal of Selected Topics in Quantum Electronics 25 (6): 1 8 (2019). doi: 10.1109/JSTQE.2019.2916923 cited on pages 30, 34, 45, and 65.

[97] M. von Edlinger, J. Scheuermann, R. Weih, C. Zimmermann, L. Nähle, M. Fischer, J. Koeth, S. Höfling and M. Kamp. *Monomode interband cascade lasers at 5.2 µm for nitric oxide sensing*. IEEE Photonics Technology Letters 26 (5): 480 482 (2014). doi: 10.1109/LPT.2013.2297447 cited on page 31.

[98] A. Bader, L. Steinbrecher, F. Rothmayr, Y. Rawal, F. Hartmann, A. Pfenning and S. Höfling. *III-V semiconductor mid-infrared interband cascade light*

Die approbierte gedruckte Originalversion dieser Dissertation ist an der TU Wien Bibliothek verfügbar.
The approved original version of this doctoral thesis is available in print at TU Wien Bibliothek.
TU Bibliothek Your knowledge hub WIEN

emitters and detectors. M. Strojnik, editor, *Infrared Remote Sensing and Instrumentation XXIX*, volume 11830, 113 122. International Society for Optics and Photonics, SPIE (2021). doi: 10.1117/12.2599140 cited on page 31.

[99] Z. Tian, R. Q. Yang, T. D. Mishima, M. B. Santos, R. T. Hinkey, M. E. Curtis and M. B. Johnson. *InAs-based interband cascade lasers near 6 μm*. Electronics Letters 45 (1): 48 49 (2009). doi: 10.1049/EL:20092779 cited on pages 31 and 45.

[100] Z. Tian, L. Li, H. Ye, R. Q. Yang, T. D. Mishima, M. B. Santos and M. B. Johnson. *InAs-based interband cascade lasers with emission wavelength at 10.4 μm*. Electronics Letters 48 (2): 113 114 (2012). doi: 10.1049/el.2011.3555 cited on page 31.

[101] L. Li, H. Ye, Y. Jiang, R. Q. Yang, J. C. Keay, T. D. Mishima, M. B. Santos and M. B. Johnson. *MBE-grown long-wavelength interband cascade lasers on InAs substrates*. Journal of Crystal Growth 425: 369 372 (2015). doi: 10.1016/J.JCRYSGRO.2015.02.016 cited on page 31.

[102] J. A. Massengale, Y. Shen, R. Q. Yang, S. D. Hawkins and J. F. Klem. *Long wavelength interband cascade lasers*. Applied Physics Letters 120 (9): 091105 (2022). doi: 10.1063/5.0084565 cited on pages 31, 34, 45, 63, and 65.

[103] R. Q. Yang and S. S. Pei. *Novel type-II quantum cascade lasers*. Journal of Applied Physics 79 (11): 8197 8203 (1996). doi: 10.1063/1.362554 cited on page 31.

[104] R. Weih. *Interbandkaskadenlaser für die Gassensorik im Spektralbereich des mittleren Infrarot*. Ph.D. thesis, Universität Würzburg (2017) cited on pages 35, 42, and 44.

[105] E. Kuramochi and Y. Takanashi. *Strain effects in InGaSb/AlGaSb quantum wells grown by molecular beam epitaxy*. Journal of Applied Physics 77 (11): 5706 5711 (1995). doi: 10.1063/1.359213 cited on page 35.

[106] T. Nilsen, M. Breivik, E. Selvig and B. Fimland. *Critical thickness of MBE-grown $Ga_{1-x}In_xSb$ (x<0.2) on GaSb*. Journal of Crystal Growth 311 (7): 1688 1691 (2009). doi: 10.1016/j.jcrysgro.2008.11.083. International Conference on Molecular Beam Epitaxy (MBE-XV) cited on page 35.

Die approbierte gedruckte Originalversion dieser Dissertation ist an der TU Wien Bibliothek verfügbar.
The approved original version of this doctoral thesis is available in print at TU Wien Bibliothek.

[107] H. P. Hjalmarson and S. R. Kurtz. *Electron Auger processes in mid-infrared InAsSb/InGaAs heterostructures.* Applied Physics Letters 69 (7): 949 951 (1996). doi: 10.1063/1.117091 cited on page 35.

[108] M. E. Flatté, C. H. Grein and H. Ehrenreich. *Sensitivity of optimization of mid-infrared InAs/InGaSb laser active regions to temperature and composition variations.* Applied Physics Letters 72 (12): 1424 1426 (1998). doi: 10.1063/1.120583 cited on page 35.

[109] M. E. Flatté, C. H. Grein, T. C. Hasenberg, S. A. Anson, D.-J. Jang, J. T. Olesberg and T. F. Boggess. *Carrier recombination rates in narrow-gap* $InAs/Ga_{1-x}In_xSb$*-based superlattices.* Physical Review B 59 (8): 5745 5750 (1999). doi: 10.1103/PhysRevB.59.5745 cited on pages 35 and 57.

[110] W. W. Bewley, J. R. Lindle, C. S. Kim, M. Kim, C. L. Canedy, I. Vurgaftman and J. R. Meyer. *Lifetimes and Auger coefficients in type-II W interband cascade lasers.* Applied Physics Letters 93 (4): 041118 (2008). doi: 10.1063/1.2967730 cited on pages 35, 39, 46, 57, and 63.

[111] I. Vurgaftman, M. Kim, C. S. Kim, W. W. Bewley, C. L. Canedy, J. R. Lindle and J. R. Meyer. *Auger recombination, internal loss, and other processes in interband cascade lasers.* M. Osinski, B. Witzigmann, F. Henneberger and Y. Arakawa, editors, *Physics and Simulation of Optoelectronic Devices XVII*, volume 7211, 248 255. International Society for Optics and Photonics, SPIE (2009). doi: 10.1117/12.816951 cited on pages 35, 46, and 57.

[112] I. Vurgaftman, J. R. Meyer, C. L. Canedy, W. W. Bewley, J. R. Lindle, C. S. Kim and M. Kim. *High-temperature interband cascade laser.* US Patent 8,125,706 B2 (February 28, 2012) cited on pages 35, 37, 40, and 44.

[113] J. R. Meyer, C. L. Felix, W. W. Bewley, I. Vurgaftman, E. H. Aifer, L. J. Olafsen, J. R. Lindle, C. A. Hoffman, M.-J. Yang, B. R. Bennett, B. V. Shanabrook, H. Lee, C.-H. Lin, S. S. Pei and R. H. Miles. *Auger coefficients in type-II* $InAs/Ga_{1-x}In_xSb$ *quantum wells.* Applied Physics Letters 73 (20): 2857 2859 (1998). doi: 10.1063/1.122609 cited on pages 35, 46, and 57.

[114] F. Janiak, M. Motyka, G. Sęk, M. Dyksik, K. Ryczko, J. Misiewicz, R. Weih, S. Höfling, M. Kamp and G. Patriarche. *Effect of arsenic on the optical properties of GaSb-based type II quantum wells with quaternary GaInAsSb layers.* Journal of Applied Physics 114 (22): 223510 (2013). doi: 10.1063/1.4846756 cited on pages 35 and 36.

Die approbierte gedruckte Originalversion dieser Dissertation ist an der TU Wien Bibliothek verfügbar.
The approved original version of this doctoral thesis is available in print at TU Wien Bibliothek.
TU WIEN Bibliothek Your knowledge hub

[115] M. Motyka, M. Dyksik, K. Ryczko, R. Weih, M. Dallner, S. Höfling, M. Kamp, G. Sęk and J. Misiewicz. *Type-II quantum wells with tensile-strained GaAsSb layers for interband cascade lasers with tailored valence band mixing.* Applied Physics Letters 108 (10): 101905 (2016). doi: 10.1063/1.4943193 cited on pages 35 and 36.

[116] K. Ryczko and G. Sęk. *Towards unstrained interband cascade lasers.* Applied Physics Express 11 (1): 012703 (2017). doi: 10.7567/apex.11.012703 cited on page 35.

[117] I. Vurgaftman, J. R. Meyer and L. R. Ram-Mohan. *Band parameters for III V compound semiconductors and their alloys.* Journal of Applied Physics 89 (11): 5815 5875 (2001). doi: 10.1063/1.1368156 cited on page 36.

[118] I. Vurgaftman, J. Meyer and L. Ram-Mohan. *High-power/low-threshold type-II interband cascade mid-IR laser-design and modeling.* IEEE Photonics Technology Letters 9 (2): 170 172 (1997). doi: 10.1109/68.553079 cited on pages 37 and 38.

[119] R. Q. Yang and Y.-M. Mu. *Issues in mid-IR type-II interband cascade lasers.* H. K. Choi and P. S. Zory, editors, *In-Plane Semiconductor Lasers III*, volume 3628, 104 112. International Society for Optics and Photonics, SPIE (1999). doi: 10.1117/12.344536 cited on pages 38 and 83.

[120] M. G. A. Bernard and G. Duraffourg. *Laser conditions in semiconductors.* physica status solidi (b) 1 (7): 699 703 (1961). doi: 10.1002/pssb.19610010703 cited on page 38.

[121] I. Vurgaftman, J. R. Meyer, C. L. Canedy, W. W. Bewley, C. S. Kim, M. Kim and C. D. Merritt. *Interband cascade lasers with engineered carrier densities.* US Patent 8,798,111 B2 (August 5, 2014) cited on pages 40, 41, 46, and 61.

[122] E. V. Arzhanov, A. P. Bogatov, V. P. Konyaev, O. M. Nikitina and V. I. Shveikin. *Waveguiding properties of heterolasers based on InGaAs/GaAs strained quantum-well structures and characteristics of their gain spectra.* Quantum Electronics 24 (7): 581 587 (1994). doi: 10.1070/qe1994v024n07abeh000144 cited on page 41.

[123] C. L. Canedy, W. W. Bewley, G. I. Boishin, C. S. Kim, I. Vurgaftman, M. Kim, J. R. Meyer and L. J. Whitman. *Molecular beam epitaxy growth and characterization of mid-IR type-II "W" diode lasers.* Journal of Vacuum Science &

Die approbierte gedruckte Originalversion dieser Dissertation ist an der TU Wien Bibliothek verfügbar.
The approved original version of this doctoral thesis is available in print at TU Wien Bibliothek.

Die approbierte gedruckte Originalversion dieser Dissertation ist an der TU Wien Bibliothek verfügbar.
The approved original version of this doctoral thesis is available in print at TU Wien Bibliothek.
TU WIEN Bibliothek Your knowledge hub

Technology B: Microelectronics and Nanometer Structures Processing, Measurement, and Phenomena 23 (3): 1119 1124 (2005). doi: 10.1116/1.1861933 cited on page 41.

[124] D. H. Chow, Y. H. Zhang, R. H. Miles and H. L. Dunlap. *Structural and transport properties of InAs/AlSb superlattices*. Journal of Crystal Growth 150: 879 882 (1995). doi: 10.1016/0022-0248(95)80065-K cited on page 42.

[125] R. Weih, A. Bauer, M. Kamp and S. Höfling. *Interband cascade lasers with AlGaAsSb bulk cladding layers*. Optics Materials Express 3 (10): 1624 1631 (2013). doi: 10.1364/OME.3.001624 cited on page 45.

[126] D. A. Díaz-Thomas, O. Stepanenko, M. Bahriz, S. Calvez, E. Tournié, A. N. Baranov, G. Almuneau and L. Cerutti. *Interband cascade lasers with AlGaAsSb cladding layers emitting at 3.3 µm*. Optics Express 27 (22): 31425 31434 (2019). doi: 10.1364/OE.27.031425 cited on page 45.

[127] L. Li, Y. Jiang, H. Ye, R. Q. Yang, T. D. Mishima, M. B. Santos and M. B. Johnson. *Low-threshold InAs-based interband cascade lasers operating at high temperatures*. Applied Physics Letters 106 (25): 251102 (2015). doi: 10.1063/1.4922995 cited on page 45.

[128] C. D. Merritt, W. W. Bewley, C. S. Kim, C. L. Canedy, I. Vurgaftman, J. R. Meyer and M. Kim. *Gain and loss as a function of current density and temperature in interband cascade lasers*. Applied Optics 54 (31): F1 F7 (2015). doi: 10.1364/AO.54.0000F1 cited on pages 45, 46, 47, 48, 69, 76, and 77.

[129] C. L. Canedy, M. V. Warren, C. D. Merritt, W. W. Bewley, C. S. Kim, M. Kim, I. Vurgaftman and J. R. Meyer. *Interband cascade lasers with longer wavelengths*. M. Razeghi, editor, *Quantum Sensing and Nano Electronics and Photonics XIV*, volume 10111, 80 86. International Society for Optics and Photonics, SPIE (2017). doi: 10.1117/12.2246450 cited on pages 46, 47, and 55.

[130] Y.-Z. Lin, J. A. Massengale, W.-X. Huang, R.-Q. Yang, T. D. Mishima and M. B. Santos. *Examination of the durability of interband cascade lasers against structural variations*. Journal of Infrared and Millimeter Waves 39 (2): 137 141 (2020). doi: 10.11972/j.issn.1001-9014.2020.02.001 cited on page 47.

[131] B. A. Ikyo, I. P. Marko, A. R. Adams, S. J. Sweeney, C. L. Canedy, I. Vurgaftman, C. S. Kim, M. Kim, W. W. Bewley and J. R. Meyer. *Temperature*

dependence of 4.1 μm mid-infrared type II "W" interband cascade lasers. Applied Physics Letters 99 (2): 021102 (2011). doi: 10.1063/1.3606533 cited on page 47.

[132] M. Y. Vinnichenko, L. E. Vorobjev, D. A. Firsov, M. O. Mashko, R. M. Balagula, G. Belenky, L. Shterengas and G. Kipshidze. *Dependence of the carrier concentration on the current in mid-infrared injection lasers with quantum wells.* Semiconductors 47 (11): 1513 1516 (2013). doi: 10.1134/S1063782613110237 cited on page 47.

[133] Y. Lin, L. Li, W. Huang, R. Q. Yang, J. A. Gupta and W. Zheng. *Quasi-fermi level pinning in interband cascade lasers.* IEEE Journal of Quantum Electronics 56 (4): 1 10 (2020). doi: 10.1109/JQE.2020.3003081 cited on page 48.

[134] J. V. Li, R. Q. Yang, C. J. Hill and S. L. Chuang. *Interband cascade detectors with room temperature photovoltaic operation.* Applied Physics Letters 86 (10): 101102 (2005). doi: 10.1063/1.1875758 cited on page 48.

[135] L. Gendron, M. Carras, A. Huynh, V. Ortiz, C. Koeniguer and V. Berger. *Quantum cascade photodetector.* Applied Physics Letters 85 (14): 2824 2826 (2004). doi: 10.1063/1.1781731 cited on page 48.

[136] J. Hillbrand, L. M. Krüger, S. Dal Cin, H. Knötig, J. Heidrich, A. M. Andrews, G. Strasser, U. Keller and B. Schwarz. *High-speed quantum cascade detector characterized with a mid-infrared femtosecond oscillator.* Optics Express 29 (4): 5774 5781 (2021). doi: 10.1364/OE.417976 cited on pages 48 and 130.

[137] M. Giparakis, H. Knötig, H. Detz, M. Beiser, W. Schrenk, B. Schwarz, G. Strasser and A. M. Andrews. *2.7 μm quantum cascade detector: Above band gap energy intersubband detection.* Applied Physics Letters 120 (7): 071104 (2022). doi: 10.1063/5.0076856 cited on page 48.

[138] R. Q. Yang, Z. Tian, Z. Cai, J. F. Klem, M. B. Johnson and H. C. Liu. *Interband-cascade infrared photodetectors with superlattice absorbers.* Journal of Applied Physics 107 (5): 054514 (2010). doi: 10.1063/1.3327415 cited on page 48.

[139] W. Huang, L. Li, L. Lei, J. A. Massengale, H. Ye, R. Q. Yang, T. D. Mishima and M. B. Santos. *Minority carrier lifetime in mid-wavelength interband cas-*

Die approbierte gedruckte Originalversion dieser Dissertation ist an der TU Wien Bibliothek verfügbar.
The approved original version of this doctoral thesis is available in print at TU Wien Bibliothek.
TU WIEN Bibliothek Your knowledge hub

cade infrared photodetectors. Applied Physics Letters 112 (25): 251107 (2018). doi: 10.1063/1.5030544 cited on page 49.

[140] R. T. Hinkey and R. Q. Yang. *Theory of multiple-stage interband photovoltaic devices and ultimate performance limit comparison of multiple-stage and single-stage interband infrared detectors*. Journal of Applied Physics 114 (10): 104506 (2013). doi: 10.1063/1.4820394 cited on page 49.

[141] L. Lei, L. Li, H. Lotfi, H. Ye, R. Q. Yang, T. D. Mishima, M. B. Santos and M. B. Johnson. *Midwavelength interband cascade infrared photodetectors with superlattice absorbers and gain*. Optical Engineering 57 (1): 1 10 (2017). doi: 10.1117/1.OE.57.1.011006 cited on pages 50, 51, 131, 132, and 135.

[142] R. Q. Yang and R. T. Hinkey. *Ultimate detectivity of multiple-stage interband cascade infrared photodetectors*. Applied Physics Letters 118 (24): 241101 (2021). doi: 10.1063/5.0054234 cited on page 50.

[143] W. Huang, L. Lei, L. Li, J. A. Massengale, R. Q. Yang, T. D. Mishima and M. B. Santos. *Current-matching versus non-current-matching in long wavelength interband cascade infrared photodetectors*. Journal of Applied Physics 122 (8): 083102 (2017). doi: 10.1063/1.4989382 cited on page 50.

[144] H. Lotfi, L. Li, L. Lei, Y. Jiang, R. Q. Yang, J. F. Klem and M. B. Johnson. *Short-wavelength interband cascade infrared photodetectors operating above room temperature*. Journal of Applied Physics 119 (2): 023105 (2016). doi: 10.1063/1.4939961 cited on page 51.

[145] L. Lei, L. Li, H. Ye, H. Lotfi, R. Q. Yang, M. B. Johnson, J. A. Massengale, T. D. Mishima and M. B. Santos. *Long wavelength interband cascade infrared photodetectors operating at high temperatures*. Journal of Applied Physics 120 (19): 193102 (2016). doi: 10.1063/1.4967915 cited on page 51.

[146] H. Lotfi, L. Li, H. Ye, R. T. Hinkey, L. Lei, R. Q. Yang, J. C. Keay, T. D. Mishima, M. B. Santos and M. B. Johnson. *Interband cascade infrared photodetectors with long and very-long cutoff wavelengths*. Infrared Physics & Technology 70: 162 167 (2015). doi: 10.1016/j.infrared.2014.08.017. Proceedings of International Conference on Quantum Structures Infrared Photodetectors, 2014 cited on page 51.

[147] A. Rogalski, P. Martyniuk, M. Kopytko, P. Madejczyk and S. Krishna. *InAsSb-based infrared photodetectors: Thirty years later on*. Sensors 20 (24): 7047 (2020). doi: 10.3390/s20247047 cited on page 51.

Die approbierte gedruckte Originalversion dieser Dissertation ist an der TU Wien Bibliothek verfügbar.
The approved original version of this doctoral thesis is available in print at TU Wien Bibliothek.

[148] E. H. Steenbergen, B. C. Connelly, G. D. Metcalfe, H. Shen, M. Wraback, D. Lubyshev, Y. Qiu, J. M. Fastenau, A. W. K. Liu, S. Elhamri, O. O. Cellek and Y.-H. Zhang. *Significantly improved minority carrier lifetime observed in a long-wavelength infrared III-V type-II superlattice comprised of InAs/InAsSb.* Applied Physics Letters 99 (25): 251110 (2011). doi: 10.1063/1.3671398 cited on page 51.

[149] W. Gawron, Ł. Kubiszyn, K. Michalczewski, J. Piotrowski and P. Martyniuk. *Demonstration of the longwave type-II superlattice InAs/InAsSb cascade photodetector for high operating temperature.* IEEE Electron Device Letters 1 (2022). doi: 10.1109/LED.2022.3188909 cited on page 51.

[150] A. Bader, F. Rothmayr, N. W. Khan, F. Hartmann, J. Koeth and S. Höfling. *Ga-free InAs/InAsSb superlattices for light detection in the mid-infrared spectral region.* Mirsens - 5th international workshop on opportunities and challenges in mid-infrared laser-based gas sensing (2022) cited on page 51.

[151] L. Lei, L. Li, H. Lotfi, Y. Jiang, R. Q. Yang, M. B. Johnson, D. Lubyshev, Y. Qiu, J. M. Fastenau and A. W. K. Liu. *Mid-wave interband cascade infrared photodetectors based on GaInAsSb absorbers.* Semiconductor Science and Technology 31 (10): 105014 (2016). doi: 10.1088/0268-1242/31/10/105014 cited on page 52.

[152] H. Lotfi, L. Li, L. Lei, H. Ye, S. M. S. Rassel, Y. Jiang, R. Q. Yang, T. D. Mishima, M. B. Santos, J. A. Gupta and M. B. Johnson. *High-frequency operation of a mid-infrared interband cascade system at room temperature.* Applied Physics Letters 108 (20): 201101 (2016). doi: 10.1063/1.4950700 cited on page 52.

[153] Y. Chen, X. Chai, Z. Xie, Z. Deng, N. Zhang, Y. Zhou, Z. Xu, J. Chen and B. Chen. *High-speed mid-infrared interband cascade photodetector based on InAs/GaAsSb type-II superlattice.* Journal of Lightwave Technology 38 (4): 939 945 (2020). doi: 10.1109/JLT.2019.2950607 cited on page 52.

[154] Z. Xie, J. Huang, X. Chai, Z. Deng, Y. Chen, Q. Lu, Z. Xu, J. Chen, Y. Zhou and B. Chen. *High-speed mid-wave infrared interband cascade photodetector at room temperature.* Optics Express 28 (24): 36915 36923 (2020). doi: 10.1364/OE.409868 cited on page 52.

[155] L. M. Krüger, J. Hillbrand, J. Heidrich, M. Beiser, R. Weih, J. Koeth, C. R. Phillips, B. Schwarz, G. Strasser and U. Keller. *High-speed interband cascade*

Die approbierte gedruckte Originalversion dieser Dissertation ist an der TU Wien Bibliothek verfügbar.
The approved original version of this doctoral thesis is available in print at TU Wien Bibliothek.

infrared photodetectors: photo-response saturation by a femtosecond oscillator. Optics Express 29 (9): 14087 14100 (2021). doi: 10.1364/OE.423498 cited on pages 52 and 147.

[156] J. Huang, Z. Shen, Z. Wang, Z. Zhou, Z. Wang, B. Peng, W. Liu, Y. Chen and B. Chen. *High-speed mid-wave infrared uni-traveling carrier photodetector based on InAs/InAsSb type-II superlattice.* IEEE Electron Device Letters 43 (5): 745 748 (2022). doi: 10.1109/LED.2022.3163660 cited on pages 52 and 147.

[157] B. Schwarz, J. Hillbrand, M. Beiser, A. M. Andrews, G. Strasser, H. Detz, A. Schade, R. Weih and S. Höfling. *Monolithic frequency comb platform based on interband cascade lasers and detectors.* Optica 6 (7): 890 895 (2019). doi: 10.1364/OPTICA.6.000890 cited on page 52.

[158] L. A. Sterczewski, M. Bagheri, C. Frez, C. L. Canedy, I. Vurgaftman and J. R. Meyer. *Mid-infrared dual-comb spectroscopy with room-temperature bi-functional interband cascade lasers and detectors.* Applied Physics Letters 116 (14): 141102 (2020). doi: 10.1063/1.5143954 cited on page 52.

[159] H. Knötig, J. Nauschütz, N. Opačak, S. Höfling, J. Koeth, R. Weih and B. Schwarz. *Mitigating valence intersubband absorption in interband cascade lasers.* Laser & Photonics Reviews n/a: 2200156 (2022). doi: 10.1002/lpor.202200156 cited on pages 54, 55, 59, 62, 65, 68, 69, 71, 73, 75, 76, 78, and 79.

[160] J. Nauschütz, H. Knötig, R. Weih, J. Scheuermann, J. Koeth, S. Höfling and B. Schwarz. *Pushing the room temperature continuous-wave operation limit of GaSb-based interband cascade lasers beyond 6 µm* (2022). doi: 10.48550/ARXIV.2207.11113 cited on pages 54 and 146.

[161] K. Fujita, S. Furuta, T. Dougakiuchi, A. Sugiyama, T. Edamura and M. Yamanishi. *Broad-gain ($\Delta\lambda/\lambda_0 \sim 0.4$), temperature-insensitive ($T_0 \sim 510K$) quantum cascade lasers.* Optics Express 19 (3): 2694 2701 (2011). doi: 10.1364/oe.19.002694 cited on page 56.

[162] Y. Bai, N. Bandyopadhyay, S. Tsao, E. Selcuk, S. Slivken and M. Razeghi. *Highly temperature insensitive quantum cascade lasers.* Applied Physics Letters 97 (25): 251104 (2010). doi: 10.1063/1.3529449 cited on page 56.

Die approbierte gedruckte Originalversion dieser Dissertation ist an der TU Wien Bibliothek verfügbar.
The approved original version of this doctoral thesis is available in print at TU Wien Bibliothek.
TU WIEN Bibliothek Your knowledge hub

[163] Y. Bai, N. Bandyopadhyay, S. Tsao, S. Slivken and M. Razeghi. *Room temperature quantum cascade lasers with 27% wall plug efficiency.* Applied Physics Letters 98 (18): 181102 (2011). doi: 10.1063/1.3586773 cited on page 56.

[164] Y. Yao, A. J. Hoffman and C. F. Gmachl. *Mid-infrared quantum cascade lasers.* Nature Photonics 6 (7): 432 439 (2012). doi: 10.1038/nphoton.2012.143 cited on page 56.

[165] K. Fujita, M. Yamanishi, T. Edamura, A. Sugiyama and S. Furuta. *Extremely high* T_0*-values (∼450 K) of long-wavelength (∼15 µm), low-threshold-current-density quantum-cascade lasers based on the indirect pump scheme.* Applied Physics Letters 97 (20): 201109 (2010). doi: 10.1063/1.3518487 cited on page 56.

[166] D. Botez, S. Kumar, J. C. Shin, L. J. Mawst, I. Vurgaftman and J. R. Meyer. *Temperature dependence of the key electro-optical characteristics for midinfrared emitting quantum cascade lasers.* Applied Physics Letters 97 (7): 071101 (2010). doi: 10.1063/1.3478836 cited on page 56.

[167] Y.-M. Mu and R. Q. Yang. *Theoretical investigation of mid-infrared interband cascade lasers based on type II quantum wells.* Journal of Applied Physics 84 (9): 5357 5359 (1998). doi: 10.1063/1.368789 cited on pages 57 and 63.

[168] P. Enders and M. Woerner. *Exact* 4×4 *block diagonalization of the eight-band* $k \cdot p$ *Hamiltonian matrix for tetrahedral semiconductors and its application to strained quantum wells.* Semiconductor Science and Technology 11 (7): 983 988 (1996). doi: 10.1088/0268-1242/11/7/002 cited on page 58.

[169] B. A. Foreman. *Elimination of spurious solutions from eight-band* $\mathbf{k} \cdot \mathbf{p}$ *theory.* Physical Review B 56 (20): R12748 R12751 (1997). doi: 10.1103/PhysRevB.56.R12748 cited on pages 58 and 66.

[170] D. Sytnyk and R. Melnik. *The Luttinger-Kohn theory for multiband Hamiltonians: A revision of ellipticity requirements* (2018). doi: 10.48550/ARXIV.1808.06988 cited on pages 58 and 66.

[171] G. Sęk, F. Janiak, M. Motyka, K. Ryczko, J. Misiewicz, A. Bauer, S. Höfling and A. Forchel. *Carrier loss mechanisms in type II quantum wells for the active region of GaSb-based mid-infrared interband cascade lasers.* Optical Materials 33 (11): 1817 1819 (2011). doi: 10.1016/J.OPTMAT.2011.06.019 cited on page 61.

Die approbierte gedruckte Originalversion dieser Dissertation ist an der TU Wien Bibliothek verfügbar.
The approved original version of this doctoral thesis is available in print at TU Wien Bibliothek.
TU WIEN Bibliothek Your knowledge hub

[172] R. Szedlak. *On the light emission from ring quantum cascade lasers and their application in spectroscopic sensing.* Ph.D. thesis, TU Wien (2017) cited on page 94.

[173] C. Schwarzer. *Advanced quantum cascade ring lasers.* Ph.D. thesis, TU Wien (2014) cited on pages 94, 97, 98, and 107.

[174] E. Mujagić. *Ring cavity surface emitting semiconductor lasers.* Ph.D. thesis, TU Wien (2010) cited on page 94.

[175] H. Kogelnik and C. V. Shank. *Coupled-wave theory of distributed feedback lasers.* Journal of Applied Physics 43 (5): 2327 2335 (1972). doi: 10.1063/1.1661499 cited on pages 94, 103, 104, and 105.

[176] N. Finger. *Grating-coupled semiconductor structures.* Ph.D. thesis, TU Wien (2000) cited on pages 94 and 106.

[177] N. Finger, W. Schrenk and E. Gornik. *Analysis of TM-polarized DFB laser structures with metal surface gratings.* IEEE Journal of Quantum Electronics 36 (7): 780 786 (2000). doi: 10.1109/3.848348 cited on pages 94 and 106.

[178] W. Schrenk. *Distributed feedback quantum cascade lasers.* Ph.D. thesis, TU Wien (2001) cited on page 94.

[179] W. Schrenk, N. Finger, S. Gianordoli, L. Hvozdara, G. Strasser and E. Gornik. *Surface-emitting distributed feedback quantum-cascade lasers.* Applied Physics Letters 77 (14): 2086 2088 (2000). doi: 10.1063/1.1313807 cited on page 94.

[180] H. Knötig, B. Hinkov, R. Weih, S. Höfling, J. Koeth and G. Strasser. *Continuous-wave operation of vertically emitting ring interband cascade lasers at room temperature.* Applied Physics Letters 116 (13): 131101 (2020). doi: 10.1063/1.5139649 cited on pages 94, 111, 118, 120, 121, 122, 124, 125, and 126.

[181] N. Opačak. *The origin of frequency combs in free-running quantum cascade lasers.* Ph.D. thesis, TU Wien (2022) cited on pages 95 and 100.

[182] M. Sorel, P. J. R. Laybourn, A. Scirè, S. Balle, G. Giuliani, R. Miglierina and S. Donati. *Alternate oscillations in semiconductor ring lasers.* Optics Letters 27 (22): 1992 1994 (2002). doi: 10.1364/OL.27.001992 cited on page 97.

TU Bibliothek, WIEN, Your knowledge hub
Die approbierte gedruckte Originalversion dieser Dissertation ist an der TU Wien Bibliothek verfügbar.
The approved original version of this doctoral thesis is available in print at TU Wien Bibliothek.

[183] M. Sorel, P. J. R. Laybourn, G. Giuliani and S. Donati. *Unidirectional bistability in semiconductor waveguide ring lasers.* Applied Physics Letters 80 (17): 3051 3053 (2002). doi: 10.1063/1.1474619 cited on page 97.

[184] O. M. F. R. S. Lord Rayleigh. *CXII. The problem of the whispering gallery.* The London, Edinburgh, and Dublin Philosophical Magazine and Journal of Science 20 (120): 1001 1004 (1910). doi: 10.1080/14786441008636993 cited on page 97.

[185] S. L. McCall, A. F. J. Levi, R. E. Slusher, S. J. Pearton and R. A. Logan. *Whispering-gallery mode microdisk lasers.* Applied Physics Letters 60 (3): 289 291 (1992). doi: 10.1063/1.106688 cited on page 97.

[186] J. Faist, C. Gmachl, M. Striccoli, C. Sirtori, F. Capasso, D. L. Sivco and A. Y. Cho. *Quantum cascade disk lasers.* Applied Physics Letters 69 (17): 2456 2458 (1996). doi: 10.1063/1.117496 cited on page 98.

[187] L. Mahler, A. Tredicucci, F. Beltram, C. Walther, J. Faist, B. Witzigmann, H. E. Beere and D. A. Ritchie. *Vertically emitting microdisk lasers.* Nature Photonics 3 (1): 46 49 (2009). doi: 10.1038/nphoton.2008.248 cited on page 98.

[188] M. R. Foreman, J. D. Swaim and F. Vollmer. *Whispering gallery mode sensors.* Advances in Optics and Photonics 7 (2): 168 240 (2015). doi: 10.1364/AOP.7.000168 cited on page 98.

[189] C. J. Saraceno, F. Emaury, C. Schriber, M. Hoffmann, M. Golling, T. Südmeyer and U. Keller. *Ultrafast thin-disk laser with 80 μJ pulse energy and 242 W of average power.* Optics Letters 39 (1): 9 12 (2014). doi: 10.1364/OL.39.000009 cited on page 98.

[190] T. J. Johnson. *Silicon microdisk resonators for nonlinear optics and dynamics.* Ph.D. thesis, California Institute of Technology (2009) cited on page 98.

[191] M. Heiblum and J. Harris. *Analysis of curved optical waveguides by conformal transformation.* IEEE Journal of Quantum Electronics 11 (2): 75 83 (1975). doi: 10.1109/JQE.1975.1068563 cited on page 98.

[192] B. Meng, M. Singleton, M. Shahmohammadi, F. Kapsalidis, R. Wang, M. Beck and J. Faist. *Mid-infrared frequency comb from a ring quantum cascade laser.* Optica 7 (2): 162 167 (2020). doi: 10.1364/OPTICA.377755 cited on page 100.

Die approbierte gedruckte Originalversion dieser Dissertation ist an der TU Wien Bibliothek verfügbar.
The approved original version of this doctoral thesis is available in print at TU Wien Bibliothek.

[193] D. Kazakov, N. Opačak, M. Beiser, A. Belyanin, B. Schwarz, M. Piccardo and F. Capasso. *Defect-engineered ring laser harmonic frequency combs.* Optica 8 (10): 1277 1280 (2021). doi: 10.1364/OPTICA.430896 cited on page 100.

[194] M. Jaidl, N. Opačak, M. A. Kainz, S. Schönhuber, D. Theiner, B. Limbacher, M. Beiser, M. Giparakis, A. M. Andrews, G. Strasser, B. Schwarz, J. Darmo and K. Unterrainer. *Comb operation in terahertz quantum cascade ring lasers.* Optica 8 (6): 780 787 (2021). doi: 10.1364/OPTICA.420674 cited on page 100.

[195] M. Piccardo, B. Schwarz, D. Kazakov, M. Beiser, N. Opačak, Y. Wang, S. Jha, J. Hillbrand, M. Tamagnone, W. T. Chen, A. Y. Zhu, L. L. Columbo, A. Belyanin and F. Capasso. *Frequency combs induced by phase turbulence.* Nature 582 (7812): 360 364 (2020). doi: 10.1038/s41586-020-2386-6 cited on page 100.

[196] T. F. Krauss, R. M. De La Rue and P. J. R. Laybourn. *Impact of output coupler configuration on operating characteristics of semiconductor ring lasers.* Journal of Lightwave Technology 13 (7): 1500 1507 (1995). doi: 10.1109/50.400718 cited on page 100.

[197] W. R. McKinnon, D.-X. Xu, C. Storey, E. Post, A. Densmore, A. Delâge, P. Waldron, J. H. Schmid and S. Janz. *Extracting coupling and loss coefficients from a ring resonator.* Optics Express 17 (21): 18971 18982 (2009). doi: 10.1364/OE.17.018971 cited on page 100.

[198] Y. M. Kang, A. Arbabi and L. L. Goddard. *Engineering the spectral reflectance of microring resonators with integrated reflective elements.* Optics Express 18 (16): 16813 16825 (2010). doi: 10.1364/OE.18.016813 cited on page 100.

[199] M. Kneissl, M. Teepe, N. Miyashita, N. M. Johnson, G. D. Chern and R. K. Chang. *Current-injection spiral-shaped microcavity disk laser diodes with unidirectional emission.* Applied Physics Letters 84 (14): 2485 2487 (2004). doi: 10.1063/1.1691494 cited on page 100.

[200] N. Yu, Q. Wang and F. Capasso. *Beam engineering of quantum cascade lasers.* Laser & Photonics Reviews 6 (1): 24 46 (2012). doi: 10.1002/lpor.201100019 cited on page 100.

[201] E. Mujagić, L. K. Hoffmann, S. Schartner, M. Nobile, W. Schrenk, M. P. Semtsiv, M. Wienold, W. T. Masselink and G. Strasser. *Low divergence single-*

TU WIEN Bibliothek Your knowledge hub
Die approbierte gedruckte Originalversion dieser Dissertation ist an der TU Wien Bibliothek verfügbar.
The approved original version of this doctoral thesis is available in print at TU Wien Bibliothek.

mode surface emitting quantum cascade ring lasers. Applied Physics Letters 93 (16): 161101 (2008). doi: 10.1063/1.3000630 cited on page 101.

[202] M. Holzbauer, R. Szedlak, H. Detz, R. Weih, S. Höfling, W. Schrenk, J. Koeth and G. Strasser. *Substrate-emitting ring interband cascade lasers.* Applied Physics Letters 111 (17): 171101 (2017). doi: 10.1063/1.4989514 cited on pages 101, 111, 119, and 120.

[203] J. Hodgkinson and R. P. Tatam. *Optical gas sensing: a review.* Measurement Science and Technology 24 (1): 012004 (2013). doi: 10.1088/0957-0233/24/1/012004 cited on page 101.

[204] T. Udem, R. Holzwarth and T. W. Hänsch. *Optical frequency metrology.* Nature 416: 233 237 (2002). doi: 10.1038/416233a cited on pages 101 and 130.

[205] I. Coddington, N. Newbury and W. Swann. *Dual-comb spectroscopy.* Optica 3 (4): 414 426 (2016). doi: 10.1364/OPTICA.3.000414 cited on pages 101 and 130.

[206] B. Bernhardt, E. Sorokin, P. Jacquet, R. Thon, T. Becker, I. T. Sorokina, N. Picqué and T. W. Hänsch. *Mid-infrared dual-comb spectroscopy with 2.4 μm* Cr^{2+}*:ZnSe femtosecond lasers.* Applied Physics B 100 (1): 3 8 (2010). doi: 10.1007/S00340-010-4080-0 cited on page 101.

[207] Z. Zhang, T. Gardiner and D. T. Reid. *Mid-infrared dual-comb spectroscopy with an optical parametric oscillator.* Optics Letters 38 (16): 3148 3150 (2013). doi: 10.1364/OL.38.003148 cited on page 101.

[208] M. Gianella, A. Nataraj, B. Tuzson, P. Jouy, F. Kapsalidis, M. Beck, M. Mangold, A. Hugi, J. Faist and L. Emmenegger. *High-resolution and gapless dual comb spectroscopy with current-tuned quantum cascade lasers.* Optics Express 28 (5): 6197 6208 (2020). doi: 10.1364/OE.379790 cited on page 101.

[209] M. Lepère, O. Browet, J. Clément, B. Vispoel, P. Allmendinger, J. Hayden, F. Eigenmann, A. Hugi and M. Mangold. *A mid-infrared dual-comb spectrometer in step-sweep mode for high-resolution molecular spectroscopy.* Journal of Quantitative Spectroscopy and Radiative Transfer 287: 108239 (2022). doi: 10.1016/j.jqsrt.2022.108239 cited on page 101.

[210] A. Bauer, K. Rößner, T. Lehnhardt, M. Kamp, S. Höfling, L. Worschech and A. Forchel. *Mid-infrared semiconductor heterostructure lasers for gas sensing*

Die approbierte gedruckte Originalversion dieser Dissertation ist an der TU Wien Bibliothek verfügbar.
The approved original version of this doctoral thesis is available in print at TU Wien Bibliothek.

applications. Semiconductor Science and Technology 26 (1): 014032 (2010). doi: 10.1088/0268-1242/26/1/014032 cited on page 101.

[211] T.-P. Lee, C. Burrus, J. Copeland, A. Dentai and D. Marcuse. *Short-cavity InGaAsP injection lasers: Dependence of mode spectra and single-longitudinal-mode power on cavity length*. IEEE Journal of Quantum Electronics 18 (7): 1101 1113 (1982). doi: 10.1109/JQE.1982.1071656 cited on page 101.

[212] B. Mroziewicz. *External cavity wavelength tunable semiconductor lasers - a review*. Opto-Electronics Review 16 (4): 347 366 (2008). doi: doi:10.2478/s11772-008-0045-9 cited on page 101.

[213] L. Dong, R. Lewicki, K. Liu, P. R. Buerki, M. J. Weida and F. K. Tittel. *Ultra-sensitive carbon monoxide detection by using EC-QCL based quartz-enhanced photoacoustic spectroscopy*. Applied Physics B 107: 275 283 (2012). doi: 10.1007/s00340-012-4949-1 cited on page 102.

[214] C. K. Akhgar, G. Ramer, M. Żbik, A. Trajnerowicz, J. Pawluczyk, A. Schwaighofer and B. Lendl. *The next generation of IR spectroscopy: EC-QCL-based mid-IR transmission spectroscopy of proteins with balanced detection*. Analytical Chemistry 92 (14): 9901 9907 (2020). doi: 10.1021/acs.analchem.0c01406 cited on page 102.

[215] P. Blood. *Quantum confined laser devices: Optical gain and recombination in semiconductors*. Oxford Master Series in Condensed Matter Physics Series. Oxford University Press (2015) cited on page 102.

[216] K. Iga. *Surface-emitting laser-its birth and generation of new optoelectronics field*. IEEE Journal of Selected Topics in Quantum Electronics 6 (6): 1201 1215 (2000). doi: 10.1109/2944.902168 cited on page 103.

[217] W. W. Bewley, C. L. Canedy, C. S. Kim, C. D. Merritt, M. V. Warren, I. Vurgaftman, J. R. Meyer and M. Kim. *Room-temperature mid-infrared interband cascade vertical-cavity surface-emitting lasers*. Applied Physics Letters 109 (15): 151108 (2016). doi: 10.1063/1.4964840 cited on pages 103, 104, 111, 123, and 126.

[218] E. Kapon and A. Sirbu. *Power-efficient answer*. Nature Photonics 3 (1): 27 29 (2009). doi: 10.1038/nphoton.2008.266 cited on pages 103 and 110.

[219] S. Sprengel, F. Demmerle and M.-C. Amann. *Novel InP- and GaSb-based light sources for the near to far infrared*. Semiconductor Science and Technology

Die approbierte gedruckte Originalversion dieser Dissertation ist an der TU Wien Bibliothek verfügbar.
The approved original version of this doctoral thesis is available in print at TU Wien Bibliothek.

31 (11): 113005 (2016). doi: 10.1088/0268-1242/31/11/113005 cited on pages 103 and 110.

[220] B. D. Padullaparthi, J. A. Tatum and K. Iga. *VCSEL Industry: Communication and Sensing*. John Wiley & Sons, Ltd (2021). doi: 10.1002/9781119782223 cited on pages 103 and 110.

[221] G. K. Veerabathran, S. Sprengel, A. Andrejew and M.-C. Amann. *Room-temperature vertical-cavity surface-emitting lasers at 4 µm with GaSb-based type-II quantum wells*. Applied Physics Letters 110 (7): 071104 (2017). doi: 10.1063/1.4975813 cited on pages 103, 110, and 111.

[222] D. I. Babic and S. W. Corzine. *Analytic expressions for the reflection delay, penetration depth, and absorptance of quarter-wave dielectric mirrors*. IEEE Journal of Quantum Electronics 28 (2): 514 524 (1992). doi: 10.1109/3.123281 cited on page 104.

[223] K. Sekartedjo, N. Eda, K. Furuya, Y. Suematsu, F. Koyama and T. Tanbun-Ek. *1.5 µm phase-shifted DFB lasers for single-mode operation*. Electronics Letters 20 (2): 80 81 (1984). doi: 10.1049/el:19840055 cited on page 106.

[224] B. Hinkov. *Radio-frequency modulation of low-dissipation distributed-feedback quantum cascade lasers*. Ph.D. thesis, ETH Zurich (2015) cited on page 106.

[225] C. S. Kim, M. Kim, W. W. Bewley, J. R. Lindle, C. L. Canedy, J. Abell, I. Vurgaftman and J. R. Meyer. *Corrugated-sidewall interband cascade lasers with single-mode midwave-infrared emission at room temperature*. Applied Physics Letters 95 (23): 231103 (2009). doi: 10.1063/1.3272676 cited on page 108.

[226] M. von Edlinger, J. Scheuermann, R. Weih, C. Zimmermann, L. Nähle, M. Fischer, J. Koeth, S. Höfling and M. Kamp. *Monomode interband cascade lasers at 5.2 µm for nitric oxide sensing*. IEEE Photonics Technology Letters 26 (5): 480 482 (2014). doi: 10.1109/LPT.2013.2297447 cited on page 108.

[227] C. S. Kim, M. Kim, J. Abell, W. W. Bewley, C. D. Merritt, C. L. Canedy, I. Vurgaftman and J. R. Meyer. *Mid-infrared distributed-feedback interband cascade lasers with continuous-wave single-mode emission to 80 °C*. Applied Physics Letters 101 (6): 061104 (2012). doi: 10.1063/1.4744445 cited on page 108.

Die approbierte gedruckte Originalversion dieser Dissertation ist an der TU Wien Bibliothek verfügbar.
The approved original version of this doctoral thesis is available in print at TU Wien Bibliothek.

[228] C. S. Kim, M. Kim, J. Abell, W. W. Bewley, C. D. Merritt, C. L. Canedy, I. Vurgaftman and J. R. Meyer. *Mid-IR distributed-feedback interband cascade lasers.* M. Razeghi, editor, *Quantum Sensing and Nanophotonic Devices X*, volume 8631, 329 336. International Society for Optics and Photonics, SPIE (2013). doi: 10.1117/12.2004163 cited on page 108.

[229] C. S. Kim, M. Kim, W. W. Bewley, C. L. Canedy, J. R. Lindle, I. Vurgaftman and J. R. Meyer. *High-power single-mode distributed-feedback interband cascade lasers for the midwave-infrared.* IEEE Photonics Technology Letters 19 (3): 158 160 (2007). doi: 10.1109/LPT.2006.889990 cited on page 108.

[230] C. D. Merritt, W. W. Bewley, C. L. Canedy, C. S. Kim, M. Kim, M. V. Warren, I. Vurgaftman and J. R. Meyer. *Distributed-feedback interband cascade lasers with reduced contact duty cycles.* M. A. Druy and R. A. Crocombe, editors, *Next-Generation Spectroscopic Technologies IX*, volume 9855, 84 89. International Society for Optics and Photonics, SPIE (2016). doi: 10.1117/12.2223178 cited on page 108.

[231] F. Xie, M. Stocker, J. Pham, F. Towner, K. Shen, J. Wang and K. Lascola. *Distributed feedback interband cascade lasers with top grating and corrugated sidewalls.* Applied Physics Letters 112 (13): 131102 (2018). doi: 10.1063/1.5009741 cited on page 108.

[232] M. Kamp, J. Hofmann, F. Schäfer, M. Reinhard, M. Fischer, T. Bleuel, J. P. Reithmaier and A. Forchel. *Lateral coupling a material independent way to complex coupled DFB lasers.* Optical Materials 17 (1): 19 25 (2001). doi: 10.1016/S0925-3467(01)00014-3. Optoelectronics I: Materials and Technologies for Optoelectronic Devices cited on page 109.

[233] M. Kamp, J. Hofmann, A. Forchel, F. Schäfer and J. P. Reithmaier. *Low-threshold high-quantum-efficiency laterally gain-coupled InGaAs/AlGaAs distributed feedback lasers.* Applied Physics Letters 74 (4): 483 485 (1999). doi: 10.1063/1.123164 cited on page 109.

[234] R. Weih, L. Nähle, S. Höfling, J. Koeth and M. Kamp. *Single mode interband cascade lasers based on lateral metal gratings.* Applied Physics Letters 105 (7): 071111 (2014). doi: 10.1063/1.4893788 cited on page 109.

[235] D. Caffey, T. Day, C. S. Kim, M. Kim, I. Vurgaftman, W. W. Bewley, J. R. Lindle, C. L. Canedy, J. Abell and J. R. Meyer. *Performance characteristics of a continuous-wave compact widely tunable external cavity in-*

Die approbierte gedruckte Originalversion dieser Dissertation ist an der TU Wien Bibliothek verfügbar.
The approved original version of this doctoral thesis is available in print at TU Wien Bibliothek.

terband cascade lasers. Optics Express 18 (15): 15691 15696 (2010). doi: 10.1364/OE.18.015691 cited on page 109.

[236] T. R. Tsai, I. Trofimov, C. W. Heaps, M. Maiorov, V. Zeidel, C. S. Kim, M. Kim, C. L. Canedy, W. W. Bewley, J. R. Lindle, I. Vurgaftman, J. R. Meyer and G. Wysocki. *Widely tunable external cavity interband cascade laser for spectroscopic applications. Conference on Lasers and Electro-Optics 2010*, CThM4. Optica Publishing Group (2010). doi: 10.1364/CLEO.2010.CThM4 cited on page 109.

[237] H. Yang, R. Q. Yang, J. Gong and J.-J. He. *Mid-infrared widely tunable single-mode interband cascade lasers based on V-coupled cavities.* Optics Letters 45 (10): 2700 2703 (2020). doi: 10.1364/OL.391308 cited on page 109.

[238] E. Mujagić, C. Schwarzer, Y. Yao, J. Chen, C. Gmachl and G. Strasser. *Two-dimensional broadband distributed-feedback quantum cascade laser arrays.* Applied Physics Letters 98 (14): 141101 (2011). doi: 10.1063/1.3574555 cited on page 109.

[239] C. Schwarzer, R. Szedlak, S. I. Ahn, T. Zederbauer, H. Detz, A. M. Andrews, W. Schrenk and G. Strasser. *Linearly polarized light from substrate emitting ring cavity quantum cascade lasers.* Applied Physics Letters 103 (8): 081101 (2013). doi: 10.1063/1.4819034 cited on pages 109 and 127.

[240] R. Szedlak, C. Schwarzer, T. Zederbauer, H. Detz, A. M. Andrews, W. Schrenk and G. Strasser. *On-chip focusing in the mid-infrared: Demonstrated with ring quantum cascade lasers.* Applied Physics Letters 104 (15): 151105 (2014). doi: 10.1063/1.4871520 cited on pages 109, 126, and 127.

[241] H. Soda, K. Iga, C. Kitahara and Y. Suematsu. *GaInAsP/InP surface emitting injection lasers.* Japanese Journal of Applied Physics 18 (12): 2329 2330 (1979). doi: 10.1143/jjap.18.2329 cited on page 110.

[242] A. Andrejew, S. Sprengel and M.-C. Amann. *GaSb-based vertical-cavity surface-emitting lasers with an emission wavelength at 3 µm.* Optics Letters 41 (12): 2799 2802 (2016). doi: 10.1364/ol.41.002799 cited on pages 110 and 111.

[243] V. Jayaraman, B. Kolasa, C. Lindblad, A. Cazabat, C. Burgner, S. Segal, K. Lascola, F. Towner and F. Xie. *Tunable room-temperature continuous-wave mid-infrared VCSELs.* L. A. Graham and C. Lei, editors, *Vertical-Cavity*

Die approbierte gedruckte Originalversion dieser Dissertation ist an der TU Wien Bibliothek verfügbar.
The approved original version of this doctoral thesis is available in print at TU Wien Bibliothek.

Surface-Emitting Lasers XXIV, volume 11300, 115 123. International Society for Optics and Photonics, SPIE (2020). doi: 10.1117/12.2541514 cited on pages 110, 111, and 123.

[244] M. Jetter and P. Michler. *Vertical External Cavity Surface Emitting Lasers: VECSEL Technology and Applications.* John Wiley & Sons, Ltd (2021). doi: 10.1002/9783527807956.ch1 cited on page 111.

[245] H. Kahle, C. M. N. Mateo, U. Brauch, P. Tatar-Mathes, R. Bek, M. Jetter, T. Graf and P. Michler. *Semiconductor membrane external-cavity surface-emitting laser (MECSEL).* Optica 3 (12): 1506 1512 (2016). doi: 10.1364/OPTICA.3.001506 cited on page 111.

[246] V. Jayaraman, S. Segal, F. Towner, K. Lascola, B. Kolasa, D. John, A. Cazabat and C. Burgner. *Room-temperature continuous-wave electrically pumped 3.3 micron vertical cavity laser. 2019 Conference on Lasers and Electro-Optics Europe & European Quantum Electronics Conference (CLEO/Europe-EQEC)*, 1. IEEE (2019). doi: 10.1109/CLEOE-EQEC.2019.8872766 cited on page 111.

[247] W. W. Bewley, C. L. Canedy, C. S. Kim, M. Kim, J. R. Lindle, J. Abell, I. Vurgaftman and J. R. Meyer. *Ridge-width dependence of midinfrared interband cascade laser characteristics.* Optical Engineering 49 (11): 111116 (2010). doi: 10.1117/1.3498772 cited on page 119.

[248] *Comsol inc. comsol multiphysics ®.* `https://www.comsol.de/`. Accessed: 2022-06-16 cited on page 120.

[249] E. Mujagić, S. Schartner, L. K. Hoffmann, W. Schrenk, M. P. Semtsiv, M. Wienold, W. T. Masselink and G. Strasser. *Grating-coupled surface emitting quantum cascade ring lasers.* Applied Physics Letters 93 (1): 011108 (2008). doi: 10.1063/1.2958910 cited on page 126.

[250] R. Szedlak, M. Holzbauer, D. MacFarland, T. Zederbauer, H. Detz, A. M. Andrews, C. Schwarzer, W. Schrenk and G. Strasser. *The influence of whispering gallery modes on the far field of ring lasers.* Scientific Reports 5: 16668 (2015). doi: 10.1038/srep16668 cited on page 127.

[251] G. Villares, A. Hugi, S. Blaser and J. Faist. *Dual-comb spectroscopy based on quantum-cascade-laser frequency combs.* Nature Communications 5: 5192 (2014). doi: 10.1038/ncomms6192 cited on page 130.

Die approbierte gedruckte Originalversion dieser Dissertation ist an der TU Wien Bibliothek verfügbar.
The approved original version of this doctoral thesis is available in print at TU Wien Bibliothek.

[252] O. Spitz, P. Didier, L. Durupt, D. A. Díaz-Thomas, A. N. Baranov, L. Cerutti and F. Grillot. *Free-space communication with directly modulated mid-infrared quantum cascade devices.* IEEE Journal of Selected Topics in Quantum Electronics 28 (1): 1 9 (2022). doi: 10.1109/JSTQE.2021.3096316 cited on pages 130 and 143.

[253] X. Pang, R. Schatz, M. Joharifar, A. Udalcovs, V. Bobrovs, L. Zhang, X. Yu, Y.-T. Sun, G. Maisons, M. Carras, S. Popov, S. Lourdudoss and O. Ozolins. *Direct modulation and free-space transmissions of up to 6 Gbps multilevel signals with a 4.65-μm quantum cascade laser at room temperature.* Journal of Lightwave Technology 40 (8): 2370 2377 (2022). doi: 10.1109/JLT.2021.3137963 cited on pages 130 and 143.

[254] B. Behroozpour, P. A. M. Sandborn, M. C. Wu and B. E. Boser. *Lidar system architectures and circuits.* IEEE Communications Magazine 55 (10): 135 142 (2017). doi: 10.1109/MCOM.2017.1700030 cited on page 130.

[255] Y. Gong, L. Bu, B. Yang and F. Mustafa. *High repetition rate mid-infrared differential absorption lidar for atmospheric pollution detection.* Sensors 20 (8) (2020). doi: 10.3390/s20082211 cited on page 130.

[256] J. L. Klocke, M. Mangold, P. Allmendinger, A. Hugi, M. Geiser, P. Jouy, J. Faist and T. Kottke. *Single-shot sub-microsecond mid-infrared spectroscopy on protein reactions with quantum cascade laser frequency combs.* Analytical Chemistry 90 (17): 10494 10500 (2018). doi: 10.1021/acs.analchem.8b02531 cited on page 130.

[257] N. H. Pinkowski, Y. Ding, C. L. Strand, R. K. Hanson, R. Horvath and M. Geiser. *Dual-comb spectroscopy for high-temperature reaction kinetics.* Measurement Science and Technology 31 (5): 055501 (2020). doi: 10.1088/1361-6501/ab6ecc cited on page 130.

[258] J. Hillbrand, D. Auth, M. Piccardo, N. Opačak, E. Gornik, G. Strasser, F. Capasso, S. Breuer and B. Schwarz. *In-phase and anti-phase synchronization in a laser frequency comb.* Physical Review Letters 124 (2): 023901 (2020). doi: 10.1103/PhysRevLett.124.023901 cited on page 130.

[259] C. Verie and M. Sirieix. *Gigahertz cutoff frequency capabilities of CdHgTe photovoltaic detectors at 10.6 μ.* IEEE Journal of Quantum Electronics 8 (2): 180 184 (1972). doi: 10.1109/JQE.1972.1076934 cited on page 130.

Die approbierte gedruckte Originalversion dieser Dissertation ist an der TU Wien Bibliothek verfügbar.
The approved original version of this doctoral thesis is available in print at TU Wien Bibliothek.

[260] A. Rogalski. *HgCdTe infrared detector material: history, status and outlook.* Reports on Progress in Physics 68 (10): 2267 2336 (2005). doi: 10.1088/0034-4885/68/10/r01 cited on page 130.

[261] B. F. Levine. *Quantum-well infrared photodetectors.* Journal of Applied Physics 74 (8): R1 R81 (1993). doi: 10.1063/1.354252 cited on page 130.

[262] H. C. Liu, J. Li, M. Buchanan and Z. R. Wasilewski. *High-frequency quantum-well infrared photodetectors measured by microwave-rectification technique.* IEEE Journal of Quantum Electronics 32 (6): 1024 1028 (1996). doi: 10.1109/3.502380 cited on page 130.

[263] P. D. Grant, R. Dudek, M. Buchanan and H. C. Liu. *Room-temperature heterodyne detection up to 110 GHz with a quantum-well infrared photodetector.* IEEE Photonics Technology Letters 18 (21): 2218 2220 (2006). doi: 10.1109/LPT.2006.884267 cited on page 130.

[264] N. Rahimi, A. A. Aragon, O. S. Romero, D. M. Shima, T. J. Rotter, G. Balakrishnan, S. D. Mukherjee and L. F. Lester. *Ultra-low resistance NiGeAu and PdGeAu ohmic contacts on N-GaSb grown on GaAs.* *2013 IEEE 39th Photovoltaic Specialists Conference (PVSC)*, 2123 2126 (2013). doi: 10.1109/PVSC.2013.6744893 cited on page 134.

[265] E. A. Plis, M. N. Kutty and S. Krishna. *Passivation techniques for InAs/GaSb strained layer superlattice detectors.* Laser & Photonics Reviews 7 (1): 45 59 (2013). doi: 10.1002/lpor.201100029 cited on page 137.

[266] N. W. Khan, F. Rothmayr, A. Bader, F. Hartmann, R. Weih, J. Koeth and S. Höfling. *Process optimization of sulfur passivated interband cascade infrared photodetectors.* Mirsens - 5th international workshop on opportunities and challenges in mid-infrared laser-based gas sensing (2022) cited on page 137.

[267] D. Burghoff, Y. Yang, D. J. Hayton, J.-R. Gao, J. L. Reno and Q. Hu. *Evaluating the coherence and time-domain profile of quantum cascade laser frequency combs.* Optics Express 23 (2): 1190 1202 (2015). doi: 10.1364/OE.23.001190 cited on page 142.

[268] M. Singleton, P. Jouy, M. Beck and J. Faist. *Evidence of linear chirp in mid-infrared quantum cascade lasers.* Optica 5 (8): 948 953 (2018). doi: 10.1364/OPTICA.5.000948 cited on page 142.

Die approbierte gedruckte Originalversion dieser Dissertation ist an der TU Wien Bibliothek verfügbar.
The approved original version of this doctoral thesis is available in print at TU Wien Bibliothek.

[269] J. Hillbrand, A. M. Andrews, H. Detz, G. Strasser and B. Schwarz. *Coherent injection locking of quantum cascade laser frequency combs*. Nature Photonics 13: 101 104 (2019). doi: 10.1038/s41566-018-0320-3 cited on page 142.

[270] O. Spitz, S. Zhao, P. Didier, D. A. Díaz-Thomas, L. Cerutti, A. N. Baranov, H. Knötig, B. Schwarz and F. Grillot. *Interband cascade technology for next-generation mid-IR communication and quantum applications*. IEEE Summer Topicals Meeting Series (2022) cited on page 143.

[271] A. Lardschneider, H. Knötig, R. Weih, P. Didier, O. Spitz, J. Koeth, F. Grillot and B. Schwarz. *Interband cascade infrared photodetectors for high-speed applications*. Mirsens - 5th international workshop on opportunities and challenges in mid-infrared laser-based gas sensing (2022) cited on page 143.

[272] P. Didier, O. Spitz, L. Cerutti, D. A. Díaz-Thomas, A. N. Baranov, M. Carras and F. Grillot. *Relative intensity noise and intrinsic properties of RF mounted interband cascade laser*. Applied Physics Letters 119 (17): 171107 (2021). doi: 10.1063/5.0070981 cited on page 143.

[273] R. Szedlak, A. Harrer, M. Holzbauer, B. Schwarz, J. P. Waclawek, D. MacFarland, T. Zederbauer, H. Detz, A. M. Andrews, W. Schrenk, B. Lendl and G. Strasser. *Remote sensing with commutable monolithic laser and detector*. ACS Photonics 3 (10): 1794 1798 (2016). doi: 10.1021/acsphotonics.6b00603 cited on page 146.

Die approbierte gedruckte Originalversion dieser Dissertation ist an der TU Wien Bibliothek verfügbar.
The approved original version of this doctoral thesis is available in print at TU Wien Bibliothek.

TU WIEN Bibliothek Your knowledge hub

Die approbierte gedruckte Originalversion dieser Dissertation ist an der TU Wien Bibliothek verfügbar.
The approved original version of this doctoral thesis is available in print at TU Wien Bibliothek.
TU WIEN Bibliothek Your knowledge hub

ABBREVIATIONS

Abbreviations

AR	anti-reflection
BER	bit error rate
cw	continuous wave
DBR	distributed Bragg reflector
DFB	distributed feedback
DTGS	deuterated triglycine sulfate
EC	external cavity
EDQE	external differential quantum efficiency
FIB	focussed ion beam
FM	frequency-modulated
FSR	free spectral range
FTIR	Fourier transform infrared spectrometer
GSG	ground-source-ground
HR	high-reflectivity
h-QW	hole quantum well
ICD	interband cascade detector
ICL	interband cascade laser
ICIP	interband cascade infrared photodetector
ICP	inductively coupled plasma
lidar	light detection and ranging
LIV	light-current-voltage
MBE	molecular beam epitaxy
MCT	mercury cadmium telluride
MECSEL	membrane external cavity surface emitting laser
MEMS	micro-electromechanical system
NEP	noise equivalent power
PCB	printed circuit board
PECVD	plasma enhanced chemical vapor deposition
QCD	quantum cascade detector
QCL	quantum cascade laser
QW	quantum well

QWIP	quantum well infrared photodetector
RF	radio frequency
RIE	reactive ion etching
RTA	rapid thermal annealing
SCL	separate-confinement layer
SEM	scanning electron microscope
SMI	semimetallic interface
SMSR	side mode suppression ratio
SNR	signal to noise ratio
SRH	Shockley-Read-Hall
SWIFTS	shifted wave interference Fourier transform spectroscopy
TEC	thermoelectric cooler
VCSEL	vertical cavity surface emitting laser
VECSEL	vertical external cavity surface emitting laser

Die approbierte gedruckte Originalversion dieser Dissertation ist an der TU Wien Bibliothek verfügbar.
The approved original version of this doctoral thesis is available in print at TU Wien Bibliothek.
TU WIEN Bibliothek Your knowledge hub

LIST OF PUBLICATIONS

Journal publications

J1 J. Nauschütz, H. Knötig, R. Weih, J. Scheuermann, J. Koeth, S. Höfling, B. Schwarz, *Pushing the room temperature continuous-wave operation limit of GaSb-based interband cascade lasers beyond 6 µm*, **arXiv**:2207.11113 (2022), doi: 10.48550/arXiv.2207.11113.

J2 H. Knötig, J. Nauschütz, N. Opačak, S. Höfling, J. Koeth, R. Weih, B. Schwarz, *Mitigating valence intersubband absorption in interband cascade lasers*, **Laser & Photonics Reviews** 2022, 2200156, doi: 10.1002/lpor.202200156.

J3 M. Giparakis, H. Knötig, H. Detz, M. Beiser, W. Schrenk, B. Schwarz, G. Strasser, A. M. Andrews, *2.7 µm quantum cascade detector: Above band gap energy intersubband detection*, **Applied Physics Letters** 120 (7), 071104 (2022), doi: 10.1063/5.0076856

J4 J. Hillbrand, L. M. Krüger, S. Dal Cin, H. Knötig, J. Heidrich, A. M. Andrews, G. Strasser, U. Keller, B. Schwarz, *High-speed quantum cascade detector characterized with a mid-infrared femtosecond oscillator*, **Optics Express** 29 (4), 5774 5781 (2021), doi: 10.1364/OE.417976

J5 H. Knötig, B. Hinkov, R. Weih, S. Höfling, J. Koeth, J., G. Strasser, *Continuous-wave operation of vertically emitting ring interband cascade lasers at room temperature*, **Applied Physics Letters** 116 (13), 131101 (2020), doi: 10.1063/1.5139649

Die approbierte gedruckte Originalversion dieser Dissertation ist an der TU Wien Bibliothek verfügbar.
The approved original version of this doctoral thesis is available in print at TU Wien Bibliothek.

Invited oral presentations

I1 B. Hinkov, M. David, G. Marschick, E. Arigliani, F. Pilat, P. Souza, H. Knötig, I. Doganlar, A. Lardschneider, N. Brandacher, D. Koukola, A. Schwaighofer, B. Lendl, G. Strasser, *Mid-IR photonic integrated circuits for on-chip applications in liquid sensing and telecom*, Optaphi Meeting, Vienna, June 21, 2022

I2 H. Knötig, B. Hinkov, R. Weih, B. Schwarz, S. Lindner, J. P. Waclawek, B. Lendl, S. Höfling, J. Koeth, G. Strasser, *Vertically emitting ring interband cascade lasers*, Photonics West, virtual, Mar 6 - 11, 2021

I3 G. Strasser, J. Hillbrand, H. Knötig, S. Dal Cin, R. Weih, A. M. Andrews, H. Detz, B. Schwarz, *Frequency performance of intersubband detectors*, Photonics West, virtual, Mar 6 - 11, 2021

I4 B. Hinkov, H. Knötig, F. Pilat, S. Lindner, R. Weih, B. Schwarz, W. Schrenk, L. Lux, H. Detz, A. M. Andrews, B. Baumgartner, J.P. Waclawek, J. Koeth, S. Höfling, B. Lendl, G. Strasser, *Mid-infrared lasers for spectroscopic applications*, Online Conference 1st Laser Components Talks, virtual, Dec 1 - 2, 2020

I5 H. Knötig, A. M. Andrews, B. Hinkov, R. Weih, J. Koeth, B. Schwarz, G. Strasser, *Interband cascade and quantum cascade ring lasers*, Conference on Lasers and Electro-Optics (CLEO) US, virtual, May 10 - 15, 2020

Oral presentations

O1 O. Spitz, S. Zhao, P. Didier, D. Diaz-Thomas, L. Cerutti, A. Baranov, H. Knötig, R. Weih, J. Koeth, B. Schwarz, F. Grillot, *Interband cascade technology for next-generation mid-IR communication and quantum applications*, IEEE Summer Topicals Meeting Series, Cabo San Lucas, Mexico, July 11 - 13, 2022

O2 H. Knötig, J. Nauschütz, N. Opačak, S. Höfling, J. Koeth, R. Weih, B. Schwarz, *Improving interband cascade laser performance: mitigating valence intersubband absorption*, Mirsens, Wrocław, Poland, July 4 - 6, 2022

O3 A. Lardschneider, H. Knötig, R. Weih, P. Didier, O. Spitz, J. Koeth, F. Grillot, B. Schwarz, *Interband cascade infrared photodetectors for high-speed applications*, Mirsens, Wrocław, Poland, July 4 - 6, 2022

Die approbierte gedruckte Originalversion dieser Dissertation ist an der TU Wien Bibliothek verfügbar.
The approved original version of this doctoral thesis is available in print at TU Wien Bibliothek.

O4 J. Nauschütz, H. Knötig, R. Weih, J. Koeth, B. Schwarz, S. Höfling, *GaSb-based interband cascade lasers beyond 6 µm*, Mirsens, Wrocław, Poland, July 4 - 6, 2022

O5 H. Knötig, R. Szedlak, J. Nauschütz, R. Weih, N. Opačak, S. Höfling, J. Koeth, G. Strasser, B. Schwarz, *The relevance of valence band engineering in interband cascade lasers*, Photonics Europe, Strasbourg, France, Apr 4 - 7, 2022

O6 H. Knötig, R. Weih, N. Opačak, J. Koeth, G. Strasser, B. Schwarz, *Improving the performance of interband cascade lasers: the influence of intersubband transitions in the valence band*, European Semiconductor Laser Workshop (ESLW), virtual, Sep 17 - 18, 2021

O7 M. Beiser, M. Giparakis, H. Knötig, H. Detz, B. Schwarz, A. M. Andrews, G. Strasser, *Strain balancing for InAs based ICL growth*, 21st International Conference on Molecular Beam Epitaxy (ICMBE), virtual, Sep 6 - 9, 2021

O8 H. Knötig, R. Weih, N. Opačak, S. Höfling, J. Koeth, G. Strasser, B. Schwarz, *Interband cascade lasers: beating intersubband transitions*, Annual Meeting of the Austrian & Swiss Phys. Soc., Innsbruck, Austria, Aug 30 - Sep 3, 2021

O9 R. Szedlak, H. Knötig, B. Hinkov, R. Weih, S. Höfling, W. Schrenk, J. Koeth, J.P. Waclawek, B. Lendl, G. Strasser, *Continuous-wave ring interband cascade lasers for spectroscopic sensing*, Annual Meeting of the Austrian & Swiss Phys. Soc., Innsbruck, Austria, Aug 30 - Sep 3, 2021

O10 M. Giparakis, H. Knötig, M. Beiser, H. Detz, W. Schrenk, B. Schwarz, G. Strasser, A. M. Andrews, *InAs/AlAsSb quantum cascade detector below 3 µm*, Annual Meeting of the Austrian & Swiss Phys. Soc., Innsbruck, Austria, Aug 30 - Sep 3, 2021

O11 H. Knötig, R. Weih, N. Opačak, S. Höfling, G. Strasser, B. Schwarz, *Interband cascade lasers: overcoming intersubband transitions in the valence band*, Photonica, Belgrad, Serbia, Aug 23 - 27, 2021

O12 B. Hinkov, H. Knötig, J.P. Waclawek, B. Lendl, G. Strasser, R. Weih, J. Koeth, S. Höfling, *Continous-wave surface-emitting ring interband cascade lasers*, Compound Semiconductor Week (CSW), virtual, May 9 - 13, 2021

O13 H. Knötig, B. Hinkov, R. Weih, S. Höfling, W. Schrenk, J. Koeth, J.P. Waclawek, B. Lendl, G. Strasser, *Continuos-wave operation of ring interband*

Die approbierte gedruckte Originalversion dieser Dissertation ist an der TU Wien Bibliothek verfügbar.
The approved original version of this doctoral thesis is available in print at TU Wien Bibliothek.
TU WIEN Bibliothek Your knowledge hub

cascade lasers, Infrared Teraherz Quantum Workshop (ITQW), Ojai, USA, Sep 15 - 20, 2019

O14 S. Lancaster, J. Hillbrand, H. Knötig, M. Schinnerl, R. Weih, A. Schade, S. Höfling, W. Schrenk, A. M. Andrews, H. Detz, J.P. Waclawek, B. Lendl, B. Schwarz, G. Strasser, *Deep etching of interband cascade laser waveguides*, Workshop on Dry Processing for Nanoelectronics & Micromechanics Deposition & Etching, Vienna, Austria, Sep 17 - 18, 2019

O15 H. Knötig, B. Hinkov, R. Weih, S. Höfling, W. Schrenk, J. Koeth, J.P. Waclawek, B. Lendl, G. Strasser, *Ring interband cascade lasers running in continuous mode operation*, Annual Meeting of the Austrian & Swiss Phys. Soc., Zurich, Switzerland, Aug 26 - 30, 2019

O16 H. Knötig, B. Hinkov, M. Holzbauer, R. Szedlak, H. Detz, R. Weih, S. Höfling, W. Schrenk, J. Koeth, J.P. Waclawek, B. Lendl, G. Strasser, *Vertically emitting interband cascade lasers*, nanoNET-meeting, Vienna Austria, Jul 12, 2019

O17 H. Knötig, B. Hinkov, M. Holzbauer, R. Szedlak, H. Detz, R. Weih, S. Höfling, W. Schrenk, J. Koeth, J.P. Waclawek, B. Lendl, G. Strasser, *Ring interband cascade lasers for environmental monitoring*, CLEO Europe & European Quantum Electronics Conference (EQEC), Munich, Germany, Jun 23 - 27, 2019

O18 B. Hinkov, H. Knötig, M. Holzbauer, R. Szedlak, H. Detz, R. Weih, S. Höfling, W. Schrenk, J. Koeth, J.P. Waclawek, B. Lendl, G. Strasser, *Interband cascade lasers for trace gas sensing*, International WORKshop on Infrared Technologies, Olching, Germany, Nov 12 - 13, 2018

O19 H. Knötig, M. Holzbauer, B. Hinkov, R. Szedlak, H. Detz, R. Weih, S. Höfling, W. Schrenk, J. Koeth, J.P. Waclawek, B. Lendl, G. Strasser, *Ring interband cascade lasers for trace gas sensing*, Field Laser Applications in Industry and Research (FLAIR), Santa Maria degli Angeli, Italy, Sep 10 -14, 2018

O20 B. Hinkov, H. Knötig, M. Beiser, N. Opacak, M. Holzbauer, R. Szedlak, H. Detz, R. Weih, S. Höfling, W. Schrenk, J. Koeth, G. Strasser, *Surface emitting ring interband cascade lasers*, 68th Yearly Meeting of the Austrian Physical Society, Graz, Austria, Sep 10 - 13, 2018

Die approbierte gedruckte Originalversion dieser Dissertation ist an der TU Wien Bibliothek verfügbar.
The approved original version of this doctoral thesis is available in print at TU Wien Bibliothek.
TU WIEN Bibliothek Your knowledge hub

Poster presentations

P1 M. Giparakis, H. Knötig, H. Detz, M. Beiser, B. Schwarz, W. Schrenk, G. Strasser, A. M. Andrews, *Growth, design, and characterisation of an InAs/AlAsSb-based QCD at 2.7 µm*, German MBE Workshop, virtual, Oct 14 - 15, 2021

P2 M. Giparakis, H. Knötig, M. Beiser, H. Detz, W. Schrenk, B. Schwarz, G. Strasser, A. M. Andrews, *InAs/AlAsSb-based quantum cascade detector at 2.7 µm*, CLEO Europe & EQEC, virtual, Jun 21 - 25, 2021

P3 M. Giparakis, H. Knötig, M. Beiser, J. Hillbrand, H. Detz, W. Schrenk, B. Schwarz, G. Strasser, A. M. Andrews, *2.7 µm short-wavelength InAs/AlAsSb quantum cascade detector*, International Quantum Cascade Laser School & Workshop (IQCLSW), virtual, Sep 7 - 10, 2020

P4 H. Knötig, B. Hinkov, R. Weih, S. Höfling, J. Koeth, J.P. Waclawek, S. Lindner, B. Lendl, G. Strasser, *Ring interband cascade lasers emitting in continuous-wave mode at room temperature*, 21st International Winterschool on New Developments in Solid State Physics, Mauterndorf, Austria, Feb 23 - 28, 2020.

P5 H. Knötig, M. Holzbauer, R. Szedlak, H. Detz, R. Weih, S. Höfling, W. Schrenk, J. Koeth, B. Hinkov und G. Strasser, *Ring interband cascade laser arrays*, IQCLSW, Cassis, France. Jul 2 - 7, 2018

P6 H. Knötig, M. Holzbauer, R. Szedlak, H. Detz, R. Weih, S. Höfling, W. Schrenk, J. Koeth, B. Hinkov, G. Strasser, *Ring interband cascade lasers for spectroscopic applications*, 20th International Winterschool on New Developments in Solid State Physics, Mauterndorf, Austria, Feb 25 - Mar 2, 2018

Die approbierte gedruckte Originalversion dieser Dissertation ist an der TU Wien Bibliothek verfügbar.
The approved original version of this doctoral thesis is available in print at TU Wien Bibliothek.

Hedwig Maria Knötig

Personal information

Date and place of birth	[redacted]
Address	[redacted]
Phone	[redacted]
E-Mail	hedwig.knoetig@tuwien.ac.at

Education

11/2018 - today **Dr.techn. (equiv. PhD) in Electrical Engineering, TU Wien**

- University/Project Assistant at the Institute of Solid State Electronics
- Fabrication and characterization of optoelectronic devices
- High-speed mid-infrared intersubband and interband detectors
- Design and simulation of interband cascade lasers

08/2015 – 10/2018 **Dipl.-Ing. (equiv. MSc.) in Technical Physics (with distinction), TU Wien**

- Special field: applied physics
- Thesis: "Characterization of single-mode emitting interband cascade lasers and their application in 2f-wavelength modulation spectroscopy"

09-12/2016 **Exchange semester, McMaster University**

- Visiting graduate student via the TASSEP exchange program

10/2012 – 08/2015 **BSc. in Technical Physics (with distinction), TU Wien**

- Thesis: "Towards a nuclear structure approach of alpha-nucleus optical potentials: coupling interaction"

09/2008 – 06/2012 **A-levels (with distinction), High school with focus on science**

- Field of attention: foreign languages

Scholarships and awards

02/2022	**Christiana Hörbiger Award**, Funding for the international mobility of young scientists
09/2021	**Best student presentation award**, European Semiconductor Laser Workshop 2021, Paris, France (online)
09/2019	**Best student presentation award**, Infrared Terahertz Quantum Workshop 2019, Ojai, USA
01/2019	**Christiana Hörbiger Award**, Funding for the international mobility of young scientists
2014 & 2015	**Leistungsstipendium**, Scholarships for excellence, TU Wien

Die approbierte gedruckte Originalversion dieser Dissertation ist an der TU Wien Bibliothek verfügbar.
The approved original version of this doctoral thesis is available in print at TU Wien Bibliothek.